LNS-228

MAGNETIC AND ELECTRONIC PROPERTIES OF THE HIGH-TEMPERATURE SUPERCONDUCTOR $La_{2-x}Sr_xCuO_4$

Dissertation

Johan Chang

Laboratorium für Neutronenstreuung
Eidg. Technische Hochschule Zürich
CH-5232 Villigen PSI

2008

Diss. ETH No. 17699

MAGNETIC AND ELECTRONIC PROPERTIES OF THE HIGH-TEMPERATURE SUPERCONDUCTOR $La_{2-x}Sr_xCuO_4$

A dissertation submitted to the
SWISS FEDERAL INSTITUTE OF TECHNOLOGY ZURICH
for the degree of
Doctor of Sciences

presented by
JOHAN CHANG
Dipl. Phys. ETH
born 03.09.1978

accepted on the recommendation of
Prof. Dr. B. Batlogg, examiner
Prof. Dr. J. Mesot, co-examiner

2008

Abstract

Strongly correlated electron compounds form a category of materials that exhibit unusual metallic properties. The electrons in these materials live in a 'twilight' regime between localized and itinerant electronic behaviors. They can be described neither by insulator physics nor by standard metal physics. These materials are often characterized by magnetic and electronic states that compete for the ground state at zero temperature. Small perturbations in the chemical composition or in the sample environment may change the balance between the competing orders and hence lead to dramatic changes in the physical properties.

This thesis is an experimental study of the strongly correlated electron system $La_{2-x}Sr_xCuO_4$, a compound known to become superconducting at low-temperatures for $0.05 < x < 0.26$. The relation between strongly correlated electrons and superconductivity is an active field of research in solid state physics. Despite enormous efforts, superconductivity in the copper-oxide materials is a problem that defies a solution for more than twenty years. The phase diagram of these materials is extremely rich and complex. A precise characterization may therefore be the key to reveal the salient features responsible for superconductivity. In this thesis work a series of very high quality single crystals of $La_{2-x}Sr_xCuO_4$ with $0.10 < x < 0.22$ was studied experimentally. Insight into the magnetic degrees of freedom is gained through neutron scattering and the electronic quasiparticle excitation spectrum is investigated by angle resolved photoemission spectroscopy.

A fresh view on the vortex lattice, incommensurate antiferromagnetic order, and quasiparticle scattering rate in LSCO is presented here.

Résumé

Les matériaux fortement corrélés sont des composés présentant des propriétés métalliques inhabituelles. Les électrons appartenant à ces matériaux se situent dans un régime intermédiaire où ils sont localisés et pouvant tout de même engendrer des comportements électroniques. Ces systèmes ne peuvent être dècrits ni par la physique des isolants ni par celle des mètaux. Ces composés sont souvent caractérisés par des états magnétiques et électroniques rivalisant avec l'état fondamental à la température zéro. De petites perturbations telles que dans la composition chimique ou environnementales peuvent créer sur l'échantillon un déséquilibre des ordres et par conséquent, engendrer des modifications s ur leurs propriétés physiques.

Cette thèse présente l'étude expérimentale du composé fortement corrélés $La_{2-x}Sr_xCuO_4$ connu pour être supraconducteur à basse température pour $0.05 < x < 0.26$. La relation entre les systèmes à électrons fortement corrélés et les supraconducteurs est un sujet de recherche très actif notamment dans la physique des solides. En effet, malgré d'énormes efforts depuis vingt ans, la supraconductivité dans les cuprates reste nexpliquée. De plus, leur diagramme de phases est riche et complexe. Une caractérisation plus précise révléerait peut être les agents responsable de la supraconductivité.

Dans ce travail de thèse, une série de cristaux $La_{2-x}Sr_xCuO_4$ de grande qualité avec $0.10 < x < 0.22$, a été étudiée expérimentalement. Les degrés de libertés magnétiques et les spectres d'excitations de quasi-particules ont été respectivement étudiés par diffusion de neutrons et par photoémission résolue en angle. Une nouvelle vue sur les vortex, l'incommensurable ordre antiferromagnétique et le taux de dispersion des quasi-particules dans LSCO y sont présentés.

ABBREVIATIONS AND ACRONYMS

Constants and Quantities:

$k_B = 0.08617343$ meV/K = Boltzmann's constant
$\hbar = h/(2\pi) = 0.66 \cdot 10^{-15}$ eVs = Planck's constant
$e = 1.6022 \cdot 10^{-19}$ C = electronic charge
$p_i = Z^{-1} \exp(-\beta E_i)$=occurrence of an initial state
T_c=Critical temperature for superconductivity
ξ = coherence length
$\kappa = 1/\xi$ = inverse coherence length
τ = life time
$\beta = \frac{1}{k_B T}$
λ = penetration depth
λ_n = neutron wavelength
ℓ = mean free path
m_n = mass of an neutron
m_e = mass of an electron
$\mu_N = e\hbar/(2m_n)$
$\mu_B = e\hbar/(2m_e)$
$\gamma_n = 1.913$
$r_0 = \frac{\mu_0}{4\pi}\frac{e^2}{m_e}$
μ=chemical potential
n_s= super fluid density
v_F= Fermi velocity
E_F = Fermi Energy
k_F = Fermi momentum
σ_{ab} = in-plane conductivity
$\rho_{ab} = 1/\sigma_{ab}$ = in-plane resistivity
ρ_c= out-of-plane resistivity
$\Phi_0 = \frac{\hbar}{2e}$=flux quantum
Δ_{SG}= Spin gap
Δ_{SC}= Superconducting gap
Δ^*= Pseudo gap
$\gamma = \sqrt{\rho_c/\rho_{ab}}$=anisotropy factor
T^*=Pseudo gap temperature
2θ= scattering angle
H_{c1}= lower critical field
H_{c2}= upper critical field
H_{cr}= 3D-to-2D crossover field
$H_{\square}$= onset field of the square lattice
k_f= final wavevector
k_i= initial wavevector
E_f= final Energy
E_i= initial Energy
J= antiferromagnetic exchange interaction

Functions:
$\Sigma(\mathbf{k},\omega)$ = Self-energy function
$\mathcal{A}(\mathbf{k},\omega)$ = Spectral function
χ= Response function
$Z = \sum_s \exp(-\beta E_s)$ = partition function
$f(\omega) = \frac{1}{1+\exp(\beta[\omega-\mu])}$
$\mathcal{F}(\mathbf{Q})$= Form factor
$\mathcal{S}(\mathbf{Q},\omega)$= Scattering function
$\mathcal{C}(\mathbf{q},\omega)$ = Correlation function
$\mathcal{G}$ = Greens function
$\mathcal{W}$ = Transisiton probability
$\mathcal{M}$ = ARPES matrix element

Common abbreviations
ZF=Zero field
ZFC= Zero field cooling
FC= Field cooling
BZ = Brillioun zone
QCP= Quantum Critical point
QP= Quasi particle
FS= Fermi surface
VL= Vortex lattice

Materials:
LSCO=$La_{2-x}Sr_xCuO_4$
LBCO=$La_{2-x}Ba_xCuO_4$
Na-CCOC=$Ca_{2-x}Na_xCuO_2Cl_2$
YBCO=$YBa_2CuO_{7+\delta}$
Bi2212=$Bi_2Sr_2CaCu_2O_{8+\delta}$
Bi2201=$Bi_2Sr_2CuO_{6+\delta}$
Hg1201=$HgBa_2CuO_{4+\delta}$
Tl2201=$Tl_2Ba_2CuO_{6+\delta}$
NCCO=$Nd_{2-x}Ce_xCuO_4$

Abbreviations
MDC=Momentum distribution curves
EDC=Energy Distribution curves
MFL= Marginal Fermi liquid
FL= Fermi liquid
PG= Pseudo gap
SDW= Spin density wave
HTSC= High temperature superconductor
SC= Superconductor
HWHM= half width at half maximum
FWHM= full width at half maximum

Lattice structures:
LLT=Low temperature tetragonal
HTT=High temperature tetragonal
LTO=Low temperature orthorhombic

Experimental techniques:
ARPES= Angle Resolved Photo Emission Spectroscopy
INS=Inelastic neutron scattering
LEED=Low-Energy Electron Diffraction
PPMS= Physical Properties Measurement System
TAS= Triple axis spectroscopy
SANS=Small Angle Neutron Scattering
AMRO= Angle magnetoresistence oscilation

Contents

List of Tables

Chapter 1

Introduction

The many-body problem appears in various fields of physics, from atomic to astronomic length scales. Our solar system, for example, is a well-known many-body problem. Although we understand the interactions between the planets, it is a non trivial problem to calculate analytically the dynamics when the number of planets exceeds three. The field of condensed matter is no exception. Quantum mechanics successfully describes the hydrogen atom which is a two-body problem. The challenge is however, how to describes the dynamics of a system with $O(10^{23})$ interacting particles.

The appearance of magnetism and the emergence of superconductivity are examples of phenomena that arise as a result of many-body interactions. Even simple elements, like aluminium, become superconducting below a critical temperature T_c. Superconductivity, which is a central theme of this thesis, is a fascinating state of matter where electrons can conduct a current without dissipation and where external magnetic fields are expelled from the sample. The issue of superconductivity is more than an academic problem, since useful applications such as levitating trains [1], high-power cables [2], electronic devices, and medical equipments stimulate the research on these materials.

1.1 Strongly correlated materials

This thesis work was performed under the research program for Materials with New Electronic Properties (MaNEP) that is dedicated to the study of novel materials with striking electronic properties. The perovskites belong to a class of materials that have revealed an exceptionally rich variation of interesting new properties that originate from complicated many-body interactions [3, 4]. For example, colossal magnetoresistance (CMR) has been discovered in the manganese-oxides (manganites) such as $La_{2-x}Sr_xMnO_4$ [5, 6]. Magnetoresistance is used in the readhead of harddisks [7], thus CMR materials are potentially useful for future data storage technologies. Another interesting member of the perovskites family are the cobalt-oxides (cobaltates). The discovery of giant thermopower effects [8] and more recently superconductivity [9] has generated considerable interest in these materials. Yet, another example are the nickel-oxides (nickelates) which under specific hole doping concentrations of the nickel-oxide layers exhibit exotic phenomena such as charge segregation into one dimensional (1D) stripe formations [10, 11].

Much of this research has been strongly accelerated by the discovery of high-temperature superconductivity in copper-oxides (cuprates) materials [12]. The initial discovery of superconductivity in $La_{2-x}Ba_xCuO_4$ had $T_c \approx 33$ K which was larger than what existing theories could explain. The subsequent realization of $YBa_2CuO_{7+\delta}$ (YBCO) [13, 14] and Bi2212 [15, 16] with $T_c \approx 90$ K made it even more evident that existing theories were insufficient. Since the initial discovery in 1986, hundreds of high-temperature superconducting compounds have been synthesized [17]. Today, the world record is $T_c \approx 135$ K at ambient pressure in $HgBa_2Ca_2Cu_3O_{8+\delta}$ [18] and $T_c \approx 165$ K under application of external pressure [19]

The history of superconductivity starts in 1911 when H. Kamerlingh Onnes discovered that the resistivity of Hg suddenly drops to zero below $T_c = 4.2$ K [20]. Perfect diamagnetism, that today is considered as the most unambiguous signature of superconductivity, was discovered by Meissner and Ochsenfeld in 1933 [21]. A microscopic theory for superconductivity was founded in the 1950s by Bardeen, Cooper, and Schrieffer [22], and is now known as the BCS theory. Superconductivity was explained by an effective attraction between electrons, mediated by lattice vibrations, which allows the formation of so-called Cooper pairs [23]. Electrons are fermions, however in pairs they have a bosonic nature which allows them to condense in a single quantum state. The BCS theory successfully explains superconductivity in many materials. Therefore superconductivity mediated by phonons is herein classified as BCS superconductivity.

As mentioned before, high-temperature superconductors belong to a class of materials that can not be explained by the BCS theory in its original form. However, even we do not know the mechanism of pairing, we know that both high-T_c and BCS superconductors involve Cooper pairs [23]. For example, they both exhibit flux quantization in the usual unit of $\Phi_0 = \frac{h}{2e}$ showing that the charge unit is $2e$ [24]. Besides the flux quantization, superconductors share a unique collection of physical properties such as zero electrical resistivity, perfect diamagnetism (Meissner-Ochsenfeld effect), an energy gap in the electronic spectrum, and the Josephson effect [25]. These properties are common to superconductors independently of the pairing mechanism.

As many other phase transitions, superconductivity can be described by the Landau-Ginzburg theory. In this phenomenological theory superconductivity is related to an order parameter Δ which is zero for $T > T_c$ and non zero for $T < T_c$. Generally the order parameter is a complex function

$$\Delta = |\Delta| \exp(i\phi_{sc}) \tag{1.1}$$

where the phase value ϕ_{sc} is arbitrary. Like magnetization in a ferromagnet spontaneously chooses a random direction below the ordering temperature, the value ϕ_{sc} is unique but arbitrary for $T < T_c$. Generally, superconductivity is the result of two remarkable quantum phenomena, namely pairing and phase coherence. The amplitude of the order parameter $\Delta(\mathbf{r})$ is a measure of the local superfluid density and a unique ϕ_{sc} is required for macroscopic phase coherence. The link between Landau-Ginzburg theory and microscopic BCS theory was established by L.P. Gorkov [26]. The order parameter was identified with the pair wavefunction and is proportional to the energy gap [27]. In momentum space representation the pair function $\Phi(\mathbf{k})$ is related to the gap function $\Delta(\mathbf{k})$ through $\Phi(\mathbf{k}) = \Delta(\mathbf{k})/\varepsilon_{\mathbf{k}}$ where $\varepsilon_{\mathbf{k}}$ is the quasiparticle dispersion. The symmetry of the gap function $\Delta(\mathbf{k})$ [which reflects the pairing symmetry] can be determined experimentally. It turns out that the gap function of BCS superconductors and HTSCs have a different symmetry. While BCS superconductors exhibit s-wave symmetry, it is now established that HTSC have predominant

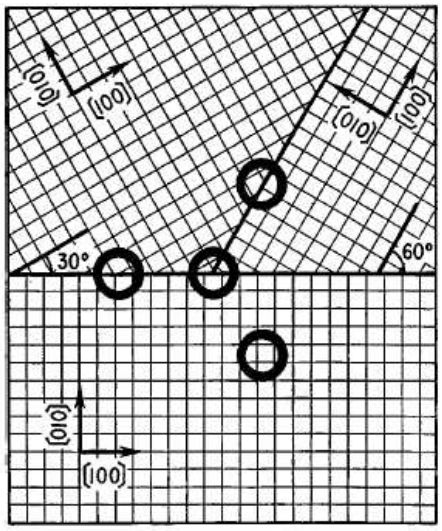

FIGURE 1.1: Superconducting rings grown on an insulating substrate. Knowing that the superconductor grows with the orientation of the substrate, the rings will have either zero, two or three grain boundaries. The tricrystal ring exhibits half integer flux quantization which can only be understood from a *d*-wave gap function. From C.C. Tsuei *et al.* [27].

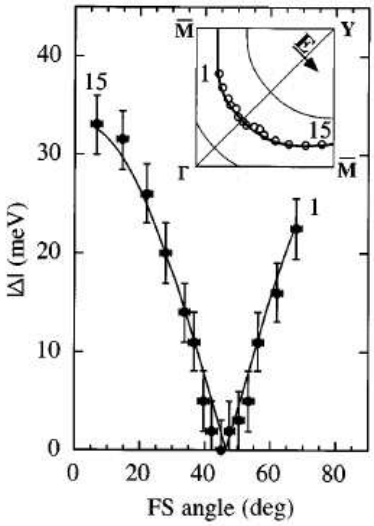

FIGURE 1.2: Superconducting gap Δ as measured by angle resolved photoemission. The gap, measured along the Fermi surface as shown in the inset, is strongly anisotropic and exhibits a node along the zone diagonal. From H. Ding *et al.* [28].

d-wave symmetry

$$2\Delta(\mathbf{k}) = \Delta\left[\cos(k_x a) - \cos(k_y a)\right], \tag{1.2}$$

where a is the lattice constant. The *d*-wave symmetry has been proven directly by phase-sensitive experiments [27] (see figure 1.1) and confirmed by angle resolved photoemission spectroscopy (ARPES) that measures the magnitude of the gap function directly [28] (see figure 1.2).

An other important difference between conventional BCS and high-T_c superconductors is the host crystal structure. While BCS superconductivity exists in cubic lattice structures, the cuprate materials have a strong tetragonal crystal structure, which is also reflected in the electronic structure. Hence the electronic structure of the BCS superconductors is typically three dimensional, while the electronic structure of cuprates is quasi two dimensional.

1.2 CONVENTIONAL AND UNCONVENTIONAL SUPERCONDUCTIVITY

The differences between BCS superconductors and HTSC materials are also reflected in many of the characteristic length and energy scales of these systems. In this section a short examination of these characteristic scales will be given.

1.2.1 Length scales. Superconductors and Bose-Einstein condensates are examples of systems where a finite fraction of the particles resides in the same quantum state. The number of involved particles is related to the carrier density concentration n_s (also known as the superfluid density). With higher carrier density a superconductor can better screen an external magnetic field. The penetration depth λ of an external field H is therefore related to the carrier density n_s

$$\lambda \sim \sqrt{\frac{1}{n_s}}. \tag{1.3}$$

Soon after the discovery of the HTSCs it became clear that the carrier density in the HTSCs is orders of magnitude lower than in the conventional BCS superconductors [29]. This fact was derived from the observation that $\lambda(HTSC) \gg \lambda(BCS)$. The penetration depth λ is often compared to the superconducting coherence length ξ_{sc}. For BCS superconductors ξ_{sc} is typically of the order of μm while HTSCs have $\xi_{sc} \sim 10$ Å (see table 1.1). In conventional BCS superconductors the coherence length is related to the superconducting gap Δ_{sc} by

$$\xi_{sc} = \frac{\hbar v_F}{\pi \Delta_{sc}} \tag{1.4}$$

where v_F is the Fermi velocity. The situation is more complicated in the HTSCs, because the electronic structure is strongly anisotropic. For example, as previously mentioned the gap function Δ_{sc} has nodes along the zone diagonals.

Superconductors are often classified by the ratio between penetration depth and coherence length, $\kappa = \lambda/\xi_{sc}$. A superconductor with $\kappa_{sc} < 1/\sqrt{2}$ is said to be a *type-I* superconductor and if $\kappa_{sc} > 1/\sqrt{2}$ it is said to be a *type-II* superconductor. From table 1.1 it is clear that HTSCs are extreme type-II superconductors, a fact that will be discussed more carefully in a later chapter.

A third length scale is the mean free path ℓ of an electron at the Fermi surface (in the normal state)

$$\ell = v_F \tau \tag{1.5}$$

where τ is the lifetime of the electron. A BCS superconductor with $\ell \gg \xi_{sc}$ is said to be in the clean limit, while if $\ell < \xi_{sc}$ it is said to be in the dirty limit. Again, the situation is more complicated in the case of HTSCs where the length scales ℓ and ξ_{sc} are momentum dependent. The anisotropies of electronic quantities Δ_{sc}, ℓ, and v_F are a subject of investigation in this thesis.

In the underdoped region of the phase diagram of cuprates, the correlation length ξ_{AF} of static incommensurate antiferromagnetism is a fourth length scale to be considered. Herein, a superconductor with $\xi_{AF} = 0$ is said to be homogeneous while if $\xi_{AF} > 0$ it is said to be inhomogeneous.

1.2.2 Temperature and Energy scales. In conventional BCS superconductors the energy scale of Cooper pair formation relates in a simple way ($2\Delta_{sc} \approx 3.5 k_B T_c$) to the critical temperature for superconductivity. In high-T_c superconductors the situation is more complex and the relevant energy scale for pair formation, if it exists, is still debated [30]. One scenario is that the pseudo gap is the energy scale for pair formation. However, as a function of underdoping the pseudo gap energy increases while T_c decreases. With this opposite trend, it is clearly not possible to establish a simple linear relation between the pseudo gap energy and the critical temperature of superconductivity.

Table 1.1: A comparison of length scales in the BCS superconductor Pb and the high-T_c compound $La_{2-x}Sr_xCuO_4$.

Material	ξ_{sc}[Å]	λ [Å]	ℓ [Å]	ξ_{AF} [Å]	κ	T_c [K]
Pb	830	390		0	~ 0.5	7
LSCO	6.8	2000	~ 30	$0-500$	~ 300	~ 40

A fundamental question is whether there exists an energy scale in the high-T_c superconductors that relates directly to the transition temperature T_c. This issue will be addressed here.

1.3 PHENOMENOLOGY OF CUPRATES

Superconductivity in the cuprates has been a problem standing for more than two decades. Although more than 10^5 scientific papers have been published on this subject, there is still no concensus about the pairing mechanism. For some recent reviews see [31–33]. However, superconductivity is not the only interesting property of cuprates. The normal state ($T > T_c$) has also anomalous properties. Still today it is a challenge to explain the normal state properties, and in particular the underdoped region of the phase diagram remains a controversial topic. This section is devoted to an examination of the generic phase diagram (see figure 1.3) of high-T_c superconductors.

1.3.1 Insulating regime. Let us start with the undoped case. Although band calculations predict a half-filled metallic band, the parent compounds of cuprate superconductors are insulators. However, they are not conventional insulators where Bloch bands are completely filled. The important ingredient to understand this class of materials is the strong Coulomb interaction U between the d-shell Cu electrons. When the energy cost t for an electron to jump to a neighbor site is much smaller than the Coulomb interaction U ($t \ll U$) the electrons localize on the Cu sites. This type of insulator is categorized as a Mott insulator [34]. In this insulating regime the Cu spins interact via superexchange that causes them to order antiferromagnetically below the Neel temperature $T_N \sim 300$ K. The characteristic energy for the antiferromagnet exchange interaction is $J = \frac{4t^2}{U}$. Neutron scattering has revealed the spin wave dispersion and extracted the nearest neighbor interaction $J = 112$ meV [35]. It should be emphasized that the 2D structure leads to a reduced ordered Cu^{2+} moment of $\sim 0.5\ \mu_B$ due to quantum fluctuation.

1.3.2 Metallic regime. In the other extreme ($t \gg U$) the electrons delocalize and form a metallic regime. Electrons in metals have been successfully described by Landau's Fermi liquid theory. In essence, it says that even in presence of interactions the low-energy excitations can still be described in terms of fermionic particles, called quasiparticles, with charge e, spin 1/2, albeit an enhanced mass m^* and reduced lifetime τ. Wiedemann-Franz law, valid at low temperatures, is a basic property of a Fermi liquid, reflecting that quasiparticles are responsible for both the heat and charge transport. Empirically it was found by Wiedemann and Franz [36] that the heat conductivity

κ_H and the electrical conductivity σ_{ab} are related by a universal constant

$$\frac{\kappa_H}{\sigma_{ab}T} = \frac{\pi^2}{3}\left(\frac{k_B}{e}\right)^2 \tag{1.6}$$

where k_B is the Boltzmann's constant.

Another signature of a Fermi liquid is a quadratic temperature dependence of the in-plane resistivity

$$\rho_{ab}(T) = \rho_0 + AT^2 \tag{1.7}$$

where A is a constant and the T^2 term stems from electron-electron interaction. At low-temperatures ($T < 50$ K) such a T-dependence has been observed in the overdoped and non-superconducting region ($x \approx 0.3$) of LSCO [37]. Verifications of the Wiedemann-Franz law, in the cuprates, have also been reported in the overdoped regime [37, 38]. These empirical observations support that conventional Fermi liquid theory applies to the overdoped regime of HTSC. Finally, the observation of a T^2-dependence of the resistivity implies that the role of electron-phonon scattering is negligible at least in the transport properties.

1.3.3 Strange metal phase. It is still debated to what extent Fermi liquid theory applies to the normal state of HTSC in general. The normal state of BCS superconductors is a Fermi liquid and the BCS theory identifies SC as an instability of the Fermi sea. The normal state of optimally doped HTSCs is, however, not a standard Fermi liquid since it exhibits anomalous metallic behavior. For example the in-plane resistivity scales linearly with temperature

$$\rho_{ab}(T) = \rho_0 + AT \tag{1.8}$$

for $T_c < T < 1000$ K [39–41], see figure 1.4. This T-dependence demonstrates unambiguously that the normal state of optimal doped HTSCs is not a conventional Fermi liquid. The normal state around optimally doping is therefore often denoted a strange metal. The microscopic mechanism for this strange metal is still controversial. To describe the T-dependence of the resistivity and other anomalous properties, Ch. Varma *et al.* proposed a phenomenological marginal Fermi liquid self-energy which will be described later in this thesis. The strange metal phase is therefore also called a marginal Fermi liquid. Besides the anomalous transport properties, departures from the Wiedemann-Franz law (Eq. 1.6) in the optimally doped and underdoped regions have been reported [42].

1.3.4 Pseudo gap phase. The normal state properties of optimally doped cuprates is a problem that remains incompletely understood. Another long standing problem is to understand the normal state of underdoped cuprates. This region of the phase diagram is often denoted *pseudo gap* (PG) phase. The pseudo gap was first discovered by the observation of a gap in the static spin susceptibility χ_{sp} by for example magnetization measurements and nuclear magnetic resonance (NMR), see figure 1.5. Later the pseudo gap was also observed in the charge sector by for example resistivity measurements [43] and infrared spectroscopy techniques. ARPES has directly confirmed the existence of a pseudo gap in electronic spectra of the underdoped normal state [44]. Near the (π,0) point a strong suppression of the density of state has been observed.

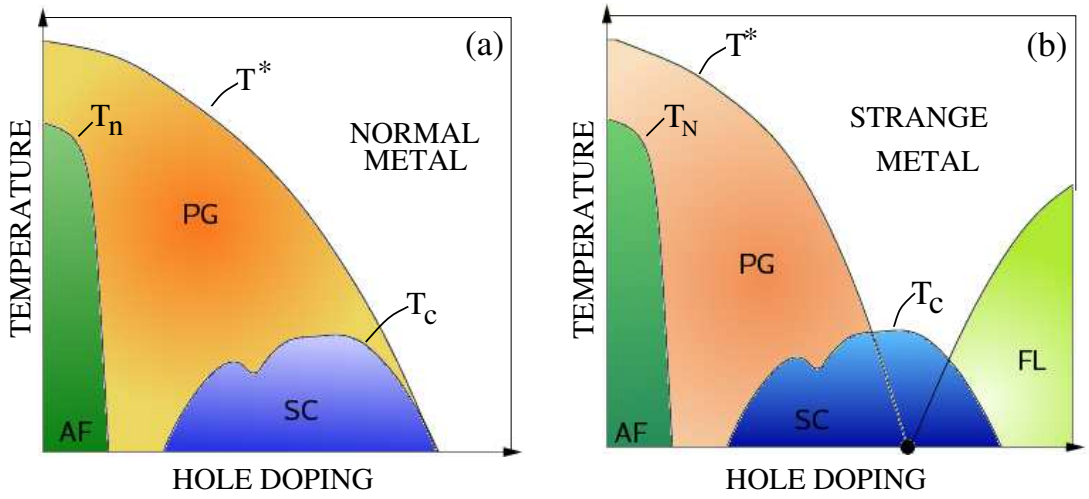

FIGURE 1.3: (a) and (b) are two different ways to draw the phase diagram. The overdoped region is a normal metal [Fermi liquid (FL)] and the undoped compound is an antiferromagntically ordered Mott insulator (AF). Between these extrema superconductivity (SC) exists. The controversy about the pseudo gap (PG) phase leads people to draw the phase diagram in two different ways as shown in the panel (a) and (b).

The temperature at which the pseudo gap opens is often denoted T^* and I will herein define the gap amplitude by Δ^*. The pseudo gap phase has been studied directly and indirectly by a vast number of experimental techniques [45]. This has lead number of different definitions of T^*. Although most experimental techniques agree that T^* and Δ^* increase with doping in the underdoped regime [44, 46], the pseudo gap phase remains an unsettled issue. The evolution of the pseudo gap as function of temperature, external magnetic field and doping is still strongly debated. For La-based cuprates the so-called 1/8-anomaly have attracted considerable interest recently. At the magic doping level $x \approx 1/8$ superconductivity is somewhat supressed as shown schematically in figure 1.3. A concomitant increase of the pseudo gap amplitude was recently reported by T. Valla *et al.* [47]. How to interpret these results are still a very open issue and the 1/8-anomaly will be a subject of careful discussion in this thesis.

Broadly speaking there exist two different interpretations of the pseudo gap phase. One school of thought considers the pseudo gap as a precursor to superconductivity. In this picture, preformed pairs exist locally but without long range phase coherence in the normal state. The gap in the spin susceptibilities is understood as the onset of spin singlet formation. This view has been supported by the observation of vortex-motions through the Nernst effect in the normal state of underdoped cuprates [48–52]. As a precursor for superconductivity the pseudo gap phase should exist above the superconducting dome. The phase diagram is therefore often drawn as shown in figure 1.3(a).

The other class of interpretations argues that the pseudo gap phase is related to a hidden order. Within this scenario, the order vanishes inside the superconducting dome as shown in figure 1.3(b). The topology of this phase diagram is similar to that of certain heavy fermion compounds where the superconducting dome appears around an antiferromagnetic quantum critical point [53]. In heavy fermion materials the appearance of superconductivity and non Fermi liquid behavior are

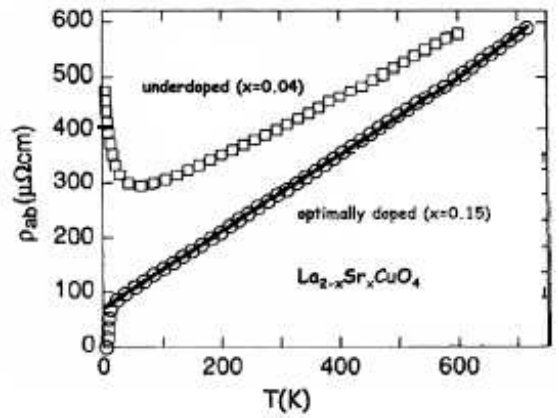

FIGURE 1.4: Normal state in-plane resistivity of optimally doped LSCO (circles). The linear resistivity observed around optimal doping persist up to temperatures as high as 1000 K. Deviation of the linear dependence is observed on both below (squares) and above optimal doping. This figure is taken from E. Miranda *et al.* [58] and the data are from H. Takagi *et al.* [40].

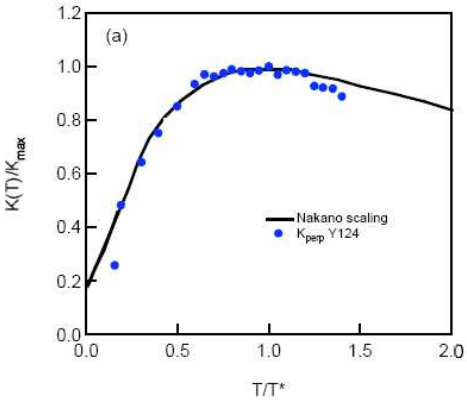

FIGURE 1.5: Copper knight shift data obtained on YBCO [59] compared with the universal scaling curve derived from magnetization measurements on LSCO [60, 61]. This figure is taken from M. Norman *et al.* [62].

often in conjunction with a quantum critical point [54]. This might suggest that there may be some aspects of quantum critical physics that are shared between the heavy fermion and cuprate materials [55].

In the case of HTSC materials it is very difficult to identify the existence of a quantum critical point under the SC dome due to the presence of superconductivity itself. Application of very high magnetic field ~ 50 tesla in order to suppress superconductivity is one way to overcome this obstacle [56, 57]. However, the magnetic field may also drive the system away from the quantum critical point of possible interest. Quantum criticality and non Fermi liquid behavior are subjects that will be discussed in more detail later on.

1.4 THEORIES OF HTSC

As mentioned a couple of times, there exists still no concensus about the microscopic mechanism of high-temperature superconductivity. A microscopic theory should not only explain superconductivity, it should also describe the phase diagram in general. That means it should provide an explanation for the strange metal phase and the pseudo gap phase. At zero hole doping the model should correctly describe the Mott insulating phase and in the strongly overdoped regime a Fermi liquid like phase should appear. Many ideas have been proposed during the last couple of decades. Here I will only mention a few of the most influential theories. For a recent discussion of the various scenarios, see [63].

Phonon-mediated HTSC: Some researchers emphasize the role of lattice-vibrations [64, 65],

suggesting that HTSC is mediated by phonons as in conventional BCS superconductors. For some doping levels, isotope effect on T_c has been observed. However, it is still debated whether the isotope effect is an indirect effect through for example slightly different chemistry or band structure.

RVB approach: Very early on, P.W. Anderson suggested the concept of a resonant-valence-bond (RVB) state in which magnetic singlet pairs exist in a spin liquid like state [66]. The RVB state is regarded as an unstable point that can lead to various other ground states such as antiferromagnetism and superconductivity. The RVB concept provides an explanation for d-wave superconductivity and the existence of the pseudo gap phase where pairing is possible but phase coherent superconductivity is absent. The RVB-approach is also able to describe the strange metal phase [67] without the use of a quantum critical point. This model provides an explanation to many of the salient features in the phase diagram of HTSCs, for a more detailed review see [31, 68].

Spin fluctuations: While the RVB approach treats the problem with a large Coulomb repulsion U, the spin fluctuation models start with a weak interaction U [69]. These models also provide a natural explanation for d-wave symmetry of the gap function. A very naive way to understand these models is to assume that the spin fluctuations play the same role as the phonon does for the conventional superconductors. These models are also able to explain the strange metal phase since a antiferromagnetic quantum critical point will lead to a marginal Fermi liquid like spectrum [70].

Inhomogeneity-induced pairing: Another class of theories emphasizes the tendency of these materials to phase separate into hole rich and hole poor regions. The fluctuations of these mesoscopic structure are then responsible for phase coherent superconductivity. In the overdoped region the system is more homogeneous, which weakens the pairing. On the other hand, in the underdoped region the system is too granular and phase coherence can therefore not be obtained. In these models that involve stripes or phase separation, the pseudo gap is a phase where local pairing is possible. For a review see [71].

Competing orders: While many models attribute the pseudo gap phase to a state with preformed pairs, an alternative group of models suggests that the pseudo gap phase is related to a hidden order. In this scenario the pseudo gap is characterized by an order parameter that vanishes in quantum critical point inside the superconducting dome. Ch. Varma have suggested that the pseudo gap phase is associated with a circular current order which vanishes at $x \approx 0.19$. The quantum critical fluctuation around this quantum critical point (QCP) is then responsible for the superconductivity and the strange metal in the normal state. The evidence of a circular current order parameter has been supported by a few experiments [72, 73]. Other proposals for hidden order parameters are a d-density wave order [74] or a nematic order [75, 76].

SO5 theories: The starting point for SO(5) theories is that a common microscopic interaction is responsible for both antiferromagnetism and superconductivity [77]. The three dimensional (Nx,Ny,Nz) antiferromagnetic order and the superconducting order parameter (ReΔ,ImΔ) are unified into a single five dimensional order parameter. In this model antiferromagnetism and superconductivity coexist microscopically in the underdoped region. The Fermi liquid in the overdoped region of the phase diagram corresponds to the disordered phase of the unified order parameter.

At the moment of writing, each of these theories has its merit and relevance. However, given the different nature of these theories it should be possible to perform an experiment that can dis-

tinguish between the scenarios. With this in mind let us now discuss the problem from an experimental point of view.

1.5 EXPERIMENTAL TECHNIQUES

Almost any conceivable experimental technique in solid state physics has been applied to the study of the HTSC materials. Except for semiconductors, the cuprates are probably the most studied class of materials. Unfortunately, experimental limitations often prevent that a specific compound is studied by all available techniques. For example, the Bi2212 compound is heavily studied by means of ARPES and scanning tunneling microscopy/spectroscopy (STM/STS) but neutron scattering experiments are scarce. In contrast, $La_{2-x}Sr_xCuO_4$ has been studied intensively by neutron scattering but only few ARPES and STM/STS studies exist. The most efficient test of the existing theories is to apply many different techniques to the very same compounds. Consequently, if there is an opportunity to bring two techniques closer together, both theory and experiments will benefit and there will be an enhanced ability to identify the salient and robust features.

The strategy of this thesis work is to apply several different techniques to the same high quality LSCO crystals. The Paul Scherrer Institute (PSI) is the ideal place for such a study since it provides the possibility to do (i) ARPES at the Swiss Light Source (SLS), (ii) neutron scattering experiments at the Swiss Spallation Source SINQ, and (iii) zero field μSR at the Swiss Muon Source.

This work focuses on the spin and charge degrees of freedom. Of particular interest is the mutual interactions between the spin and charge sectors. The main experimental tools used for this purpose are inelastic neutron scattering (INS) and angle resolved photoemission spectroscopy. Spin dynamics and static magnetic order can be probed by neutron scattering experiments and the electronic excitations and structures can be investigated by ARPES. Although the spin fluctuations can be studied by neutron scattering up to energies of several hundreds of meV, this work limits itself to the low-energy $[0-10$ meV$]$ spin fluctuations since it is in this energy range that there is a complex interplay between superconductivity and the spin degrees of freedom. With ARPES both the low-energy and high-energy electronic excitations will be investigated. While the low-energy electronic properties are important for the understanding of the superconductivity, the high-energy excitations and structures reveal insight into the fundamental interactions in the cuprates.

To understand why neutron scattering is such a powerful technique, it is useful to look at the dispersion relation of free particles

$$\varepsilon = \frac{(\hbar \mathbf{k})^2}{2m} = \frac{h^2}{2m\lambda^2} \tag{1.9}$$

where m is the mass and λ is the de Broglie wavelength. Thus the energy ε of the particle is related to λ^2 through the constant $h^2/2m$. The mass of a neutron, $m = m_{\text{proton}}$ gives that neutrons with a wavelength of atomic length scale have energies in the meV range. For electrons the mass is thousand times lighter than neutrons. Therefore electrons with energies of the order $\varepsilon \sim$ 1000 eV is required to get the appropriate atomic length scale of the de Broglie wavelength. Fundamental excitations in such as phonons or spin waves have energies in the order of meV. Neutrons are therefore ideal to study such excitations because they have both the right energy and the appropriate wavelength.

For light the dispersion reads

$$\varepsilon = \hbar\omega = \hbar ck = \frac{hc}{\lambda}, \tag{1.10}$$

thus the energy is related to the wavelength λ by the constant hc. As for electrons, to get the suitable wavelength for diffraction experiments, photons with $E \sim 10^4$ eV are required. The main drawback with such high-energies is that it is very difficult to perform meV spectroscopy since it requires a meV precision of the beam.

Photoelectron spectroscopy is a modern technique that uses photons of ~ 50 eV to emit electrons from a solid. With modern electron analyzers it is possible to analyze the photoemitted electrons with an energy resolution $\Delta E < 10$ meV. Although the energy resolution is a limitation, it is still good enough to study the excitations in the meV range.

1.6 STRUCTURE OF THIS THESIS

It is my hope that this thesis will be helpful to future Ph.D. students interested in strongly correlated electron materials. Although this is not a textbook I found it worth to introduce, in a rudimentary fashion, some functions related to the experimental techniques. A reader who is already acquainted with ARPES and triple axis neutron scattering may therefore skip chapter 2. Crystal quality is crucial for the experiments presented in this thesis. A few bulk measurements to characterize the samples are therefore presented in chapter 3. The main results of this thesis, obtained by neutron scattering and photoemission spectroscopy, are presented in chapter $4-6$. The last chapter summarizes the conclusions drawn from the experiments presented in this thesis.

Chapter 2

Concepts in condensed matter physics

2.1 SCATTERING THEORY

Experimental techniques involving scattering processes have been applied in various fields of physics [78]. Here I will give a short introduction to scattering theory that is the basis for the experimental techniques used during this thesis work. For the sake of simplicity only weak interactions will be considered. In that case the scattering process can be described in terms of first order perturbation methods.

2.1.1 The self-energy function. Let us start by considering a free particle that can be described by a propagating wave. It is often convenient to label such a particle by its wavevector $\mathbf{k}$. In the Dirac notation $\langle \mathbf{k}, s|$ denotes a particle with momentum $\hbar\mathbf{k}$ and spin s.

Let us now consider a gas of electrons that interact weakly through Coulomb interaction $\mathcal{V}_{e-e}$. The scattering rate Γ of an electron $\langle \mathbf{k}_i|$ on another electron $\langle \mathbf{k}_f|$ can be calculated to first order through the Fermi golden rule

$$\Gamma_{i,f} = \frac{2\pi}{\hbar} \left| \langle \mathbf{k}_i + \mathbf{Q}, \mathbf{k}_f - \mathbf{Q} | \mathcal{V}_{e-e} | \mathbf{k}_i, \mathbf{k}_f \rangle \right|^2 \delta(E_{\mathbf{k}_i} + E_{\mathbf{k}_f} - E_{\mathbf{k}_i+\mathbf{Q}} - E_{\mathbf{k}_f-\mathbf{Q}}) \tag{2.1}$$

where δ is the delta Dirac function. The lifetime τ of the electron state $\langle \mathbf{k}_i|$ is

$$\tau = \frac{\hbar}{\Gamma} = \frac{\hbar}{2\mathrm{Im}\Sigma} \tag{2.2}$$

where Γ is the scattering rate of all possible scattering processes and Σ is the so-called self-energy. The Pauli exclusion principle stating that two electrons can not have the same wavevector $\mathbf{k}$ and spin s restrict strongly the number of possible scattering processes. To minimize the energy an electron will try to occupy the lowest energy state that is not yet filled. At $T = 0$ K this results in a sharp Fermi surface that separates the highest-energy occupied and the lowest-energy unoccupied states. This arrangement puts restrictions to the possible scattering processes, and for thermally induced electron-electron scattering Γ scales with the temperature squared; $\Sigma \sim (k_B T)^2$. The square dependence of scattering rate is a fundamental result of Landau Fermi liquid theory that applies to metals.

In more general terms, the self-energy contains information of all possible interactions in a given system. To a first approximation the self-energy Σ can be written as a sum

$$\Sigma = \Sigma_{e-e} + \Sigma_{e-ph} + \Sigma_{imp} + ... \tag{2.3}$$

where Σ_{e-e}, Σ_{e-ph}, and Σ_{imp} denote electron-electron, electron-phonon, and impurity scattering, respectively. The self-energy function therefore contains information about the mutual interaction between spin, charge, and lattice degrees of freedom. The self-energy can be derived from microscopic models or introduced in a phenomenological way, and experiments can extract the self-energy by measuring the scattering rate. The self-energy function is therefore a meeting point between theory and experiments.

2.1.2 Single-particle spectral function. To describe the excitation created by removing(adding) an electron from(to) a Fermi liquid, I will now introduce the spectral function $\mathcal{A}(\mathbf{k},\omega)$. This function describes how well-defined an excitation created by adding or removing a particle in the state $\langle \mathbf{k}, s|$ is. For example for a noninteracting electron gas where electrons are described by Bloch waves, the spectral function is a δ-function. With increasing interactions the spectral function broadens and consists of both a coherent part and an incoherent part.

The spectral function is often expressed through the single-particle Green's function. Generally the single-particle Green's function $\mathcal{G}(\mathbf{k},\omega)$ is defined in terms of the correlation function of the particle creation and annihilation operators $\hat{c}_{\mathbf{k}}(t)$ and $\hat{c}^{\dagger}_{\mathbf{k}}(t)$ [79, 80]

$$\mathcal{G}(\mathbf{k},t,t') = \mathcal{G}^{+}(\mathbf{k},t,t') + \mathcal{G}^{-}(\mathbf{k},t,t') = -i\left[\langle \hat{c}_{\mathbf{k}}(t)\hat{c}^{\dagger}_{\mathbf{k}}(t')\rangle + \langle \hat{c}^{\dagger}_{\mathbf{k}}(t)\hat{c}_{\mathbf{k}}(t')\rangle\right] \tag{2.4}$$

where $\mathcal{G}^{+}(\mathbf{k},t,t')$ and $\mathcal{G}^{-}(\mathbf{k},t,t')$ are known as the addition and removal Green's functions respectively. The spectral function $\mathcal{A}(\mathbf{k},\omega)$ is defined by

$$\mathcal{A}(\mathbf{k},\omega) \equiv -2Im\mathcal{G}(\mathbf{k},\omega). \tag{2.5}$$

Angle resolved photoemission spectroscopy is a technique that removes an electron from the target sample, therefore only the removal Green's function will be treated here. The removal Green's function $\mathcal{G}^{-}(\mathbf{k},t,t')$ reads

$$\mathcal{G}^{-}(\mathbf{k},t,t') = -i\langle \hat{c}^{\dagger}_{\mathbf{k}}(t)\hat{c}_{\mathbf{k}}(t')\rangle = \frac{-i}{Z}\sum_{if}\exp(-\beta E_i)\langle i|\hat{c}^{\dagger}_{\mathbf{k}}|f\rangle\langle f|\hat{c}_{\mathbf{k}}|i\rangle\exp(i\left[E_i - E_f\right]\left[t-t'\right]) \tag{2.6}$$

where $Z = \sum_s \exp(-\beta E_s)$ is the partition function. In frequency domain the removal Green's function takes the form

$$\mathcal{G}^{-}(\mathbf{k},\omega) = 2\pi i\sum_{if} p_i \left|\langle f|\hat{c}_{\mathbf{k}}|i\rangle\right|^2 \delta(E_i - E_f - \omega) \tag{2.7}$$

where $p_i = \exp(-\beta E_i)/Z$ is the occupation probability. With a few manipulations one finds that the spectral function relates to the one-electron removal and addition Green's functions through

$$-i\mathcal{G}^{-}(\mathbf{k},\omega) = \mathcal{A}(\mathbf{k},\omega)f(\omega) \quad \text{and} \quad i\mathcal{G}^{+}(\mathbf{k},\omega) = \mathcal{A}(\mathbf{k},\omega)[1-f(\omega)] \tag{2.8}$$

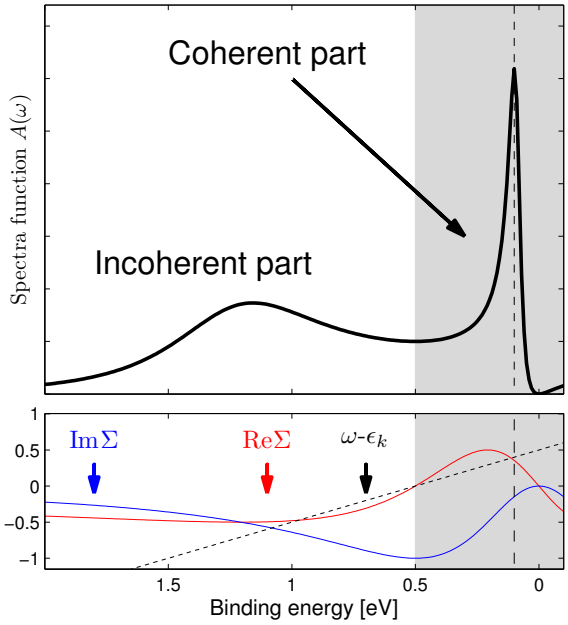

FIGURE 2.1: The top panel shows the spectral function model with a selfenergy given by $\Sigma(\omega) = F\omega/(\omega + i\gamma)^2$ with $F = 1$ and $\gamma = 1/2$. The bottom panel display ImΣ and ReΣ as a function of the binding energy ω. The peak of the coherent and incoherent part is determined by the solution of $\omega - \varepsilon_k - \mathrm{Re}\Sigma(\omega) = 0$.

where $f(\omega) = 1/\exp(\beta[\omega - \mu])$ is the Fermi-Dirac distribution. Especially the relation to the removal Green's function will be useful in later chapters.

Finally it should be mentioned that the Green's function and the spectral function also can be represented through the self-energy Σ by

$$\mathcal{A}(\mathbf{k},\omega) = \frac{1}{\pi}\frac{\mathrm{Im}\Sigma(\mathbf{k},\omega)}{[\omega - \varepsilon_{\mathbf{k}} - \mathrm{Re}\Sigma(\mathbf{k},\omega)]^2 + [\mathrm{Im}\Sigma(\mathbf{k},\omega)]^2}. \tag{2.9}$$

As will become clear in a coming chapter, ARPES measures $\mathcal{A}(\mathbf{k},\omega)f(\omega)$ multiplied by a matrix element. Therefore the spectra function $\mathcal{A}(\mathbf{k},\omega)$ is the meeting point between ARPES experiments and theory. The spectral funtion $\mathcal{A}(\mathbf{k},\omega)$ consist of a coherent and an incoherent part as shown in figure 2.1.

2.1.3 Form factor. Now let us consider a freely propagating neutron $\langle \mathbf{k}_i, s|$. Neutrons have no charge and interact therefore only weakly with matter. Hence the probability $\mathcal{W}$ that a neutron scatters at for example an atom can be calculated through the Fermi Golden rule

$$\mathcal{W} = 2\pi \left|\langle \mathbf{k}_f|\mathcal{V}(\mathbf{r})|\mathbf{k}_i\rangle\right|^2 \delta(E_i - E_f - \hbar\omega) \tag{2.10}$$

where $\hbar\omega = E_{\mathbf{k}_i} - E_{\mathbf{k}_f}$, E_i and E_f is the energy of the atom before annd after the scattering process. $\mathcal{V}(\mathbf{r})$ is the interaction potential between the neutron and the atom. Let us for simplicity start by considering elastic scattering ($\hbar\omega = 0$).

Neutron experiments are practically always performed under conditions where it is reasonable to assume that the incident and scattered neutron can be described by plane waves $\langle \mathbf{k}| = \exp(i\mathbf{k}\cdot\mathbf{r})$.

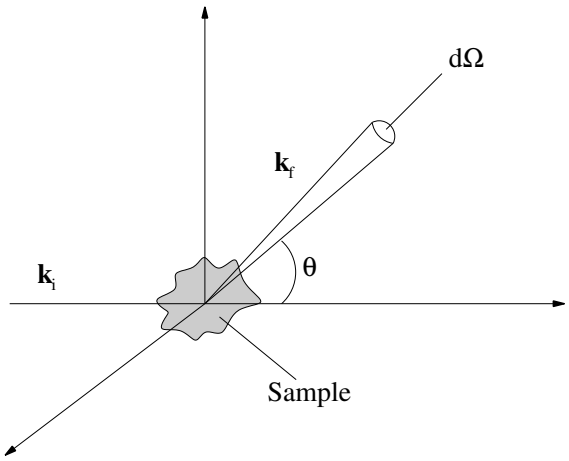

FIGURE 2.2: Geometry of a typical scattering experiment. An incident beam of particles with wavevector $\mathbf{k}_i$ and energy E_i is scattered by the sample into a state with wavevector $\mathbf{k}_f$ and energy E_f.

A scattering experiment measures typically the differential cross section $d\sigma/d\Omega$ which is

$$d\sigma/d\Omega = \frac{\text{number of neutrons per sec.}}{d\Omega\Psi} \tag{2.11}$$

where $d\Omega$ is a solid angle (see figure 2.2) and Ψ is the incident neutron flux. In this wave approach, the cross section is related to the form factor through

$$\frac{d\sigma}{d\Omega}(2\theta) \sim \mathcal{W} \sim |\mathcal{F}(2\theta)|^2 \tag{2.12}$$

where $\mathcal{F}(2\theta)$ is the amplitude of the wave $\langle\mathbf{k}|$ to scatter on the single potential $\mathcal{V}(\mathbf{r})$ by an angle 2θ.

Momentum conservation implies that $|\mathbf{k}_i| = |\mathbf{k}_f|$. The scattering angle 2θ is therefore related to the scattering vector $\mathbf{Q} = \mathbf{k}_f - \mathbf{k}_i$ by $|\mathbf{Q}| = 2|\mathbf{k}_i|\sin(2\theta)$. Hence the form factor can also be written as a function of amplitude of the scattering vector $|\mathbf{Q}| = Q$. The amplitude of the scattering event $\mathbf{k}_i \rightarrow \mathbf{k}_f$ can be calculated from the Fermi golden rule

$$\mathcal{F}(Q) = -\frac{m}{2\pi\hbar^2}\int \mathcal{V}(\mathbf{r})\exp(-i\mathbf{Q}\cdot\mathbf{r})d^3\mathbf{r} = -\frac{m}{2\pi\hbar^2}\mathcal{V}_\mathbf{Q} \tag{2.13}$$

where $\mathcal{V}_\mathbf{Q}$ is the Fourier transform of the interaction potential $\mathcal{V}(\mathbf{r})$.

2.1.4 Structure factor. For a many-particle system, the scattering potential can be written as the sum of the individual particles

$$\mathcal{V}(\mathbf{r}) = \sum_\alpha \mathcal{V}(\mathbf{r} - \mathbf{r}_\alpha) \tag{2.14}$$

where $\mathbf{r}_\alpha$ is the position of the individual particle. For a many-body system the cross section reads

$$\frac{d\sigma}{d\Omega} = |\mathcal{F}(\theta)|^2 \mathcal{S}(\mathbf{Q}) \tag{2.15}$$

where the structure factor $\mathcal{S}(\mathbf{Q})$ is given by

$$\mathcal{S}(\mathbf{Q}) = \left\langle \sum_{\alpha\alpha'} \exp(-i\mathbf{Q}\cdot\mathbf{r}_\alpha)\exp(i\mathbf{Q}\cdot\mathbf{r}_{\alpha'}) \right\rangle. \tag{2.16}$$

The structure factor is a general function that applies to solids, liquids, and gasses [81]. However, in this work only regular solid structures are investigated.

2.1.5 Correlation function. Let us now consider an ensemble of particles that are organized in a certain structure. We imagine the situation where each particle is localized on a lattice site. In other words we think of a system where the particles are organized in a periodic lattice structure. The density ρ of particles is then

$$\rho(\mathbf{r}) = \sum_\alpha \delta(\mathbf{r}-\mathbf{r}_\alpha) \quad \rightarrow \quad \rho(\mathbf{Q}) = \int d\mathbf{r}\rho(\mathbf{r})e^{-i\mathbf{Q}\cdot\mathbf{r}} = \sum_\alpha \exp(-i\mathbf{Q}\cdot\mathbf{r}_\alpha). \tag{2.17}$$

The two-particle density-density correlation function is defined by

$$\mathcal{C}_{nn}(\mathbf{r}_1,\mathbf{r}_2) = \langle\rho(\mathbf{r}_1)\rho(\mathbf{r}_2)\rangle \quad \rightarrow \quad \mathcal{C}(\mathbf{Q}) = \int d\mathbf{r}_1\mathbf{r}_2\mathcal{C}_{nn}(\mathbf{r}_1,\mathbf{r}_2)exp(-i\mathbf{Q}\cdot(\mathbf{r}_1-\mathbf{r}_2)). \tag{2.18}$$

From Eqs. 2.16,2.17, and 2.18 we see that the correlation function $\mathcal{C}(\mathbf{Q})$ is directly related to the static structure factor $\mathcal{S}(\mathbf{Q})$

$$\mathcal{C}(\mathbf{Q}) = \langle\rho(\mathbf{Q})\rho(-\mathbf{Q})\rangle = \mathcal{S}(\mathbf{Q}). \tag{2.19}$$

The structure factor is thus a function that describes to what extent the system can be considered as a periodic order crystal. So far we have restricted ourself to static systems but the formalism of correlation function can be easily generalized to dynamic systems. Particles can for example oscillate around their equilibrium positions thus the density of particles is: $\rho(\mathbf{r}(t)) = \sum_\alpha \delta(\mathbf{r} - \mathbf{r}_\alpha(t))$. The dynamic density-density function is then defined as

$$\mathcal{C}(\mathbf{Q},\omega) = \langle\rho(\mathbf{Q},\omega)\rho(-\mathbf{Q},\omega)\rangle = \mathcal{S}(\mathbf{Q},\omega), \tag{2.20}$$

where $\mathcal{S}(\mathbf{Q},\omega)$ is the dynamical structure factor.

2.1.6 Susceptibility. Linear response theory is widely used in many branches of physics. This theory states that the response of a physical observable to an external perturbation is proportional to the perturbation. Here I will not derive the theory in thorough detail but instead refer the reader to some useful textbooks on the subject [79, 82, 83]. The response function, also known as the generalized susceptibility, is defined as

$$\chi(\mathbf{Q},\omega) = \frac{\delta\mathcal{M}(\mathbf{Q},\omega)}{\mathcal{F}_{ext}(\omega)} \tag{2.21}$$

where $\delta\mathcal{M}(\mathbf{Q},\omega)$ is the response of the physical observable $\mathcal{M}$ and $\mathcal{F}_{ext}(\omega)$ is a weak external perturbation. The observable $\mathcal{M}$ could for example be the magnetization of a system and $\mathcal{F}_{ext}(\omega)$ could be an oscillating external magnetic field. The response is not always in phase with the external perturbation thus there can be a phase shift between the perturbation and the response of the physical observable. In that case the susceptibility χ is an imaginary function

$$\chi(\mathbf{Q},\omega) = \chi'(\mathbf{Q},\omega) + i\chi''(\mathbf{Q},\omega). \tag{2.22}$$

The imaginary part χ'' is closely related to the dissipation W in the system

$$W \propto \omega\chi''(\mathbf{Q},\omega). \tag{2.23}$$

The imaginary part of the generalized susceptibility $\chi''(\mathbf{Q},\omega)$ is also related to the two-particle correlation function $\mathcal{C}$ and thus the structure factor $\mathcal{S}$ via the fluctuations-dissipation theorem [82, 83]

$$\chi''(\mathbf{Q},\omega) = \frac{\pi}{\hbar}[1-\exp(-\beta\hbar\omega)]\mathcal{S}(\mathbf{Q},\omega), \tag{2.24}$$

where $[1-\exp(-\beta\hbar\omega)]$ is the so-called Bose factor. This result is important since it tells that an absorption or response experiment that probes $\chi''(\mathbf{Q},\omega)$ contains the same information as a scattering experiment that probes $\mathcal{S}(\mathbf{Q},\omega)$.

2.2 EXPERIMENTAL TECHNIQUES

One goal of this thesis is to reveal information about the dominant many-body interaction in the cuprates. This is done by the use of two very powerful experimental techniques. Angle resolved photoemission spectroscopy measures ideally the spectral function $\mathcal{A}(\mathbf{k},\omega)$ and thereby the self-energy $\Sigma(\mathbf{k},\omega)$. On the same crystals neutron scattering was applied to study the spin-spin correlation function $\mathcal{S}(\mathbf{Q},\omega)$.

Many response experiments such as AC and DC magnetization measurements probe χ'', however only momentum integrated information is obtained. This is often insufficient in the HTSCs where the electronic structure is strongly anisotropic. The strength and uniqueness of ARPES and neutron scattering is that they provide information about the momentum dependence of $\mathcal{A}(\mathbf{k},\omega)$ and $\mathcal{S}(\mathbf{Q},\omega)$.

Chapter 3

Bulk properties

This chapter is devoted to bulk measurements that have been done in order to characterize the crystals studied by ARPES and neutron scattering. The crystals have been characterized with respect to their crystalinity, to the superconducting transition T_c, and to the concentration of dopants to mention a few properties. The $La_{2-x}Sr_xCuO_4$ crystals, used for the experiments presented here, are all grown by the TSFZ method [84]. To get a homogeneous distribution of oxygen the samples were annealed in an ambient oxygen atmosphere with a temperature of 850 degrees Celsius.

3.1 Crystal structure

The basic building blocks of superconducting cuprates are CuO_2 planes separated by layers with rare-earth elements. From a chemical point of view, LSCO is among the most simple cuprates. Holes are doped into the CuO_2 plane by substituting La with Sr. The hole doping content is therefore directly determined by the concentration of Strontium. An advantage of LSCO over other cuprate materials is that it is possible to synthesize crystals with hole doping content from $x = 0$ to $x = 0.3$. The entire phase diagram from the Mott insulator to the non-superconducting metal can therefore be studied. The lattice constants of LSCO, at room temperature, are $a \approx b \approx 3.8$ Å and $c \approx 13.2$ Å (tetragonal notation), see figure 3.1. The structure of LSCO is tetragonal or orthorhombic depending on doping and temperature. The second order transition from low-temperature orthorhombic (LTO) to high-temperature tetragonal (HTT) is used in this work to estimate the doping level of the samples. From structure-factor considerations one can show that the Bragg peak (104) is allowed in the orthorhombic structure but forbidden in the tetrag-

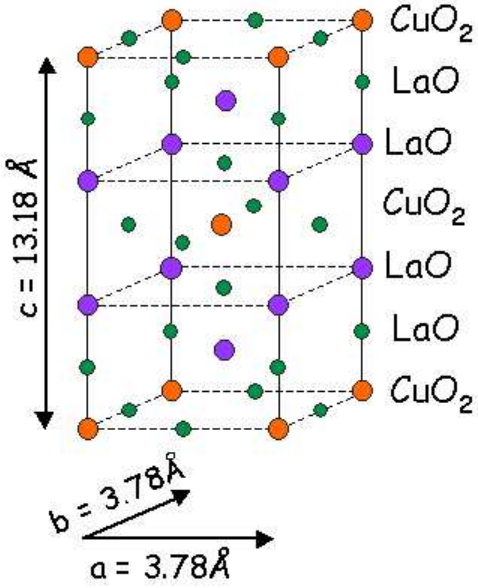

Figure 3.1: Crystal structure of LSCO. This figure is taken from [85].

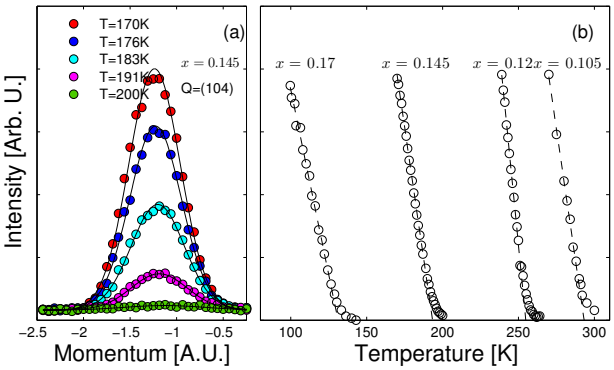

FIGURE 3.2: (a) Temperature dependence of the (104) Bragg peak (orthorombic notation) in LSCO $x = 0.145$. (b) Integrated intensity of the (104) peak as a function of temperature for various dopings. The $x = 0.17$ data are adapted from [87].

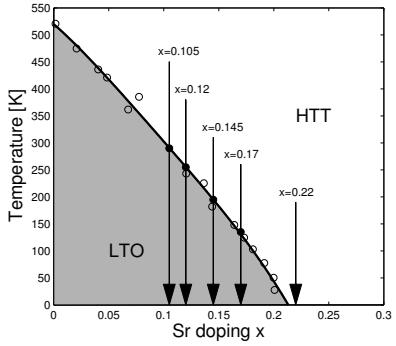

FIGURE 3.3: The transition temperature between HTT and LTO as a function of doping. The open points are from [86] while the filled circles are from our samples. The solid line is a guide to the eye.

onal structure. Figure 3.2(a) shows the results of a neutron diffraction experiment where **Q**-scans through (104) were performed as a function of temperature near the structural transition. The integrated intensity of the $\mathbf{Q} = (104)$ Bragg peak as a function of temperature is shown for various dopings in figure 3.2(b). The structural phase diagram is shown in figure 3.3 where the open points are from literature (see references in [86]). We used this structural transition to estimate the doping level of our samples, see figure 3.3.

3.2 MAGNETIZATION AND SUSCEPTIBILITY MEASUREMENTS

I will now present some magnetization and susceptibility measurements which have mainly been performed on a commercial Quantum Design Physical Property Measurements System (PPMS) [88] at PSI. This instrument is equipped with a 9 tesla magnet and it can measure specific heat, resistivity, and DC/AC magnetization. Here I will only report on DC magnetization and AC susceptibility measurements on underdoped LSCO.

Magnetization is the property of a material that describes to what extent it is affected by an external magnetic field. The magnetization is defined as the amount of magnetic moment per unit volume. The origin of the magnetic moment that creates the magnetization can be either from moments due the movement of electrons or from localized spins of electrons. Magnetic susceptibility χ is defined as:

$$\chi = \frac{M}{H} \tag{3.1}$$

where M is the magnetization and H is the applied static magnetic field. The magnetic moment is measured by the voltage induced upon moving the moment of the sample in a copper pick-up coil. The normal state magnetic susceptibility of LSCO is strongly dependent on the doping concentration, for a systematical study see [60, 61, 89].

3.2.1 Meissner Effect. The fact that superconductors can conduct a current without dissipation means that perfect screening against an external magnetic field is possible. This effect is also

known as the Meisner-Ochsenfeld effect. Type I superconductors can expel a magnetic field completely and are therefore perfect diamagnets. The onset of a diamagnetic response as a function of temperature is often used as a measure of the critical temperature of superconductivity T_c. The diamagnetic signal is strongest when the field is applied at $T \ll T_c$ since the superconducting order parameter is fully developed. The magnetization curves are therefore often measured as a function of T after zero field cooling (ZFC). The field cooled (FC) magnetization curve exhibits a smaller response compared the ZFC curve, but the transition temperature remains essentially unchanged.

3.2.2 Pressure effect. Now I will present an experiment designed to study the effect of hydrostatic pressure. This experiment was performed on a commercial SQUID at the Cavendish laboratory* (United Kingdom) using a Cu-Be pressure cell. A small piece of Indium was introduced in the pressure cell in order to estimate the pressure by measuring the superconducting transition†.

Figure 3.4 shows the magnetization as a function of temperature under ambient pressure and a hydrostatic pressure of $P \approx 10$ kBar for LSCO with $x = 0.105$ and $x = 0.145$. Consistently with previous reports [90, 91] we find that for both compounds hydrostatic pressure increases the onset temperature for superconductivity by approximately 0.15 K/kBar.

The pressure effect is most likely of indirect character. Under pressure the lattice constant a decreases ‡. To demonstrate this a neutron diffraction experiment was performed. Under pressure the neutron scattering angle 2θ of the (200) Bragg peak (orthorhombic notation) decreases compared to the ambient pressure scattering angle, see the inset of figure 3.4. Through the Bragg law [$\lambda_n = 2a\sin(2\theta)$] we find a lattice constant of $a = 5.30$ under $P \approx 10$ kBar which should be compared to $a = 5.334$ under ambient pressure.

With a smaller lattice constant, one would expect the hopping integral t to increase. The superconducting transition temperature is likely to depend on t. The effect of pressure on SC is therefore more likely related through the electronic degrees of freedom than the lattice degrees of freedom since pressure acts to suppress lattice degrees of freedom. For an comprehensive review of pressure experiments on superconductors see [93].

3.2.3 Spin-glass. The underdoped regime of LSCO is characterized by competing magnetic and superconducting order parameters. This competition leads to a rich variation of ground states. Frustrated spins are a natural consequence of competing orders and at low-temperature such systems might freeze into a spin-glass [94]. Spin-glass-like behavior has been observed in lightly doped LSCO [95–97] and related compounds [98, 99].

Here I present a magnetization study of $La_{1.48}Nd_0.4Sr_0.12CuO_4$ (NdLSCO) at low external field and as a function of temperature. This experiment was done on a 0.3 g crystal and the field was applied perpendicular to the CuO_2 planes. This system has a structural transition from orthorhombic to tetragonal at $T = 70$ K and here the focus will be on the temperature regime $T < 70$ K. Figure 3.5 shows the magnetization measured upon application of H =200 Oe in the temperature range between 8 K and 80 K. For $T > 30$ K, the magnetization decreases with decreasing

*This experiment was carried out in collaboration with C. Panagopolous, M. Saxena, and G. Jelbert.

†The superconducting transition temperature T_c for most phonon mediated BCS superconductors decrease with increasing external pressure. However, Indium is a rare counter example.

‡An other way to decrease the lattice constant and thereby to increase T_c is by applying strain to thin films [92].

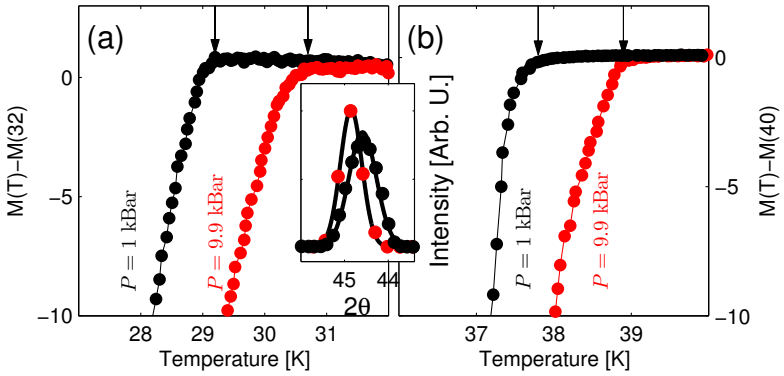

FIGURE 3.4: Magnetization as a function of temperature under ambient pressure (black) and under an external hydrostatic pressure (red). (a) and (b) are LSCO with $x = 0.105$ and $x = 0.145$, respectively. The inset shows the neutron scattering intensity of the (200) Bragg peak as a function of scattering angle 2θ, measured on LSCO $x = 0.105$ at $T \approx 2$ K. The red points are $P = 10$ kBar and the black points are taken under ambient pressure.

temperature. The opposite T-dependence was found for $T < 30$ K where the dependence can be described by the Curie-Weiss law,

$$\chi(T) = \chi_0 + \frac{C}{T}. \tag{3.2}$$

Here χ_0 and C are the T-independent susceptibility and the Curie constant, respectively. A fit to the data suggests that $\chi_0 = 5.9 \times 10^{-6}$ cm^3/g and $C = 25.3 \times 10^{-6}$ cm^3 K/g. The Curie constant C is a factor of about ten times larger than for LSCO with $x \sim 0.03 - 0.05$ [96]. There are at least two different possible reasons for this. First the increased doping concentration would naturally lead to an increased number of nearly free spins, and second the Nd-moments align along the c-axis, however the Curie-Weiss behavior might be contaminated by the Nd-moments. I will later argue that Nd-moment alone can not explain the T-dependence of the magnetization. Let us for a moment assume that the Curie-Weiss behavior stems from spin half electrons in the CuO_2 plane. The effective number of free spins N_{eff} can then be estimated from the Curie constant [96]

$$C = N_{\text{eff}} \frac{(g\mu_B)^2 S(S+1)}{3k_B} \tag{3.3}$$

where $g = 2$ and $S = 1/2$. The ordered moment μ of the Cu-spins in these materials is strongly reduced due to quantum fluctuation which becomes important in low dimensional systems. In the undoped parent compound the order moment is $\mu \approx 0.6\ \mu_B$ [100]. Upon hole doping the ordered moment is further reduced [101, 102]. Both neutron and μSR experiments suggest that the ordered moments at $x \sim 0.05$ and $x \sim 1/8$ are comparable. However, neutron diffraction experiments estimate $\mu \sim 0.1\ \mu_B$ while μSR experiments find $\mu \sim 0.35\ \mu_B$. Assuming $\mu \sim 0.1\ \mu_B$ one finds that the number of effective spins is about $N_{\text{eff}} \sim 0.1$ percent of the total electrons in the CuO_2 plane.

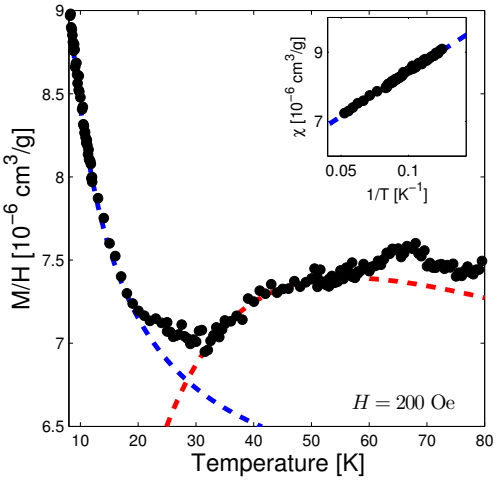

FIGURE 3.5: Magnetization as a function of temperature with $H = 200$ Oe. Dashed lines are explained in the text. The inset shows the Curie-Weiss behavior at low-temperature.

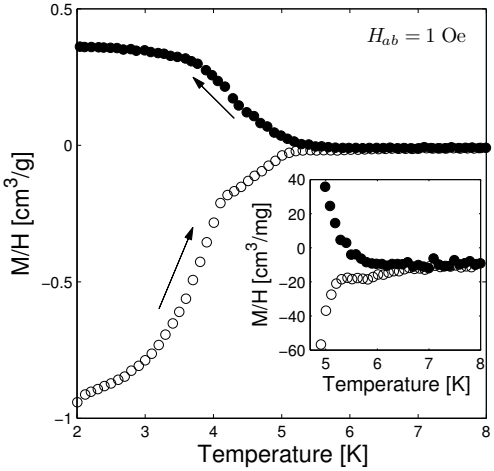

FIGURE 3.6: Magnetization measured upon application of $H = 1$ Oe as a function of temperature. The open circles are ZFC data and filled circles are FC data. The inset shows the onset temperature.

Hence even when the Curie-Weiss behaviour stems entirely from the in-plane electrons only a tiny fraction of these contribute.

Now I turn to the T-dependence in the range $T > 30$ K. In this NdLSCO compound it has been argued that the charges segregate into one dimensional stripes, in an otherwise antiferromagnetic background [103]. In this picture the spin structure consist of coupled spin ladders. The magnetization of even spin ladders is [104–106]:

$$\chi(T) = \frac{A}{\sqrt{T}} \exp\left(\frac{\Delta}{k_B T}\right) \tag{3.4}$$

where $\Delta = k_B T_{gap}$ is the gap energy and A is the amplitude. By fitting this function to the data I find $\Delta = 2.4$ meV or $T_{gap} = 28.2$ K, see the dashed red line in figure 3.5.

To round off this section I would like to point the attention to the low-temperature regime ($T < 8$ K) of the magnetization. Figure 3.6 displays field cooled (black) and zero field cooled (white) measurements upon application of $H = 1$ Oe. Under ZFC the response is effectively diamagnetic in contrast to the FC response which is paramagnetic. The inset shows the onset of the diamagnetic response at $T_g = 6.8 \pm 0.2$ K. Interestingly the superconducting onset temperature coincides with T_g. To investigate the nature of the paramagnetic response I performed the following experiment. The system was field cooled below the temperature T_g with for example $H = 10$ Oe. Then the external field was switched off and the relaxation of the magnetization was measured as a function of time. Figure 3.7 shows this relaxations for $T = 2$ K and 3 K. The time dependence was fitted to a stretched exponential function

$$M(t) = M(0) \exp\left(-\left[\frac{t}{\tau}\right]^{\alpha}\right) \tag{3.5}$$

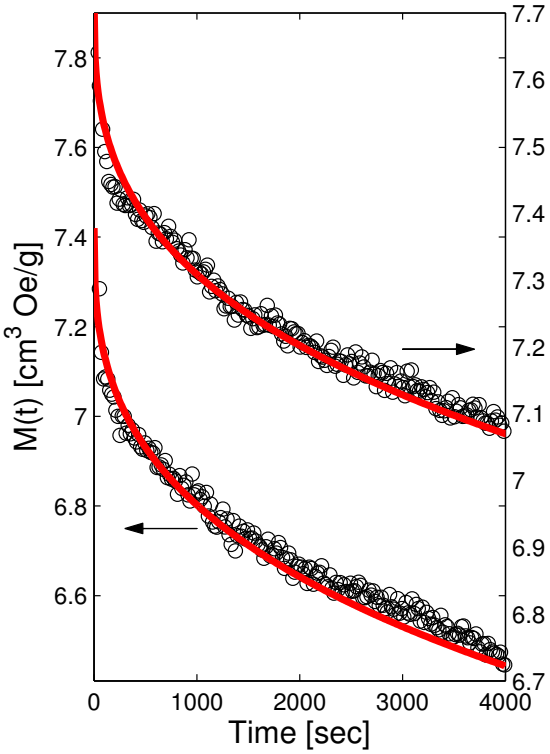

FIGURE 3.7: Time dependence of the magnetization at $T = 2$ K and $T = 3$ K after the field was set to zero. The lines are fits to a stretched exponential function.

where t is the time and τ serves as a characteristic time of *memory*. For both temperatures the fit gives $\alpha = 0.35$ and $\tau \approx 300$ hours. The exponent α compares well with the theoretical prediction for a spin-glass ($\alpha = 1/3$). A similar relaxation was observed in the spin-glass phase of lightly doped LSCO [95–97].

Since the same memory effect occurs in systems without Nd-moments I find it unlikely that the paramagnetic signal and the time relaxation originate from the Nd-moments that are known to order along the c-axis below $T_N \sim 3$ K [107]. Therefore I conclude that the paramagnetic signal stems from a spin-glass-like state.

A spin-glass is a typical signature of competition between two or more order parameters. In the case of cuprates there is a competition between magnetic and itinerant orders. This leads to the frustration of the Cu-spins. The spin-glass signature is most likely strongly dependent on the detailed sample chemistry. Therefore the spin-glass observed here is probably not a salient feature. However, the competion between different order parameter will be discussed in more detail in a later chapter.

3.3 AC SUSCEPTIBILITY

In AC magnetometry an AC magnetic field is superimposed on the DC field. The time dependent field will induce a time dependent moment in the sample. Without moving the sample, one measures $\chi = dM/dH$ from the current induced in the pick-up coil. At high frequencies the moments of the sample can not follow the applied AC field. Therefore AC magnetometry measures the susceptibility χ and a phase shift ϕ. It is often useful to think of the susceptibility as having an in-phase component χ' (real part) and an out-of-phase component χ'' (imaginary part). The real and imaginary components are related by

$$\chi' = \chi\cos(\phi) \tag{3.6}$$

$$\chi'' = \chi\sin(\phi). \tag{3.7}$$

Alternatively, one can express $\chi = \sqrt{\chi'^2 + \chi''^2}$ and $\phi = \tan(\chi''/\chi')$. In the low-frequency limit there will be no phase shift and the real part χ' is equivalent to χ as measured by DC magnetization. The imaginary part χ'' is a measure of dissipation in the sample, more precisely χ'' is the dissipation of heat during one AC period [82].

The experiments were performed with an external field $H_{ex} = H_{DC} + H_{AC}\cos(\omega t)$, where $H_{AC} = 10$ Oe and $\omega = 10$ Hz. Figures 3.8(a) and (b) show the temperature dependence of χ' and χ'' for LSCO with $x = 0.145$. For $H_{DC} = 0$ T, χ' becomes negative upon entering the superconducting state and χ'' peaks when the slope of χ' is steepest. Following R. Gilardi *et al.* [108], I will here denote the peak temperature by T_{FOT}, where FOT stands for first order transition. As H_{DC} is increased, T_{FOT} decreases systematically, as shown in figure 3.8(a). In figure 3.9, the field dependence of T_{FOT} is shown. In order to compare the result of various doping levels x, the temperature axis is normalized to the $T_c(x)$. Interestingly T_{FOT} seems to follow different lines for $x < 0.13$ and $x > 0.13$.

The transition T_{FOT} has been interpreted in terms of vortex physics. $T_{\mathrm{FOT}}(H)$ is most likely related to some kind of depinning of the vortices. To describe quantitatively the transition line $T_{\mathrm{FOT}}(H)$ the sublimation scenario [108, 109]

$$H_{\mathrm{FOT}} = \frac{2.85}{\gamma^2 s}\,(T_c/T - 1) \tag{3.8}$$

has proved to be the most successful. Here γ is the anisotropy factor and s is the layer spacing. For detailed discussion, see Ref. [108]. As will become clear in the coming chapters we used the knowledge of T_{FOT} to anneal the vortex lattice. The transition from pinned to depinned vortices can also be used to estimate the maximum current J_c that can be carried without dissipation [110].

In this sublimation scenario that measurements of T_{FOT}, shown in figure 3.9, suggest that the anisotropy factor γ is larger for $x < 0.13$ than for $x > 0.13$. One would therefore expect the vortex lattice to be more two-dimentional for $x < 0.13$. The vortex lattice structure is the topic of the coming chapter.

3.4 SUMMARY

Table 3.1 is compilation of the samples studied in this thesis. The doping concentration is derived, when possible, from the structural transitions, otherwise the nominal doping concentration

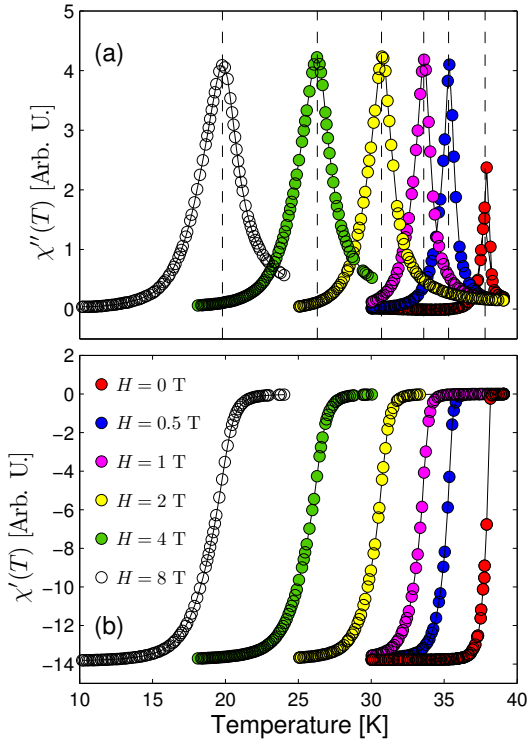

FIGURE 3.8: (a) and (b) are χ'' and χ' measured on $x = 0.145$ as a function of temperature and applied DC field.

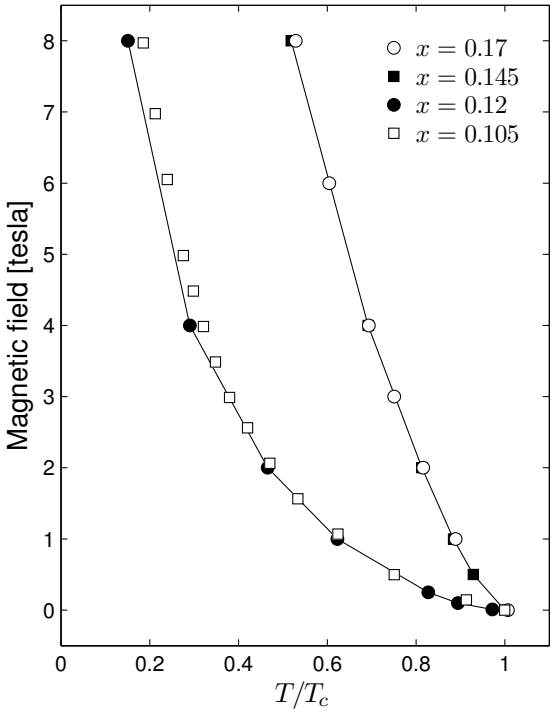

FIGURE 3.9: 'Melting' line for LSCO $x = 0.105$, $x = 0.12$, $x = 0.145$, and $x = 0.17$. The temperature axis is normalized to the T_c of the respective doping level.

is given. Finally the superconducting transition together with the width of the transition, obtained from magnetization measurements, is indicated for each sample.

Table 3.1: List of samples studied in this thesis. The superconducting transition temperature T_c and the transition width ΔT_c together with the lattice structure transitions are given.

Compound	Doping	T_c	ΔT_c	$T_{LTO-HTT}$	Origin
$La_{2-x}Sr_xCuO_4$	$x = 0.105$	30 K	1.5 K	290 K	N. Momono
$La_{2-x}Sr_xCuO_4$	$x = 0.12$	27 K		255 K	N. Momono
$La_{2-x}Sr_xCuO_4$	$x = 0.145$	36 K	1.5 K	190 K	N. Momono
$La_{2-x}Sr_xCuO_4$	$x = 0.17$	36 K	1.5 K	135 K	N. Momono
$La_{2-x}Sr_xCuO_4$	$x = 0.22$	26 K		-	O. Libscompe

Compound	Doping	T_c – onset	$T_{LTT-HTO}$	Origin
$La_{2-x-y}Nd_ySr_xCuO_4$	$x = 0.12$, $y = 0.4$	7 K	70 K	N. Momono

Chapter 4

Investigation of the vortex lattice in LSCO

In type-II superconductors vortices occur upon application of a magnetic field larger than H_{c1}. Vortices are formed at the point where the magnetic field penetrates the superconductor in a flux tube through the sample. The flux tubes that penetrate the superconductor are quantized in units of the flux quantum $\Phi_0 = \frac{h}{2e}$. Consequently, the core of the vortex acts as a normal state in an otherwise superconducting environment, see figure 4.1. This coexistence of normal and superconducting phases is often denoted the *mixed* phase. With increasing applied field, the density of vortices increases and a vortex lattice might be formed due to the repulsive interaction between the flux tubes. By increasing the applied field beyond a critical field H_{c2}, superconductivity is eventually completely destroyed.

Many applications of superconductors rely on the stabilization of the vortices. For example the vortices need to be immobile in order to have a dissapationless current. Therefore the upper critical current j_c depends on the pinning force of vortices [111]. The vortex core physics are also challenging from an academic point of view. For example, the density of states (DOS) of the superconducting phase and in the non-superconducting core can be studied by STM/STS as shown in figure 4.1. The density of state is gapped in the superconducting state while inside the core a gapless tunnelling current can be observed. As a bulk sensitive technique, the inelastic neutron scattering response in the mixed phase is a measure of both the cores and the superconducting phase. Hence the vortex cores may alter significantly the inelastic neutron scattering response. The vortex phase diagram is therefore of particular interest in the context of inelastic neutron scattering under an external applied magnetic field.

The structure of the vortex lattice is in itself an interesting topic. In isotropic superconductors the vortices align in a periodic triangular lattice structure. Due to the anisotropic pairing symmetry, it has been speculated that a square vortex lattice would be preferential in high-T_c superconductors [112]. Indeed, a transition from a hexagonal to a square structure has been observed in LSCO $x = 0.17$ [113] and YBCO [114, 115]. However, the critical field for the hexagonal-to-square transition varies by an order of magnitude from LSCO to YBCO. Even more puzzling is that the orientation of the square lattice is along the Cu-O-Cu direction in LSCO, but 45 degrees rotated in YBCO. Most likely the square vortex lattices stem as well from anisotropies in the electronic structures

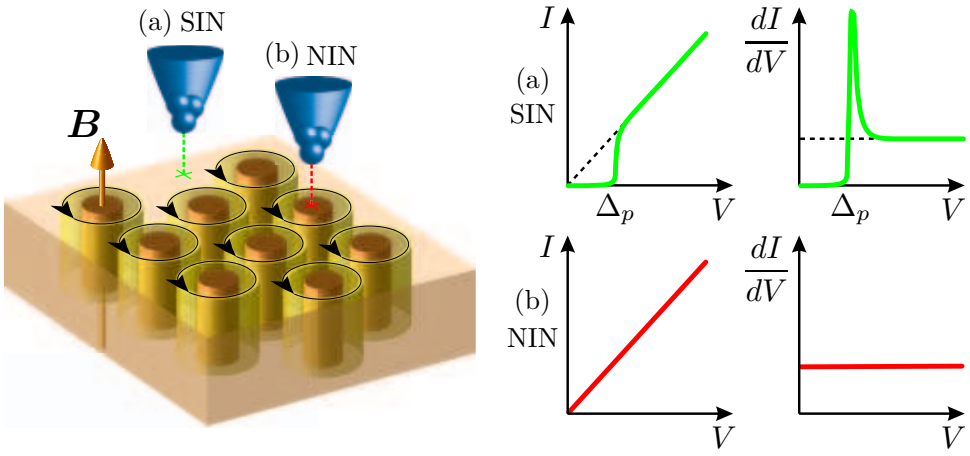

FIGURE 4.1: Left panel shows a superconductor with a vortex lattice. The core of the vortex lattice is non-superconducting. Right panel shows schematically the tunnelling spectra from the superconducting and non-superconducting regions. The main difference is that the superconducting region has a gap in the density of state while the non-superconducting region has no gap. This figure is taken from O. Fischer *et al.* [116].

of these materials. To shed more light to this problem, a systematic study of the vortex lattice in LSCO at low-temperature and as a function of magnetic field H and doping x was performed.

4.1 MAGNETIC PHASE DIAGRAM

The magnetic phase diagram of HTSCs reveals a tremendously rich variety of phenomena associated with flux vortices, for a review see [117]. A schematic field-temperature phase diagram is shown in figure 4.2. As mentioned in the introduction, the high-T_c cuprates are extreme type-II superconductors ($\kappa \gg 1$). Part of the magnetic phase diagram can be understood from the coherence length ξ_{sc} and the penetration depth λ. The lower and upper critical field H_{c1} and H_{c2} are controlled by these length scales and according to Landau-Ginzburg phenomenology [118]

$$H_{c1} \sim \frac{\Phi_0}{2\pi\mu_0\lambda^2}\ln(\kappa) \quad \text{and} \quad H_{c2} \sim \kappa^2 H_{c1}, \tag{4.1}$$

where $\kappa = \lambda/\xi_{sc}$ and μ_0 is the magnetic permeability of the free space. Extreme type-II superconductors are therefore characterized by low values of H_{c1} and high values of H_{c2}. Hence, the phase diagram is dominated by the so-called mixed phase.

For the cuprates there is an other important length scale, namely the Josephson length $\lambda_J = \gamma s$, where $\gamma = \sqrt{\rho_c/\rho_{ab}}$ is the anisotropy factor and s is the interplane distance. Across the different cuprate materials like YBCO, Bi2212, and LSCO, the interplane distance is approximately constant $s \sim 10$ Å. However, the anisotropy factor γ can vary by orders of magnitude among the mentioned materials. For example, for YBCO $\gamma \sim 10$ while for Bi2212 $\gamma \sim 100$ [121]. A higher value of γ indicates a stronger decoupling of the CuO_2 planes. The tendency to form quasi-2D

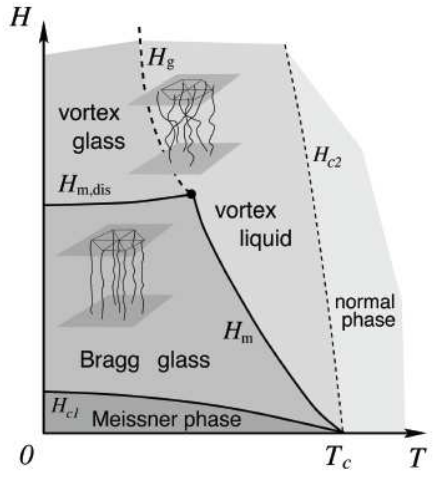

FIGURE 4.2: Schematic field-temperature phase diagram of extreme type-II superconductors. From G. Blatter *et al.* [119].

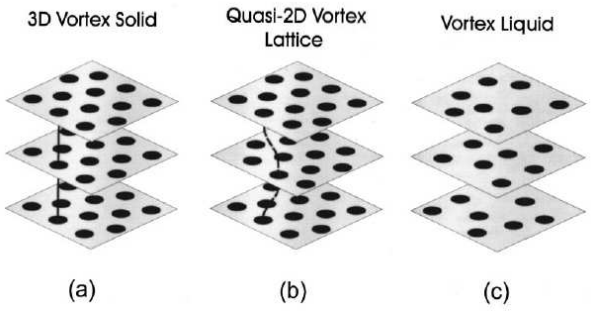

FIGURE 4.3: Schematics of the different vortex phases in high-T_c cuprates. (a) The vortices are perfectly aligned between the CuO_2 layers. (b) In the weak coupling limit, the vortices are aligned in-plane but quasi disorder between the planes resulting in a quasi 2D lattice structure. (c) Liquid or gas phase of the vortices. From J.E. Sonier *et al.* [120].

vortex lattices is therefore enhanced with larger values of γ. If we turn it around, one would expect more 3D like vortex structures for smaller values of γ. The 3D and 2D structures are schematically shown in figure 4.3.

Due to defects, the correlation length of a vortex lattice is always finite. Therefore the term *Bragg glass* is often used to describe the 3D vortex lattice. Likewise for the quasi 2D lattice, the term *vortex glass* is often used, see figures 4.2 and 4.3. To finish the examination of the magnetic phase (figure 4.2), it should be mentioned that the vortices can also exist in a liquid phase. A vortex lattice can melt due to thermal fluctuations. Although lattice instabilities are, in general, a source of ongoing research [122, 123], focus will here be entirely on the low temperature part of the phase diagram.

Now let us start by discussing the extreme anisotropy case. For Bi2212, the Josephson length is comparable to the penetration depth, $\lambda_J/\lambda \geq 1$. A 3D-to-2D crossover was observed at very low field $H_{cr} \sim 0.05$ T in this compound [124, 125]. This crossover field H_{cr} is believed to be controlled by the Josephson length [126, 127]

$$H_{cr} \sim \frac{\Phi_0}{\lambda_J^2}. \tag{4.2}$$

Thus in the strongly decoupled limit the crossover field H_{cr} is determined by the degree of anisotropy.

In the other limit, where the Josephson length is very small compared to the penetration depth ($\lambda_J/\lambda \ll 1$), a 3D vortex lattice is more likely to be formed. For YBCO, a 3D vortex lattice has been directly observed by small angle neutron scattering up to $H \sim 10$ T [115].

Now the topic of this chapter is to study the vortex lattice in LSCO. It turns out that the anisotropy factor of LSCO is $10 < \gamma < 100$, which is in between the extreme cases of Bi2212 and YBCO. To be more specific, the anisotropy factor γ is doping dependent as shown in figure 4.7(b).

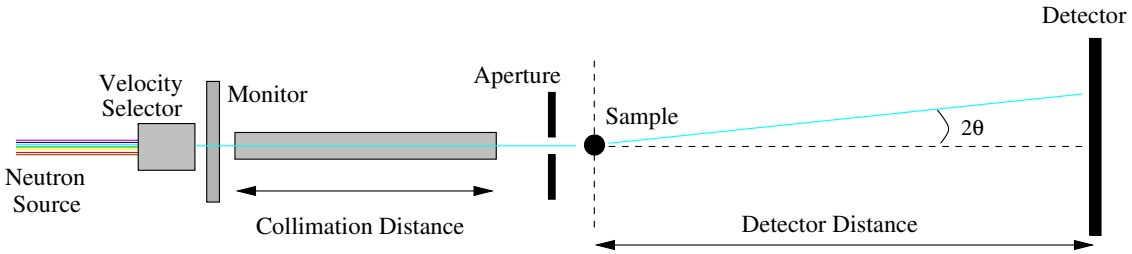

FIGURE 4.4: Schematic view of a small angle neutron scattering instrument. Using a velocity selector, monochromatic neutrons with wavelength λ_n are produced. Collimation and detector distances can be varied.

In LSCO, the ratio λ_J/λ as estimated from experiments ranges from ~ 0.05 in the overdoped region to ~ 0.1 in the underdoped region. As a function of doping it is therefore possible to tune the anisotropy factor.

Vortex physics can be studied by a variety of direct or indirect techniques. For example STM [116], μSR [120, 128], AC susceptibility, and Bitter decoration [129, 130] are all powerful experimental techniques to explore vortex physics. Here, the 3D vortex lattice of LSCO is studied by small angle neutron scattering (SANS) at low-temperatures. As mentioned before, the density of the vortices is related to the applied magnetic field. In the vortex lattice phase, the flux quantization dictates the lattice distance d

$$d = \sqrt{\frac{\sigma\Phi_0}{H}}, \tag{4.3}$$

where H is the applied field and σ is a dimensionless constant that depends on the VL structure. A square lattice has $\sigma = 1$ while $\sigma = \sqrt{3}/2$ for a hexagonal lattice.

Let us for a moment consider a square vortex lattice in an external field of $H = 1$ T. From Eq. 4.3 the lattice distance is $d \approx 450$ Å. To perform a diffraction experiment on such a lattice a wavelength comparable to the lattice distance d is required. The Bragg law [$\lambda_n = 2d\sin(\theta)$] gives the relation between the wavelength λ_n of the neutrons, the lattice distance d, and the scattering angle θ.

For neutrons the longest practically available wavelength is $\lambda_n \approx 25$ Å. According to the Bragg law this leads to rather small scattering angle $\theta \approx 3$ degrees. To resolve such a small scattering angle from the direct beam one needs very good resolution. Small angle neutron scattering instruments are constructed for that purpose.

4.2 SMALL ANGLE NEUTRON SCATTERING

4.2.1 Experimental procedure. A schematic view of a typical SANS instrument is shown in figure 4.4. The incident neutron beam is monochromated by a mechanical velocity selector. In practice it is impossible to create a truly monochromatic beam thus a finite spread of wavelength/energy of the neutrons is unavoidable. In fact a finite spread of neutrons is necessary

in order gain sufficient neutron flux. With wavelengths λ_n in range from 5 to 20 Å a spread $\Delta\lambda_n/\lambda_n \approx 0.1$ is a typical condition. After the velocity selector a monitor is situated in order to estimate the incident flux which is used for normalization. The divergence of the incident beam is controlled by two pinholes whose distance can be varied. The pinholes effectively act as a collimator and the distance between the pinholes is therefore also denoted *collimation* distance.

Usually the samples are aligned with one axis in the horizontal plane and the edges of the crystals are masked with Cadmium in order to minimize the background scattering. As sample environment a horizontal cryomagnet which can rotate around the vertical axis and tilt along the beam direction is used. The sample is carefully centered in the middle of the beam and in front of the magnet an aperture corresponding to the sample size is used, see figure 4.4.

The scattered neutrons are detected by a position sensitive detector (PSD). The detector is placed in an evacuated tank in order to avoid air scattering. The vacuum is in the order of 10^{-5} Bar and the detector distance can be varied inside the tank. The minimum distance between the sample and the detector is typically one meter while the maximum distance depends on the length of the tank which can be up to 40 meters.

The small angle neutron scattering experiments presented here were performed on SANS-I [131] and SANS-II [132] instruments at the Swiss Spallation source SINQ and on the D11 and D22 instruments at the Institute Laue-Langevin in Grenoble.

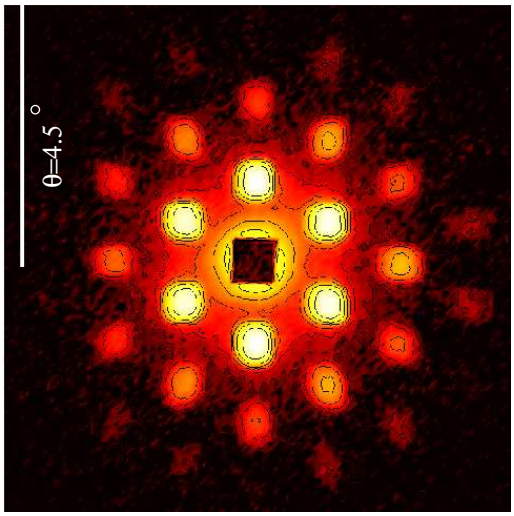

FIGURE 4.5: Diffraction pattern from a vortex lattice in Niobium taken with $H = 0.2$ T after field cooling. The intensity is displayed in logarithmic color scale. ($\lambda_n = 8$ Å)

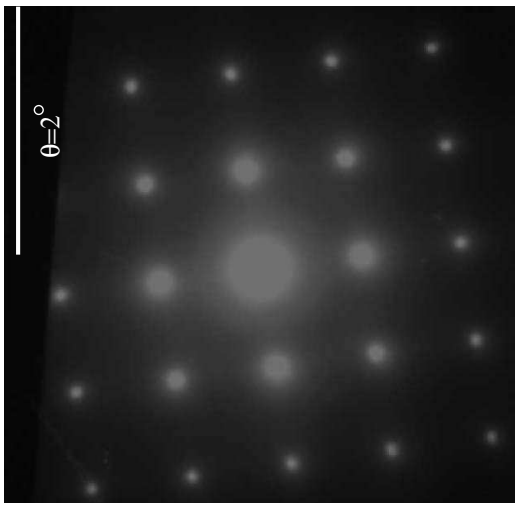

FIGURE 4.6: An example of a diffraction pattern from the crystal lattice of silicon obtained using a TEM with 300 KeV electrons ($\lambda = 0.0197$ Å).

4.2.2 Resolution and background subtraction. The resolution of SANS instruments is rather poor mainly due to the large spread in the wavelength of the incident beam. In figure 4.5 the diffraction pattern from a vortex lattice in Niobium is shown. The diffraction spots are rather broad features due to the poor resolution. For comparison, the diffraction pattern of a silicon

lattice, recorded in a transmission electron microscope (TEM), is shown in figure 4.6. The electron beam in a standard TEM has $\Delta\lambda_n/\lambda_n \approx 0.01$, thus the resolution is about an order of magnitude better than a SANS instrument. Accordingly, the diffraction spots are much better defined.

The resolution of a SANS instrument is also affected by the beam divergence. Therefore collimation of the incident beam improves the resolution. Finally, the resolution can be improved by increasing the detector distance. As a compromise between incident flux on the sample and the resolution, the experiments are usually performed with comparable collimation and detector distances. For a more comprehensive discussion of the resolution of SANS instruments see [87, 133].

The intensity of the neutrons scattered by the vortex lattice is usually comparable to the intensity of the background. Therefore to visualize the intensity of the neutrons scattered by the vortex lattice, a background subtraction is performed. This can be done in two different ways. The first method is to measure the background in the normal state, $T > T_c$, using the same field as was used for the forground measurement. An alternative, is to measure the background at the same temperature as the forground measurement but in zero field. In this work, the last mentioned method was preferred.

4.2.3 Differential cross section. In the experiments described here, the magnetic field was applied in the horizontal plane parallel to the beam direction. Now the magnetic dipole moment of a neutron interacts weakly with a flux tube that penetrates the sample. The interaction potential reads

$$\mathcal{V}(\mathbf{r}) = \mu_n \cdot \mathbf{B}(\mathbf{r}) \tag{4.4}$$

where $\mu_n = -\gamma_n \mu_N \vec{\sigma}$ is the magnetic dipole moment of a neutron. Since the spin of the neutrons and the field distribution $\mathbf{B}(\mathbf{r})$ are approximately parallel, the vector product simplifies to a product of the amplitudes.

The differential cross section can be calculated through the Fermi golden rule as discussed in chapter 2

$$\frac{d\sigma}{d\Omega} = |\mathcal{F}(\mathbf{Q})|^2 = \left(\frac{\gamma_n}{4\Phi_0}\right)^2 \left| \int \mathbf{B}(\mathbf{r}) \exp(-i\mathbf{Q}\cdot\mathbf{r}) d^3\mathbf{r} \right|^2 \tag{4.5}$$

where $\gamma_n = 1.913$ and $\mathbf{Q}$ is the scattering vector. The total counts in the detector area ΔA are

$$I = \psi \frac{d\sigma}{d\Omega} d\Omega \approx \psi \frac{d\sigma}{d\Omega} \lambda_n^2 \Delta A \propto \psi \lambda_n^2 \left(\frac{\gamma_n}{4\Phi_0}\right)^2 \left| \int \mathbf{B}(\mathbf{r}) \exp(-i\mathbf{Q}\cdot\mathbf{r}) d^3\mathbf{r} \right|^2 \tag{4.6}$$

where ψ is the incident flux. Next, a few simplifications are done in order to express the scattered intensity more elegantly. First, in the long wavelength limit, the flux scales approximately like $\psi \sim \lambda_n^{-4}$. Second, the field distribution $\mathbf{B}(\mathbf{r})$ can be calculated by various approaches, for a systematic review see [120]. According to London equations [134], the field distribution of a single vortex core is

$$B_z(\mathbf{r}) = \frac{\Phi_0}{2\pi\mu_0\lambda^2} K_0(r/\lambda), \tag{4.7}$$

where K_0 is the modified Bessel function of zero order. The scattered intensity then reads

$$I(Q) \sim \left(\frac{\gamma_n}{8\pi^2\mu_0\lambda^2\lambda_n}\right)^2 \left| \int K_0(r/\lambda) \exp(-i\mathbf{Q}\cdot\mathbf{r}) d^3\mathbf{r} \right|^2 \tag{4.8}$$

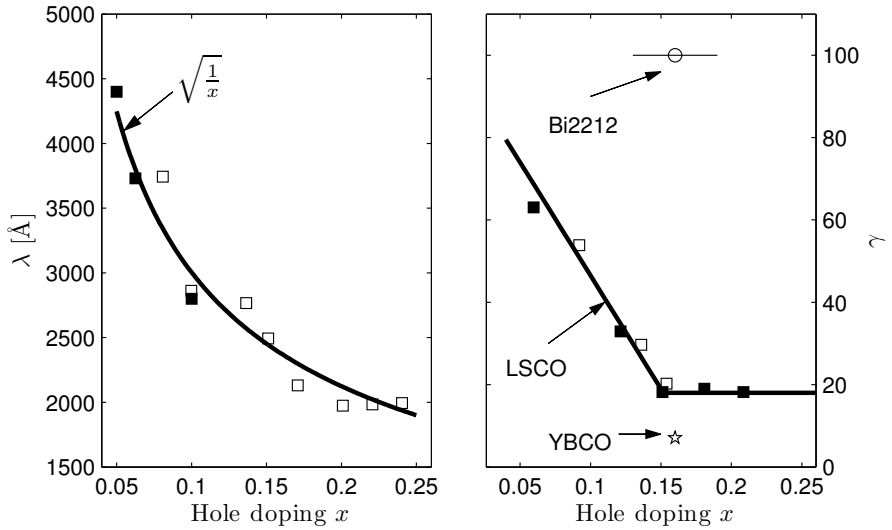

FIGURE 4.7: (a) Doping dependence of the penetration depth λ where the open squares are from [135] and the solid squares are from [136]. The solid line is $\lambda \approx \sqrt{m_e/n_s} \sim \sqrt{1/x}$. (b) Anisotropy factor γ as a function of doping from [121, 137]. Here the solid line is a guide to the eye.

where the integral gives a function that falls off with increasing Q. The prefactor yields two important informations. First, the intensity depends on the incident wavelength by λ_n^{-2}. Second, the scattered intensity relates to the penetration depth as λ^{-4}. For the HTSCs the penetration depth is an order of magnitude larger than in conventional BCS superconductors, as mentioned in chapter 1. The expected intensity for a high-T_c superconductor is therefore four orders of magnitude lower than for a BCS superconductor. The super fluid density n_s is lower in the underdoped region and increases gradually with doping. Consequently, the penetration depth is larger in the underdoped region as shown in figure 4.7(a). Therefore the intensity is expected to be stronger in the overdoped region of the phase diagram. This region of the phase diagram is hence a natural starting point.

4.3 VORTEX LATTICE IN THE OVERDOPED REGION OF LSCO

This section is devoted to describe the vortex lattice (VL) in the overdoped region of LSCO. In particular a study of the vortex lattice at low temperatures ($T = 2$ K) in $x = 0.22$ will be discussed. As shown in figure 3.3, the crystal structure of LSCO is tetragonal down to lowest temperatures for $x > 0.21$. It has been argued that the orthorhombic crystal structure for $x < 0.21$ might have an effect on the vortex lattice. So far the VL has only been studied for $x < 0.21$ in LSCO [87, 113]. Therefore to test the effect of crystal structure, we decided to study the VL in a crystal with tetragonal structure. This study was also motivated by the fact that the VL structure is believed to depend on the electronic properties which change with overdoping. An investigation of the VL as a function of overdoping would provide the best possibility to test whether or not there is a correlation between VL structure and electronic properties.

The $x = 0.22$ sample was aligned with the c-axis and one Cu-O-Cu axis approximately in the horizontal plane, see figure 4.8(a) and (b). As previously reported [87], we found that the signal was enhanced by wiggling the field close to the FOT transition line, see section 3.3. The results reported here were therefore obtained after a damped oscillation of the field at $T = T_{FOT}(H)$. The exact procedure is the following. The field is always ramped in the normal state ($T > T_c$). The system is then cooled to the FOT transition line, that can be measured by AC susceptibility. Here the field is oscillated around its set point. For example, if $H = 0.5$ T then an oscillation like $H = 0.5 - 0.6 - 0.4 - 0.55 - 0.45 - 0.5$ was performed. After the wiggling, the system was cooled to the desired temperature where the real measurement was performed. For a systematic study of the wiggling effect see [87].

The magnet was usually aligned from the VL of Niobium such that the field was parallel to the incident beam. The LSCO crystal was then installed in the magnet with the c-axis approximately in the beam direction. The experiment was performed by rotating or tilting the magnet by ± 5 degrees with steps of ~ 0.5 degrees. The signal is monitored at each step. A rocking curve denotes the intensity as a function of rotation angle $\bar{\omega}$. An example of a rocking is shown in figure 4.9(b) where the intensity of the two horizontal diffraction spots in figure 4.9(a) is displayed as a function of $\bar{\omega}$. Figure 4.9(a) shows the integrated intensity of the rocking curve. The intensity of the 2D detector can be analyzed in terms of polar coordinates (ϕ,2θ) where ϕ is the polar angle and the scattering angle 2θ is directly related to the distance from the direct beam center [see figure 4.4]. The origin of these coordinates was determined by the direct beam which is not visible in figure 4.9(a) due to a beam stop. The data can now be analyzed as a function of scattering angle 2θ [see figure 4.9(c)] or as a function of ϕ [see figure 4.9(d)].

At the lowest measured field $H = 0.05$ T, the scattered signal is distributed in a ring resembling the scattering from a poly-crystal, see figure 4.10(a). At higher fields (0.25 T $< H < 1$ T) clear diffraction spots, along the Cu-O-Cu crystal axis, were observed, see figure 4.10(c-f). A reader with a sharp eye might notice that second order diffraction spots were observed for $H = 0.5$ T, indicating a very well ordered vortex lattice.

Next in figure 4.11(a) the intensity as a function of scattering angle 2θ is shown for applied fields of $H = 0.25$ T and $H = 1$ T. These data were recorded with a constant incident wavelength of $\lambda_n = 8$ Å. The solid lines are fits to a Lorentzian lineshape. From the Bragg law ($\lambda_n = 2d\sin(\theta)$), a lattice constant d can be calculated for each field. Recall from equation 4.3 that the lattice constant

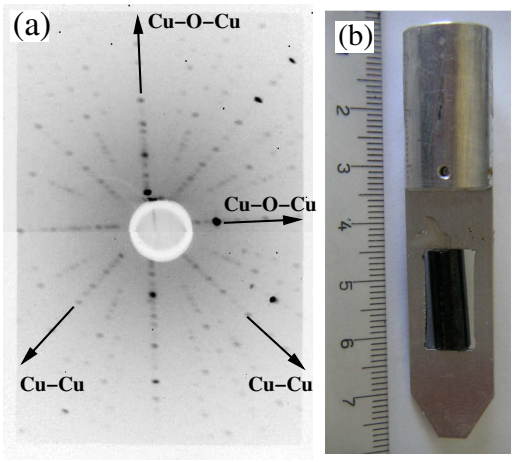

FIGURE 4.8: (a) Laue back-scattering diffraction spots of the crystal structure. The crystal symmetry axis are indicated by the black arrows. See also appendix A. (b) The sample holder with the LSCO crystal.

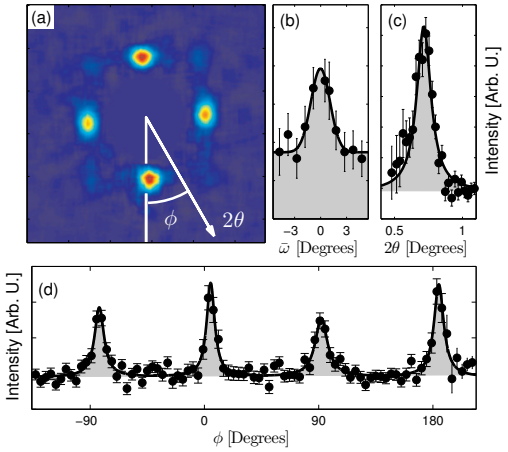

FIGURE 4.9: (a) An example of a 2D intensity map of the scattered intensity from a vortex lattice in single crystal LSCO with $x = 0.22$ under an applied field of $H = 0.5$ T. (b) Intensity of the horizontal spots as a function of rotation angle ω. (c) Scattered intensity as a function of scattering angle 2θ. (d) ϕ dependence of the signal.

d is related to the constant σ by

$$\sigma = d^2 \frac{B}{\Phi_0} \tag{4.9}$$

where $\sigma = 1$ for a square structure and $\sigma = \sqrt{3}/2$ for a hexagonal structure. Knowing the incident wavelength λ_n, the detector distance D, and the applied field H, σ can thus be derived. As a function of applied field, σ was measured in a systematic fashion from $H = 0.05$ T to $H = 1$ T as shown in figure 4.11(b). For $H > H_\square = 0.4$ T, σ is approximately constant and close to one as expected for a square lattice. By contrast, for $H < H_\square = 0.4$ T significant lower values of σ were found. For $H = 0.05$ T, a value close to $\sqrt{3}/2$ was found. The systematic change from $\sigma = 1$ to $\sigma = \sqrt{3}/2$ indicates that the vortex lattice undergoes a structural phase transition from square to hexagonal structure.

Let us now discuss the possible origin of the hexagonal-to-square transition. The repulsive interaction between the vortices forces them to align in some structure. The equilibrium structure can be calculated by minimizing the free energy of the system. For an isotropic *s*-wave superconductor, a hexagonal lattice is the most favorable structure [138]. By contrast for *d*-wave superconductors an anisotropic screening current and field distribution have been predicted [139, 140]. For low field the vortex cores are well separated and these anisotropies are irrelevant. With increasing field the vortex cores start to interact. The fourfold symmetry of the gap anisotropy may disturb the hexagonal structure and pushes the system into a square structure. Therefore, from a theoretical point of view, it is not completely unexpected to observe a hexagonal-to-square transition as a function of applied magnetic field. The *d*-wave scenario predicts a square lattice oriented along the Cu-Cu direction. It is therefore a surprise that the square lattice in LSCO is oriented along the

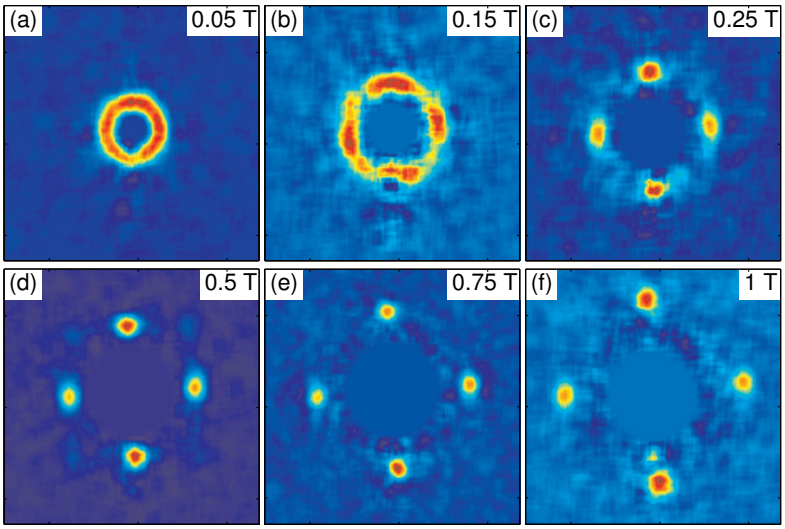

FIGURE 4.10: (a)-(f) Field dependence of the scattered intensity of the vortex lattice with $H = 0.05$, $H = 0.15$, $H = 0.25$, $H = 0.5$, $H = 0.75$, and $H = 1$ T, respectively.

Cu-O-Cu direction. This issue will be discussed in more detail later.

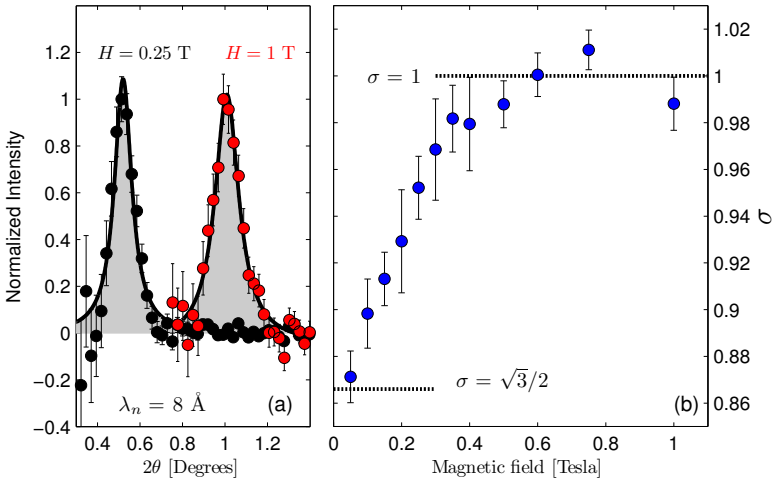

FIGURE 4.11: (a) Normalized intensity as a function of scattering angle 2θ for applied field of $H = 0.25$ T and $H = 1$ T. These data were recorded with an incident wavelength $\lambda_n = 8$ Å. The solid lines are Lorentzian fits to the data. (b) The constant σ (see Eq. 4.9) as a function of applied field H.

4.4 VORTEX LATTICE IN THE UNDERDOPED REGION OF LSCO

Now, I turn to discuss the vortex lattice in the underdoped region of LSCO. Let's start with the slightly underdoped compound $x = 0.145$. The VL of the slightly underdoped region has so far not been investigated directly by SANS. Recently, it has been demonstrated that application of a magnetic field perpendicular to the CuO_2-layers induces static incommensurate magnetism above a critical threshold field [141]. As will be described later, we observe field-induced static magnetism for $H > 7$ Tesla in our $La_{1.855}Sr_{0.145}CuO_4$ sample. Due to the competition between static magnetism and superconductivity, one would expect that the signal from the VL will decrease upon entering the ground state where magnetism and superconductivity coexist. Therefore we decided to investigate the H-dependence of the VL in $La_{1.855}Sr_{0.145}CuO_4$ at base temperature ($T = 2$ K).

Two different experiments were done. First, at the D11 instrument the VL was investigated in fields ranging from 0.05 T to 1.3 T. In a second experiment at the SANSI instrument the range from 1 T to 7 T was studied. The experimental setup and procedure were essentially the same as for the above described experiment on $x = 0.22$.

Now I am going to describe the low field ($H < 1.3$ T) experiment. Again we tested the effect of wiggling the field, but for this compound no significant effect was observed. Therefore we decided not to perform the wiggling procedure during this experiment. At the D11 instrument it is possible to have a distance of up to 40 meters between the sample and the detector. The result shown in figure 4.12(a) is obtained with a detector distance of 34 meters and an applied field of $H = 0.05$ T. Similarly to the result obtained on $x = 0.22$ with $H = 0.05$ T, the scattered intensity is distributed in a ring. Note that the intensity is shifted slightly downward. The reason is that the neutrons due to gravity have a downward trajectory and this becomes more evident when long detector distances are used. For $H = 0.3$ T and $H = 1.3$ T, clear diffraction spots are visible as shown in figure 4.12(b) and (c). In the latter case the spots have a fourfold symmetry, and they are oriented along the Cu-O-Cu direction. For $H = 0.3$ T, this fourfold symmetry is clearly not present. It should be emphasized that for the measurements shown in figure 4.12(a) and (b), the c-axis was rotated 10 degrees away from the field direction. This was done in order to avoid a superposition of different domains with hexagonal coordination. The effect of this procedure has previously been discussed in a number of works [87, 113, 142], and for this experiment the effect was discussed in the master thesis of L. Maechler [143].

In figure 4.12(d) and (e) the integrated intensity as a function of scattering angle 2θ is shown for $H = 0.05$ T and $H = 1.3$ T. Here the solid lines are Lorentzian fits to the data. The constant σ can be derived from the peak position and the full H-dependence of σ is shown in figure 4.12(f). At low field $H < 0.4$ T, the values of σ suggest that the system is closest to a hexagonal structure. Although the extracted values of σ scatter considerably for $H < 0.4$ T, the data show unambiguously that the square lattice structure is stabilized only for $H > H_{\square} = 0.9$ T. For intermediated fields the values of σ suggest a crossover from hexagonal-to-square. This is significantly different from $x = 0.22$ where the square lattice was stable for $H > H_{\square} = 0.4$ T. A direct comparison will be done later in this chapter.

Now, let's turn to the high field (1.2 T $< H < 7$ T) experiment performed at the SANSI instrument. Although no significant effect of wiggling of the field was observed, we decided to perform the wiggling throughout this experiment. In figure 4.13(a), the diffracted intensity distribution

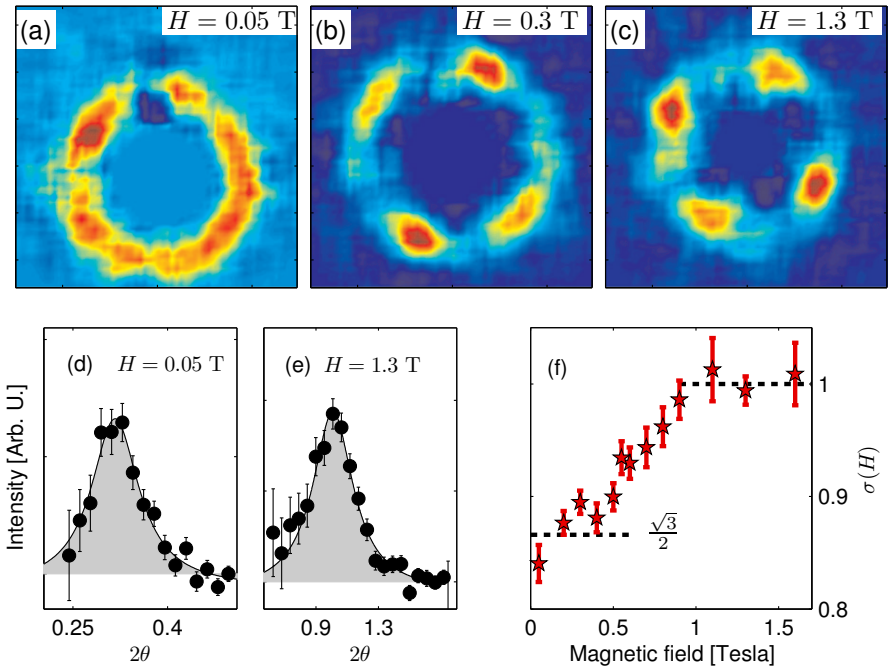

FIGURE 4.12: (a)-(c) Diffracted intensity for applied fields of $H = 0.05$ T, $H = 0.3$ T, and $H = 1.3$ T. These data were recorded with detector distance 34 m, 16.5 m, and 10.5 m, respectively. The c-axis was rotated 10 degrees away from the field direction for (a) and (b), as explained in the text. (d) and (e) Integrated intensity as a function of scattering angle 2θ for (a) and (c). (f) Field dependence of the dimensionless constant σ. Except for the $H = 0.05$ T measurement all values of σ were extracted from data recorded with the c-axis along the magnetic field direction.

for $H = 2$ T is shown. Consistently with the measurements at $H = 1.3$ T [see figure 4.12(c)], a square lattice is observed. We then decided to measure the H-dependence of the diffracted intensity. For that purpose we fixed the detector distance $D = 7$ m and the incident wavelength $\lambda_n = 6$ Å. Figure 4.13(b)-(d) display the diffracted intensity for $H = 2.5$ T, $H = 3$ T, and $H = 4$ T on the same intensity scale. It can be seen that the intensity decreases rapidly with increasing field. In figure 4.14 (a) and (b) the integrated intensity as a function of scattering angle 2θ is shown for different applied fields. For $H = 1.6$ T and $H = 3$ T, the intensity profile could be fitted to a Lorentzian line shape. By contrast, for $H = 7$ T no evidence for a VL could be observed. Figure 4.15 shows the intensity extracted from the Lorentzian fits as a function of field H. It can be seen that the intensity decreases very fast as a function of applied field. The inset shows a comparison of data recorded on $x = 0.105$* and $x = 0.145$ in logarithmic scale. In this figure the solid lines are $I \sim H^{-2}$.

It was expected that the intensity would decrease fast for $H > 7$ T due to the appearance of a competing magnetic order. However, the experiment indicates that the intensity vanishes before

*The result obtained on LSCO $x = 0.105$ differs from experiment to experiment. A sober presentation of the differences is presented in the thesis of R. Gilardi [87]. For comparison I used the data which had the best quality.

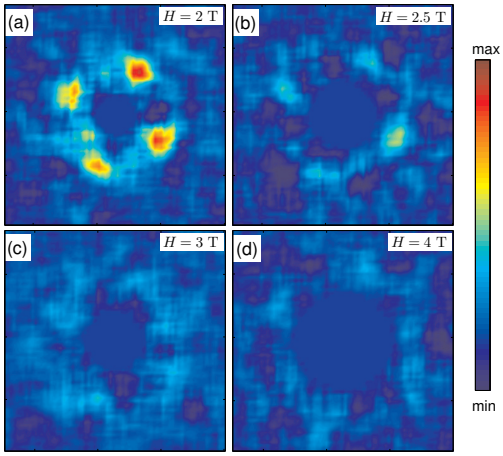

FIGURE 4.13: (a)-(d) 2D intensity maps of the scattered intensity for $H = 2$ T, $H = 2.5$ T , $H = 3$ T, and $H = 4$ T, respectively. Here the intensity is shown on absolute scale.

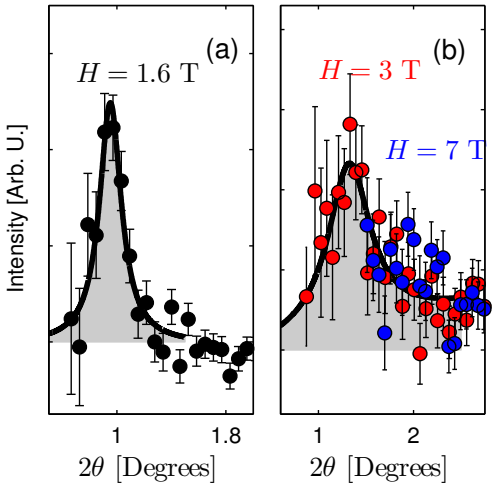

FIGURE 4.14: (a) and (b) Integrated intensity as a function of scattering angle 2θ for $H = 1.6$ T, $H = 3$ T, and $H = 7$ T. Solid lines are Lorentzian fits to the data.

the system enters the state with static magnetic order. Several explanations are possible. The disordering of the vortex lattice might be interpreted as a precursor of the static magnetism. As the system is tuned from a pure d-wave superconductor into a state with coexistence of static magnetism and superconductivity, strong quantum fluctuations are present. One could imagine that the vortex lattice melts due to these fluctuations similar to the VL melting due to thermal fluctuations.

An alternative and probably more plausible explanation is that the VL undergoes a 3D-to-2D crossover. As mentioned before, the crossover field is controlled by the anisotropy factor, $H_{cr} = \Phi_0/(\gamma s)^2$. Since the anisotropy γ increases with underdoping this explains qualitatively why the crossover appears at a lower field in $x = 0.105$ and why the crossover is not observed in $x = 0.17$ for $H < 10$ T [144]. Although $H_{cr} = \Phi_0/(\gamma s)^2$ can describe the observed crossover in the extreme anisotropic material Bi2212 [124], the situation is probably more complicated in LSCO. Using the experimentally obtained values of γ, the here observed crossover fields can not be captured on a quantitative level, see figure 4.16.

It should be mentioned that consistently with our observations a melting of the vortex lattice at $H = 5$ T was deduced from specific heat and magnetization measurements in $x = 0.14$ [145].

4.4.1 Search for a vortex lattice near the anomalous $x \sim 1/8$. A search for a vortex lattice in the $x = 0.12$ compound was done on D22 which is the most powerful SANS machine in the world. Different types of wiggling procedures were tried. However, no vortex lattice could be observed in this compound. Even with very long counting times no evidence for a vortex lattice was found for $H = 0.03$ T, $H = 0.05$ T, and $H = 0.1$ T. A comparison with a previous experiment

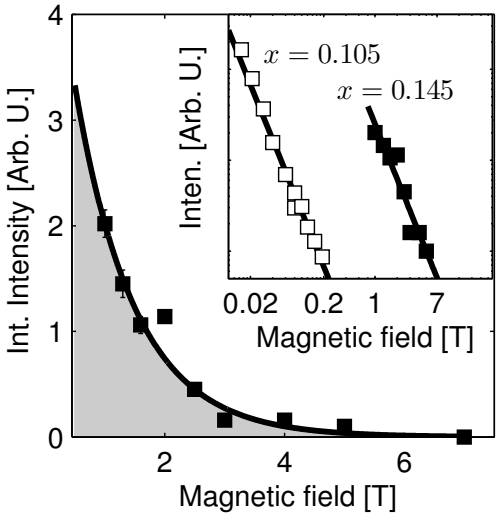

FIGURE 4.15: Intensity extracted from the Lorentzian fits as a function of applied field H. Here the solid line is a guide to the eye. The inset is a log-log plot of the intensity versus H for $x = 0.105$ and $x = 0.145$. The solid lines are $I \sim H^{-2}$ fits to the data.

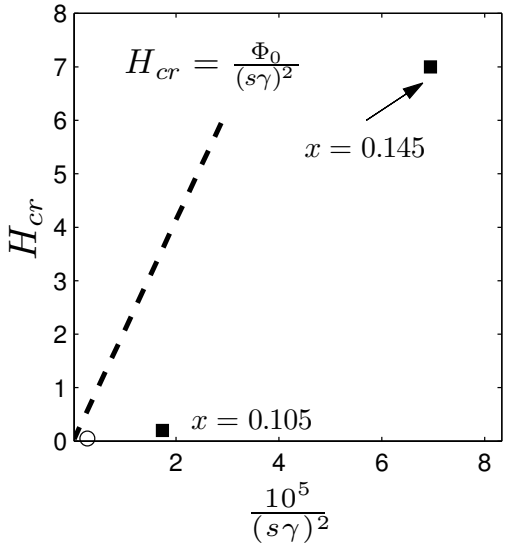

FIGURE 4.16: Observed crossover field H_{cr} as a function of $\lambda^{-2} = (s\gamma)^{-2}$. The open point is from Cubitt *et al.* [124] and the filled points are from LSCO with doping as indicated. The dashed line indicates the crossover field as predicted by theory [126, 127].

on $x = 0.105$ was done by considering the incident flux and the mass of the crystals. If there is any vortex lattice in $x = 0.12$, the signal must be more than 100 times weaker than that observed in $x = 0.105$. The reason for this is most likely related to the strong competition between magnetism and superconductivity around $x \sim 1/8$ [146].

4.5 SUMMARY

The last section of this chapter is devoted to a short summary of the doping evolution of the vortex lattice in LSCO, observed by SANS. Here the work of R. Gilardi [87] will be presented together with the experiments performed during this thesis work. The purpose is to create an overview of the doping dependence, from the underdoped region with the anomalous $x = 1/8$ to the overdoped region.

4.5.1 Doping dependence of the 3D vortex lattice in LSCO. In order to piece together all information obtain from SANS experiments on LSCO, I am now going to give a short summary of the data.

$x = 0.10$**:** Although the details vary for one experiment to the other [87], a 3D vortex lattice was observed in underdoped LSCO $x = 0.105$ [147] for $H < 0.2$ T. Figure 4.17(a) shows the diffracted intensity for an applied field of $H = 0.03$ T. A detailed discussion of these results is given in the dissertation of R. Gilardi [87].

$x = 0.12$**:** As shown in figure 4.17(b), no vortex lattice could be observed in the $x = 0.12$ sample upon application of $H = 0.03$ T. In this compound no evidence for a 3D vortex lattice could be found.

$x = 0.145$**:** A 3D vortex lattice could only be observed for $H < 7$ T. A hexagonal-to-square crossover is observed for 0.4 T $< H <$0.9 T, i.e. the lattice structure is hexagonal for $H < 0.4$ T and square for $H > 0.9$ T. The square lattice is oriented along the Cu-O-Cu direction.

$x = 0.17 - 0.22$**:** A hexagonal-to-square crossover was observed for 0.05 T $< H <$ 0.4 T [113, 148] for $x = 0.17$, 0.20 and 0.22. For $H > 0.4$ T a square lattice was observed up the highest experimental applicable field $H \approx 10$ T in $x = 0.17$ [144] and $x = 0.2$ [148].

Figure 4.17(c) to (f) shows the diffracted intensity upon application of a magnetic field $H = 0.3$ T for $x = 0.145 - 0.22$. For $x = 0.145$ the vortex lattice is hexagonal, in contrast to $x = 0.17$ to $x = 0.22$ where the structure is predominantly square. For a more direct comparison, $\sigma(H)$ is shown in figure 4.20 for these compounds. For $x = 0.17$, 0.20, and 0.22 there is hardly any difference of the H-dependence of σ. By contrast, for $x = 0.145$, the onset of the square VL appears at $H_{\square} = 0.9$ T compared to $H_{\square} = 0.4$ T for $x = 0.17$, 0.20, and 0.22.

The resulting phase diagram is schematically depicted in figure 4.21. In the underdoped region of the phase diagram is dominated by quasi 2D structures in contrast to the overdoped region where a 3D vortex lattice is observed up to the highest measurable fields.

4.5.2 Discussion. I am now going to discuss the hexagonal-to-square transition observed in LSCO. Various scenarios are able to explain a field induced hexagonal-to-square transition. It has been proposed that the anisotropic vortex cores in a d-wave superconductor would result in a hexagonal-to-square transition at high fields. Alternatively, coupling to other source of anisotropies such as those provided by fluctuations of segregated charges (stripes) or Fermi velocity anisotropies might also lead to the formation of a square lattice.

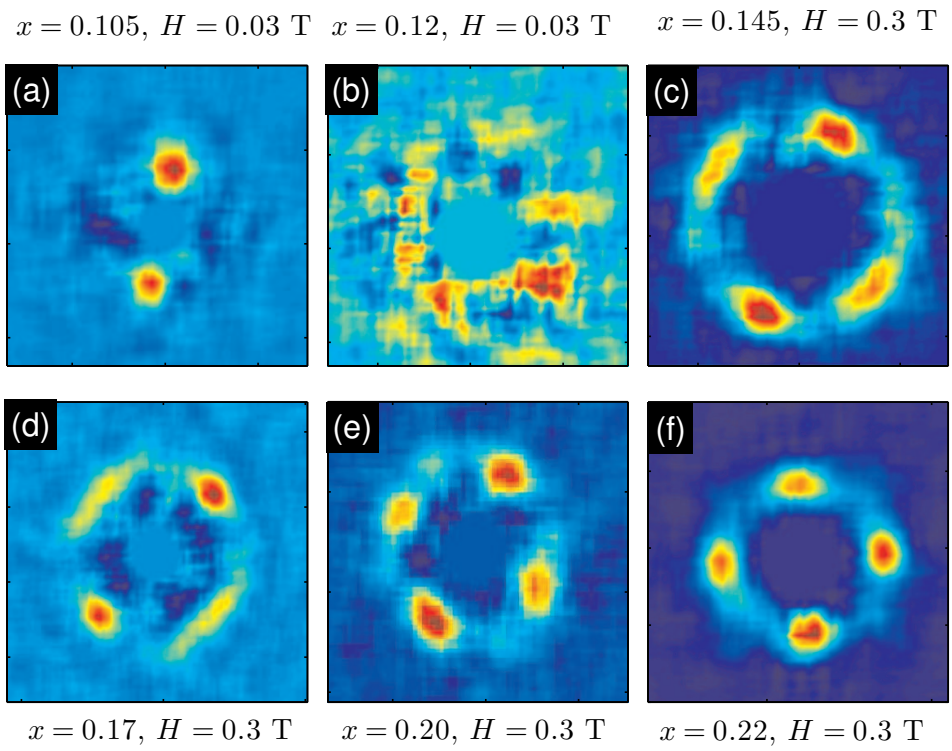

FIGURE 4.17: (a)-(f) Intensity map of the diffracted neutrons for $x = 0.105$, 0.12, 0.145, 0.17, 0.2, and 0.22. For (a) and (b) the applied field was $H = 0.03$ T and for (c) to (f) the field was $H = 0.3$ T. The measurements on $x = 0.145$ and $x = 0.17$ were recorded with $T = 3$ K and $T = 10$ K respectively. All other measurements were done at $T = 2$ K.

In the scenario where stripe correlations are the driving force of the hexagonal-to-square transition, one would expect that the onset field for the square structure is smallest near the $x = 1/8$ doping and that it increases with overdoping. The fact that we observe the opposite trend indicates that the stripe scenario is not responsible for the hexagonal-to-square transition.

Next, I am going to discuss the relevance of the anisotropies in the gap function Δ_{SC} and the Fermi velocity v_F. The core size of a single isolated vortex core is defined loosely by the coherence length ξ_{sc} [128]. The coherence length is related to the Fermi velocity and the gap function by $\xi_{sc} = v_F/\Delta_{SC}$ for BCS superconductors, as discussed in chapter 1. In HTSCs the situation is more complicated since both v_F and Δ_{SC} are anisotropic and there exists no simple relation to the superconducting coherence length. However if we naively apply BCS theory to the HTSCs, then the anisotropies of v_F and Δ_{SC} would lead to an anisotropic field distribution of the vortex cores.

The anisotropies of v_F and Δ_{SC} are schematically depicted in figure 4.18. The d-wave scenario favors a square lattice aligned along the Cu-Cu direction (nodal direction) as observed in YBCO [114, 115]. By contrast, the anisotropy in the Fermi velocity leads to a square lattice aligned along the Cu-O-Cu direction (anti-nodal direction) as observed in LSCO.

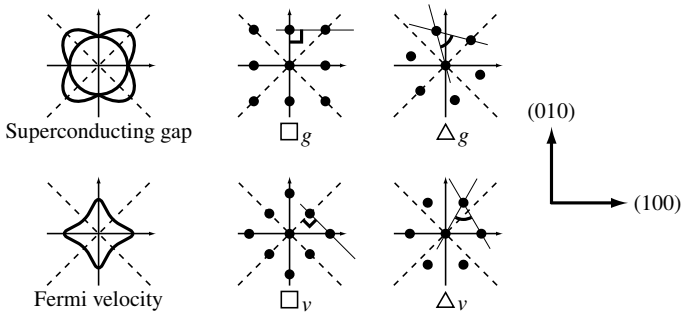

FIGURE 4.18: Superconducting gap and Fermi velocity anisotropies and the resulting square and hexagonal vortex structures. Here the positions of the vortex cores are indicated by a •. The crystal structure is here given in orthorhombic notation where (100) is the nodal direction (Cu-Cu direction). From N. Nakai *et al.* [112].

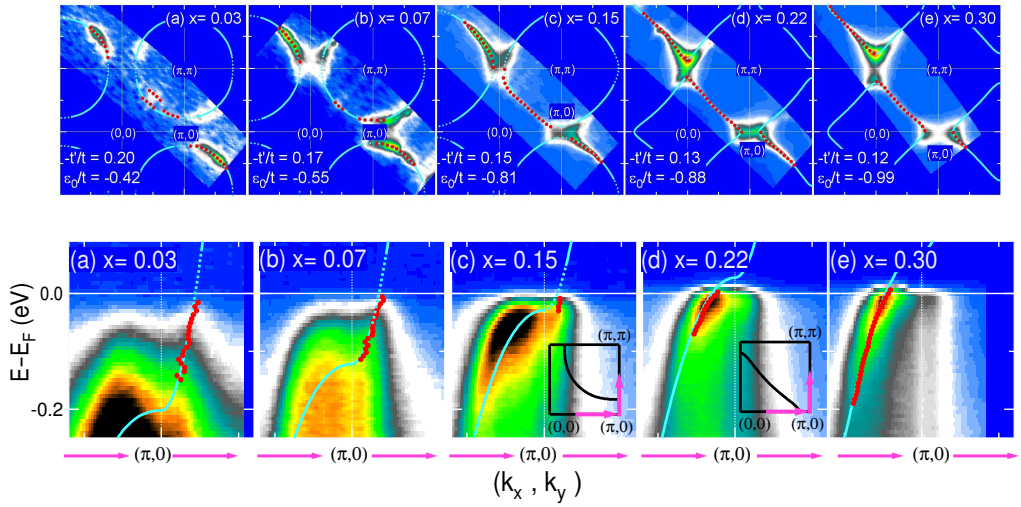

FIGURE 4.19: Top panel: Spectral weight maps at E_F obtained from ARPES on LSCO. The red dots indicate k_F and the blue curves are the Fermi surface obtained by tight-binding fits to the data. Bottom panel: The electronic band structure as observed by ARPES. The red dots are the dispersion extracted from momentum distribution analysis and the blue curves are tight-binding fits to the data. Notice that the van Hove singularity crosses the Fermi level for $0.15 < x < 0.22$ thus the van Hove singularity is very close to the Fermi level E_F in this doping interval. Both top and bottom panels are from T. Yoshida *et al.* [149].

To explain the difference between YBCO and LSCO, Nakai *et al.* [112] suggested that the observation of the square lattice in LSCO is stabilized by the proximity of the van Hove singularity close to the Fermi level at (π,0) of the Brilliuon zone. The strongest anisotropy in the Fermi velocity will occur when the van Hove singularity coincides with the Fermi level. The doping evolution of the van Hove singularity, as observed by ARPES, is shown in figure 4.19.

At the doping level where this crossing appears the square vortex lattice should be more stable. Remember that both the d-wave anisotropy and the Fermi velocity anisotropy are present at the same time. Nakai *et al.* [112] therefore predicted that for high field ($H > 6$ T) the d-wave anisotropy should be dominating and hence trigger a transition to a square lattice oriented along the Cu-Cu direction.

The Fermi velocity scenario explains the square structure of the vortex lattice in LSCO. From

ARPES measurements we know that the van Hove singularity crosses the Fermi level for $0.17 < x < 0.22$ [150], see also figure 4.19. Based on these ARPES data, we can assume that the Fermi velocity anisotropy is maximum for $x \approx 0.2$. The square lattice is therefore expected to be very stable in the doping range $0.17 < x < 0.23$.

The Fermi velocity scenario agrees very well with the experiments. In the doping range $0.17 < x < 0.22$ the square lattice is stable for $H > 0.4$ T. Moving to the more underdoped sample $x = 0.145$ where the van Hove singularity is further away from the Fermi level, the square structure is less stable and occurs only for $H > 0.9$ T.

However the predicted rotation of the square lattice was not observed in LSCO. In the optimally doped region, a clearly visible square lattice oriented along the Cu-O-Cu direction was observed up to the highest possible applicable field $H = 10.5$ T [144]. Similar results were observed for overdoped LSCO $x = 0.20$ [148].

4.5.3 Conclusion. Two main conclusions can be drawn from the investigation of the vortex lattice in LSCO.

1. A hexagonal-to-square crossover of the vortex lattice structure was observed for $x = 0.145$ to $x = 0.22$. The square structure which is aligned along the Cu-O-Cu direction is more stable in the overdoped region of the phasediagram. For $x = 0.145$ the square lattice is stabilized only for $H > 0.9$ T while for $x = 0.17$ to $x = 0.22$ the square lattice appears for $H > 0.4$ T. These observations support the idea that the square lattice is stabilized by the vicinity of the van Hove singularity to the Fermi level as proposed by Nakai *et al.*[112].

2. In the underdoped region of the phase diagram a crossover from a well ordered 3D lattice to a more disordered structure was observed as a function of applied field. The crossover field is strongly doping dependent since it appears at $H = 0.2$ T for $x = 0.105$ and $H = 7$ T for $x = 0.145$. The nature of the crossover was discussed in terms of a 3D-to-2D transition.

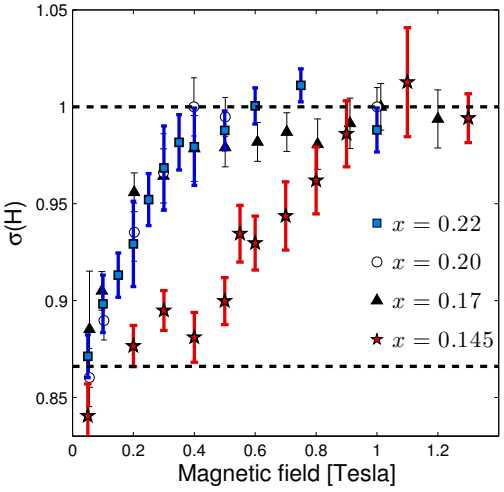

FIGURE 4.20: Field dependence of σ for $x = 0.145$, 0.17, 0.20, and 0.22. Colored red ($x = 0.145$) and blue ($x = 0.22$) points are from this work and circular and triangular points are recorded on $x = 0.17$ (from Ref. [113]) and $x = 0.20$ (from Ref. [148]).

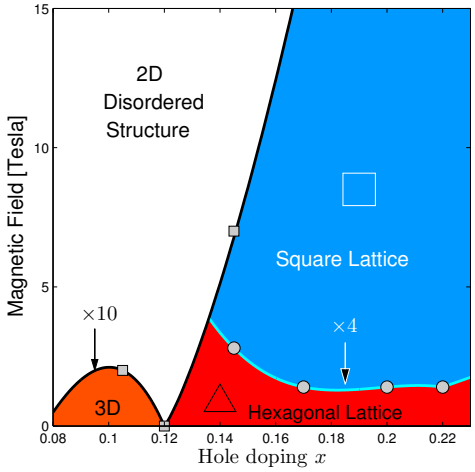

FIGURE 4.21: Schematic doping-field phase diagram at low temperature deduced from the experimental result presented here. At low doping a 3D-to-2D crossover is observed and for slightly underdoping to the overdoped region a hexagonal-to-square transition is observed as indicated by the red and blue phases.

Chapter 5

Spin degrees of freedom in LSCO

Conventional BCS superconductivity is destroyed by just a tiny amount of magnetic impurities. Therefore it came as surprise that many unconventional superconductors coexist with magnetic order. For both heavy fermion superconductors and HTSCs, magnetism is intimately connected. Magnetism in condensed matter can be studied by a diverse number of experimental techniques such as NMR, μSR, or magnetization measurements. Neutron scattering is an outstanding technique that provides a direct measure of the spin-spin correlation function $\mathcal{S}(\mathbf{Q},\omega)$.

In some theories of HTSCs, dynamic magnetism is the pairing glue for superconductivity. On the other hand, static magnetic order seems to compete with superconductivity. To investigate whether magnetism is cooperative or destructive in respect to SC, neutron scattering is one of the most powerful techniques.

5.1 Neutron scattering

Neutron scattering is an extremely powerful technique to study elementary excitations in condensed matter. The advantage and disadvantage of neutrons is that they interact weakly with matter. Neutrons have no charge and can therefore easily penetrate most materials. The scattered neutrons therefore reflect the bulk properties of the sample. The disadvantage is that the scattering events occur very rarely because of the weak interaction.

The neutron scattering technique is widely celebrated and applied to a variety of different systems. For example, neutron scattering can be used to study large scale biological materials such as polymers and vesicles, hydrogen diffusion in potential hydrogen storage material, and quantum magnetism in low dimensional systems. Neutron scattering has also provided important information about the energy and momentum dependence of the magnetic excitations in high-temperature superconductors, for a review see [151–153]. In this chapter neutron scattering is used to study the static and dynamic magnetic properties of underdoped LSCO. In particular the low-energy ($\hbar\omega < 10$ meV) spin fluctuations affected by superconductivity will be investigated.

5.1.1 Neutron scattering cross section. Scattered neutrons are detected by placing a detector along a direction defined by a vector $\Omega = \mathbf{k}_f$. The detector counts neutron within a solid angle $d\Omega$. The differential cross section is defined by the count rate at Ω per unit solid angle $d\Omega$ and per

dE_f normalized with the incident flux ψ

$$\frac{d^2\sigma}{d\Omega dE_f} = \frac{neutrons/sec\ in\ d\Omega\ between\ E_f\ and\ E_f + dE_f}{\Psi d\Omega dE_f}. \tag{5.1}$$

I am now going to show how the differential cross section is related to the sample properties by considering single scattering processes. Let $|\lambda\rangle$ be the state of the sample and $|\mathbf{k}, s\rangle$ the state of a neutron with momentum $\mathbf{k}$ and spin s. The probability of a single scattering event from the initial state $|\mathbf{k}_i, s_i, \lambda_i\rangle$ to $|\mathbf{k}_f, s_f, \lambda_f\rangle$ is given by the Fermi golden rule

$$\mathcal{W}_{i\to f} = \frac{2\pi}{\hbar} \left|\langle \mathbf{k}_i s_i \lambda_i | \mathcal{V}(\mathbf{r}) | \mathbf{k}_f s_f \lambda_f \rangle\right|^2 \delta(E_i - E_f + \hbar\omega) \tag{5.2}$$

where $\mathcal{V}(\mathbf{r})$ is the interaction potential between the neutron and the sample. The differential cross section is proportional to the probability of a scattering event $\mathcal{W}$. The exact relation can be found in many textbooks about neutron scattering [81, 154]

$$\frac{d^2\sigma}{d\Omega dE_f} = \frac{k_f}{k_i}\left(\frac{m}{2\pi\hbar^2}\right)^2 \sum_{\lambda_f \lambda_i} p_{\lambda_i} \mathcal{W}, \tag{5.3}$$

where p_{λ_i} is the occupation probability of the initial state $|\lambda_i\rangle$.

5.1.2 Nuclear neutron scattering. Neutrons interact with the nucleus of a solid through short-range (10^{-4} Å) nuclear forces. The wavelength of thermal neutrons is of the order 1 Å, thus the scattering potential can be approximated with Fermi pseudo-potential

$$\mathcal{V}_{neu}(\mathbf{r}) = \frac{2\pi\hbar^2}{m} b \sum_j \delta(\mathbf{R}_j - \mathbf{r}) \tag{5.4}$$

where δ is the Dirac-delta function and b is the so-called scattering length [81]. Since there exists no microscopic model to describe the interactions between neutrons and nucleus, the scattering length can not be calculated. Knowledge of the scattering length b relies therefore uniquely on experimental determinations. From the Fermi golden rule, the cross section of coherent and incoherent scattering yield

$$\left(\frac{d^2\sigma}{d\Omega dE_f}\right)^{Nucl}_{coh} = \frac{\sigma_{coh}}{4\pi}\frac{k_f}{k_i}\mathcal{S}(\mathbf{Q},\omega) \tag{5.5}$$

$$\left(\frac{d^2\sigma}{d\Omega dE_f}\right)^{Nucl}_{inc} = \frac{\sigma_{inc}}{\pi}\frac{k_f}{k_i}\mathcal{S}_i(\mathbf{Q},\omega) \tag{5.6}$$

where $\sigma_{coh} = 4\pi\bar{b^2}$, $\sigma_{inc} = 4\pi\left(\bar{b^2} - \bar{b}^2\right)$, and the dynamical structure factor $\mathcal{S}(\mathbf{k},\omega)$ is given by

$$\mathcal{S}(\mathbf{Q},\omega) = \frac{1}{2\pi\hbar}\sum_{\alpha'\alpha}\int dt\, \langle \exp[i\mathbf{Q}\mathbf{r}_{\alpha'}(0)] \exp[i\mathbf{Q}\mathbf{r}_{\alpha}(t)]\rangle \exp(-i\omega t), \tag{5.7}$$

and the incoherent scattering function $\mathcal{S}_i(\mathbf{k},\omega)$ yields

$$\mathcal{S}_i(\mathbf{Q},\omega) = \frac{1}{2\pi\hbar}\sum_{\alpha}\int dt\, \langle \exp[i\mathbf{Q}\mathbf{r}_{\alpha}(0)] \exp[i\mathbf{Q}\mathbf{r}_{\alpha}(t)]\rangle \exp(-i\omega t). \tag{5.8}$$

5.1.3 Magnetic neutron scattering. The spin of a neutron couples to magnetic moments via the magnetic dipole interaction. In the previous chapter we discussed the cross section that stems from an interaction between the momentum of a moving electron and the neutron. Here the interaction between a neutron and the electronic spin of an electron will be considered. The magnetic field at a point $\mathbf{r}$ from the magnetic dipole moment of an electron is [81]

$$\mathbf{B}_s(\mathbf{r}) = \frac{-2\mu_B\mu_0}{4\pi}\nabla\times\left[\frac{\mathbf{s}\times\mathbf{r}}{|\mathbf{r}|^2}\right]. \tag{5.9}$$

The interaction between the magnetic dipole moment of the neutron and $\mathbf{B}_s(\mathbf{r})$ reads

$$\mathcal{V}_{mag}(\mathbf{r}) = \mu_n\cdot\mathbf{B}_s(\mathbf{r}) = \frac{2\mu_0\mu_B}{4\pi}\mu_n\cdot\left(\nabla\times\left[\frac{\mathbf{s}\times\mathbf{r}}{|\mathbf{r}|^2}\right]\right) = \frac{\gamma_n r_0\hbar^2}{4m_n}\sigma\cdot\left(\nabla\times\left[\frac{\mathbf{s}\times\mathbf{r}}{|\mathbf{r}|^2}\right]\right) \tag{5.10}$$

where $\gamma_n = 1.913$ is the gyromagnetic ratio, $r_0 = \mu_0 e^2/(4\pi m_e)$, and σ is the spin operator.

The cross section for magnetic scattering was first derived by O. Halpern *et al.* [155]. Since the evaluation of the Fermi golden rule is explained in great detail in many textbooks [81, 154], I will here just give the result. As for nuclear scattering the magnetic cross section as a product of the form factor $\mathcal{F}(Q)$ and the scattering function $\mathcal{S}(\mathbf{Q},\omega)$

$$\left(\frac{d^2\sigma}{d\Omega dE_f}\right)^{mag}_{coh} = \frac{k_f}{k_i}(\gamma r_0)^2|\mathcal{F}(\mathbf{Q})|^2\sum_{\alpha\beta}\left(\delta_{\alpha\beta}-\frac{Q_\alpha Q_\beta}{Q^2}\right)\mathcal{S}^{\alpha\beta}(\mathbf{Q},\omega) \tag{5.11}$$

where the form factor is a Fourier transform of the spin density ρ_s

$$\mathcal{F}(\mathbf{Q}) = \int d\mathbf{r}\rho_s\exp(i\mathbf{Q}\cdot\mathbf{r}) \tag{5.12}$$

and the magnetic scattering function $\mathcal{S}^{\alpha\beta}(\mathbf{Q},\omega)$ yields

$$\mathcal{S}^{\alpha\beta}(\mathbf{Q},\omega) = \frac{1}{2\pi}\sum_l\int_{-\infty}^{\infty}dt\exp\left[i\left(\mathbf{Q}\cdot\mathbf{r}_l-\omega t\right)\right]\left\langle s_0^\alpha(0)s_l^\beta(t)\right\rangle \tag{5.13}$$

where α and β are Cartesian coordinates and the index l runs over the spin sites. The magnetic scattering therefore measures the Fourier transform of the spin-spin correlation function. Finally the magnetic cross section contains a polarization factor $\delta_{\alpha\beta}-Q_\alpha Q_\beta/Q^2$ which describes that the scattering is strongest perpendicular to $\mathbf{Q}$.

5.1.4 Total neutron scattering response. The scattered intensity $I(\mathbf{Q},\omega)$ is finally a sum of all possible scattering mechanisms

$$I(\mathbf{Q},\omega)\propto\left(\frac{d^2\sigma}{d\Omega dE_f}\right)^{Nucl}_{coh}+\left(\frac{d^2\sigma}{d\Omega dE_f}\right)^{mag}_{coh}+\left(\frac{d^2\sigma}{d\Omega dE_f}\right)^{Nucl}_{inc}+.... \tag{5.14}$$

In many systems coherent nuclear and magnetic scattering appear with the same wavevector. In this case one needs to disentangle the two responses, which can be done either by the use of

polarized neutrons or by studying the different form factor dependence on **Q**. Fortunately, the magnetic response in LSCO is incommensurate. The coherent nuclear and magnetic responses are therefore well separate in **Q**-space. However, even if the magnetic response is incommensurate and well distinguishable from coherent nuclear scattering, we should keep in mind that the coherent scattering might still have more than one scattering mechanism. This is especially relevant for systems with multiple order parameters.

5.2 TRIPLE AXIS SPECTROSCOPY (TAS)

Triple axis spectrometers are very powerful instruments for investigations of elementary excitations in matter. It allows in a controlled manner to measure the scattering rate as a function of scattering vector **Q** and energy transfer $\hbar\omega$. In figure 5.1 a schematic view of a typical triple axis spectrometer is shown. Bragg scattering from the monochromator crystal (typically silicon or graphite) defines the incoming neutrons with wavevectors $\mathbf{k}_i$. The incident neutrons are of course not truly monochromatic due to the mosaicity of the monochromator crystal. Since the incoming neutrons are selected via the Bragg scattering condition $n\lambda_n = d\sin(\theta)$, the beam also contains high order contaminations, $2\lambda_n$, $3\lambda_n$. These higher order neutrons can be filtered out by the use of, for example, a Be-filter which allows only neutrons with a certain range of λ to pass through.

The direct neutron beam from the source is usually not very well collimated. A better defined beam can be obtained by use of collimators that consist of parallel sheets of a neutron absorbing material.

As illustrated in figure 5.1 one can, with a monochromator, filters, and collimators, create a quasi monochromatic and collimated beam. When these neutrons hit the sample some of them will be scattered as discussed before. These scattered neutrons can be analyzed with respect to scattering vector **Q** and energy transfer $\hbar\omega$. This is done with an analyzer crystal that selects the neutrons that fulfill an appropriate Bragg condition. The rate of these neutrons is finally recorded by a neutron detector. The counting rate is usually normalized to the incident number of neutrons measured by the monitor.

Triple axis spectrometers are thus able to measure the scattering rate as a function of momentum $\mathbf{Q} = \mathbf{k}_f - \mathbf{k}_i$ and energy transfer $\hbar\omega = E_f - E_i$. Needless to say that the triple axis technique is very demanding since only few of the produced neutrons will hit the sample and only a few of them will scatter with the specified momentum and energy transfer. Therefore the main drawback of this technique is the low counting rates.

Generally neutrons can be produced with a *cold* or a *thermal* distribution. A *cold* distribution contains mainly low-energy ($0.1 - 10$ meV) neutrons while a *thermal* distribution consists of neutrons with a energy range of $2 - 100$ meV. A cold (thermal) triple axis instrument is placed in front of a cold (thermal) neutron source.

During this thesis work, the static and dynamic magnetic properties in the underdoped region of $La_{2-x}Sr_xCuO_4$were studied. For this purpose, several different cold triple axis instruments were used. Static magnetism was mainly studied on the RITA II instrument [156, 157] at the Swiss Spallation Source SINQ, PSI. The inelastic magnetic scattering was on the other hand studied mainly on the IN14 instrument at the Institute Laue-Langevin ILL (Grenoble in France) and on the PANDA instrument at FRM-II (Munchen in Germany).

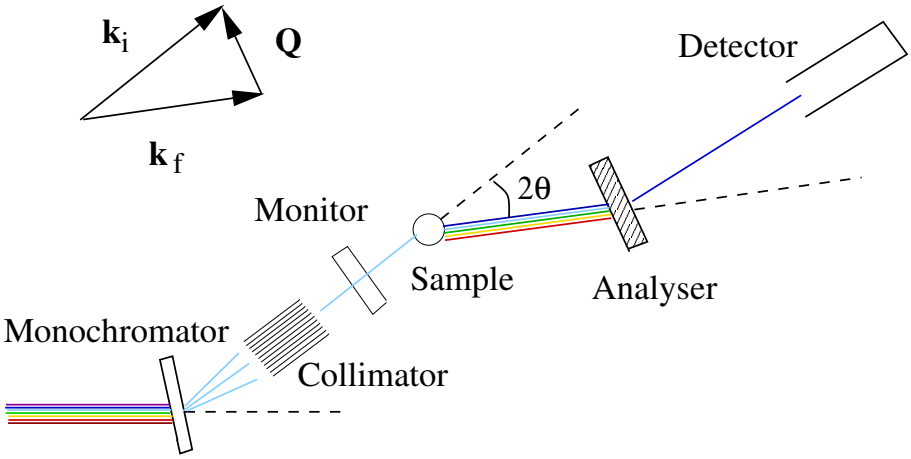

FIGURE 5.1: Schematic drawing of a typical triple axis spectrometer.

5.2.1 Momentum and energy resolution. Needless to say that each instrument in a given setup will have a finite momentum and energy resolution. Let us start by discussing the momentum resolution. Since the neutron beam is not very well collimated compared to, for example, a synchrotron light beam, the momentum resolution is correspondingly worse. One can easily get an idea of the momentum resolution by measuring the width of a nuclear Bragg reflex. Since we are working with single crystals, the nuclear order is long range and without any collimation a typical triple axis instrument will not be able to resolve the peak. The measured Bragg peak is therefore resolution limited and the width of the peak gives the momentum resolution. Figure 5.2 shows the intensity on logarithmic scale of the nuclear reflex (020) as a function of momentum $(Q_h, Q_k, 0)$ (orthorhombic notation is used here). The elliptical shape of the intensity distribution $I(h,k)$ defines the **Q**-resolution. To improve the momentum resolution one has to collimate the incident neutron beam. Finally it should be mentioned that the momentum resolution perpendicular to the scattering plane is much worse, thus the effective resolution function has a cigar like shape.

In this thesis work we were mainly interested in the magnetic properties of $La_{2-x}Sr_xCuO_4$. The inverse correlation length $\kappa = 1/\xi$ of the magnetic excitations in $La_{2-x}Sr_xCuO_4$ is typically comparable to the momentum resolution of a TAS instrument. Therefore it is in some cases not necessary to collimate the neutrons. For the elastic experiments we typically used a $80'$ collimator situated after the monochromator. The spin excitations are on the other hand so broad that no collimation is required.

For a given monochromator and analyser the energy resolution is dependent on the chosen k_i and k_f through

$$\Delta E_f \sim \frac{\hbar k_f}{m} \Delta k_f. \tag{5.15}$$

The energy resolution can be estimated by scanning through the elastic line with an incoherent scattering vector $\mathbf{Q}_{inc}$ (see figure 5.3). We typically use $k_f = 1.5$ Å^{-1} resulting in an energy resolution $\Delta E \approx 0.15$ meV. When low-energy transfers ($\hbar\omega < 0.5$ meV) were investigated $k_f = 1.3$ Å^{-1} was used. This results in a better energy resolution $\Delta E \approx 0.1$ meV and ensures that there is

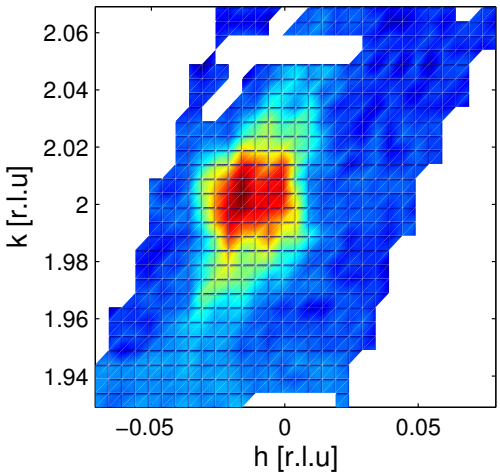

FIGURE 5.2: Example of a grid scan around (020) on LSCO $x = 0.12$ taken on the RITAII spectrometer using the image mode. Colorscale gives $\log(I(h,k))$. The elliptical shape of the intensity distribution defines the momentum resolution of the instrument with the given setup.

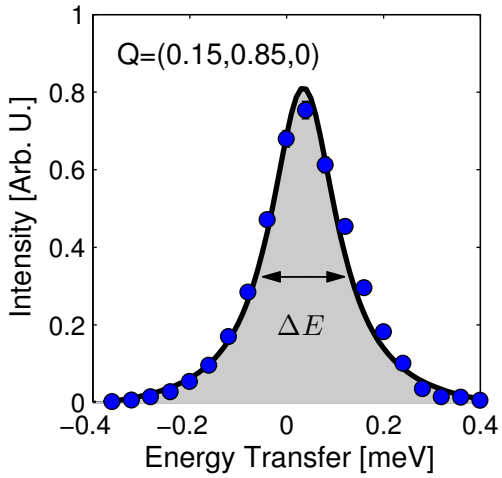

FIGURE 5.3: Incoherent scattering as a function of energy transfer. The width gives the energy resolution. Taken on IN14 (LSCO $x = 0.14$) with $k_f = 1.5$ Å^{-1}.

no elastic component in the signal.

5.2.2 Sample environment and background scattering. The samples were aligned such that the scattering plane was identical with the CuO_2 layers. In other words, scattering vectors with (Q_h,Q_k,0) were accessible. For elastic experiments, usually only one crystal of ∼1.5 g was used. When the inelastic response was investigated two crystals of ∼1.5 g were co-aligned with a mosaicity of better than one degree, see Appendix A. When a magnetic field was applied perpendicular to the CuO_2 planes a commercial 15 tesla cryomagnet from Oxford was used. Otherwise standard cryostats or displex were used to cool the sample.

Usually the signal we measure is comparable to the background noise. Therefore the instrumental setup was optimized with respect to the signal to noise ratio. The background noise can have several origins. Electronic noise and incoherent scattering from the sample are unfortunately difficult to avoid. However, one can do a lot to hinder that uncontrolled neutrons enter the detector. This is usually done by screening the neutrons with neutron absorbing materials. Our sample holders are for example masked with Cadmium such that only neutrons that hit the sample can pass. Generally the sample holders are constructed to minimize the background scattering. The sample holder is therefore made out of 99.99% pure aluminium and as little as possible glue* is used to fix the sample. For inelastic neutron scattering experiments the signal-to-background ratio is typically of the order one-to-two. With the high flux reactor source at ILL, a count rate of the signal is typically one neutron per minute. Therefore relatively long counting times are necessary

*Two types of glue were used during this thesis work: (i) Araldite is a strong two-component glue and (ii) Boothstick is a single-component glue which can be dissolved in acetone.

to obtain statistically significant data.

The best way to measure the signal-to-backgound ratio is to perform a **Q**-scan with four to five points on both sides of the peak. However, due to the very low counting it is practically impossible within the available time to perform such **Q**-scans in a systematic fashion. Therefore we did the second best, which is to do three-point scans; one point at the peak position and one background point at each side of the peak. This strategy is useful as long as the peak position and the width of the peak remain constant. When the signal was measured as a function of energy transfer or temperature, the background was measured as well. Usually the background varies smoothly as a function of for example temperature. In such a case the background can be fitted with a polynomial function which then is used to substract the background from the signal.

5.3 MAGNETISM IN $La_{2-x}Sr_xCuO_4$

In the generic phase diagram of the high-temperature superconductors, static or dynamic magnetism exists from the insulating phase to the strongly overdoped region. As mentioned in Chapter 1, the undoped parent compound LCO is a Mott insulator and the Cu spins align antiferromagnetically. Inelastic neutron scattering has revealed that spin-waves disperse out from the antiferromagnetic ordering vector $\mathbf{Q}_{AF} = (0.5, 0.5, 0)$ [35, 158]. Upon a small amount of hole doping the antiferromagnetic phase is destroyed and an insulating spin-glass-like phase emerge. For $0.02 < x < 0.05$ neutron scattering experiments have revealed the existence of incommensurate static magnetism with ordering vector $\mathbf{Q} = \mathbf{Q}_{AF} + (\delta, \pm\delta, 0)$ and $\mathbf{Q} = \mathbf{Q}_{AF} + (-\delta, \pm\delta, 0)$ (see figure 5.4(a)). The incommensurability δ depends on the doping content. At the critical doping level $x_c \approx 0.05$ for superconductivity the incommensurate static ordering changes to $\mathbf{Q}_{IC} = \mathbf{Q}_{AF} \pm (\delta/\sqrt{2}, 0, 0)$ and $\mathbf{Q}_{IC} = \mathbf{Q}_{AF} \pm (0, \delta/\sqrt{2}, 0)$ [159], see figure 5.4(b). In $La_{2-x}Sr_xCuO_4$ static incommensurate magnetism coexists with superconductivity for $x_c < x < 0.13$, while for $x > 0.13$ there is no static order [146] in zero field, see figure 5.5. However spin excitations at the same IC wavevectors remain and are gaped for $T < T_c$. Even in the extreme overdoped regime, spin fluctuations persist [160–162].

Although the low-energy ($\hbar\omega < 10$ meV) part of the spin fluctuation spectra is strongly doping dependent the high-energy exhibits an universal hourglass-like shape [163], as shown in figure 5.4(c). For $\hbar\omega < 40$ meV the four incommensurate branches disperse toward $\mathbf{Q}_{AF}$ and at higher energies ($\hbar\omega > 40$ meV) a dispersion away from $\mathbf{Q}_{AF}$ is observed. This hourglass shape seems to be common feature cross the various cuprate compounds [163–166]. However, the actual distribution of the spectral weight varies from compound to compound. For example, the cuprates with $T_c^{max} \approx 90$ K all have an intense response at $\Omega_c \approx 40$ meV (the so-called resonance) [167] while for La-based compounds with $T_c^{max} < 40$ K the spectral weight is more concentrated at lower energies [164]. It has been shown empirically that the resonance energy Ω_c scales with T_c [168], suggesting that the spin fluctuations are linked directly or indirectly to superconductivity.

The purpose of this chapter is twofold. First the incommensurate magnetism is studied under application of a magnetic field in the doping region around the 1/8-anomaly. Second the low-energy ($\hbar\omega < 10$ meV) spin fluctuations are studied as a function of underdoping.

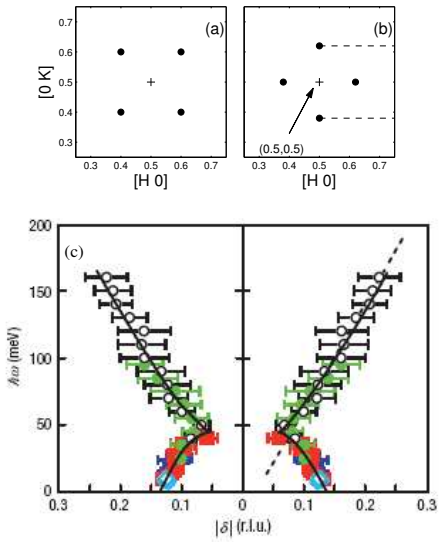

FIGURE 5.4: (a) and (b) Schematical position in reciprocal space of the incommensurate ordering vectors in the doping range $0.02 < x < 0.05$. and $0.05 < x < 0.13$, respectively. (c) The spin fluctuation spectrum for LSCO with $x = 0.16$. From [163].

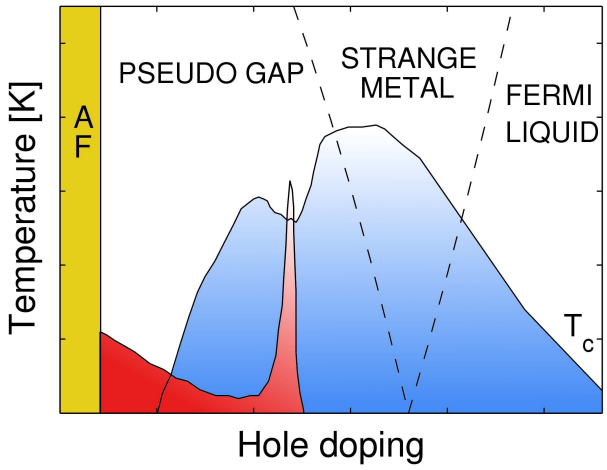

FIGURE 5.5: Schematic phase diagram of LSCO. The antiferromagnetic dome is shown in yellow color. Static incommensurate magnetism is depicted by the red color and the superconducting dome is the blue phase. This figure is adapted from H.-M. Julien [146].

5.4 STATIC MAGNETISM IN UNDERDOPED $LA_{2-x}SR_xCUO_4$

Competing order parameters are a central theme in condensed matter physics. This is especially true for the study of high-temperature superconductors (HTSCs), where superconductivity occurs upon hole doping of an antiferromagnetic Mott insulator. As a consequence of the competition between superconductivity (SC) and antiferromagnetism (AF) a variety of ground states have been identified in the underdoped regime of La-based cuprates. Among those are a disordered spin-glass-like state which coexists with SC over a broad range of doping [169] and a spin density wave (SDW) state with suppressed superconductivity around a specific hole concentration $x \approx 1/8$. This so-called 1/8-anomaly was first observed in $La_{15/8}Ba_{1/8}CuO_4$ [170], where the effect is concomitant to a structural phase transition from a low-temperature orthorhombic (LTO) to a low-temperature tetragonal (LTT) phase [171]. Later, a similar anomaly was observed in the LSCO system at $x \approx 0.115$ [172, 173], however without a structural LTO to LTT transition and without a complete suppression of SC. A stripe model [71] with spatial modulations of spin and charge densities has been suggested to account for the incommensurate magnetic and simultaneous charge order observed in neutron diffraction experiments on $La_{1.48}Nd_{0.4}Sr_{0.12}CuO_4$ [71, 103, 107, 174, 175]. In this model dynamic stripe correlations of spins and holes are stabilized in the LTT phase and suppress superconductivity.

Starting from $La_{1.88}Sr_{0.12}CuO_4$, there are several routes to reach the 1/8 ground state. One way is simply to substitute Sr with Ba [176–178] or La with Nd. An alternative route is to introduce pinning centers into the CuO_2 planes. μSR results on Zn doped $La_{2-x}Sr_xCu_{1-y}Zn_yO_4$ show an

enhancement of static magnetism around 1/8 doping [179], supporting the suggestion that small amounts of nonmagnetic impurities act as pinning centers for dynamical stripe correlations. The observation of similar magnetic anomalies on Zn substituted Bi-2212 and $YBa_2Cu_3O_{6+x}$ seems to indicate that the 1/8-anomaly is not just a specific feature of the La-based compounds, but a more general property of high-T_c superconductors [180, 181].

The subtle balance between the competing orders may also be changed by external perturbations such as magnetic fields [182, 183] or pressure [184]. For example, it was demonstrated that the static IC magnetic neutron response for LSCO with doping close to 1/8 is enhanced by the application of a magnetic field perpendicular to the CuO_2-planes [182, 183]. A similar field effect was found in La_2CuO_{4+y} [185, 186]. On the other hand no field effect was observed in $La_{1.976}Sr_{0.024}CuO_4$ [187] and $La_{1.45}Nd_{0.4}Sr_{0.15}CuO_4$ [188]. The microscopic mechanisms behind the 1/8-anomaly, as well as the primary cause of the field effect, remain poorly understood. In this section a combined μSR and neutron diffraction study of the static magnetism around the particular $x = 1/8$ doping is presented. The muon experiments were carried out by Ch. Niedermayer on the GPS and LTF instruments at PSI. The dilution experiments were kindly assisted by C. Baines. For a short introduction to the μSR technique see appendix B. The magnetic onset temperature was determined by both μSR ($T_f^{\mu SR}$) and neutron scattering (T_f^n). The difference among $T_f^{\mu SR}$ and T_f^n is due to the different observation time scales of the two different experimental techniques. Table 5.1 summarizes the properties of the single crystals used in this study.

5.4.1 Experimental setup. The elastic neutron diffraction experiments were carried out on the cold neutron spectrometers FLEX at the Hahn-Meitner Institute, IN14 at Institute Laue-Langevin, and RITA II at PSI. We used a vertically curved graphite monochromator and for the $x = 0.105$ and $x = 0.12$ experiments we used a flat graphite analyzer while the $x = 0.145$ experiment was done with a doubly curved analyzer. The NDLSCO experiment was performed using the monochromatic imaging mode of RITA II [157]. The experiments were performed with a fixed initial and final energy ($k_f = k_i = 1.5$ or 1.9 Å^{-1}). A Be- or PG-filter was installed before the analyzer in order to eliminate higher order contamination. The samples were mounted in vertical 15 tesla cryomagnets such that (Q_h,Q_k,0) were accessible. All measurements in an external magnetic field H were performed after field cooling.

5.4.2 Static response. Figure 5.6 summarizes the results of our elastic neutron diffraction experiments. Figures 5.6(a) to (d) are presented with increasing ZF elastic response. For LSCO with $x = 0.145$ (figure 5.6(a)) no elastic response is observed in ZF. However, application of $H = 13$ T induces an elastic response at $\delta \approx 0.13$, consistently with previous reports [189]. For LSCO with $x = 0.105$ and $x = 0.12$ an elastic response exists already in ZF and an applied magnetic field enhances the magnetic response for $T < T_f^n$ (figure5.6(b),(c) and (e)). NDLSCO shows the strongest ZF response and the absence of a field effect at all T, see figure 5.6(d).

Next, we plot in figure 5.6(e) the T-dependence of the intensity I at $\mathbf{Q}_{IC}$. The T-axis and I-axis are normalized to T_f^n and $I(T = 2$ K), respectively. Due to the absence of a field effect in NDLSCO we plot, for simplicity, only the ZF data in this figure. For $x = 0.105$ and $x = 0.12$ the T-dependence in ZF and in field are significantly different. In a magnetic field the elastic response follows an order parameter like T-dependence as observed for NDLSO. The T-dependence of the

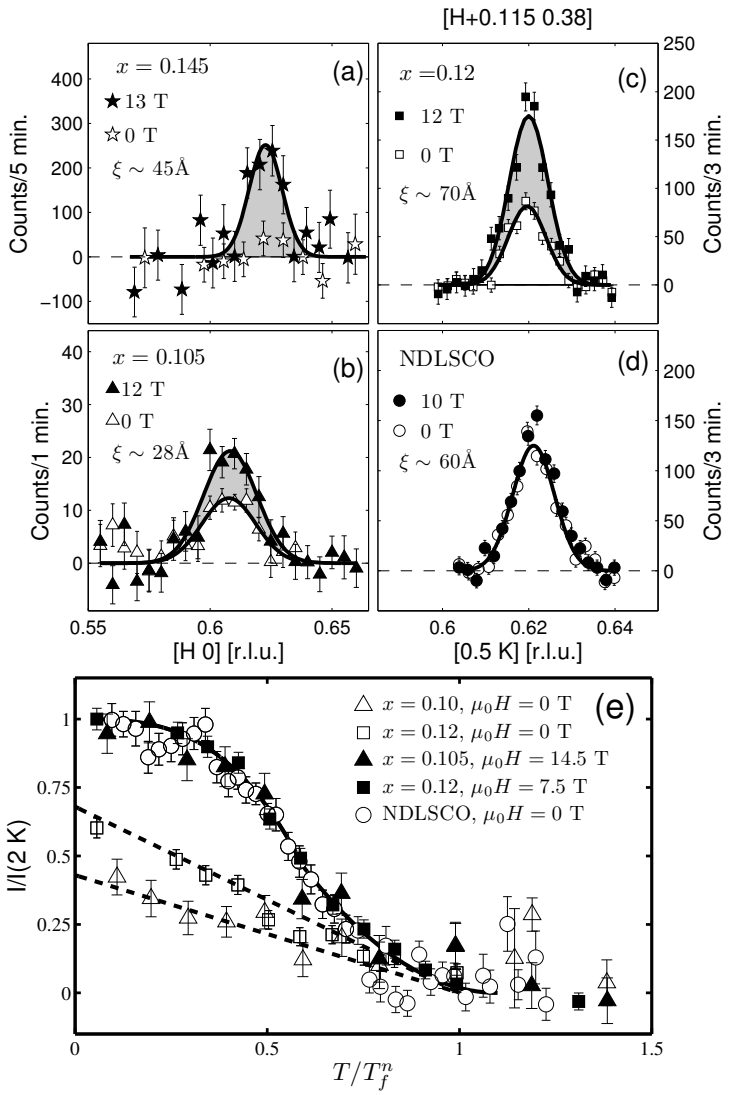

FIGURE 5.6: (a)-(d) **Q**-scans around $\mathbf{Q}_{IC}$ performed on $x = 0.145$, $x = 0.105$, $x = 0.12$, and NDLSCO, respectively. Data in (a)-(c) are recorded with $T = 2$ K while data in (d) are taken with $T = 25$ in order to advoid the Nd-ordering at low temperatures. Solid lines are Gaussian fits to the data. Note the different x-axis scale for the left and right panel. The magnetic correlaton length ξ is derived from the FWHM of the magnetic peaks. (e) T-dependence of the intensity at $\mathbf{Q}_{IC}$ for $x = 0.105$, $x = 0.12$, and NDLSCO. Open symbols indicate data taken in ZF while filled symbols are recorded upon application of a magnetic field.

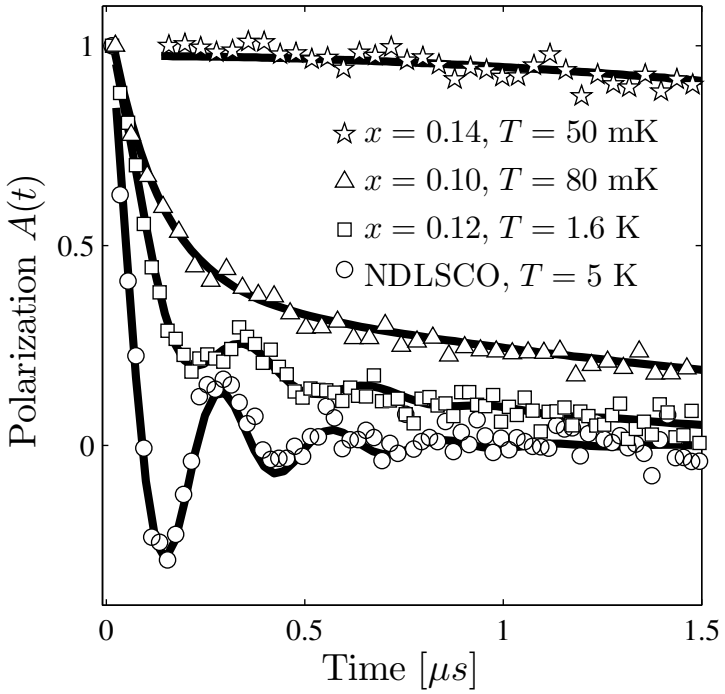

FIGURE 5.7: μSR time spectra obtained in zero field and low-temperatures. The solid lines are fits to the data with a Bessel function for NDLSCO and $La_{2-x}Sr_xCuO_4$ with $x = 0.12$, a simple exponential decay ($x = 0.105$), and a Kubo-Toyabe function ($x = 0.145$).

ZF response is closer to a linear dependence as indicated by dashed lines.

The superconducting transition temperature is strongly suppressed in NDLSCO ($T_c \approx 7$ K) and we therefore consider this compound to closest mimic the physics of the so-called 1/8 ground state. The time evolution of the muon spin polarization $A(t)$ (see appendix B) exhibits a strongly damped oscillatory behavior that can be well described by a Bessel function with a frequency $\nu \approx 3.5$ MHz, see figure 5.7. The observation of a Bessel function is consistent with the existence of an IC SDW state [190, 191].

We stress that similar results are obtained for $La_{15/8}Ba_{1/8}CuO_4$ [192–194] and for the AF ordered volume fraction in superoxygenated $La_{2-x}Sr_xCuO_{4+y}$ [195]. The latter compound was shown to phase separately into optimally doped SC regions and a AF ordered phase closely related to the 1/8 ground state.

The characteristic features of the 1/8 ground state therefore are

Table 5.1: Compilation of μSR and neutron scattering results on La-based compounds. μ_{lo} and μ_{av} denote the local and average Cu^{2+} moment as determined by μSR and neutron scattering, respectively. $T_f^{\mu SR}$ and T_f^n are the corresponding, time scale dependent freezing temperatures. δ is the incommensurability.

1/8 Compounds	Doping	T_c onset	μ_{lo}	μ_{av}	$T_f^{\mu SR}$	T_f^n	δ
NDLSCO	$x = 0.12$, $y = 0.4$	7 K	0.36 μ_B	0.08 μ_B	50 K	65 K	0.122(4)
$La_{2-x}Ba_xCuO_4$	$x = 0.125$	5 K [193]	0.35 μ_B[191]	-	40 K[200]	50 K[193]	0.118[193]
Compound	Doping	T_c	$\frac{\mu_{lo}}{\mu_{lo}(1/8)}$	$\frac{\mu_{av}}{\mu_{av}(1/8)}$	$T_f^{\mu SR}$	T_f^n	δ
$La_{2-x}Sr_xCuO_4$	$x = 0.120$	27±1.5 K	0.5	0.33	15 K	30 K	0.125(3)
$La_{2-x}Sr_xCuO_4$	$x = 0.105$	30±1.5 K	0.36	0.22	10 K	25 K	0.108(2)
$La_{2-x}Sr_xCuO_4$	$x = 0.145$	36±1.5 K	<0.014	0	-	-	0.13(2)

★ a strongly suppressed T_c,

★ the observation of a Bessel-like relaxation with $\nu \approx 3.5$ MHz in the μSR time spectra [192],

★ incommensurate SDW order with $\delta \approx 0.125$ and the absence of a field effect.

The 1/8 ground state consists, most likely, of static stripes with an associated SDW order, which in turn suppresses the SC order parameter. The 1/8-anomaly is limited to a very narrow doping range and slight variations of the doping level lead to very noticeable changes in the physical properties.

Due to its dipolar character the measured internal magnetic field is directly proportional to the ordered Cu^{2+} moment. For NDLSCO the internal field at base temperature is found to be 27 mT which is about 2/3 of the value observed in the undoped compound La_2CuO_4 [196–198]. Assuming a value of 0.6 μ_B for the Cu^{2+} moment in La_2CuO_4, the internal field corresponds to a local ordered moment $\mu_{lo} \approx 0.36\ \mu_B$. The average ordered moment estimated from the neutron diffraction experiments[†] suggests $\mu_{av} = 0.08\ \mu_B$, consistently with a previous report [107]. Note that for a sinusoidal SDW there is a factor of two between μ_{lo} and μ_{av} [191]. However, there is still a discrepancy between μ_{lo} estimated by μSR and μ_{av} determined by neutron diffraction (see also [199]). A full knowledge of the microscopic spin topology might be necessary to solve this issue.

When moving away from 1/8 doping the ordered moment at ZF decreases systematically with decreasing doping. At the same time a field induced enhancement of the magnetic intensity is observed. For $x = 0.12$, $A(t)$ still exhibits the characteristic Bessel type oscillation, albeit with a reduced frequency and an increased damping. We stress that we observe the full muon asymmetry, i.e. all muons experience a nonzero local magnetic field. This implies that the magnetic

[†]The average ordered moments given in table 5.1 were obtained by normalizing the magnetic response to the response of a phonon measured at $T = 200$ K. The absolute values were obtained by comparison to the parent compound LCO where the ordered moment is assumed to be 0.6 μ_B. The experiments and analysis were carried out by N.B. Christensen.

order persists throughout the entire volume of the sample, which is a remarkable result for a superconductor with a T_c as high as 27 K. We emphasize that the magnetic ground state may still be inhomogeneous but the characteristic length scale for this inhomogeneity has to be smaller than about $10-20$ Å, which is a typical range for dipolar fields which originate from AF ordered moments. In fact, a nano-scale inhomogeneous state consisting of SC droplets and patches of AF correlated regions is a very likely candidate for the ground state in a region of the phase diagram where the antiferromagnetic and superconducting phases are very close in energy [201, 202].

The neutron diffraction results confirm the existence of IC magnetic order in ZF and in addition reveal a significant enhancement of the elastic intensity by an applied magnetic field, see figure 5.6(c). The field effect observed here is stronger than a previous report [182], but given the significantly lower $T_c = 12$ K of their $x = 0.12$ sample the different magnitude of the field enhancement can easily be understood. It can be seen from figure 5.8 that for $x = 0.12$ the magnetic field tends to restore the magnetism characteristic for 1/8 doping. This might suggest that the effect of the field is to drive the system toward the 1/8 ground state.

For $x = 0.105$, $A(t)$ does no longer show the features of a Bessel function, but is now well described by a simple exponential decay. The static nature of the internal field was verified by longitudinal field experiments. We deduce a static field distribution $\Delta \approx 10$ mT which is significantly reduced from the 27 mT observed in the "stripe" compounds. Application of an external field doubles the amplitude of the elastic signal, see figure 5.6(b). The value characteristic for static stripe order, however, can not be restored in this system, see figure 5.8.

For the $x = 0.145$ compound with a doping level in excess of 1/8, $A(t)$ does not exhibit any relaxation due to electronic moments. The very slow Gaussian decay of the polarization is well fitted by a static Kubo-Toyabe function, which describes the field distribution arising from nuclear moments alone [203]. The width of this field distribution defines an upper limit for the size of electronic moments $\mu < 0.005\ \mu_B$. Neutron diffraction studies on this sample show field-induced static AF order resembling that of underdoped compounds for $H > H_c$ with $H_c \approx 7$ T. A previous report found $H_c \approx 3$ T [189], which might indicate that the doping level of this work is slightly lower [204].

Now let us turn back to figure 5.8 that displays the field dependence of the static incommensurate AF order for the four discussed compounds. In the phenomenological Ginzburg-Landau model of Demler *et al.* [204–206] the field dependence is predicted to exhibit a logarithmic dependence at low fields

$$\mu \sim \sqrt{I} \sim \sqrt{\frac{H}{H_{c2}} \ln\left(\frac{H_{c2}}{H}\right)}. \tag{5.16}$$

The solid lines in figure 5.8 are fits to this field dependence. The fit works well for all compounds where a field effect is observed. Although the Demler model describes the field effect of LSCO $x = 0.105$, 0.12, and 0.145 the model does not predict the doping dependence of the field effect and currently the model does not encompass the 1/8-anomaly.

The fact that observed field effect obeys this particular dependence lead B. Lake *et al.* [183], based on the model of Demler *et al.*, to interpret the field effect as a signature of vortex physics. In this view the field effect should be understood from the vortex cores induced by the magnetic field. As the field is increased the vortices become denser leading to an increased elastic response.

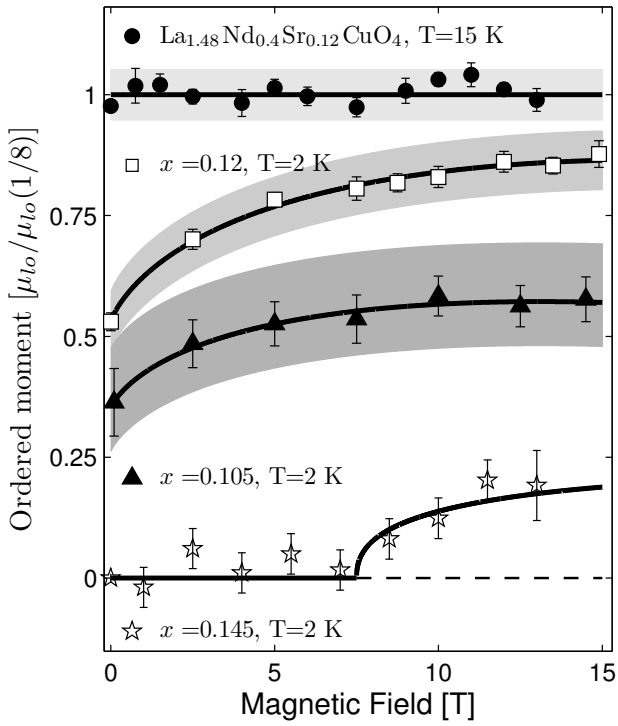

FIGURE 5.8: H-dependence of the response at $\mathbf{Q}_{IC}$ for LSCO with $x = 0.105$, $x = 0.12$, $x = 0.145$, and NDLSCO. The solid lines are explained in the text. The gray colors indicate the error related to the determination of the ZF ordered moment. Data for $x = 0.145$ are presented in arbitrary units.

5.4.3 Discussion. Our combined μSR and neutron diffraction experiments lead us to propose the schematic $H - x$ phase diagram depicted in figure 5.9, where the ordered moment is given by false color scheme. The 1/8 and the SC ground states are pictured by the dark red and the dark blue regions, respectively. From this figure it is obvious that the underdoped regime of the phase diagram is dominated by a competing magnetic order parameter centered cone-like around 1/8 doping [207].

Since the field-induced enhancement of the static incommensurate AF order has been interpreted in terms of vortex physics [183], a comparison to the study of the vortex lattice by means of SANS is relevant. The phase diagram in figure 5.9 showing schematically the field effect on the static incommensurate AF order can be directly compared with the vortex phase diagram shown in figure 4.21. It seems very difficult to correlate the field-induced static AF order with the 3D vortex lattice observed by SANS. The field-induced enhancement of the elastic response appears mainly in the region of the phase diagram where the vortices arrange in disordered structures. This fact seems to indicate that the elastic field effect is not directly related to vortex physics.

An other possible interpretation of the field-induced enhancement of the static AF order is in

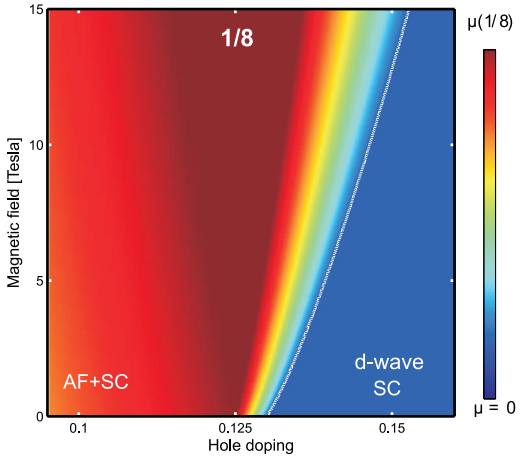

FIGURE 5.9: Schematic doping-field phase diagram for $La_{2-x}Sr_xCuO_4$. The ordered moment is given in false colors with red as the maximum and blue is $\mu = 0\ \mu_B$.

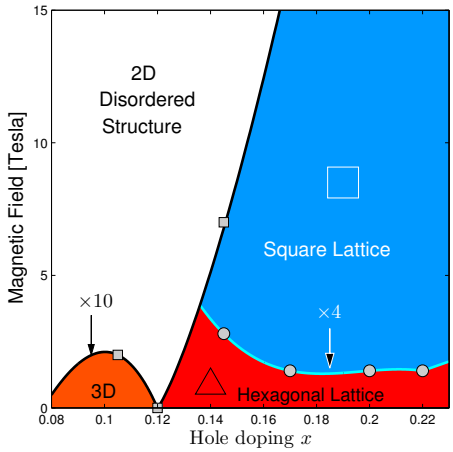

FIGURE 5.10: The vortex phase diagram shown in figure 4.21 is displayed again fro convinience. For a detailed explanation see chapter 4.

terms of competing order parameters. In this view the IC static AF order is competing with an itinerant order. The role of the applied magnetic field is to change the balance between the order parameters. The field experiment on $x = 0.145$ is especially illustrative. In zero field no static order exists and as will be shown in a later chapter a large Fermi surface can be observed throughout the whole Brillouin zone. A field-induced spin-density-wave was observed by application of fields larger than 7 tesla. Such a SDW instability of the Fermi surface has also been observed in other strongly correlated metals [55] with V-doped Cr as one of the most prominent examples [208, 209]. The onset of the SDW order implies a smooth reconstruction of the Fermi surface [210]. The quasiparticle spectral weight will be suppressed near the *hot spots*, the portions of the Fermi surface that are connected by the AF wave vector. It is in this fashion that the SDW and the SC orders compete about the very same Fermi surface.

This picture of competing order parameters is compelling for several reasons. First, it naturally explains the observation that superconductivity is strongly suppressed when a fully developed spin-density-wave order is present. Second, it provides an explanation to the recently observed quantum oscillations under application of very high magnetic fields ($H \sim 50$ T) in underdoped YBCO [211–214]. These measurements suggest that the Fermi surface consists of small pockets at $H \sim 50$ T. As pointed out by Sudip Chakravarty *et al.* [215] this observation can be interpreted as a consequence of competing order parameters. The enhanced SDW order upon application of magnetic field will in this view enhance the formation of pockets [69].

5.4.4 The role of disorder. As mentioned previously, a small amount of non magnetic impurities in the CuO_2 planes can enhance the static magnetism. Substituting a few precent of the Cu atoms with Zn in optimally doped LSCO leads to a systematic decrease of T_c and induces static incommensurate magnetism [216]. This might suggest that the observation of static magnetism in

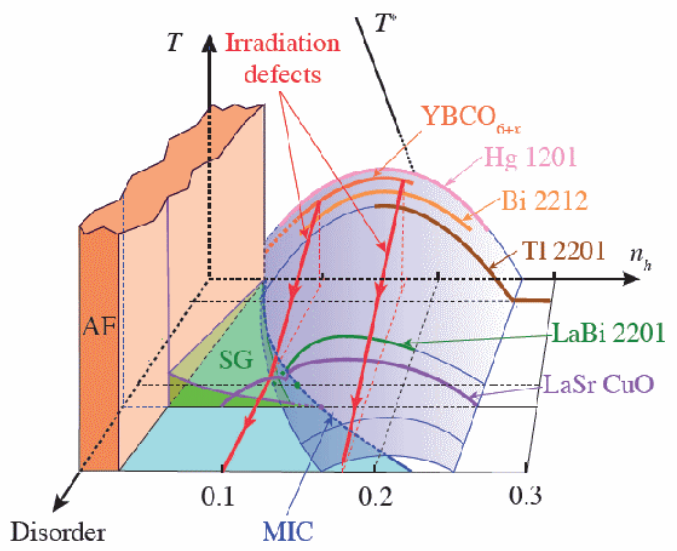

FIGURE 5.11: Schematic phase diagram of cuprate materials as a function of temperature, hole doping, and disorder. The region with static magnetism is indicated by SG. From F. Rullier-Albenque *et al.* [219].

underdoped LSCO is induced by extrinsic impurities. Our observation of the field-induced SDW order in LSCO with $x = 0.145$ demonstrate, on the other hand, that the static magnetism is not controlled solely by impurities. The systematics of our observations and the consistency with the existing literature seem also to suggest that the magnetism in underdoped LSCO is an intrinsic property.

The magnetism might be induced by out-of-plane disorder as discussed by B.M. Andersen *et al.* [217]. In LSCO the dopants are introduced by the Sr ions which are distributed randomly on a La-site. Substituting La with Nd for a given Sr doping will increase further the out-of-plane disorder. Fujita *et al.* [218] have demonstrated how the transition temperature T_c decreases systematically with increasing out-of-plane disorder. As argued by B.M. Andersen *et al.* [217] the degree of out-of-plane disorder may be one of the main differences between the different cuprate materials. A schematic phase diagram based on resistivity measurements [219] is shown in figure 5.11. Here the SC dome is displayed as a function of both hole doping and disorder. YBCO is one of the cleanest systems known. By introducing disorder into YBCO by means of electron irradiation F. Rullier-Albenque *et al.* [219] investigated in a systematic fashion the role of disorder and it was demonstrated that disorder strongly changes the physical properties.

The magnetism studied here is to some extent specific to LSCO. However even in the cleanest known cuprate materials such as YBCO static magnetism appears in the underdoped region of the phase diagram [220]. I would therefore argue that the study of LSCO has general relevance for the understanding of the cuprate materials.

5.5 SPIN GAP IN UNDERDOPED LSCO

Common for superconductors is that they have an energy gap Δ_{SC} in the single-particle excitation spectrum [221]. In high-temperature superconductors a spin gap [‡] Δ_{SG} has been discovered in the spin excitation spectrum [222]. This spin gap seems to be related to the superconducting order parameter since it opens at T_c, see figure 5.12. Evidence for a spin gap was early reported in LSCO [222] and increasing crystal quality lead to increased data quality [223]. It is now well established that for LSCO with $x = 0.16 \pm 0.02$ a clean spin gap, of the order $\sim 4-8$ meV, opens at T_c [222–227]. The spin gap seems to be a universal energy scale for optimally doped cuprate superconductors since it has been observed both in hole doped compounds [226] and in electron doped cuprates [228].

The fact that the spin gap opens at T_c shows that there is an intimate interplay between magnetism and superconductivity. Despite intense research this complex interplay between magnetism and superconductivity remains incompletely understood. In the previous section, static magnetism was interpreted in terms of a competing order to superconductivity. However, in some theories, antiferromagnetic spin fluctuations constitute the pairing glue for superconductivity [229, 230] and the fact that the spin gap opens at T_c tells that spin fluctuations are connected directly or indirectly in superconductivity.

Much effort has been done to find an energy scale that, like the superconducting gap of BCS superconductors, exhibits a simple relation with T_c [231]. To test the connection between antiferromagnetic spin fluctuations and superconductivity, we decided to investigate the spin gap as a function of underdoping and thereby T_c. So far, no systematic study has been done in the underdoped region of LSCO. Therefore it is not clear if the spin gap amplitude Δ_{SG} scales with T_c or if Δ_{SG} increases with underdoping as the pseudo gap does.

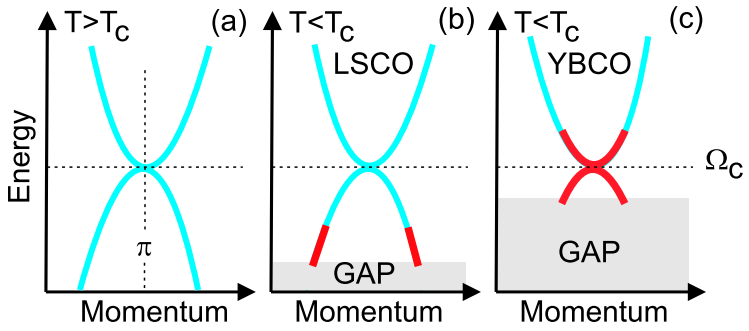

FIGURE 5.12: Schematic dispersion of the spin excitations of optimally doped cuprates. (a) Normal state ($T > T_c$). (b-c) In superconducting state ($T < T_c$) of LSCO and YBCO a clean gap opens and spectral weight shifts from below to above the gap as shown by the red region.

[‡]In the literature, the term spin gap is also used for the gap observed by magnetization and NMR measurements [59–61], see figure 1.5. However this gap is not directly related to the superconducting order parameter since it opens at much higher temperatures.

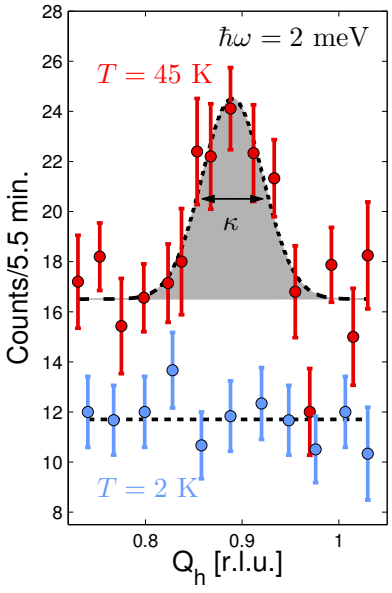

FIGURE 5.13: **Q**-scan through $\mathbf{Q}_{IC}$ with energy transfer $\hbar\omega = 2$ meV in the normal state ($T = 45$ K) and in the superconducting state ($T = 2$ K). The dashed lines are a fit to Gaussion and a constant function, respectively. ($\kappa \approx 0.012$Å^{-1})

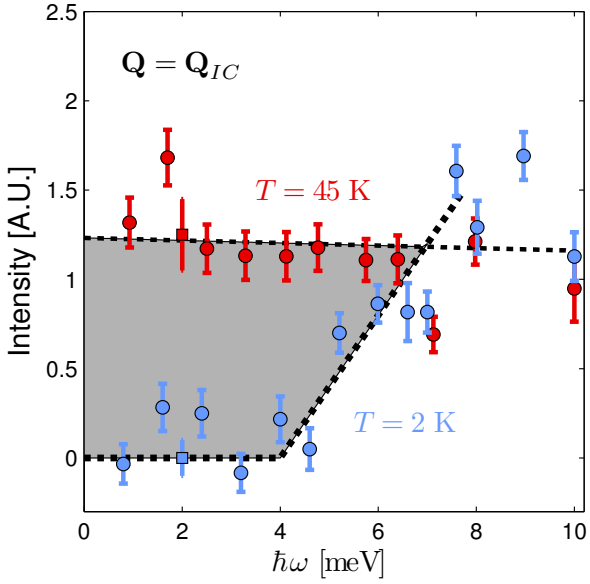

FIGURE 5.14: Background subtracted intensity at $\mathbf{Q}_{IC}$ as a function of energy transfer in the normal state (red) and in the superconducting state (blue). Circular and square points are derived from three point scans and real Q-scans, respectively. The dashed lines are guides to the eye.

5.5.1 Spin gap in LSCO $x = 0.145$. Now let us start by an examination of the normal state spin fluctuations. The T- and ω-dependence of the spin fluctuations in the normal state of $x = 0.14$ have been carefully investigated and interpreted in terms of a quantum critical phenomenon by G. Aeppli *et al.* [232].

In figure 5.13, an inelastic **Q**-scan with energy transfer $\hbar\omega = 2$ meV is shown for $T = 45$ K (normal state) and $T = 2$ K (superconducting state). In the normal state a clear spin excitation is observed at $\mathbf{Q}_{IC}$. The FWHM of this inelastic spin excitation is $\kappa_{AF} \sim 0.012$ Å^{-1} (corresponding to a correlation length $\xi \sim 10a$ with $a \sim 5.4$ Å), consistently with a previous report on similar doping [232]. At $T = 2$ K, in the superconducting state, this excitation is however completely suppressed (see blue points in figure 5.13) due to the spin gap.

The ω-dependence of the background subtracted inelastic response at $\mathbf{Q}_{IC}$ is shown in figure 5.14 for $T = 45$ K and $T = 2$ K. In the normal state ($T = 45$ K) the dependence is approximately constant for energy transfers $\hbar\omega = 0 - 10$ meV. In the same energy range the inelastic response is completely suppressed for $\hbar\omega < 4.5$ meV in the superconducting state ($T = 2$ K). The spin gap amplitude Δ_{SG} at $T = 2$ K is therefore approximately 4.5 meV.

5.5.2 General features of the spin gap. Besides the complete suppression of inelastic response for $\hbar\omega < \Delta_{SG}$ and $T \ll T_c$, the spin gap has several other features.

Let us start by discussing the temperature dependence. In the normal state the inelastic response at $\mathbf{Q}_{IC}$ increases with decreasing temperature [232]. At T_c the spin gap opens and the response is suppressed for $\hbar\omega < \Delta_{SG}$ and $T < T_c$. Thus the opening of the spin gap effectively leads to an anomaly at T_c in the inelastic response for $\hbar\omega < \Delta_{SG}$. Such an anomaly has indeed been observed by ourself (not shown) and other groups, see for example T. Mason *et al.* [225].

An other feature of the spin gap is the appearance of in-gap states upon application of a magnetic field perpendicular to the CuO_2 plane. The field effect on the spin gap in $x = 0.16 - 0.18$ has been investigated by several groups. Although the details vary from experiment to experiment [233–235], magnetic field-induced excitations for $\hbar\omega < \Delta_{SG}$ and $T < T_c$ remain a common observation.

5.5.3 Field dependence of the spin gap in $x = 0.145$. The field-induced in-gap states have been studied carefully in the optimally doped to slightly overdoped region ($x = 0.16$ to $x = 0.18$) [233–235] of the phase diagram. Here, I will describe a field experiment on a slightly underdoped composition. Remember that in the $x = 0.145$ compound a field-induced SDW order was observed for $H > H_c = 7$ T. The critical field H_c was interpreted as a signature of a quantum critical point separating two different ground states. For $H < H_c$ the ground state resembles that of optimally doping and for $H > H_c$ that of underdoped ($x < 0.13$) compounds with coexisting SC and static magnetic order. In this view, the application of a magnetic field therefore allows us to tune the system between the two ground states.

We are now going to investigate the field effect on the inelastic scattering in the $x = 0.145$ compound.

The blue points in figure 5.15 indicate a **Q**-scan taken at base temperature with $\hbar\omega = 2$ meV in zero field (also shown in figure 5.13). As described before the spin excitations are completely gaped for $\hbar\omega < 4.5$ meV and $T \ll T_c$. Now upon application of $H = 13$ T a clear field-induced spin excitation appears as demonstrated in figure 5.15 (orange points). Next, the amplitude of the spin excitation as a function of field was studied by performing three-point scans. Figure 5.16 displays the signal and background (orange and gray points) dependence as a function of field For $H < 2.5$ T it is impossible, within the statistical errorbars of the data, to distinguish the signal from the background. This might suggest that the field-induced spin excitations have an onset field $H^{AF}(\omega)$.

To test this hypothesis a set of **Q**-scans in a non-zero field was performed. Figure 5.17(a) shows a **Q**-scan with $\hbar\omega = 1$ meV and applied field of $H = 3.5$ T and $H = 7$ T. Under application of $H = 3.5$ T no field-induced spin excitation could be detected within the experimental errorbar. In contrast a clear field-induced spin excitation could be observed for $H = 7.5$ T. This suggests that field-induced spin excitations have an onset field of 3.5 T$< H^{AF}(\omega) <$ 7 T.

In figure 5.17(b) the blue area, limited by the dashed line, indicates the parameter space $(H, \hbar\omega)$ where no field-induced excitation could be observed. The measured onset field is here given by the blue points with horizontal errorbars. The red points, associated with the right hand axis, are the static incommensurate responses which have an onset at $H^{AF}(0) \approx 7$ T, as discussed in section 5.4. These results suggest that the spin gap decreases systematically upon application of a magnetic field and extrapolates to zero near the onset of static incommensurate order. A similar systematic linear decrease of the spin gap was observed in $Nd_{2-x}Ce_xCuO_4$ (NCCO) with $x = 0.15$ [228]. However in the case of NCCO the spin gap extrapolates to zero at $H \approx H_{c2}$.

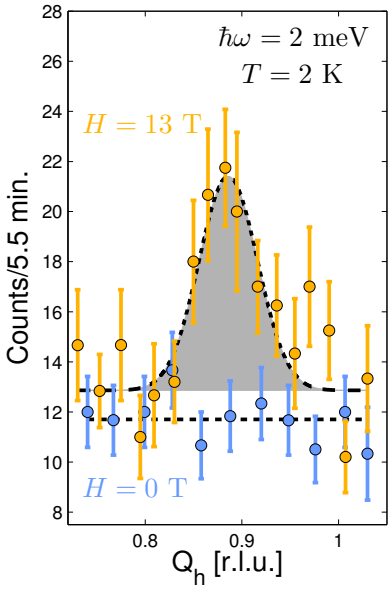

FIGURE 5.15: Q-scan through $\mathbf{Q}_{IC}$ with energy transfer $\hbar\omega = 2$ meV in zero field ($H = 0$ T) and under application of $H = 13$ T. The dashed lines are a fit to Gaussian and a constant function, respectively. ($\kappa \approx 0.012$ Å^{-1})

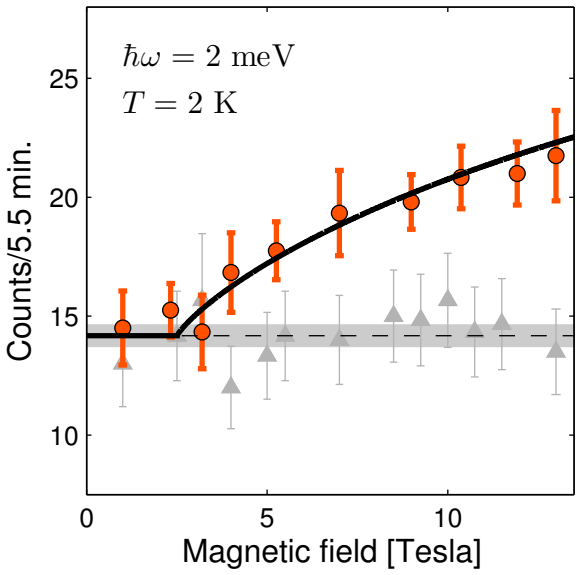

FIGURE 5.16: The intensity at $\mathbf{Q}_{IC}$ (orange points) as a function of applied magnetic field together with the background which is approximately independent of the applied field. The dashed line is a fit to the background data with a constant function. The gray shaded line indicates the error of the fit.

I am now coming back to the discussion of the field effect. In the optimally doped to slightly overdoped region of the phase diagram field-induced in-gap states were interpreted in terms of vortex physics [233–235]. The observation of a spin gap that decreases systematically with an applied magnetic field is however difficult to reconcile with vortex physics [228] since in this view field-induced excitations should appear for $H < H_{c1}$. Our observation seems more consistent with the picture where the critical field $H_c \approx 7$ T is related to a QCP separating two different ground states. The spin gap Δ_{SG} is, in this scenario, the energy of the lowest possible spin excitation above the ground state, as displayed in the inset of figure 5.17(b). As the QCP is approached the spin gap is expected to vanish [236]

$$\Delta_{SG} \sim (H - H_c)^{z\nu} \tag{5.17}$$

where $z\nu$ is a critical exponent. The fact that we observe a spin gap that extrapolates to zero for $H \to H_c$ is therefore consistent with the interpretation of a QCP.

A more detailed study of the spin gap dependence on applied magnetic field and the spin excitations at the possible QCP is the subject of an upcoming experiment on the PANDA instrument.

5.5.4 Summary. To recapitulate, I summarize here the most prominent characteristics of the spin gap Δ_{SG} in slightly underdoped to slightly overdoped LSCO.

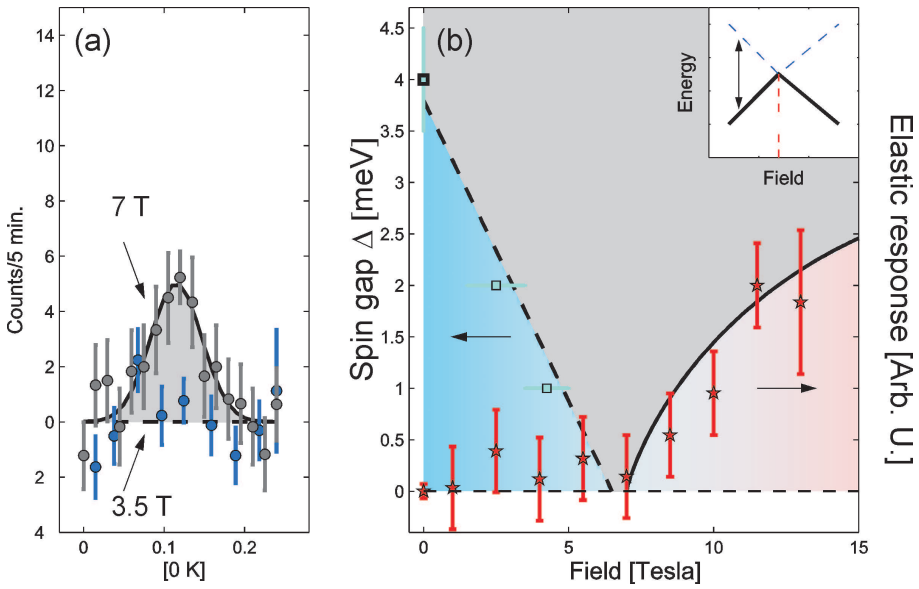

FIGURE 5.17: (a) **Q**-scan through $\mathbf{Q}_{IC}$ with energy transfer $\hbar\omega = 1$ meV and under application of $H = 3.5$ T and 7 T. For convenience a linear background has been subtracted. The solid line is a fit to Gaussian function. (b) The blue points indicate the spin gap as a function of applied field and the red points are the neutron response at $\mathbf{Q}_{IC}$ in arbitrary units. The inset shows how an energy scale Δ vanishes at the quantum critical point.

★ A strong suppression of the inelastic responce for $\omega < \Delta_{SG}$.

★ Magnetic field-induced response for $\omega < \Delta_{SG}$ and $H > H^{AF}(\omega)$.

★ An anomaly at T_c in the temperature dependence for $\omega < \Delta_{SG}$.

5.5.5 Hidden spin gap in LSCO $x = 0.105$.

Until now I have described the spin gap in LSCO compounds where static incommensurate magnetism is absent in zero field. Let us now turn to the strongly underdoped region of the phase diagram. For $x = 0.105$ weak static incommensurate AF coexists with SC, as previously discussed. The driving question is whether there exists a spin gap in the strongly underdoped region of the phase diagram. In a previous section the ground state of LSCO $x > 0.13$ was interpreted in terms of pure d-wave SC. However in the underdoped region ($x < 0.13$) the ground state is different because static magnetism coexists with superconductivity. So far no neutron scattering evidence of a spin gap has been reported in the region $x < 0.13$ [237].

Therefore we decide to perform high resolution inelastic neutron scattering experiments as a function of energy transfer $\hbar\omega$, magnetic field H, and temperature T on LSCO with $x = 0.105$. These measurements were done on the cold triple axis spectrometer IN14 at ILL. The setup was similar to previously described inelastic experiments. However, for the low-energy transfers $\hbar\omega <$ 0.5 meV we used $k_f = 1.3$ Å^{-1} in order to avoid contamination from the elastic line.

Before discussing the results, it should be emphasized that the sample has been characterized by means of several other techniques. The static incommensurate AF has been investigated by elastic neutron scattering, as discussed in a previous section. The magnetic phase diagram has been explored by magnetization and AC susceptibility measurements in magnetic fields H up to 8 tesla along the c-axis [108], see figure 5.18(a). The vortex lattice was investigated by small angle neutron scattering and μSR [147]. All these measurements indicate that in underdoped region of LSCO, the vortex liquid phase dominates the magnetic phase diagram while quasi-long-range ordered vortex lattice can only be observed at low fields and low-temperatures [147].

In figure 5.18(b), we show the effect of H on the T-dependence of the intensity at $\mathbf{Q}_{IC}$ with an energy transfer of $\hbar\omega = 1$ meV. These data demonstrate that the intensity is enhanced by application of $H = 10$ T in an intermediated temperature range 10 K$< T < T_c$, corresponding roughly to the liquid region of the vortex phase diagram, see figure 5.18(a). A similar behavior was previously reported for LSCO samples close to optimal doping [234, 235]. This was interpreted in terms of induced excitations inside the vortex core [234]. In effect, H shifts and broadens the cusp-like anomaly at T_c to a lower $T_c(H)$. The shift corresponds qualitatively to the shift in T_c as seen in figure 5.18(a). We note that the lower limit on the field effect might be related to the onset at $T_f^{\mu SR} = 10$ K of Cu moment freezing observed by μSR on the same sample, see table 5.1.

The dependence on $\hbar\omega$ and $\mathbf{Q}$ of the intensity, taken at different temperatures and fields, is shown in figure 5.19. In figure 5.19(a) the intensity at $\mathbf{Q}_{IC}$ and at $H = 0$ T shows a smooth dependence on $\hbar\omega$ above T_c. At $T = 2$ K, an anomaly is exhibited at $\hbar\omega = 1.5$ meV below which intensity is reduced relative to that in the normal state. Figure 5.19(b) shows the effect of cooling through T_c in the $\mathbf{Q}$-scan through $\mathbf{Q}_{IC}$ at $H = 0$ T and with $\hbar\omega = 0.5$ meV. Cooling from 33.5 K to 2 K results in a two-fold reduction of the intensity at $\mathbf{Q}_{\rm IC}$. Figures 5.19(c) and (d) show the change in the dependence on $\hbar\omega$ and $\mathbf{Q}$ of the intensity at fixed $T = 22.3$ K upon applying $H = 10$T, respectively. The effect of the applied field, in figure 5.19(c), is to remove the zero field anomaly at $\hbar\omega = 1.5$ meV, and is similar to the effect of raising the temperature above T_c, in figure 5.19(a). Note that here the magnetic field-induced redistribution of spectral weight is limited to frequencies smaller than 1.5 meV.

To better appreciate the features of the excitation spectrum described above, a comparison with the SG signatures observed in optimally doped LSCO is relevant. Remember that: (i) Although the details vary from experiment to experiment [233–235], magnetic field-induced excitations for $\hbar\omega < \Delta_{SG}$ and $T < T_c$ remain a common observation. (ii) For $\hbar\omega < \Delta_{SG}$, besides the suppression of intensity at low-temperatures, an anomaly was reported at T_c that marks the closing of the spin gap as the temperature crosses T_c [225]. (iii) A strong suppression of the intensity below $\hbar\omega \approx \Delta_{SG}$ is observed in the SC state but not in the normal state [164]. In our underdoped LSCO sample, we infer from figures 5.18(b) and 5.19 similar spin gap features as in optimally doped LSCO. (i) An applied magnetic field acts to redistribute the spectral weight for 10 K $< T < T_c$ at $\hbar\omega < 1.5$ meV (figures 5.18(b) and 5.19(c)). (ii) There is the cusp-like anomaly at T_c scanning the temperature for fixed energy below 1.5 meV. (iii) Energy scans reveal an anomaly at $\hbar\omega = 1.5$ meV which disappears in the normal state. The field effect (i) alone provides compelling evidence for a spin gap at 1.5 meV. This is further supported by the cusp at T_c (ii), and consistent with the energy dependence (iii). We also find that the intensity at $\mathbf{Q}_{IC}$ displays the same functional dependence as that reported near optimal doping [232] as a function of $T > T_c$ or $\hbar\omega > 1.5$ meV.

Now, let us discuss how the data can be modelled. In the overdoped region of YBCO, the

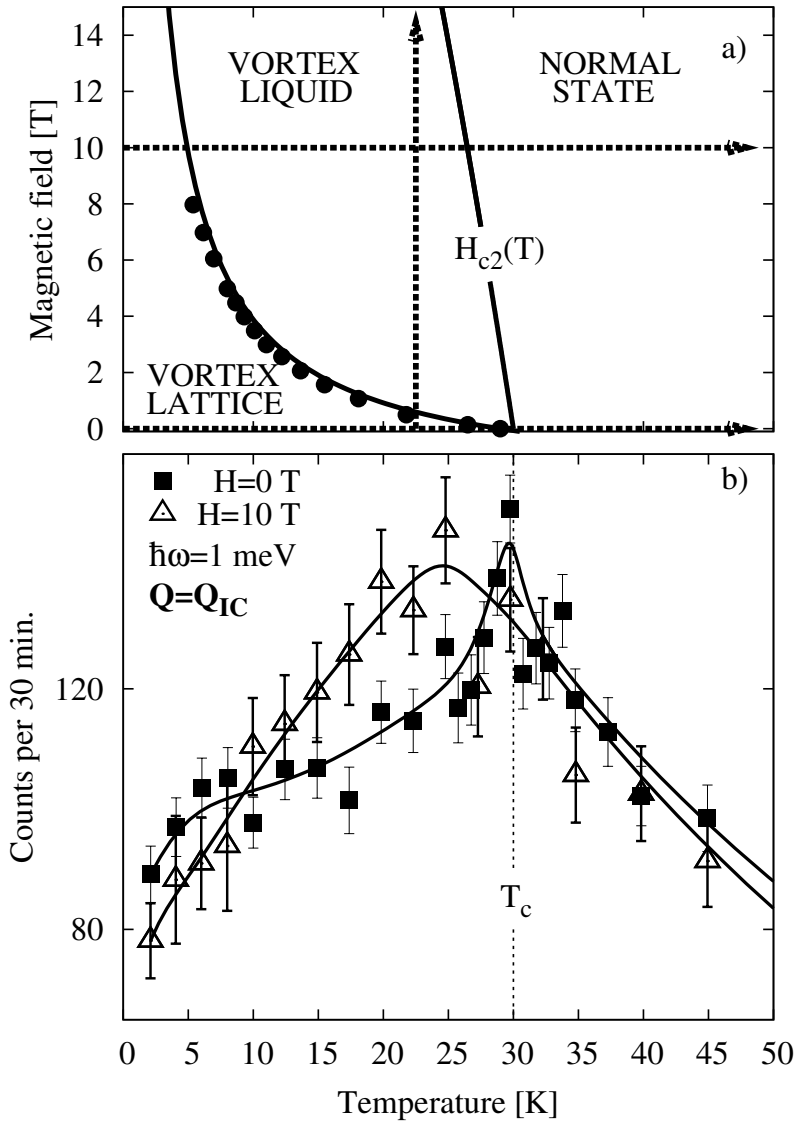

FIGURE 5.18: (a) Phase diagram of underdoped LSCO ($x = 0.105$) as a function of magnetic field H and temperature T [108]. Filled circles are the measured values for the melting line of the vortex lattice [108]. The straight line is the position of T_c as a function of H. The dashed arrows indicate the T- and H-scans that are described in the text. (b) Two T-scans at $\mathbf{Q}_{IC}$ and $\hbar\omega = 1\,\text{meV}$. Open triangles (filled squares) denote the measured intensity at $H = 10$ T ($H = 0$ T) and solid lines are guides to the eye.

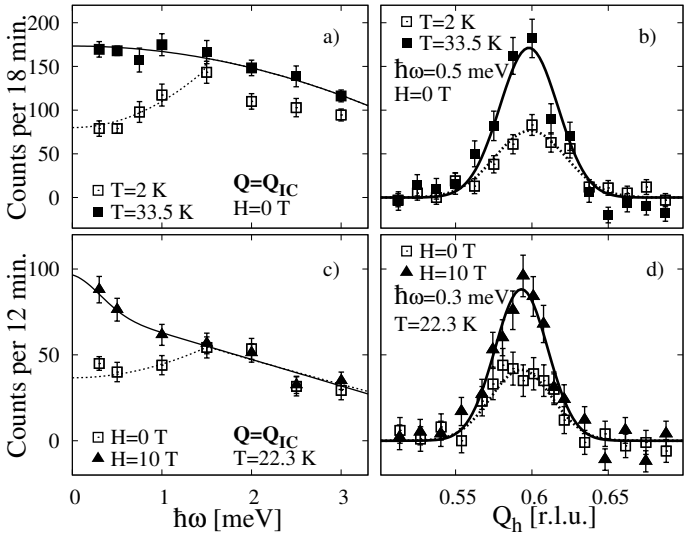

FIGURE 5.19: Energy and **Q**-dependence of magnetic scattering from LSCO ($x = 0.105$). Energy scans are taken at $\mathbf{Q}_{IC}$: (a) Comparison of the response in the SC phase with that of the normal state in zero field. (c) Effect of a 10T field at $T = 22.3$ K. Q scans through $\mathbf{Q}_{IC}$: (b) Comparison of the response in the SC phase with that of the normal state using $\hbar\omega = 0.5$ meV. (d) The effect of a 10T field at $T = 22.3$ K, $\hbar\omega = 0.3$ meV, and $E_f = 3.5$ meV. In this configuration the resolution (HWHM) was 0.03 meV. The data have been background subtracted and lines are guide to the eye.

neutron response has successfully been described by Fermi liquid phenomenology [238, 239]. Here the imaginary part of the magnetic susceptibility of a weakly interacting gas of quasiparticles is calculated within the random phase approximation (RPA)

$$\chi''_{RPA}(\omega,\mathbf{q}) = \frac{\chi''_0(\omega,\mathbf{q})}{[1-U\chi'_0(\omega,\mathbf{q})]^2 + [U\chi''_0(\omega,\mathbf{q})]^2}. \tag{5.18}$$

The non interacting magnetic susceptibility χ''_0 reads [240]

$$\begin{aligned}
\chi_0(\omega,\mathbf{q}) &= \sum_k \frac{1}{2}\left(1+\frac{\varepsilon_\mathbf{k}\varepsilon_{\mathbf{k}+\mathbf{q}}+\Delta_\mathbf{k}\Delta_{\mathbf{k}+\mathbf{q}}}{E_\mathbf{k}E_{\mathbf{k}+\mathbf{q}}}\right)\frac{f(E_{\mathbf{k}+\mathbf{q}})-f(E_\mathbf{k})}{\omega-(E_{\mathbf{k}+\mathbf{q}}-E_\mathbf{k})+i\Gamma} \\
&+ \frac{1}{4}\left(1-\frac{\varepsilon_\mathbf{k}\varepsilon_{\mathbf{k}+\mathbf{q}}+\Delta_\mathbf{k}\Delta_{\mathbf{k}+\mathbf{q}}}{E_\mathbf{k}E_{\mathbf{k}+\mathbf{q}}}\right)\frac{1-f(E_{\mathbf{k}+\mathbf{q}})-f(E_\mathbf{k})}{\omega+(E_{\mathbf{k}+\mathbf{q}}+E_\mathbf{k})+i\Gamma} \\
&+ \frac{1}{4}\left(1-\frac{\varepsilon_\mathbf{k}\varepsilon_{\mathbf{k}+\mathbf{q}}+\Delta_\mathbf{k}\Delta_{\mathbf{k}+\mathbf{q}}}{E_\mathbf{k}E_{\mathbf{k}+\mathbf{q}}}\right)\frac{f(E_{\mathbf{k}+\mathbf{q}})+f(E_\mathbf{k})-1}{\omega-(E_{\mathbf{k}+\mathbf{q}}+E_\mathbf{k})+i\Gamma}
\end{aligned}$$

with $E_\mathbf{k} = \sqrt{\varepsilon_\mathbf{k}^2+\Delta_\mathbf{k}^2}$, where $\varepsilon_\mathbf{k}$ is the band dispersion, $\Delta_\mathbf{k}$ is the momentum dependent superconducting gap, and Γ is the inverse lifetime [240, 241]. All these quantities can be measured by ARPES and this is the subject of the next chapter.

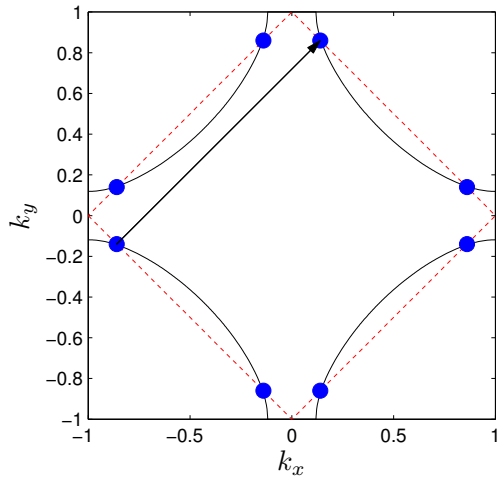

FIGURE 5.20: Shematic Fermi surface of LSCO. The antiferromagnetic zone boundary is indicated by the dashed line and the socalled hot spots are shown by blue points.

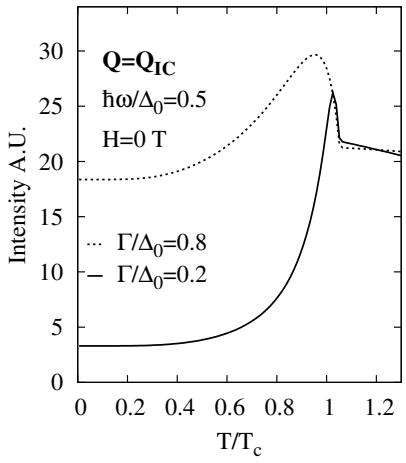

FIGURE 5.21: Intensity vs T calculated within the phenomenological Fermi liquid approach by Andreas Schnyder.

In this phenomenological Fermi liquid (PFL) picture, which is relatively successful at optimal doping, the SG is directly related to the SC gap. Although its maximum increases with underdoping, the slope of the superconducting d-wave gap has been measured to soften at the nodes with underdoping [242, 243]. This means that the ratio $\Delta_{SG}/(k_B T_c)$ will decrease with underdoping [244].

The neutron response of LSCO was calculated numerically by Andreas Schnyder (Condense Matter Theory Group at PSI) using Eq. 5.18. The fermiology parameters are chosen to reproduce the T-dependence of the INS response at optimal doping in LSCO (see Refs. [242, 243]), with the Ansatz $\Delta(\mathbf{Q},T) = \Delta_0(\mathbf{Q})\sqrt{1-(T/T_c)^4}$ and $\Delta_0(0,\pi) = 10$ meV for the T-dependence of the superconducting d-wave gap.

In this picture, the anomaly at T_c in the temperature dependence displayed in figure 5.18(b) is caused by the closing of the SG upon entering the normal state. Figure 5.21 shows the calculated dependence on temperature of the zero field neutron intensity at $\mathbf{Q}_{IC}$ and energy transfer $\hbar\omega = 0.5\Delta_0$ using the PFL parameters chosen to reproduce the T-dependence at optimal doping. A cusp-like anomaly at T_c separates the normal regime from a d-wave superconducting regime with a decreasing residual intensity due to a phenomenological inverse lifetime of $\Gamma = 0.2\Delta_0$. In this spirit, to reproduce the measured residual spectral weight at low-T in $x = 0.105$ LSCO would require $\Gamma \approx \Delta_{SG}$ resulting in strong broadening of the peak at T_c as shown in figure 5.21. Thus, the naive PFL approach is unable to reconcile a sharp anomaly at T_c (Δ_{SG}) for small enough $\hbar\omega$ (T) and the large, compared to optimal doping, residual intensity in the low-T (low-$\hbar\omega$) tail of figure 5.18(b) (figure 5.19(a)).

One way to explain the large residual intensity at low-temperatures and energies in strongly underdoped HTSC could be in terms of a two-component model. The first component would cor-

respond to the gaped response seen around optimal doping. The second (quasi-elastic) component could be related to the slowing down of the magnetic signal observed by μSR [169], and the central mode recently reported in YBCO ($T_c = 18$ K) [245]. The fact that both components develop well-defined peaks at $\mathbf{Q}_{IC}$ suggests an inter-twinning of the two components on a nanometer length scale. This could possibly be explained within a picture of static and fluctuating stripes, although it remains a challenge to quantify this picture to describe the detailed field and temperature effects of the magnetic response reported here.

5.5.6 Spin fluctuations in the anomalous $x = 0.12$ compound. An unambiguous clean gap of $\Delta_{SG} = 4.5$ meV was observed in the slightly underdoped compound $x = 0.145$. Furthermore we found a hidden gap in the underdoped $x = 0.105$ sample. Next, we decided to investigate the low-energy spin fluctuations at the anomalous doping $x = 0.12$. Remember from previous sections that this sample has a slightly suppressed $T_c = 27$ K (lower than that of $x = 0.105$).

The leading question is now whether we can observe a hidden gap in this compound or not? From the slightly lower T_c compared to that of $x = 0.105$, one would naively expect that the gap is even stronger renormalized compared to $x = 0.105$. To test this hypothesis, we decided to perform a high-resolution inelastic neutron scattering experiment as a function of field, energy transfer $\hbar\omega$, and temperature. The strategy was to identify the same type of spin gap features as we observed in $x = 0.105$. In other words, we were looking for field effects at low-energy transfers and anomalies at T_c. The PANDA instrument at FRM-II is ideal for this purpose since it provides both a high neutron flux and a good energy resolution [246].

Figure 5.22(a) show a $\mathbf{Q}$-scan through $\mathbf{Q}_{IC}$ with energy transfer $\hbar\omega = 0.5$ meV and $T = 30$ K. The red and black points are taken in ZF and with $H = 10$ T, respectively. As expected, no field effect could be observed in the normal state. Next, we investigated the T-dependence of the response at $\mathbf{Q}_{IC}$, see figure 5.22(b). In the temperature range $T = 1.5$ to 80 K the background (open triangles) was found to be approximately T-independent. The signal at $\mathbf{Q}_{IC}$, on the other hand, had a broad maximum at $T \approx 30$ K. The signal was measured both in ZF and under application of $H = 10$ T in the mentioned temperature range. Interestingly no field effect could be observed neither in the superconducting state nor in the normal state. At low-temperature, $T = 2$ K, a weak but finite signal is observed. Figure 5.22(d) shows the imaginary part of the susceptibility, $\chi''(T)$, derived from the background subtracted data (see Eq. 2.24). $\chi''(T)$ is approximately constant for $T < 30$ K and it decreases very fast for $T > 30$ K, see red and black points in figure 5.22(d). Finally, the ω-dependence of the signal at $T = 30$ K is shown in figure 5.22(c). A rapid decrease with increasing energy transfer was found. Correcting with the Bose factor a saturation seems to appear for $\omega < 2$ meV. A more comprehensive study of the zero field low-energy spin fluctuation is given in the master thesis of L. Maechler [143].

To summarize, this paragraph, we did not find any field effect of the low-energy response at any temperature. Furthermore, no sharp anomaly at T_c could be identified. Therefore, if there exists a spin gap related to superconductivity, it must be smaller than 0.5 meV. The proximity to a quantum critical point may be one way to interpret this result. The field experiment on $x = 0.145$ suggested that the spin gap vanishes at the onset of the spin-density-wave order. In zero field the onset of the spin-density-wave order in LSCO is at $x \approx 0.13$ as shown in figure 5.9. The proximity to this quantum critical may be the reason that the spin gap is strongly reduced.

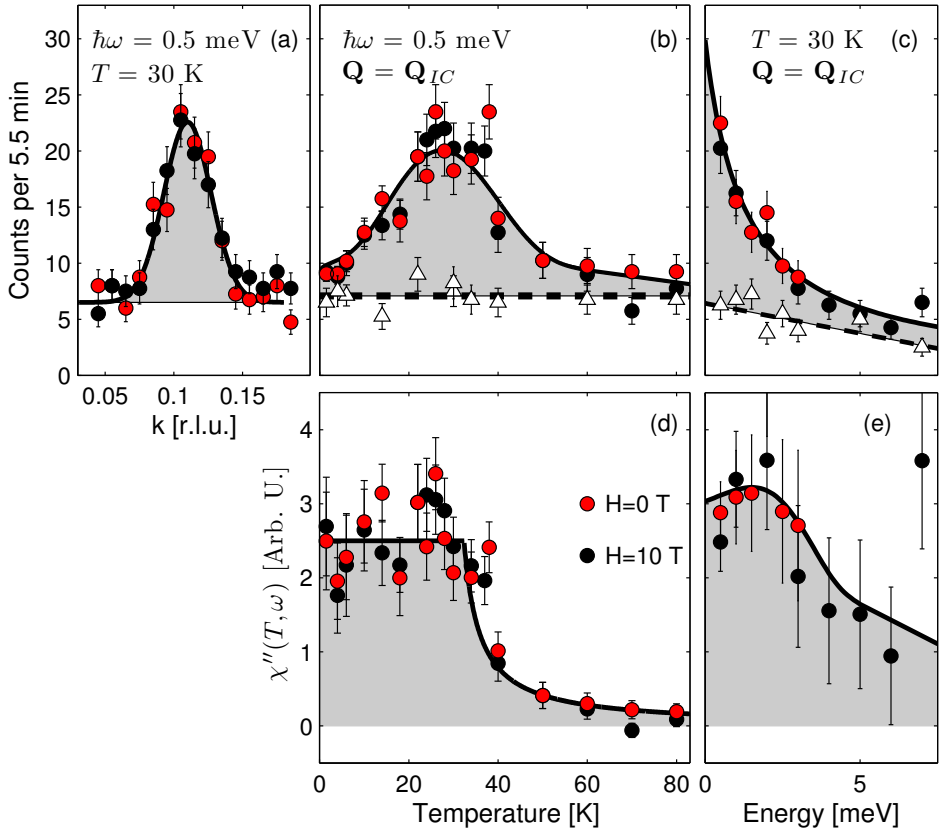

FIGURE 5.22: Inelastic response in LSCO $x = 0.12$, red (black) points are taken in zero field ($H = 10$ T) (a) Q-scan with energy transfer $\hbar\omega = 0.5$ meV and $T = 30$ K. (b) Temperature dependence of the response at $\mathbf{Q}_{IC}$ and with energy transfer $\hbar\omega = 0.5$ meV. (c) The response at $\mathbf{Q}_{IC}$ with $T = 30$ K as a function of energy transfer. (d) and (e) Background subtracted and Bose corrected data. The solid line in (a) is a Gaussian fit to the data, all other solid lines are guides to the eye.

5.6 SUMMARY AND DISCUSSION

This last section of this chapter is devoted to summarize and discuss the elastic and inelastic field effect (FE) which was studied in a systematic fashion as a function of underdoping. A discussion of the spin gap on its possible relation to the electronic energy scales will also be given.

5.6.1 Doping dependence of the spin gap. To summarize, the spin gap dependence on T_c for LSCO and YBCO samples is shown in figure 5.23. Vertical and horizontal axes have been normalized by the values of the SG and SC critical temperature at optimal doping, respectively. The ratio $\Delta_{SG}/(k_B T_c)$ exhibits a strong downward multiplicative renormalization in the underdoped regime. This strong renormalization was also observed in YBCO [247–249], in which context it was attributed to inhomogeneities induced by oxygen doping [248]. We must, however, rule out this explanation for our $x = 0.105$ LSCO sample in view of the sharpness of the SC transition

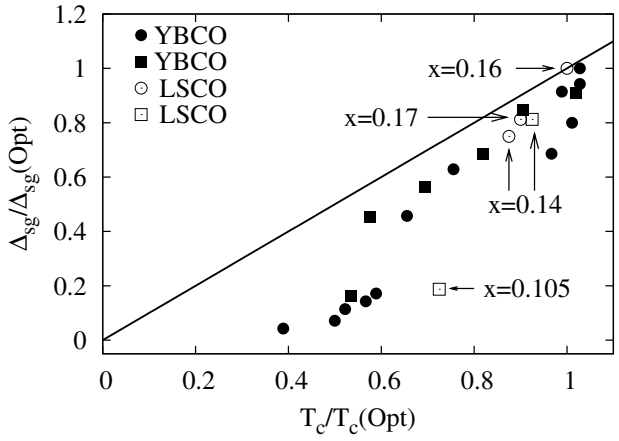

FIGURE 5.23: Normalized Δ_{SG} versus normalized T_c for LSCO (open symbols) and YBCO (filled circles [247] and filled squares [248]). The open circles are taken from previously published data, $x = 0.14$ [225], $x = 0.16$ [227], and $x = 0.17$ [235], while open squares are from this work ($x = 0.105$ and $x = 0.14$).

($\Delta T_c = 1.5$ K). Instead, we believe that the proper interpretation of figure 5.23 is that of a universal doping dependence of $\Delta_{SG}/\Delta_{SG}(\mathrm{Opt})$ with a linear regime that defines the approach to optimal doping and an underdoped regime whose defining property is a doping dependent $\Delta_{SG}/(k_B T_c)$.

It is remarkable that $\Delta_{SG}/(k_B T_c)$ decreases in the underdoped regime, since this is opposite to the doping dependence of most energy features (maximum SC gap or pseudo gap at (π,0)) which are found, from ARPES measurements, to increase with underdoping [250, 251]. Some very recent ARPES data show however that while the (π,0) gap increases with underdoping the gap close to the nodal point decreases with underdoping [252], as shown in figure 5.24. It should be emphasized that this is consistent with the earlier observation of a flattening of the gap nodes reported by J. Mesot *et al.* [242] and S. V. Borisenko *et al.* [243]. Nevertheless these results have been challenged by a recent report, see A. Kanigel *et al.* [253]. It is not the purpose of this section to judge which set of data reveals the correct physics of the cuprates. However, it should be emphasized that the observation of a near nodal gap that decreases with underdoping is consistent with the observation of a strongly renormalized spin gap in the underdoped region of the phase diagram [244].

Next I turn to discuss some recent STM/STS data taken on LSCO films in the doping range $0.08 < x < 0.18$ [254]. In contrast to ARPES, the STM technique can not resolve the momentum dependence of the gap. Hence STM measures an average gap. In the work of O. Yuli *et al.* the gap was found to decrease with underdoping. More intriguingly, no gap could be observed for $x = 0.12$ with $T_c = 27$ K. These STM/STS observations of the superconducting gap therefore corroborate very well with our observations of the spin gap that decreases with underdoping and the absence of a spin gap for $x = 0.12$.

Another evidence for an electronic energy scale that decreases with underdoping stems from

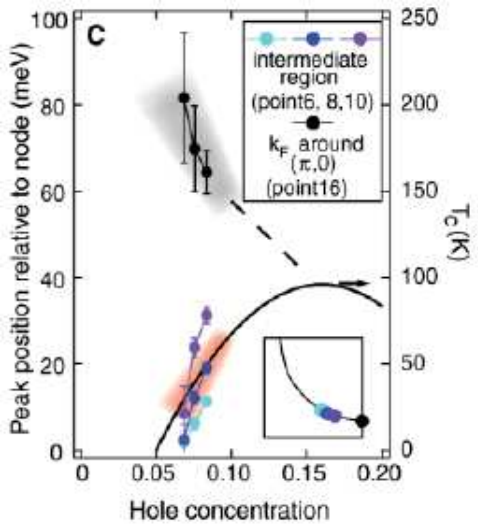

FIGURE 5.24: Distint doping dependence of the gap measured near the nodal point and of the gap measured at the (π,0) in Bi2212. From K. Tanaka *et al.* [252].

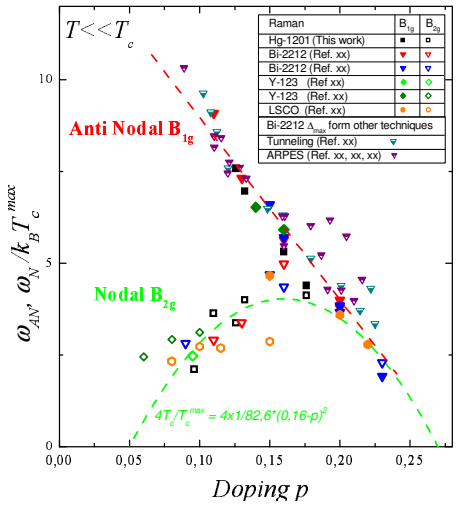

FIGURE 5.25: Doping dependence of the gap measured by Raman spectroscopy in the nodal and antinodal region. From M. Le Tacon *et al.* [255].

Raman spectroscopy. By using the polarization of light M. Le Tacon *et al.* [255] managed to disentangle the nodal and antinodal response. The results of these experiments suggest that the antinodal gap increases with underdoping oppositely to the nodal gap which decreases with underdoping, see figure 5.25.

Assuming that the spin gap is directly related to the superconducting gap both neutron scattering, ARPES, Raman spectroscopy and STM provide evidence for an energy scale the decreases with underdoping and thereby T_c. This gap energy could therefore be the characteristic energy scale related to the pair formation. However, the presented study of the spin gap both as a function of applied magnetic field and doping clearly demonstrates that there is no one-to-one correspondence between T_c and the spin gap amplitude. Two examples of a vanishing spin gap in compounds with finite T_c were given. This seems to indicate that the spin gap is not directly related to a pair formation energy scale.

The momentum, doping, and temperature dependence of the superconducting gap is still heavily debated both experimentally and theoretically. It is an open question whether the superconducting gap dependence on for example doping should be understood in terms of one or two characteristic energy scales. In the phenomenological Fermi liquid picture the spin gap observed by neutron scattering is directly connected to the superconducting gap in vicinity to the nodes. If so, our study of the spin gap as a function of doping and magnetic field would indirectly provide information about the electronic gap function. An equally carefully study of the superconducting gap, by for example ARPES, on the sample crystal would therefore increase the ability to make the link to the spin gap. Work along such lines are in progress.

5.6.2 Discussion of the field effect in LSCO. The vortex phase diagram and static and dynamic magnetism were investigated systematically as a function of magnetic field and doping in the last two chapters. Table 5.2 summarizes these results in a qualitative fashion. It was previously argued by R. Gilardi [87] that there might be connection between the vortex phase diagram and the field effect (FE) of the low-energy spin fluctuations in LSCO with $x = 0.17$. Herein the focus was entirely on the underdoped region of the phase diagram. In this regime it was very difficult to correlate the field effect of the static and dynamic incommensurate AF with the vortex phase diagram. Instead, the field effect was interpreted in terms of competing order parameters.

5.6.3 Conclusion. In this chapter the static and dynamic antiferromagnetism was studied in a systematic fashion as a function of doping and magnetic field. Below is a short summary of the results:

1. Static incommensurate AF magnetic order was studied systematically around the special $x = 1/8$ doping. On an experimental level all the results were fully consistent with the existing literature. These results were herein interpreted in terms of competition between a spin-density-wave order and superconductivity.

2. The spin gap in the spin excitation spectrum was studied systematically as a function of underdoping.

   (a) In the strongly underdoped LSCO with $x = 0.105$ a hidden spin gap was identified for the first time. The spin gap amplitude was strongly renormalized compared to the spin gap observed at optimally doped LSCO.

   (b) An other key result is the spin gap dependence on applied magnetic field in LSCO with $x = 0.145$. It was shown that the spin gap decreases systematically upon application of magnetic field and that the spin gap extrapolates to zero at the onset field for static magnetic AF order. This result was interpreted in terms of a SDW instability of the Fermi surface through a quantum critical point.

   (c) For the special doping $x = 0.12$ no signature of a spin gap could be observed for $\hbar\omega > 0.5$ meV. Therefore it was concluded, if any spin gap related to superconductivity exists it has to be smaller than 0.5 meV.

Table 5.2: Summary of the magnetic field experiments on LSCO. Notice that in case of LSCO with $x = 0.105$ and $x = 0.12$ the conclusions concerning the spin gap relies partially on the inelastic field effect.

Compound	$x = 0.105$	$x = 0.12$	$x = 0.145$	$x = 0.17$
Elastic FE	yes	yes	yes	no
Inelastic FE	yes	no	yes	yes
Vortex Lattice	yes	no	yes	yes
Spin gap	yes	no	yes	yes

Chapter 6

Electronic degrees of freedom in LSCO

In solid state physics there exist a number of complementary probes that couple directly to the electronic charge. For example charge transport can be studied by resistivity measurements and the sign of the charge carrier can be induced from the Hall coefficient measurements. More sophisticated techniques such as de Haas-van Alphen (dHvA) [256] and angle magnetoresistance oscillation (AMRO) [257] measurements provide even information about the Fermi surface structure. A number of spectroscopy techniques have also provided insight into the metallic properties of the high-T_c materials. For example infrared spectroscopy measurements can probe the frequency dependence of the scattering rate through the Drude peak [258]. Another complementary technique is STM/STS which provides information about spatial distribution of the local density of state [116].

As mentioned in chapter 1 the application of several complementary techniques enhances the possibility to identify the salient and robust features. Knowledge of the electronic structure may also provide insight into the two-particle response function that can be observed by inelastic neutron scattering. In this chapter, the electronic structure and scattering rate of LSCO will be studied by means of ARPES. The advantage of this technique is that it can resolve the momentum and frequency dependence of the electronic excitations.

6.1 The photoemission process

The photoelectric effect is the emission of electrons from matter upon absorption of electromagnetic radiation, see figure 6.1. The discovery of the photoelectric effect is usually credited to H. Hertz [259]. In 1905 it was known that the kinetic energy E_{kin} of the photoelectrons increased with increasing frequency ν of the incoming light but not with increasing intensity. This led Einstein to postulate that light is quantized with an energy of $h\nu$. Photons are the modern name for such light quanta.

Before Einstein was awarded the Nobel prize in 1921 for the explanation of the photoelectric effect, it was experimentally demonstrated by Millikan* that the photoelectron energy E_{kin} scales linearly with the photon frequency ν

$$E_{kin} = h\nu - \phi, \tag{6.1}$$

*Millikan was awarded the Nobel prize for his contribution in 1923.

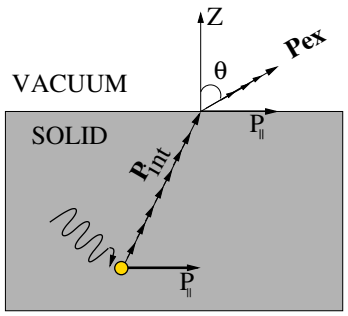

FIGURE 6.1: Schematic drawing of the photoemission process, which can be described by three steps: (i) absorption of a photon with energy $h\nu$, (ii) the photoelectron is transported to the surface of the sample, and (iii) the electron escapes from the material.

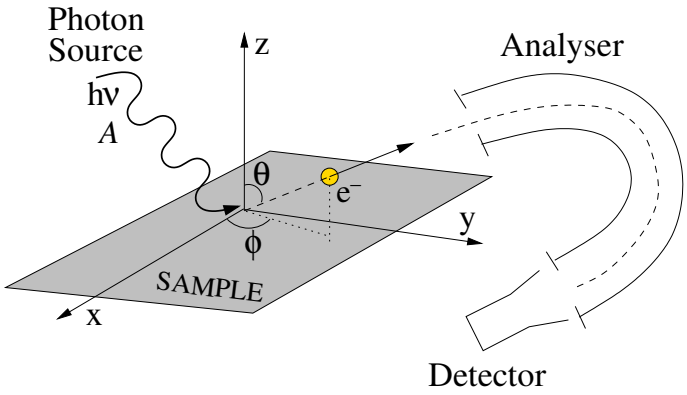

FIGURE 6.2: Principles of an angle resolved photoemission spectrometer. Monochromatic and polarized photons with energy $h\nu$ are produced from a light source. The kinetic energy of the photoemitted electrons is analyzed with respect to the emission angles (θ,ϕ).

where ϕ is the work function of the cathode material.

Spectroscopy methods using photoemitted electrons were not developed before the 1960's. A schematic sketch of the photoemission spectroscopy method is shown in figure 6.2. It was discovered that the analysis of the energy distribution of the photoemitted electrons yields information about the electronic density of state $n(E)$ of the cathode material, see the sketch in figure 6.3(a). Knowing the energy of the photons $h\nu$ and the work function ϕ, it is possible to determine the binding energy E_B of the electron in the material by measuring the kinetic energy $E_{kin} = h\nu - \phi - E_B$ of the photoemitted electron. Experimentalists usually display the measured photoemission current as a function of binding energy, as shown in figure 6.3(a).

The more sophisticated angle resolved photoemission technique was developed during the 1970's. Analyzing the photoemission current as a function of the emission angles θ and ϕ, shown in figure 6.2, allows full insight into the electronic band structure. This is schematically depicted in figure 6.3(b).

The main obstacle related to photoemission spectroscopy is the energy resolution. Hence there is an ongoing effort to obtain a better resolution. Today an energy resolution of less than 10 meV and an angular resolution of 0.3 degrees can be achieved routinely. To obtain high resolution, monochromatic and well collimated radiation is required. Such radiation can be produced by lasers, lamps, and synchrotron facilities.

The ARPES technique has proven to be a powerfull probe of two dimensional electronic structures. The cuprate materials have highly anisotropic crystal structures leading to a quasi two dimensional electronic structure. ARPES is therefore a very useful tool to investigate the electronic properties of high-T_c materials. Insight into many important features of high-T_c superconductors such as, the Fermi surface topology [260], the band dispersion [261], the identification of the d-wave symmetry [28] of the superconducting order parameter, and the detection of the pseudo gap [44, 262, 263] in the underdoped regime, have been provided by ARPES experiments. ARPES

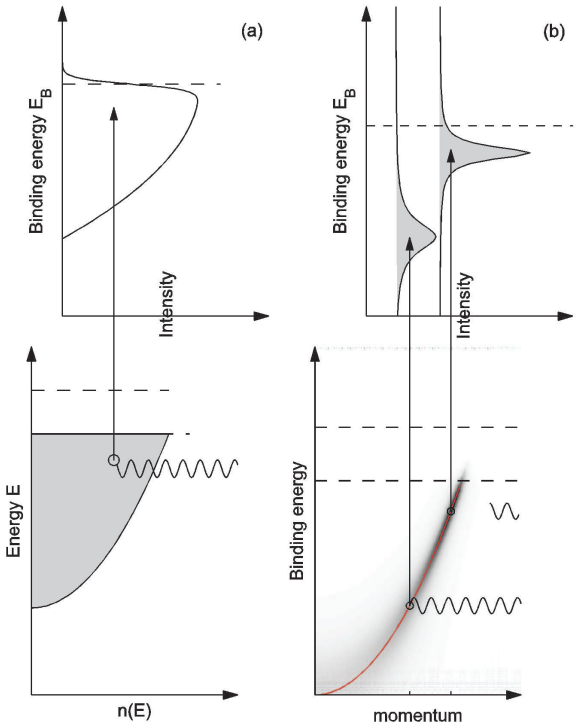

FIGURE 6.3: Schematic view of the photoemission process within the single-particle paradigm. (a) Angle integrated photoemission spectroscopy yields information about the density of state $n(E)$. (b) Angle resolved photoemission spectroscopy can probe the electronic band structure. The work function ϕ is the difference between the vacuum level E_{vac} and the Fermi level E_F. From energy conservation the kinetic energy of the photoemitted electron yields $E_{kin} = h\nu - \phi - E_B$. The observed photoemission current is typically displayed versus the binding energy by experimentalists.

also reveals insight into the self-energy $\Sigma(\mathbf{k},\omega)$ [264, 265] (see Eq. 2.9) which contains information about all the interactions. This function is of special interest since it is related to the scattering rate and hence makes comparison with transport measurements possible.

The ARPES technique has been heavily applied to the study of Bi-based compounds because they are easy to cleave and because they have a quasi 2D electronic structure. Ino *et al.* [266–268] were one of the first to study LSCO by means of ARPES. The La-based compounds are significantly harder to cleave and the existing data are therefore correspondingly scarce. During the years improved data quality has been obtained due to improved resolution and knowledge about matrix element effects.

In this work we have focused on the importance of the sample quality and in particular on the quality of the sample surface. Sample quality and the homogeneity of the sample chemistry are crucial for the quality of the ARPES spectra. Although the energy and momentum resolution are comparable to previous studies, we have, due to high sample quality, been able to extract significantly improved ARPES spectra. Before presenting these results, a short discussion of the photoemission process and the ARPES technique is given.

6.1.1 The three-step model. Although A. Einstein got the Nobel prize for the explanation of the photoelectric effect, it is still difficult to describe the photoemission process. Sophisticated models have been developed for this purpose. Here the photoemission process will be described within the so-called three-step model [269], where the photo-current is decomposed into three separate factors.

Step 1: Optical excitation of the electron in the material.

A free electron that interacts with a photon can be described by the Hamiltonian $\mathcal{H} = -\frac{\hbar}{2m}\nabla^2 + \mathcal{V}_{e-p}(\mathbf{r})$, where $\mathcal{V}_{e-p}(\mathbf{r})$ is the electron-photon interaction. Under the assumption that this interaction is weak, $\mathcal{V}_{e-p}(\mathbf{r})$ reads to first order [270–272]

$$\mathcal{V}_{e-p}(\mathbf{r}) = -\frac{e}{2mc}\left[\mathbf{A}\cdot\mathbf{p} + \mathbf{p}\cdot\mathbf{A}\right] \tag{6.2}$$

where $\mathbf{p}$ is the electronic momentum operator and $\mathbf{A}$ is the electromagnetic vector potential. The choice to work with the Coulomb gauge $\nabla\cdot\mathbf{A} = 0$ implies that $\mathbf{p}\cdot\mathbf{A} - \mathbf{p}\cdot\mathbf{A} = i\hbar\nabla\cdot\mathbf{A} = 0$. The electron-photon interaction $\mathcal{V}_{e-p}(\mathbf{r})$ then simplifies to

$$\mathcal{V}_{e-p}(\mathbf{r}) = -\frac{e}{mc}\left[\mathbf{A}\cdot\mathbf{p}\right] = \frac{ie\hbar}{mc}\left[\mathbf{A}\cdot\nabla\right]. \tag{6.3}$$

The assumption of weak interaction between the electron and the photon implies furthermore that perturbation approaches can be used. For a non-interacting electron gas, the photoelectron current can be calculated through the Fermi golden rule

$$I = \frac{2\pi}{\hbar}\left|\langle\Phi_f|\mathcal{V}_{e-p}|\Phi_i\rangle\right|^2\delta(E_f - E_i - \hbar\omega) \tag{6.4}$$

where Φ_i and Φ_f are the initial and final N-electron state. For a more comprehensive discussion of the validity of the single-particle picture and the perturbation approach, the reader can consult the textbooks of S. Hufner [272] and Wolfgang Schattke *et al.*[270].

Step 2: Transport of the electron to the surface.

Some of the photoemitted electrons will be scattered, by for example electron-electron interactions or other scattering mechanisms, before reaching the sample surface. Here it is assumed that most of the photoemitted electrons travel to the surface without being scattered. Effectively the scattering processes are considered as a kind of attenuation of the photoemitted electrons that reach the surface without being scattered. In other words, some electrons simply do not reach the surface due to various scattering processes. These electrons are here disregarded.

This assumption is better known as the sudden approximation which can be formulated in terms of classical transport terminology. The escape depth is the distance that the photoexcited electron has to travel to reach the surface. This distance is determined by the penetration depth of the radiation which depends on the photon energy. For photons with $h\nu = 20 - 100$ eV the escape depth is in the order of $d_e \sim 10$ Å [251], see also figure 6.4. The sudden approximation is valid in the limit $d_e \ll \ell$, where ℓ is the mean free path of the photoemitted electron. Therefore the smaller the escape depth is, the more correct is the sudden approximation. The sudden approximation applies therefore only to surface sensitive techniques and is not valid for bulk probes.

The energy resolution of an ARPES experiment improves when low-energy photons are used and according to figure 6.4 low-energy photons are more sensitive to bulk properties. However the sudden approximation becomes more crude and in worst case invalid. The experiments presented in this thesis used 55 eV photons leading to an escape depth of 10 Å. Under this condition it is reasonable to apply the sudden approximation.

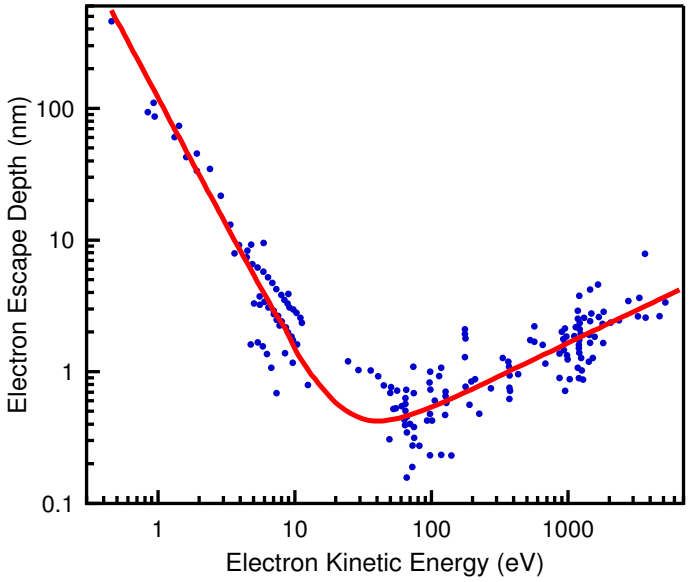

FIGURE 6.4: Escape depth of photoemitted electrons as a function of kinetic energy. For inorganic compound the escape depth seems to follow a universal curve. This figure is from [273] and the data are from [274].

Step 3: Escape of the electrons into vacuum.

The transmission of the photoexcited electrons from the solid to the vacuum must obey energy and momentum conservation. Energy conservation dictates

$$E_{kin} = h\nu - E_B - \phi \tag{6.5}$$

where E_{kin} is the kinetic energy of the outgoing electrons, $h\nu$ is the photon energy of the light shined onto the surface of the sample, E_B is the binding energy, and ϕ is the work function of the surface. The escaping electrons are those who have enough kinetic energy to overcome the surface potential ϕ. Otherwise, if $E_{kin} < 0$, the electrons can not escape from the solid.

The fact that cuprate materials are strongly electronically anisotropic, $\gamma^2 = \rho_c/\rho_{ab} \sim 10^3$, implies that $\mathbf{p}_\perp \ll \mathbf{p}_{||}$, where $\mathbf{p}_\perp$ and $\mathbf{p}_{||}$ are the out-of-plane and in-plane momentum, respectively. For LSCO the experimentally observed anisotropy factor γ^2 varies from ~ 400 in the overdoped region to ~ 3000 in the underdoped region as shown in figure 4.7(b). To proceed in a simple way, I will assume that $\mathbf{p}_\perp \approx 0$. The momentum of the photons can also be neglected. The momentum parallel to the surface $\mathbf{p}_{||}$ is conserved in the transmission from the solid to the vacuum, thus

$$\mathbf{p}_{||} = \hbar\mathbf{k}_{||} = \sqrt{2mE_{kin}}\sin(\theta) \tag{6.6}$$

where the meaning of θ is shown in figure 6.1. This relation between $\mathbf{k}_{||}$ and θ reveals that for larger values of θ, one can probe electrons with $\mathbf{k}_{||}$ lying in higher-order Brillouin zones. Using

lower photon energy $\hbar\nu$ results in lower E_{kin} and electrons with a given $\mathbf{k}$ are probed with larger angle θ which results in better angular resolution.

6.1.2 Spectral function $\mathcal{A}(\mathbf{k},\omega)$. So far it has been described how an electron can be photoemitted from a solid. These photoemitted electrons can be measured as a function of the kinetic energy and the momentum. I am now going to show that the measured electrons are directly related to the spectra function $\mathcal{A}(\mathbf{k},\omega)$.

Let us for simplicity consider a non-interacting electron gas. In this single-particle picture, the N-body state Φ^N can be expressed as a product of the single-particle wavefunctions ϕ_n. The initial and final N-particle state Φ_i^N and Φ_f^N can therefore be expressed as

$$\Phi_i^N = \hat{S}\phi_i\Phi_i^{N-1} \quad \text{and} \quad \Phi_f^N = \hat{S}\phi_f\Phi_f^{N-1}, \tag{6.7}$$

where ϕ_i and ϕ_f are the initial and final wavefunction of the photoemitted electron. $\hat{S}$ is the fermionic anti-symmetrization operator which ensures that the wavefunction satisfies the Pauli principle.

Assuming that there is a weak interaction between the electron and the photon, the effective transition rate from the combined initial state $|i\rangle = |\lambda\rangle|\Phi_i^N\rangle$ (photon+N-electron) to final state $|f\rangle = |\phi_F^{\mathbf{k}}\rangle|\Phi_f^{N-1}\rangle$ (photoemitted electron+(N-1)-electron) can be calculated through the Fermi golden rule

$$\mathcal{W}_{|i\rangle\to|f\rangle} = \frac{2\pi}{\hbar}\left|\langle i|\mathcal{V}_{e-p}|f\rangle\right|^2\delta(E_f - E_i). \tag{6.8}$$

Now the ARPES intensity is proportional to the transition rate between incoming photon and the photoemitted electron. This can be obtained by summing Eq. 6.8 over all final and initial states of the sample which should be weighted by the occurrence p_i of the initial state

$$\begin{aligned} I(\mathbf{k},\omega) &\propto \mathcal{W}_{|\lambda\rangle\to|\phi_F^{\mathbf{k}}\rangle} \propto \sum_{i,f} p_i \mathcal{W}_{|\lambda\Phi_i^N\rangle\to|e\Phi_f^{N-1}\rangle} \\ &= \sum_{i,f} p_i \left|\langle\lambda|\mathcal{V}_{e-p}|\phi_F^{\mathbf{k}}\rangle\right|^2 \left|\langle\Phi_i^N|\Phi_f^{N-1}\rangle\right|^2 \delta(E_f - E_i - \hbar\omega) \\ &= \left|\langle\lambda|\mathcal{V}_{e-p}|\phi_F^{\mathbf{k}}\rangle\right|^2 \sum_{i,f} p_i \left|\langle\Phi_i^N|\hat{c}_{\mathbf{k}}|\Phi_f^N\rangle\right|^2 \delta(E_f - E_i - \hbar\omega) \end{aligned} \tag{6.9}$$

where $p_i = Z^{-1}\exp(-\beta E_i)$. Recall the definition of the removal Green's $\mathcal{G}^-(\mathbf{k},\omega)$ from Eq. 2.7 which allows the ARPES intensity $I(\mathbf{k},\omega)$ to be expressed by

$$I(\mathbf{k},\omega) \propto \left|\mathcal{M}(\hbar\omega,\mathbf{k},E_B)\right|^2 \mathrm{Im}\,\mathcal{G}^-(\mathbf{k},\omega) = \left|\mathcal{M}(\hbar\omega,\mathbf{k},E_B)\right|^2 \mathcal{A}(\mathbf{k},\omega) f(\omega) \tag{6.10}$$

where $\mathcal{M}(\hbar\omega,\mathbf{k},E_B) = \langle\lambda|H_{int}|\phi_F^{\mathbf{k}}\rangle$ is the matrix element, $\mathcal{A}(\mathbf{k},\omega)$ is the spectral function defined in equation 2.5, and $f(\omega)$ is the Fermi-Dirac distribution.

6.2 EXPERIMENTAL SETUP

6.2.1 The SIS beamline. All the ARPES experiments presented in this thesis were carried out at the Surface and Interface Spectroscopy (SIS) beamline at the Swiss Light Source (SLS) facility at the Paul Scherrer Institute (PSI). The SLS synchrotron facility consists of an electron storage ring with a circumference of ∼500 meters. The synchrotron radiation is created by accelerating electrons in magnetic insertion devices, and at the SIS beamline the photon flux is about 2×10^{15} photon/sec for photons with $h\nu = 20\pm1$ eV. The size of the photon spot is typically 50×100 μm^2. Finally, the ARPES endstation of the SIS beamline is equipped with a SCIENTA SES 2000 electron analyzer.

Next, the procedure of the experiments performed at the SIS beamline will be described. The first step is to find the orientation of the LSCO crystal. Then a facet with the *c*-axis perpendicular is created with use of a wire-saw. The cutting process, however, introduces some uncertainness and eventually we always have a finite angle of $0-10$ degrees between the normal of the facet and the *c*-axis. In order to minimize this misalignment, a special sample holder that can be used on both the Laue-instrument and the wire-saw has been created.

Finally an other holder compatible with both the manipulator of the SIS endstation and the Laue instrument was created. With this holder the sample orientation can be inspected directly on the Laue instrument. With a wedge-shaped sample support, it was then possible to compensate for the misalignment introduced through the cutting process. With this method, an overall misalignment, when the sample is glued and cleaved *in-situ*, of less than five degrees was achieved. The samples were always glued to the sample support via an electrical silver epoxy[†]. This ensured that the sample was in thermal equilibrium with the sample holder.

At the beamline, the sample was first loaded into a prechamber which was then pumped until the pressure reached $O(10^{-7})$ mBar. The sample is then transported into a second chamber which is kept under a vacuum of $O(10^{-9})$ mBar. Here the sample holder was sputtering with Argon for 20 min. using a voltage of 1000 KeV and a current of 10 mA. The sputtering removes any remaining dirt on the sample holder and the polycrystal copper of the sample holder is then clean enough to collect a spectrum for a reference. During the Argon milling fine pumping was stopped and the vacuum was then $O(10^{-6})$ mBar.

The prechamber was pumped down to $O(10^{-9})$ mBar after the sputtering process. Finally, the sample was transfered to the sample chamber which is kept under ultra high vacuum (UHV), typically $O(10^{-11})$ mBar. The manipulator used during these experiments was able to span temperatures from 10 K to 300 K. However, since the He consumption below 15 K was enormous most experiments were done at $T = 15$ K. The samples were always cooled to base temperature and then cleaved. Under this vacuum and with $T = 15$ K a high quality of the sample surface could be preserved for many days. A typical lifetime of a LSCO surface is $4-5$ days or more.

To cleave the LSCO samples Martin Maanson *et al.* [275] have designed a special tool that can be operated *in-situ*. This tool acts both as a sample holder and as a cleaver. The individual pieces of the cleaver are shown in figure 6.5. The cleaver is mounted with a razor blade which can be translated with an *in-situ* operational in-bus arm. The sample was mounted in the translation plane of the razor blade. When the razor blade is pressed toward a crystal facet parallel with the *c*-axis the

[†]We used EPO-TEK E4110 from POLYSCIENCE AG.

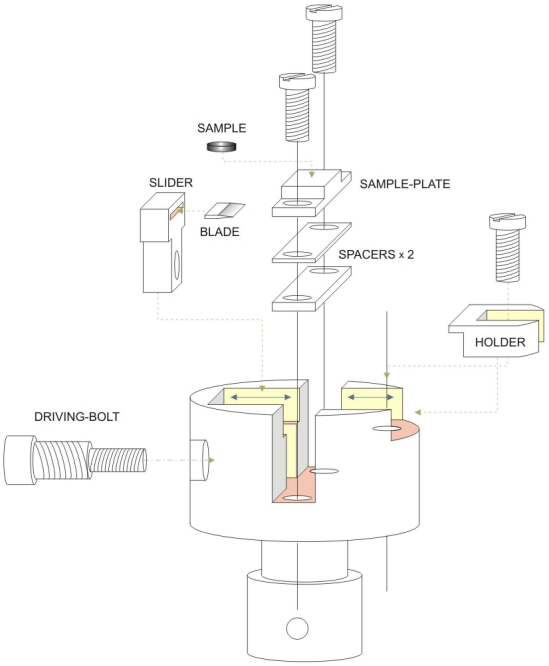

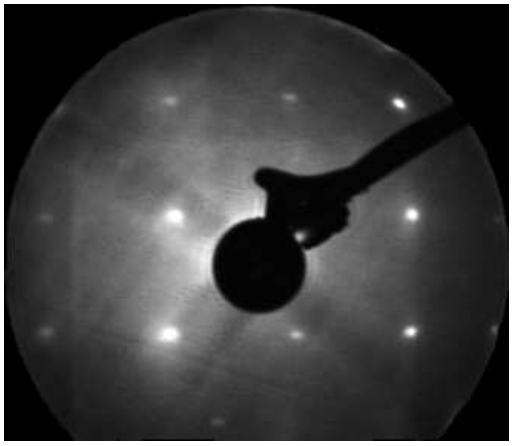

FIGURE 6.5: Schematic drawing of the cleaving tool used to cleave the samples in-situ [275].

FIGURE 6.6: LEED pattern of a cleaved LSCO $x = 0.105$ sample. The bright diffration spots indicate that the sample surface is of very good quality.

LSCO crystal cleaves in the ab-plane. The high quality of the cleaved surface was demonstrated from a Low-Energy Electron Diffraction (LEED) pattern of the surface, see figure 6.6.

6.2.2 Transformation from detector angles to k-space. In this paragraph, it will be described (i) how the instrument angles are translated into **k**-space, and (ii) how to correct the data for slight misalignment of the crystal compared to the manipulator coordinates.

The analyzer slit can be installed in two different configurations. Either with a *vertical* slit opening as shown in figure 6.7 or with a *horizontal* slit opening as shown in figure 6.8. Here the sample surface is the $x-y$ plane, and the azimuthal angle ϕ denotes the sample rotation around the normal of the sample surface.

Let us start with the vertical setup, where each spectrum is recorded with a constant azimuthal angle ϕ, and electrons are measured as a function of polar angle θ. In this setup the effective polar angle θ_e is simply the polar angle of the manipulator plus the detector angle β thus $\theta_e = \theta + \beta$.

In the horizontal setup the situation is more complicated since neither the effective azimuthal angle ϕ_e nor the effective polar angle θ_e is constant. From geometrical consideration one can deduce the effective azimuthal angle

$$\phi_e = \phi + \sin^{-1}\left[\frac{\tan(\beta)}{\sqrt{\sin^2(\theta)+\tan^2(\beta)}}\right], \tag{6.11}$$

and the effective polar angle

$$\theta_e = \sin^{-1}\left[\cos(\beta)\sqrt{\sin^2(\theta)+\tan^2(\beta)}\right], \tag{6.12}$$

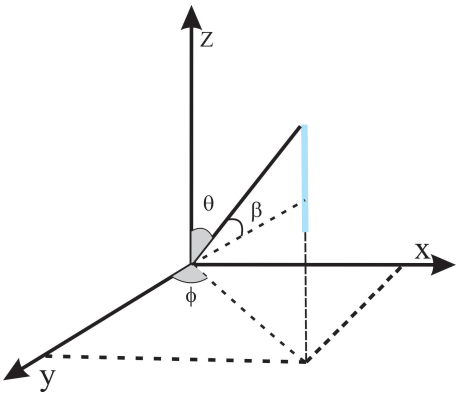

FIGURE 6.7: Schematic drawing of the vertical setup of SCIENTA analyzer. The blue line indicates the SCIENTA slit. The manipulator angles θ and ϕ are indicated by the gray arcs. The detector angles are given by β.

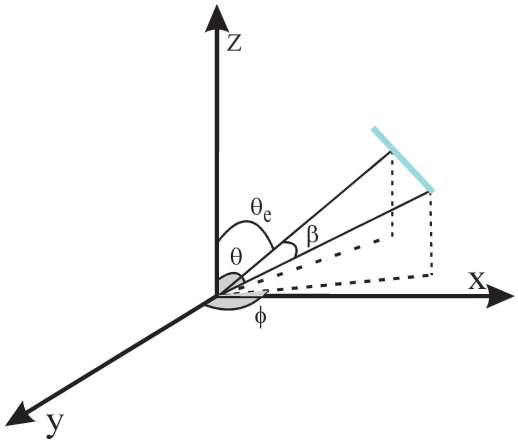

FIGURE 6.8: Schematic drawing of the horizontal setup. Blue line indicates the SCIENTA slit. The manipulator angles θ and ϕ are indicated with gray arcs. Detector angles are defined as β. θ_e is the effective polar angle for a given detector channel as discussed in the text.

where the meaning of β and θ is depicted in figure 6.8. Except for the data recorded on LSCO with $x = 0.17$, we used the horizontal setup.

If we now assume that the crystallographic axes are identical to that of the manipulator coordinate system shown in figure 6.8, the in-plane momentum (k_x, k_y) of a photoelectron with θ_e and ϕ_e is [251]

$$\begin{bmatrix} \hat{k_x} \\ \hat{k_y} \\ \hat{k_z} \end{bmatrix} = \begin{bmatrix} \cos(\phi_e) & -\sin(\phi_e) & 0 \\ \sin(\phi_e) & \cos(\phi_e) & 0 \\ 0 & 0 & 1 \end{bmatrix} \begin{bmatrix} \cos(\theta_e) & 0 & \sin(\theta_e) \\ 0 & 1 & 0 \\ -\sin(\theta_e) & 0 & \cos(\theta_e) \end{bmatrix} \begin{bmatrix} 0 \\ 0 \\ k_i \end{bmatrix} = \begin{bmatrix} \cos(\phi_e)\sin(\theta_e)k_i \\ \sin(\phi_e)\sin(\theta_e)k_i \\ \cos(\theta_e)k_i \end{bmatrix} \quad (6.13)$$

where $k_i = \sqrt{2m_e E_{kin}}/\hbar$. However, the crystal axes are not necessarily exactly identical to that of the manipulator axes. Here we define η as the angle between the z-axis in figure 6.8 and the c-axis of the crystal. The angle ζ defines the angle between x-axis in the coordinate system in figure 6.8 and the a-axis of the crystal. Correcting for the mismatch between the coordinate system of the crystal and the manipulator can be done by the following rotations [276]

$$\begin{bmatrix} k_x \\ k_y \\ k_z \end{bmatrix} = \begin{bmatrix} \cos(\zeta) & \sin(\zeta) & 0 \\ -\sin(\zeta) & \cos(\zeta) & 0 \\ 0 & 0 & 1 \end{bmatrix} \begin{bmatrix} \cos(\eta) & 0 & \sin(\eta) \\ 0 & 1 & 0 \\ \sin(\eta) & 0 & \cos(\eta) \end{bmatrix} \begin{bmatrix} \cos(-\zeta) & \sin(-\zeta) & 0 \\ -\sin(-\zeta) & \cos(-\zeta) & 0 \\ 0 & 0 & 1 \end{bmatrix} \begin{bmatrix} \hat{k_x} \\ \hat{k_y} \\ \hat{k_z} \end{bmatrix}. \quad (6.14)$$

From now on the data are represented in terms of k_x and k_y. A final remark is that the spectra were usually collected in the 2nd BZ. However, for convenience it is often presented as if it was in the 1st BZ.

6.2.3 Detector issues. All experiments presented here have been recorded with a modern Scienta 2002 electron analyzer. The new generation of electron analyzers are far more sophisticated than previous ones. With the modern multi-channel electron analyzers it is possible to simultaneously record electrons with different momenta. However, complexity is often followed by complications. One complication is that the detector efficiency can vary strongly across the channels. An example of this is shown in figure 6.9(a) which displays the raw ARPES intensities recorded on polycrystalline copper. Ideally the intensity should be constant for constant binding energy. However, as seen in figure 6.9(a), this is clearly not the case. In fact the intensity has a strong variation across the detector channels. To visualize this, the integrated intensities

$$I_{int}(n) = \sum_{E_B} I(E_B, n) \tag{6.15}$$

as a function of detector channel number n are shown in figure 6.9(e). The integrated intensity gives a good measure of the relative detector efficiencies. As can be seen from figure 6.9(e) the efficiencies can vary up to a factor of three. Knowing the relative detector efficiencies, a normalization of the detector intensities is possible

$$I_{norm.}(n, E_B) = \frac{I_{mea.}(n, E_B)}{I_{int}(n)}. \tag{6.16}$$

The result of the normalization is shown in figure 6.9(b). Now the intensities are approximately constant across the detector channels.

An other complication is that the kinetic energy position can vary across the channels. Figure 6.9(c) shows the intensity as a function of binding energy for one detector channel, indicated by the dashed white line in figure 6.9(a). This energy dependence of the intensity can be fitted to the Fermi-Dirac distribution $f(\omega)$, see the solid red line. From such a fit the chemical potential μ can be extracted. Figure 6.9(f) shows μ as a function of channel number and as seen in our system the variation from edge to edge of the detector can be up to 30 meV.

Knowing the chemical potential for each channel is now possible to calibrate the kinetic energy

$$E_B(n) = E_{kin}(n) - \mu. \tag{6.17}$$

The result of the efficiency normalization and the calibration of the kinetic energy is shown in figure 6.9(b). We see that the efficiency normalization worked satisfactorily since the intensity is now perfectly homogeneous across the detector channels. Second we now have that $E_B = 0 = E_F$ for all the detector channels. From now on all shown spectra have been normalized and calibrated with a relevant copper reference in the fashion described above.

6.2.4 Momentum and energy resolution. I will now discuss the momentum and energy resolution of the SIS instrument. Due to highly collimated beam the momentum resolution is generally very good. With $\hbar\nu \sim 50$ eV the momentum resolution is typically ~ 0.15 degrees corresponding to $\sim 1/100$ of a BZ. Therefore the momentum resolution is usually not a limitation for the experiments.

During the last three decades the energy resolution of the ARPES technique has improved by orders of magnitude [277, 278]. On the SIS instrument an energy resolution of about 10 meV or

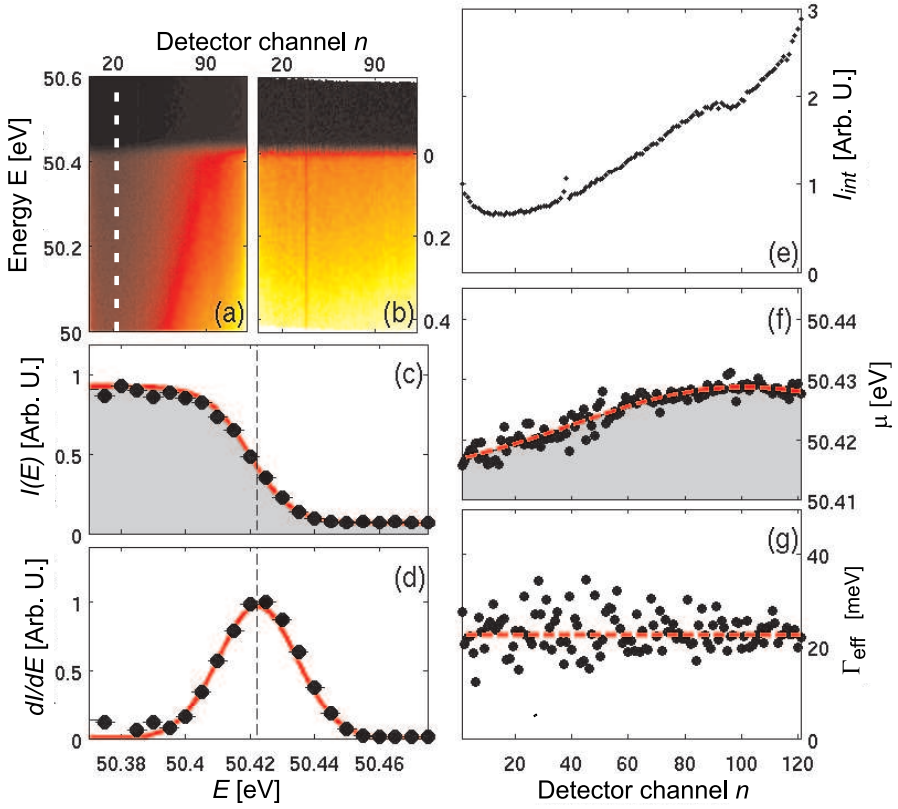

FIGURE 6.9: (a) Energy distribution map of spectra taken on polycrystalline copper. (b) Same spectra as (a) but corrected for detector efficiency and the chemical potential has been subtracted. (c) Energy distribution curve along the dashed white line in (a), the red line is a fit with a Fermi-Dirac function. (d) Derivative of the energy distribution curve shown in (c). (e) Detector efficiency of each channel. (f) Chemical potential for each detector channel. (g) Energy resolution of each channel. Dashed line indicates the average resolution.

less can be obtained. However this is at the cost of the photon flux. To get an idea of the energy resolution for a given setup, we look at the spectra from polycrystalline copper. Figure 6.9(d) shows dI/dE which is peaked at $E_{kin} = \mu$ and the width of the peak is the effective energy resolution Γ_{eff}. In figure 6.9(g) the resolution Γ_{eff} across the detector channels is shown. We typically use an energy resolution of $\Gamma_{\text{eff}} \sim 20 - 30$ meV since this is a good compromise between energy resolution and photon flux.

6.3 DATA ANALYSIS

Modern 2D electron analyzers provide the opportunity to collect data with a high density in both momentum and energy. The ARPES intensity can therefore be displayed as a function of momentum and binding energy as shown in figure 6.10(a). If we neglect for a moment possible matrix element effects, the 2D intensity plot $I(\mathbf{k},\omega)$ is a visualization of the spectral function $\mathcal{A}(\mathbf{k},\omega)$ plus an extrinsic background. The excitation spectra can now be analyzed via either the momentum distribution curves (MDC) or energy distribution curves (EDC). With this is meant that the ARPES intensity can be plotted either as a function of momentum at fixed binding energy or as a function of binding energy at fixed momentum. The two types of curves are shown in figure 6.10(b) and (c), respectively. This section is devoted to describe the advantage and disadvantage of the two methods. let us start by the MDC method.

6.3.1 MDC analysis. The advantage of MDC over EDC analysis is that the MDC peaks are symmetric and have a simple background. Ambiguities are not introduced due to the cutoff of the Fermi distribution function [265]. Under the assumption that matrix elements are neglectable the intensity of a MDC is related to the self-energy $\Sigma(\mathbf{k},\omega)$ by

$$I_\omega^{MDC}(\mathbf{k}) \propto \frac{\Delta k}{[\omega - \varepsilon_\mathbf{k} - \mathrm{Re}\Sigma_\omega(\mathbf{k})]^2 + \Delta k^2}. \tag{6.18}$$

with

$$\hbar v_\mathbf{k} \Delta k = 2\mathrm{Im}\Sigma(\mathbf{k}), \tag{6.19}$$

where $v_\mathbf{k}$ is the bare band velocity. When the inverse lifetime $\tau^{-1} \propto \mathrm{Im}\Sigma$ is independent of the momentum, $I_\omega^{MDC}(\mathbf{k})$ has a Lorentzian lineshape. The full width at half maximum (FWHM) Δk is then related to the inverse mean free path by $\ell = 1/\Delta k$. In table 6.1 the MDC FWHM Δk at the Fermi level close to the nodal point is given for $x = 0.145$ and $x = 0.22$. In the same table the mean free path ℓ is calculated from Δk. From our measurements a weak doping dependence of the mean free path was found. For $x = 0.22$, a mean free path $\ell \approx 50$ Å was measured and in the slightly underdoped $x = 0.145$, a shorter mean free path $\ell \approx 38$ Å was found.

The simple background of the MDC has the advantage that it is possible to fit both the MDC peak and the background. Doing this as a function of binding energy, it is possible to extract the background level. A systematic study by A. Kaminski *et al.* [279] revealed that the background is purely extrinsic and not related to the spectral function $\mathcal{A}(\mathbf{k},\omega)$. The MDC intensity can therefore be described by two components

$$I(\mathbf{k},\omega) \propto \mathcal{A}(\mathbf{k},\omega) + B(\mathbf{k},\omega), \tag{6.20}$$

where $B(\mathbf{k},\omega)$ is the extrinsic background. The two components are indicated by light gray and blue in figure 6.10(b). The background is identified by a fit to the MDC lineshape with a Lorentzian plus a linear component of the form $a + bk$ [279], where a and b are constants and k is the momentum along the cut. Doing the fits in a systematic fashion as a function of binding energy, a and b are obtained. Knowing $a(\omega)$ and $b(\omega)$, the background can be subtracted from the MDC peaks. Figure 6.11(a) shows a spectrum recorded on LSCO $x = 0.17$ before background subtraction. In the next panel, figure 6.11(b), the spectrum is shown after background subtraction. Finally, in

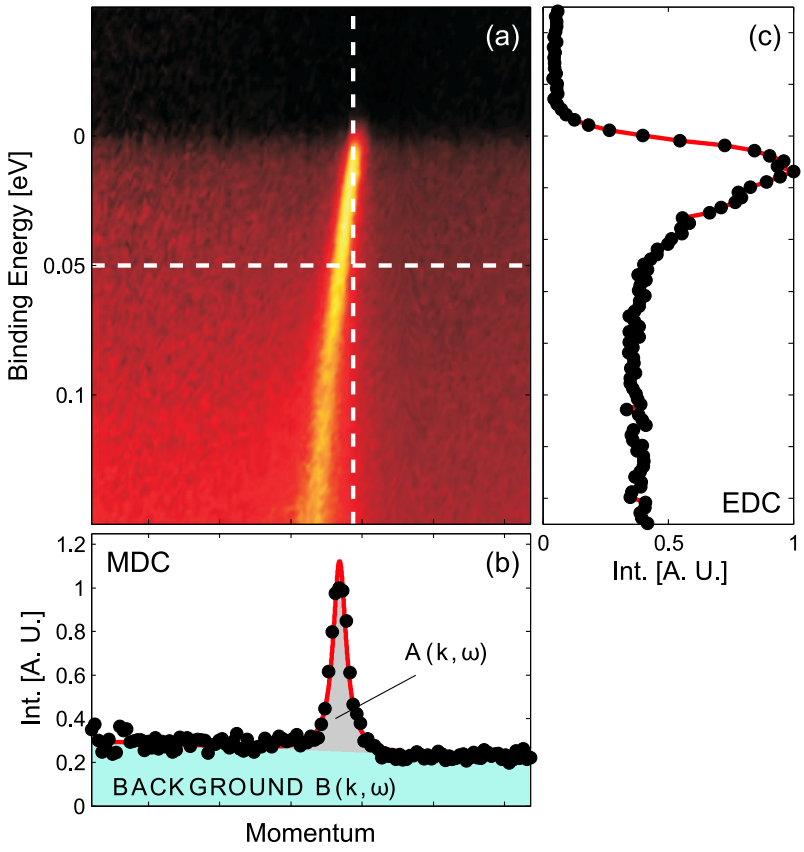

FIGURE 6.10: (a) ARPES intensity as a function of momentum and binding energy for a cut close to the nodal point on a $x = 0.145$ sample. (b) Momentum distribution curve (MDC) with constant binding energy $E = 0.05$ eV [dashed horizontal line in (a)]. The solid red line is a Lorentzian fit to the data. (c) Energy distribution curve (EDC) with constant momentum [dashed vertical line in (a)]. Here the red line is a guide to the eye.

order to better visualize the dispersion at high binding energy, one can normalize the maximum intensity at each binding energy, see figure 6.11(c).

Although A. Kaminski *et al.* [279] concluded that the background is purely extrinsic, this study was carried out at low energies $E < 0.2$ eV. At high binding energies $E \sim 0.5$ eV both extrinsic and intrinsic background scattering may be present. The intrinsic background could for example originate from the incoherent part of the spectral function. It is therefore possible that the high-energy background is composed of both an extrinsic and intrinsic background. Unfortunately, there is no obvious way to distinguish these two components. However, the above mentioned method to subtract background is still useful to illustrate the coherent part of $\mathcal{A}(\mathbf{k}, \omega)$. Throughout this thesis, the data are presented with as few manipulations as possible. Therefore if not explicitly mentioned the background procedure has not been performed.

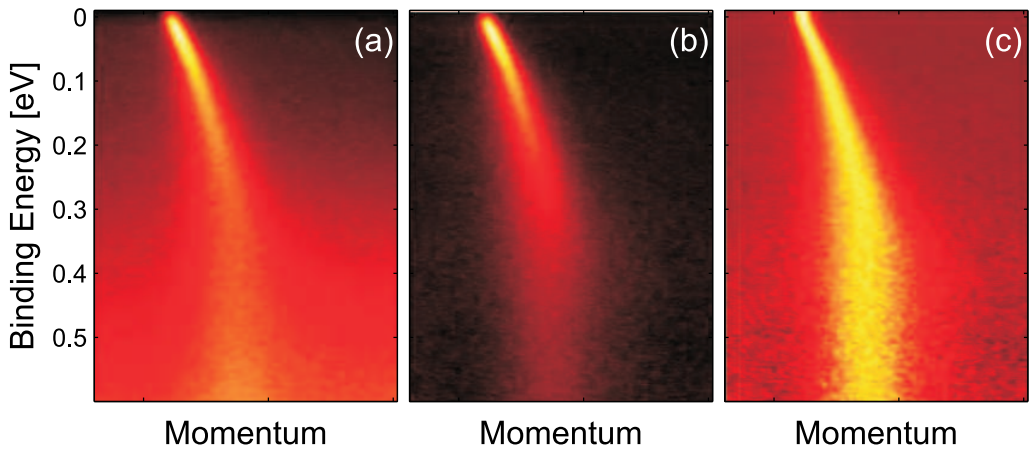

FIGURE 6.11: Three different ways to represent the same spectrum. (a) The energy and intensity have been calibrated. (b) A sloping background has been subtracted from the MDCs at each binding energy. (c) After background subtraction the intensities have been normalized to the maximum intensity at each binding energy.

6.3.2 EDC analysis. Traditionally, ARPES spectra were collected in point-by-point fashion with constant momentum using electron analyzers with pinhole aperture. This meant usually limited information of the momentum dependence and analysis was primarily done via energy distribution curves (EDC). Disregarding matrix element effects, the EDC can then be related to the self-energy $\Sigma(\mathbf{k},\omega)$ by

$$I_{\mathbf{k}}^{EDC}(\omega) \sim f(\omega)\frac{\mathrm{Im}\Sigma_{\mathbf{k}}(\omega)}{[\omega-\varepsilon_{\mathbf{k}}-\mathrm{Re}\Sigma_{\mathbf{k}}(\omega)]^2+\mathrm{Im}\Sigma_{\mathbf{k}}(\omega)^2}, \tag{6.21}$$

where $f(\omega)$ is the Fermi distribution. The EDC linewidth reflects the inverse lifetime, $\tau^{-1}(\omega) \sim |2\mathrm{Im}\Sigma(\omega)|$. However, the lifetime τ is usually not a constant function of ω. Therefore the EDCs have an asymmetric lineshape which is difficult to analyze. The background might also vary with the binding energy as discussed before. An other difficulty is related to the Fermi distribution $f(\omega)$ that influences the spectrum near the Fermi energy E_F. However, for the EDC with $\mathbf{k}=\mathbf{k}_F$, there exists a method to sum out the Fermi distribution [280]. The trick is to symmetrize the EDC in the following way

$$\begin{aligned} I_{sym}(\mathbf{k}_F,\omega) &= I(\mathbf{k}_F,\omega)+I(\mathbf{k}_F,-\omega) \\ &= I_0\mathcal{A}(\mathbf{k}_F,\omega)f(\omega)+I_0\mathcal{A}(\mathbf{k}_F,-\omega)f(-\omega) \\ &= I_0\mathcal{A}(\mathbf{k}_F,\omega)f(\omega)+I_0\mathcal{A}(\mathbf{k}_F,\omega)\left[1-f(\omega)\right] \\ &= I_0\mathcal{A}(\mathbf{k}_F,\omega). \end{aligned} \tag{6.22}$$

where I_0 is a constant. This mathematical operation is displayed in figure 6.12(a), using a spectrum of $x=0.22$ recorded at $T=15$ K close to the nodal point. The red and blue curves are $I(\mathbf{k}_F,\omega)$ and $I(\mathbf{k}_F,-\omega)$, respectively. The sum, $I_{sym}(\mathbf{k}_F,\omega)$, is displayed by the black curve. Now close to

Table 6.1: Nodal quasiparticle properties at $\omega = 0$ for $x = 0.145$ and $x = 0.22$. Δk, ℓ, Γ, and τ are the FWHM MDC linewidth, mean free path, FWHM EDC linewidth, and the lifetime, respectively. The mean free path and the lifetime were derived from the MDC and EDC FWHM by $\ell = 1/\Delta k$ and $\tau = \hbar/\Gamma$.

Compound	x	ϕ_{FS}	Δk [Å^{-1}]	ℓ[Å]	Γ [meV]	τ [fs]
$La_{2-x}Sr_xCuO_4$	0.145	44	0.027	38	31.0	21.3
$La_{2-x}Sr_xCuO_4$	0.22	40	0.0200	50	23.8	28

the Fermi level, it is reasonable to assume that the lifetime is approximately independent of the binding energy, *i.e.* $\mathrm{Im}\Sigma(\omega) = K$ where K is a constant. Under this assumption the lineshape of $I_{sym}(\mathbf{k}_F, \omega)$ is Lorentzian.

An example is shown in figure 6.12(b). Here, $I_{sym}(\mathbf{k}_F, \omega)$ is plotted for a spectrum of $x = 0.145$ taken at $T = 15$ K close to the nodal point. The solid red line is a Lorentzian fit to the data. The EDC FWHM is $\Gamma = 31$ meV corresponding to a lifetime of $\tau \approx 21$ fs.

Now, the energy resolution is not always good enough to resolve the excitation. In that case the $I_{sym}(\mathbf{k}_F, \omega)$ is a convolution of the spectral function $\mathcal{A}(\mathbf{k}_F, \omega)$ with the energy resolution $\mathcal{R}(\omega)$

$$I_{sym}(\mathbf{k}_F, \omega) = I_0 \mathcal{A}(\mathbf{k}_F, \omega) \otimes \mathcal{R}(\omega). \tag{6.23}$$

If we assume that the resolution function has a Gaussion lineshape, then $I_{sym}(\mathbf{k}_F, \omega)$ is a convolution of a Lorentzian and Gaussion which gives a Voigt profile [‡]. In figure 6.12(c), $I_{sym}(\mathbf{k}_F, \omega)$ of $x = 0.22$ is fitted to a Voigt profile. Here the Gaussion width was fixed by the energy resolution extracted from the copper reference. The Lorentzian FWHM was then found to be $\Gamma = 23.8$ meV corresponding to a lifetime of $\tau \approx 28$ fs.

The main conclusion of this section is therefore that there is a weak doping dependence of the nodal quasiparticle properties. The lifetime and the mean free path are longer in the overdoped region compared to the slightly underdoped part of the phase diagram. This result is consistent with a recent high resolution laser-excited angle resolved photoelectron spectroscopy study on Bi2212 [282].

6.4 LOW-ENERGY ELECTRONIC PROPERTIES

The low-energy electronic structures and interactions of high-T_c superconductors have been intensively studied by means of ARPES. The low-energy excitations are interesting to study because they underly many bulk properties. In this section, I will describe the doping evolution of the Fermi surface (FS) topology and the low-energy band dispersion.

6.4.1 Evolution of the Fermi surface with overdoping. There exist several methods to determine the Fermi surface from ARPES measurements [283]. Here we use the so-called MDC-method. This method simply looks at the maximum of a MDC which crosses through the Fermi

[‡]The same procedure was applied to the MDC analysis by D.V. Evtushinsky *et al.* [281].

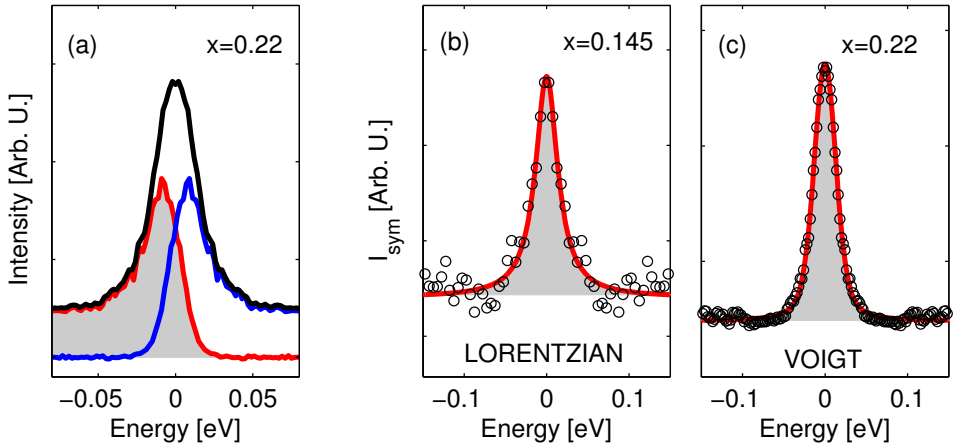

FIGURE 6.12: (a) Symmetrization method employed on $I(\mathbf{k}_F,\omega)$ for a spectrum taken close to the nodal point on $x = 0.22$. Red line is the raw EDC and the blue line is $I(\mathbf{k}_F,-\omega)$. The black line is the sum $I(\mathbf{k}_F,\omega)$+$I(\mathbf{k}_F,-\omega)$ in arbitrary units. (b) Nodal EDC symmetrized and fitted to a Lorentzian. (c) The symmetrized data from (a) fitted to a Voigt profile.

surface at $E = E_F$. The maximum spectral weight at E_F corresponds to the position of a single-particle pole. Therefore the **k**-position of the MDC maximum corresponds to $\mathbf{k}_F$. This method benefits from the simple Lorentzian lineshape of the MDCs. Notice also that with this method, the underlying Fermi surface can be determined for gaped systems.

First, the evolution of the Fermi surface topology as a function of overdoping will be described. Although measurements were done in the superconducting state we probe the Fermi surface since the superconducting gap Δ_{SC} in the overdoped part of the phase diagram is much smaller than the applied energy resolution. The Fermi surface was determined by making systematic cut through at least a quarter of the 2nd BZ. For slightly overdoped $x = 0.17$ samples the Fermi surface is centered around the Y-point [(1,1)-point], see figure 6.13. In the literature a FS centered around the Y-point is called a hole-pocket or an open FS. Going to $x = 0.22$, the FS is now centered around the Γ-point, see figure 6.14. Such a Fermi surface topology is denoted an electron-pocket or a closed FS. This evolution of the FS with overdoping is fully consistent with the existing ARPES literature [149, 260, 268, 284], see also figure 4.19. The topological shift from a hole-pocket to an electron-pocket at $x \approx 0.2$ observed by ARPES seems to be in contradiction with Hall coefficient measurements that find a sign change only for $x > 0.3$. This apparent discrepancy was recently reconciled by considering a combination of strong band anisotropy and basal-plane anisotropy in the elastic scattering rate, see A. Narduzzo *et al.* [285].

6.4.2 Collapse of the Fermi surface. The evolution of the FS as a function of underdoping is even more dramatic. In figure 6.15 the underlying FS of LSCO with $x = 0.145$ is shown. The topology is very similar to the FS observed for $x = 0.17$. For both compounds a spectral peak

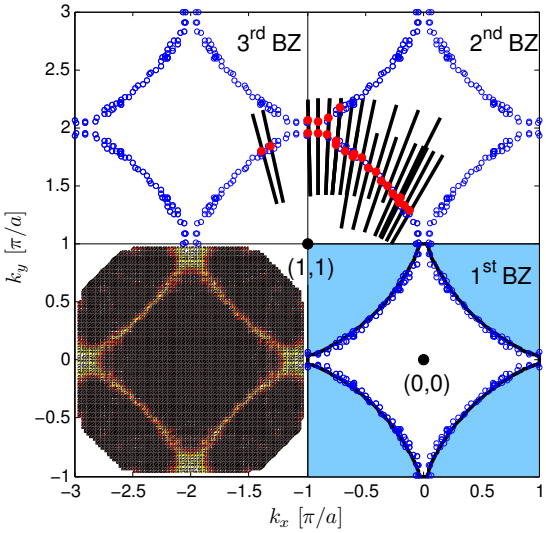

FIGURE 6.13: The Fermi surface of LSCO $x = 0.17$ is centered around the Y-point. The red points are extracted from the cuts shown by the black lines. Symmetrization with respect to tetragonal crystal structure is indicated by the blue points. The solid black line in 1st BZ is a tight-binding fit to determined Fermi surface and the blue shaded area is the Fermi surface volume x_{FS}. The lower left panel shows the distribution of intensity around the FS. Here the intensity is normalized such that the maximum intensity of all cuts is identical.

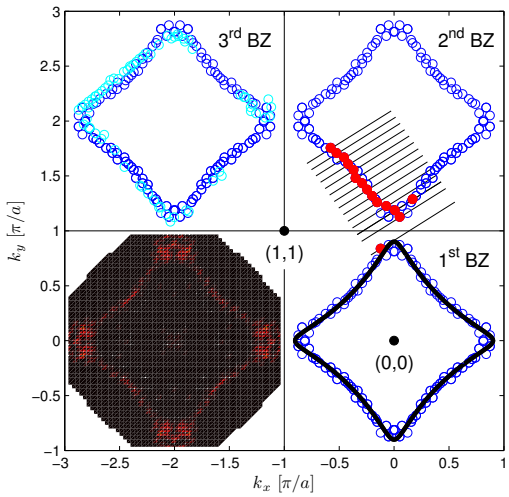

FIGURE 6.14: The Fermi surface of LSCO $x = 0.22$ is centered around the Γ-point. The color code is identical to figure 6.13. The light blue points in 3rd BZ are from a second experiment, showing that the FS is reproducible.

is observed for all momenta along the Fermi surface. However, for $x = 0.145$ we could identify the superconducting gap. The spectral peaks observed along the FS were therefore shifted away from the leading edge, as will be discussed in detail later. With the so-called MDC-method it is however still possible to determine the underlying FS. This is shown in figure 6.15 where the blue points indicate the underlying FS and the red points are the nodes where gapless excitations exist. If we now move further into the underdoped regime this situation changes dramatically. I am now going to discuss the FS of NDLSCO ($x = 1/8$) which has a strongly suppressed $T_c \approx 7$ K. The measurements were performed in the normal state with $T = 15$ K. In figure 6.16 the FS of NDLSCO is shown. The FS topology is still centered around the Y-point but spectral peaks are observed only in a small range of momenta around the nodal point, indicated by red points. The black points in figure 6.16 indicate momenta where no spectral peak could be observed and the so-called pseudo gap exists. The momentum dependence of the pseudo gap will be discussed later. The observation of the pseudo gap and an arc of gapless excitations in the underdoped part of the phase diagram is consistent with the ARPES data collected on many different cuprate materials including LSCO [286]. Measurements on LSCO suggest that the length of the Fermi arc decreases systematically with underdoping [150].

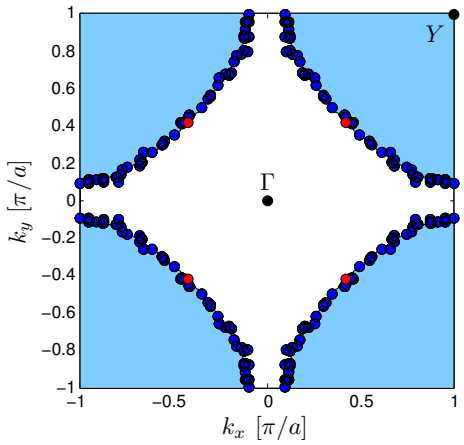

FIGURE 6.15: Underlying Fermi surface recorded in the superconducting state of LSCO with $x = 0.145$. The red points indicate the nodes where gapless excitations are observed. The blue points are the underlying Fermi surface and the blue shade area is the Fermi volume x_{FS}.

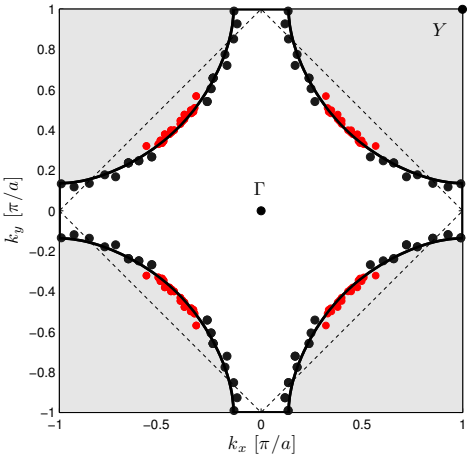

FIGURE 6.16: The Fermi surface of NDLSCO at $T = 15$ K. The FS is broken into arcs of gapless excitations situated around the zone diagonal indicated by red points. Black points are the Fermi surface underlying the pseudo gap.

6.4.3 Band dispersion. The low-energy electronic structure can be fitted to a tight-binding dispersion $\varepsilon_{\mathbf{k}}$, herein defined by

$$\begin{aligned}\varepsilon_{\mathbf{k}} = &-\mu - 2t[\cos(k_x a) + \cos(k_y a)] - 4t' \cos(k_x a)\cos(k_y a) \\ &- 2t''[\cos(2k_x a) + \cos(2k_y a)]\end{aligned} \tag{6.24}$$

where μ is the chemical potential, and t, t', and t'' denote nearest, second nearest, and third nearest neighbor hopping integrals on a square lattice, respectively. The ratios μ/t, t'/t, and t''/t, given in table 6.2, are chosen such that $\varepsilon_{\mathbf{k}} = 0$ fits the experimentally determined Fermi surfaces, see figures 6.13, 6.14, 6.15, and 6.16.

One fundamental result of Landau Fermi liquid theory is the Luttinger theorem [288] stating that the FS volume x_{FS} is equal to the number of particles x [289]. Assuming that the Luttinger theorem is valid, the hole number x can be estimated from the Fermi surface volume x_{FS}. However, there are several difficulties related to this estimate. First, in the strongly underdoped regime it is not clear how to extract an area from the Fermi arcs and it is not clear if Fermi liquid theory is valid in this region of the phase diagram. Second, in the overdoped regime the out-of-plane coupling becomes increasingly important, *i.e.* k_z is not necessarily neglectable [290]. For example angle magnetoresistance oscillation (AMRO) experiments have demonstrated the 3D character of FS in the overdoped region [291]. For a proper discussion of these issues, see T. Yoshida *et al.* [149]. Now, if we naively neglect these possible complications, we find that x_{FS} is slightly higher than the nominal doping x, see table 6.2. However, as shown in figure 6.17(a), x_{FS} scales approximately with x and is perfectly in agreement with a previous report [149].

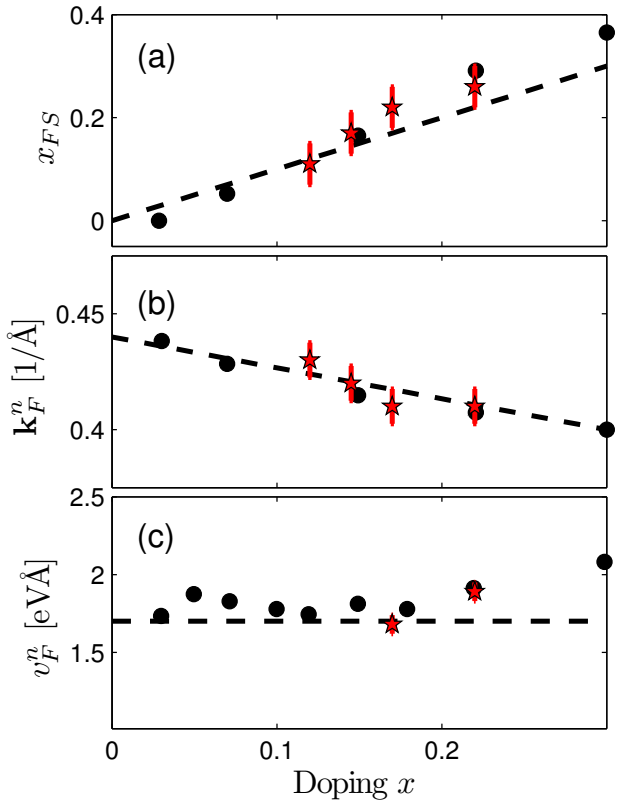

FIGURE 6.17: (a)-(c) Doping dependence of x_{FS}, $\mathbf{k}_F^n$, and v_F^n, respectively. The red points are extracted from the tight-binding fit to our data. The fit parameters are given in table 6.2. The black points in (a) and (b) are from T. Yoshida *et al.*[149] and the black points in (c) are from [287].

Although the fit parameters might not be unique, the tight-binding values obtained here are consistent with a previous report [149]. Herein, $\mathbf{k}_F^n$ denotes the Fermi momentum along the zone diagonal. From the tight-binding fit we can extract $\mathbf{k}_F^n$. In table 6.2 and in figure 6.17(b) it is seen that $\mathbf{k}_F^n$ for LSCO increases slightly with underdoping, consistently with ref. [149].

Now, I will turn to the Fermi velocity along the zone diagonal, v_F^n. According to a previous report [287] the nodal Fermi velocity is universal for the cuprates and independent of doping. In this mentioned report, v_F^n was extracted experimentally from cuts along the zone diagonal. However, a slight mis-alignment will introduce an error in the estimate. To overcome this problem I will here use, a new method to extract v_F^n.

In figure 6.18(a)-(c) the ARPES intensity recorded on $x = 0.22$ at $T = 15$ K is shown as a function of binding energy and momentum as indicated in the bottom inset. The data are of excellent quality since sharp peaks can be observed in both the EDCs and the MDCs, see also table 6.1. The dashed lines, in figure 6.18(a)-(c), are a tight-binding fit of $\varepsilon_{\mathbf{k}}$ (see Eq. 6.24) to the observed band dispersion. Remember that t', t'', and μ were already determined by the FS. Therefore, t is the only remaining fit parameter. With a single value of t, the fit describes the observed band over a broad part of the whole BZ.

Having determined all the tight-binding parameters, it is now possible to calculate the Fermi

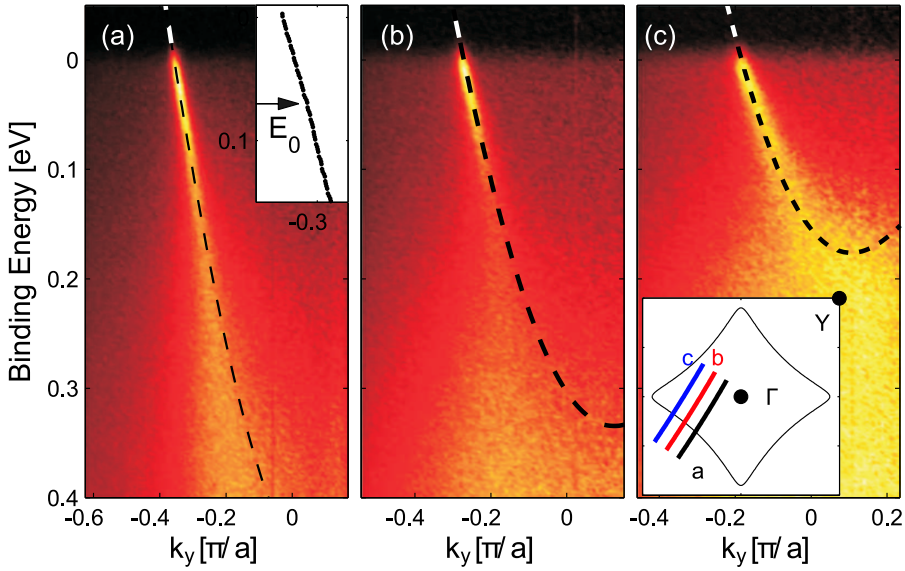

FIGURE 6.18: (a)-(c) Normalized ARPES intensity recorded on $x = 0.22$ as a function of binding energy and momentum taken along the three cuts shown in the bottom inset. The dashed lines represent a global tight-binding fit to the dispersion. The fitting parameters can be found in table 6.2.

.

velocity along the zone diagonal

$$v_F^n = \left(\frac{d\varepsilon_{\mathbf{k}}}{d\mathbf{k}} \right)_{k_x = k_y} . \tag{6.25}$$

This method was applied to $x = 0.17$ and $x = 0.22$, and the results are shown in figure 6.17(c) and in table 6.2. Good agreement with a previous report [287] on the Fermi velocity was found.

Then main conclusion of this section is therefore that the low-energy electronic structure that we observed in LSCO is in complete agreement with the literature.

Table 6.2: **Tight-binding parameters of hole doped single layer HTSC compounds.** From the tight binding parameters the nodal Fermi momentum and the Fermi surface volume can be extracted. t and the nodal Fermi velocity can be derived from the band dispersion. The values for LSCO are derived from data presented in this work. Similar values have been found by T. Yoshida *et al.*[149]. The values given for the Na-CCOC compounds are from the dissertation of K.M. Shen [276].

Compound	x	T_c [K]	t [eV]	t'/t	t''/t	μ/t	$\mathbf{k}_F^n$ [$\frac{\pi}{a}$]	x_{FS}	v_F^n [eVÅ]
NDLSCO	0.12	7	-	-0.136	0.068	0.6	0.43	0.11	-
$La_{2-x}Sr_xCuO_4$	0.145	36	-	-0.125	0.078	0.68	0.42	0.15	-
$La_{2-x}Sr_xCuO_4$	0.17	36	0.165	-0.144	0.072	0.84	0.41	0.22	1.7
$La_{2-x}Sr_xCuO_4$	0.22	26	0.184	-0.136	0.068	0.86	0.41	0.26	1.9
Na-CCOC	0.1	-	-	-0.276	0.162	0.27			-
Na-CCOC	0.12	-	-	-0.227	0.168	0.486			-

Compound	T_c [K]	T_c^{max} [K]	$\mathbf{k}_F^n$ [π/a]	t'/t	Ref.
Hg1201	96	98	0.374	0.249	[292]
Tl2201	$\sim$25	93	0.357	0.251	[293]
Bi2201	35	35	0.367	0.204	[292]

6.5 SUPERCONDUCTING GAP AND PSEUDO GAP IN LSCO

This section is devoted to the superconducting gap Δ_{SC} and the pseudo gap Δ^* in the underdoped region of LSCO. For underdoped samples, an energy gap persists above T_c [44, 262, 263]. This so-called pseudo gap Δ^* is most prominent in the $(\pi,0)$ region of the Brillouin zone, giving rise to a gapless arc of states centered around the zone diagonal known as a Fermi arc [280]. How the gap evolves from the superconducting state to the pseudo gap phase remains one of the most important questions being debated in the cuprates [62].

6.5.1 Two-gap secnario. It has been suggested that the superconducting gap exists only on the Fermi arcs, and thus is distinct from the pseudo gap [294]. This 'two-gap' scenario has been supported by recent ARPES studies on heavily underdoped Bi2212 [252, 295], as well as on optimally doped $La_{2-x}Sr_xCuO_4$ (LSCO) [296] and $Bi_2Sr_2CuO_6$ (Bi2201) [297]. In these studies, below T_c sharp spectral peaks are only observed along the arc, whereas the states in the region around the $(\pi,0)-(\pi,\pi)$ Fermi crossing (the antinode) remain incoherent just as above T_c. Moreover, the size of the energy gap in the antinodal region is significantly larger than that expected from a simple extrapolation of the gap from the arc.

The two-gap scenario has also been supported by Raman spectroscopy [255]. With use of different polarization of the light one can either probe the antinodal region or the nodal region. It was found that the gap in the antinode increases with underdoping while the nodal gap decreases [255, 298]. A theorectical describtion of this opporsite trend of the nodal and antinodal gap by M. Aichhorn *et al.*[299] emphasizes that the above mentioned Raman and ARPES studies can also be understood by a single gap scenario.

6.5.2 Single-gap scenario. This brings us to a second interpretation where the pseudo gap is a remnant of the superconducting gap. Hence the pseudo gap is considered as a precursor to superconductivity. In this picture, SC is destroyed by fluctuations of the SC order in the underdoped region. The pseudo gap phase above T_c is a state which has no long-range phase coherence but with local pairing. The pseudo gap therefore reflects the pairing strength. This view has been supported by several ARPES experiments. For example, T. Valla *et al.* [47] have observed, by means of ARPES and STM/STS, a d-wave gap in LSCO and LBCO. The gap amplitude is largest at $x = 1/8$ where superconductivity is strongly suppressed. Thus the d-wave gap shape persists even when superconductivity is completely suppressed. A recent study of the pseudo gap in Bi2212 also provides evidence for a d-wave shaped gap however only for $T \to 0$ K [300]. The exact momentum dependence of the pseudo gap is therefore still debated.

6.5.3 Motivation. The evolution of the superconducting gap with underdoping is far from being settled. The same can be said about the interpretation of the pseudo gap. Given the very different nature of the above mentioned scenarios, it should be possible to perform experiments to distinguish between them. Experimental concensus about the superconducting gap and the pseudo gap would strongly restrict the possible theories of high-T_c superconductors. This motivated us to study the superconducting gap and the pseudo gap in the underdoped region of LSCO.

Now, if this problem is so important, a reader might ask: why have these experiments not been done yet? The fact is that there exists little literature about the Δ_{SC} and Δ^* in the underdoped region

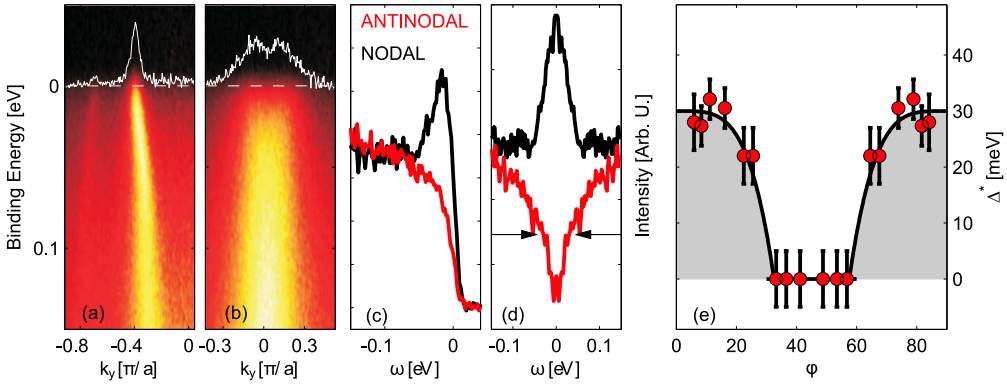

FIGURE 6.19: (a) and (b) ARPES spectra taken close to the nodal and antinodal point, respectively. The white curves are the MDCs at E_F. (c) and (d) Raw EDCs and symmetrized EDCs at $\mathbf{k}_F$ for the spectra shown in (a) and (b). (e) Angular dependence of the gap.

of LSCO. The reason for this might be related to the following facts. First of all, the T_c and Δ_{SC} are much lower in LSCO compared to the much studied Bi2212 compound. This means that a much better energy resolution is required. Second, the matrix elements in LSCO are different from, for example, Bi2212. It is an experimental fact that matrix element effects attenuate strongly the signal in the 1st Brillouin zone (BZ) in LSCO. Or in other words the ARPES signal is much stronger in the 2nd BZ. The best instrumental energy resolution is obtained with low-energy photons $\hbar\nu = 20$ eV. However, with this setup only momenta in the 1st BZ are accessible. Since high resolution is obtained at the cost of intensity, this setup suffers from both matrix element effects and low photon flux. This is probably the reasons why the superconducting gap has not yet been explored in great detail by ARPES in the LSCO compounds.

6.5.4 Pseudo gap in NDLSCO. Now, let us start by discussing the pseudo gap in NDLSCO. This compound has a strongly suppressed superconducting transition temperature ($T_c \approx 7$ K). The ARPES experiments are done at $T = 15$ K well above T_c. The spectra are therefore collected in the so-called pseudo gap phase. It was previously shown how the Fermi surface of this compound breaks into Fermi arcs, see figure 6.16.

In figure 6.19(a) and (b), ARPES spectra collected close to the nodal and antinodal point are shown. The raw EDCs with $\mathbf{k} = \mathbf{k}_F$ for the two spectra are shown in figure 6.19(c). The nodal spectrum is characterized by a sharp spectral peak and the leading edge reaches E_F. In contrast, the antinodal spectrum shows no evidence of a spectral peak and the leading edge is shifted away from E_F. The symmetrized EDCs are shown in figure 6.19(d). For near nodal spectrum a Lorentzian peak at E_F with a FWHM of 48 meV was found. The symmetrized EDC of the antinodal spectrum is on the other hand characterized by a minimum at E_F. An inflection point could be observed as indicated by the arrows in figure 6.19(d). Next, I follow Tanaka *et al.* [252] and define the pseudo gap by the position in energy of this inflection point. In figure 6.19(e), the momentum dependence of the pseudo gap is shown. The pseudo gap exists around the $(\pi, 0)$ region and vanishes on the arc where gapless excitations exist.

Our observation of a pseudo gap with an amplitude of ~ 30 meV is in good agreement with what has been reported in LBCO $x = 1/8$ [47]. However, a d-wave shaped pseudo gap as reported in LBCO $x = 1/8$ [47] was not observed. Instead a Fermi arc with clear spectral peaks is observed. On this arc the pseudo gap is zero with in the experimental uncertainty. Thus the pseudo gap that we observe resembles more the pseudo gap observed in the normal state of Bi2212 [300].

6.5.5 Superconducting gap in $x = 0.145$. Now let us turn to discuss the superconducting gap. In contrast to NDLSCO, the Fermi surface of $x = 0.145$ was characterized by the existence of spectral peaks throughout the whole Brillouin zone. Although this sample is slightly underdoped, it was verified by means of μSR and neutron scattering that no static magnetic order is observed down to $T = 70$ mK in zero field. This means that our $x = 0.145$ sample does not contain any magnetic contamination related to the $x = 1/8$ phase and that superconductivity does not compete with static magnetic order.

In order to resolve the superconducting gap high resolution and good statistics are required. For this study, the energy resolutions were 17 meV and 12 meV for the high-flux and high-resolution measurements, respectively. Data acquisition was done with a constant temperature $T = 12$ K.

Let us start by inspecting the nodal and antinodal spectra. In figure 6.20(a) and (b) the ARPES intensity is shown as a function of binding energy and momentum $\mathbf{k}$, along cuts through the nodal and antinodal points, respectively. The nodal spectrum is characterized by a sharp peak and the leading edge of the energy distribution curve (EDC) at $\mathbf{k}_F$ reaches the Fermi level E_F. The MDC linewidth are much broader in the antinodal spectrum and the leading edge of the EDC at $\mathbf{k}_F$ is shifted away from E_F due to the presence of an energy gap Δ. This is better illustrated by the so-called symmetrization method, see section 6.3.2. In figure 6.20(c) the symmetrized EDCs at $\mathbf{k} = \mathbf{k}_F$ are shown for the nodal (blue points) and the antinodal (red points). The nodal curve has a maximum at E_F, in contrast to the antinodal curve which is minimum at E_F. This observation unambiguously demonstrates the existence of a gap in the antinodal spectrum.

Next, in order to study the gap in a systematic fashion as a function of momentum, a series of spectra were collected with momenta ranging from the nodal point to the antinodal point. This is shown in figure 6.21 where the energy distribution maps (a) to (g) are indexed by number from 1 to 7 in the bottom right panel [figure 6.21(h)]. Due to symmetry of the electronic band, spectra 3 to 7 contain two branches. To distinguish between these two branches the EDCs are presented in red and black.

The EDC at $\mathbf{k} = \mathbf{k}_F$ for these seven spectra are presented in figure 6.22(b). To determine the superconducting gap, we 'symmetrize' the EDCs at $\mathbf{k}_F$ to effectively eliminate the Fermi function from the measured ARPES spectra [280], see figure 6.22(a). At the antinode, the symmetrized EDC shows two sharp peaks with a clearly defined gap, see figure 6.20. Moving from the antinode toward the node along the underlying Fermi surface, the separation between the two peaks becomes smaller, and the spectral weight at zero energy fills in, but a two-peak structure is always evident, even for EDC 3 where the gap and spectral width are comparable. Closer to the node, the spectral gap continues to decrease, and finally, when the node is reached, a single peak in the symmetrized EDC is seen (EDC 1).

In order to perform a more quantitative analysis of the superconducting gap, we use a simple

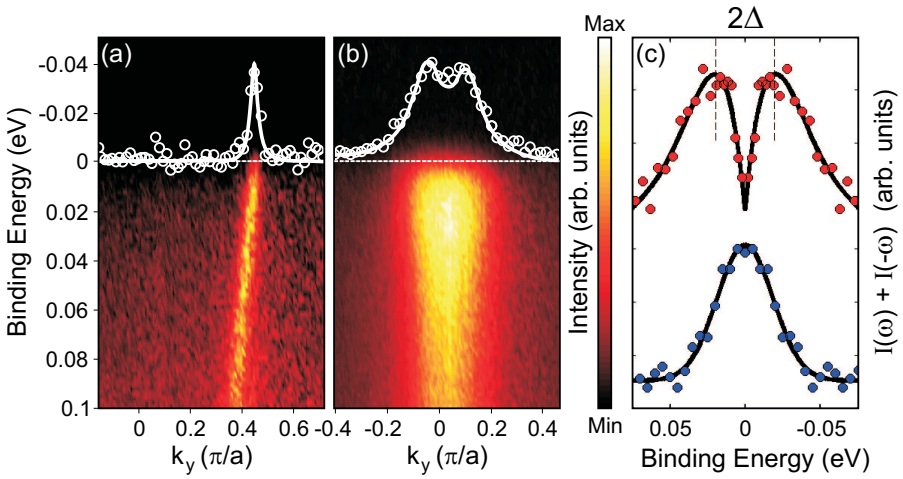

FIGURE 6.20: (a) and (b) ARPES intensity, recorded on $x = 0.145$, for nodal and antinodal cuts, respectively. The white points are the MDC at E_F. The intensity ratio between nodal and antinodal is $\sim 1/3$. (c) Symmetrized EDCs for nodal direction (blue) and antinodal direction (red) at $\mathbf{k} = \mathbf{k}_F$.

form for the self-energy that was shown to be successful in modelling ARPES data [301]

$$\Sigma(\mathbf{k}_F, \omega) = -i\Gamma_1 + \frac{\Delta^2}{\omega + i\Gamma_0} \tag{6.26}$$

which is then used to calculate the spectral function

$$\mathcal{A}(\mathbf{k}_F, \omega) = \frac{1}{\pi} \frac{\mathrm{Im}\Sigma}{(\omega - \mathrm{Re}\Sigma)^2 + (\mathrm{Im}\Sigma)^2}. \tag{6.27}$$

This is then convolved with the experimental resolution and fitted to the symmetrized EDC. Here Γ_1 is the single-particle scattering rate and Γ_0 is related to the inverse pair lifetime. The fitted curves are plotted as solid lines in figure 6.22(a). The best fit was achieved at the antinode where the separation of the two peaks is the largest, with $\Delta = 13.8 \pm 1.5$ meV, $\Gamma_1 = 38 \pm 3$ meV, and Γ_0 is negligibly small (less than 0.1 meV). The linewidth parameters are similar to those reported earlier for Bi2212 in the superconducting state [301]. The negligibly small value of Γ_0 indicates that the gap at the antinode is associated with pairs which have a quasi-infinite lifetime in the superconducting state. Moreover, the variation of the amplitude of the gap follows a simple *d*-wave form over the entire Fermi surface, see figure 6.22(e).

We now address the issue about the existence of the pseudo gap above T_c in LSCO ($x = 0.145$) samples. Figure 6.22(b) shows EDCs taken at 41 K along the underlying FS and compare them with those taken at 12 K. While at the node the EDC at 41 K is still characterized by a sharp spectral peak, the EDCs for the antinodal region are characterized by broad peaks with a suppression of spectral weight relative to those below T_c. The symmetrized EDCs (figure 6.22c) clearly show that above T_c there is a gap in the electronic excitation spectra in the antinodal region and there

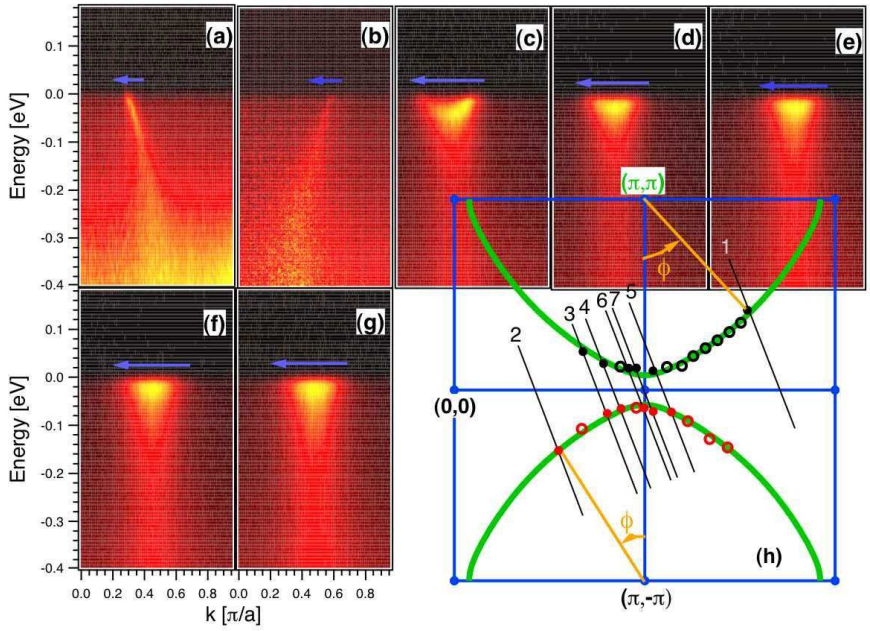

FIGURE 6.21: ARPES intensities along momentum cuts that cross the Fermi surface (a) at the node, (b) to (f) between the node and the antinode, and (g) at the antinode. The corresponding cuts 1 – 7 are indicated in (h). The circles in (h) are the Fermi surface determined from our measurements, while the solid lines are the Fermi surface from a tight-binding fit to our data.

is a Fermi arc along which the excitation spectra are gapless. The maximal size of the pseudo gap as extracted from the fits by using Eqs. 6.26 and 6.27 has a similar amplitude to that of the superconducting gap (figure 6.22(e)). It should be noted that the determined pseudo gap is much smaller than that reported in Refs. [150, 296].

Our ARPES results on LSCO for $x = 0.145$ are inconsistent with a gap having two components in the superconducting state, namely, a superconducting gap along the Fermi arc and a pseudo gap in the antinodal region with a higher energy scale as seen in previous photoemission studies of LSCO [150, 296], as well as optimally doped Bi2201 [297]. The first difference is that we observe sharp spectral peaks along the entire underlying Fermi surface, while spectra in these other studies are broad in the antinodal region. In figure 6.22(b) one can see that at an intermediate Fermi angle, the EDCs from Ref. [296] cross over from having a sharp spectral peak nearer the node to having a very broad spectrum nearer the antinode. The second difference concerns the momentum dependence of the energy gap. In the arc region, the gaps from all of these studies follow a simple *d*-wave form. But in the antinodal region, the gaps in the other ARPES studies cross over to a large pseudo gap at the same location where the sharp spectral peak disappears. But in our case, the sharp spectral peak remains and the gap continues to follow the simple *d*-wave form, with a maximum value of 14 meV at the antinode. This is most easily appreciated in figure 6.22(e) where

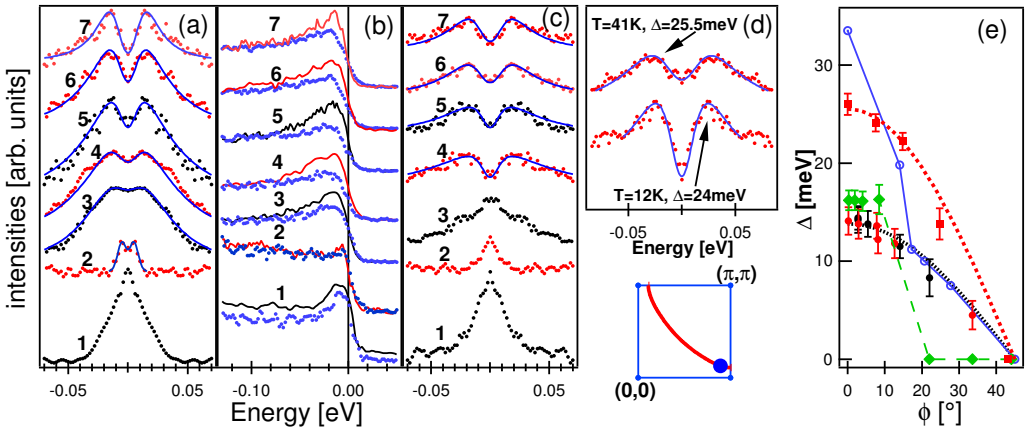

FIGURE 6.22: (a) and (c) Symmetrized EDCs for $x = 0.145$ at various $\mathbf{k}_F$ from the antinode (top) to the node (bottom) (each curve is offset for clarity) at 12 K and 41 K, respectively. The corresponding $\mathbf{k}_F$ from cuts 1 – 7 are indicated in Fig. 1(h) by filled circles. The $\mathbf{k}_F$ for cuts 1, 3, and 5 are on the upper FS curve, and the rest are on the lower FS curve. The solid lines are fits using Eqs. (1) and (2). (b) The EDCs at 12 K (solid lines) and at 41 K (dotted lines) from which the symmetrized EDCs in (a) and (c) are obtained. (d) Symmetrized EDCs for $x = 0.105$ at the $\mathbf{k}_F$ shown below the panel. (e) The superconducting gaps for $x = 0.105$ (filled squares), the superconducting gaps (filled circles) and the pseudo gaps for $x = 0.145$ (diamonds connected with a dashed line) from the fit as a function of the Fermi surface angle ϕ indicated in Fig. 1(h), with the dotted lines the simple d-wave gap $\Delta_{max}|\cos(2\phi)|$ with Δ_{max} = 13.8 meV and 25.5 meV, respectively. The open circles are the gaps determined by Terashima *et al.* for a LSCO sample with $x = 0.15$ [296].

we compare our gap anisotropy to that of Terashima *et al.* on a similarly doped ($x = 0.15$) LSCO sample [296].

The results on underdoped LSCO $x = 0.145$ is further supported by our ARPES results on more underdoped LSCO ($x = 0.105$). As for the $x = 0.145$ samples, our studies reveal: (i) the symmetrized EDCs near the antinode below (above) T_c are characterized by sharp (broad) peaks (figure 6.22(d)), (ii) the maximal gap in the electronic excitation spectra below and above T_c has a similar amplitude, and (iii) the anisotropy of the energy gap in the superconducting state has a simple d-wave form (Fig. 3(e)). In addition, we find that the maximal gap for $x = 0.105$ is almost twice that of $x = 0.145$. This increase in the energy gap with underdoping follows the same trend as previously observed in Bi2212 [250, 251].

This trend of the (π,0) gap as a function of underdoping is also displayed in figure 5.24. As discussed in chapter 5 several ARPES experiments [242, 243, 252] have provided evidence for a rounding of the gap nodes as a function of underdoping. This rounding of the gap nodes leads to a near nodal gap that decrease with underdoping, see figure 5.24. Effectively this leads to an opposite dependence of the $(\pi, 0)$ gap and the gap near the nodes. Naively this could be interpreted in terms of two distinct energy scales. However, Aichhorn *et al.* [299] have recently demonstrated that the opporsite dependence of the gap function can be reconciled with a single gap picture.

From our measurements on LSCO it is difficult to conclusively demonstrate whether there is a rounding or not of the gap node. To resolve this issue a specially dedicated experiment with an

improved energy resolution is probably required.

6.5.6 Conclusions. To summarize, the **k**-dependence of the normal state pseudo gap and the superconducting gap were investigated in NDLSCO and LSCO with $x = 0.105$ and $x = 0.145$.

The amplitude of the antinodal pseudo gap of NDLSCO was found to be approximately 30 meV consistently with a previous report on the pseudo gap of LBCO $x = 1/8$. However, the pseudo gap does not have a simple d-wave shape as was observed on LBCO $x = 1/8$. Instead the pseudo gap vanishes on a Fermi arc that is characterized by gapless excitations. This observation compares well with the pseudo gap observed in the normal state of Bi2212.

Next, a simple d-wave shape of the superconducting gap was observed in LSCO with $x = 0.105$ and $x = 0.145$. The amplitude of the antinodal gap was estimated to be ~ 25 meV and ~ 13 meV, respectively. The pseudo gap of LSCO $x = 0.145$ was found to exist only near the (π,0) point as in NDLSCO. As discussed this result is in severe contrast to a very recent study of the gap in LSCO with $x = 0.15$ [296]. However, as for NDLSCO our results are in good agreement with previous observations of the gap in Bi2212 [250, 251].

Wether the data should be interpreted in favor of the single-gap or the two-gap scenario is still an open question. It remains unclear if the gap nodes in LSCO exhibits a rounding as a function of underdoping as reported in Bi2212. Very high resolution measurements would be an obvious next step to clarify this issue. With the presented data is it unfortunately also impossible to give a conclusive answer to the nature of the pseudo gap. Our observation of a pseudo gap that vanishes on an arc of gapless excitations can be interpreted in favor of both competing order parameters and in terms of a precursor for superconductivity.

6.6 ENERGY SCALES IN THE CUPRATES (KINKOLOGY)

Single-particle excitations are characterized by an energy E and a momentum $\mathbf{k}$, which are related through the dispersion $E_{\mathbf{k}}$. A coupling to collective excitations may lead to abrupt changes (kinks) in the dispersion. Typically a kink appears as a sudden change in the band velocity. In a simple picture one can understand the kink as a sudden mass renormalization of the single-particle. When the electrons become heavier the band velocity slows down. The observation of a kink in the dispersion may carry important information about how electrons couple to other excitations. Recently, it has been demonstrated theoretically that a kink can also appear due to pure electronic interactions alone [302]. Thus the observation of a kink is not necessarily an evidence of an electron-boson coupling.

Kinks in the band dispersion appear in many different systems such as manganites [303], kish graphite [304], and metal surfaces [305]. In this section, I will discuss the kinks observed in the band dispersion of cuprates. This is a subject that has been heavily studied and debated, because in many theories superconductivity is mediated by an electron-boson coupling.

6.6.1 Low-energy kink. The existence of a low-energy kink, $E_0 \approx 70$ meV in the nodal dispersion is well established in hole doped cuprate materials [287, 306–310]. This nodal kink E_0 has been observed in large number of hole doped materials including LSCO, Bi2212, and Bi2202 [307]. Independently of materials the kink E_0 appears in the range 50-90 meV. The kink structure is observed both in the nodal dispersion and in the scattering rate [306, 307, 311, 312]. Finally, the kink is present for wide range of doping [287, 307] and a general trend is that the kink effect is stronger in the underdoped region and gets weaker with increasing doping [273].

Here I present the kink as it appears in our data recorded on overdoped samples. Figure 6.23(a) shows the MDC dispersion for two spectra recorded on $x = 0.17$ with momenta as indicated in the inset. Consistently with the above mentioned literature a clear change in the dispersion is observed at $E_0 \approx 70$ meV. Notice that both below and above E_0 the band velocity is approximately constant. Thus the kink can be described as a change in the band velocity. To characterize the kink more quantitatively, we define

$$\mathcal{Z}_k = \frac{v_L}{v_H} \tag{6.28}$$

where v_L and v_H are the low-energy ($\omega < E_0$) and high-energy ($\omega > E_0$) velocities. (Here I use the notation v_L for the Fermi velocity instead of v_F, in order to distinguish clearly between v_L and v_H.)

On the most basic level, $\mathcal{Z}_k$ is just a factor that indicates the strength of the kink, *i.e.* how much the velocity changes. However, $\mathcal{Z}_k$ might be a more meaningful constant. According to M. Randeria *et al.* [313], $\mathcal{Z}_k$ is the quasiparticle spectra weight.

Now let us turn back to figure 6.23(a). The dispersion shown in black is taken close to the nodal point while the dispersion in red is in between the nodal and antinodal point. For this off-nodal cut (red points) the effect of the kink is much stronger than for the nodal cut (black points). To support this observation, let us examine the MDC linewidth for the same two spectra, see figure 6.23(b). For the nodal cut only a weak change in the ω-dependence of the MDC linewidth is observed at E_0. By contrast, for the off-nodal spectrum a clear effect of the kink is seen at $E_0 \approx 70$ meV. I therefore argue that the strength of the kink is momentum dependent.

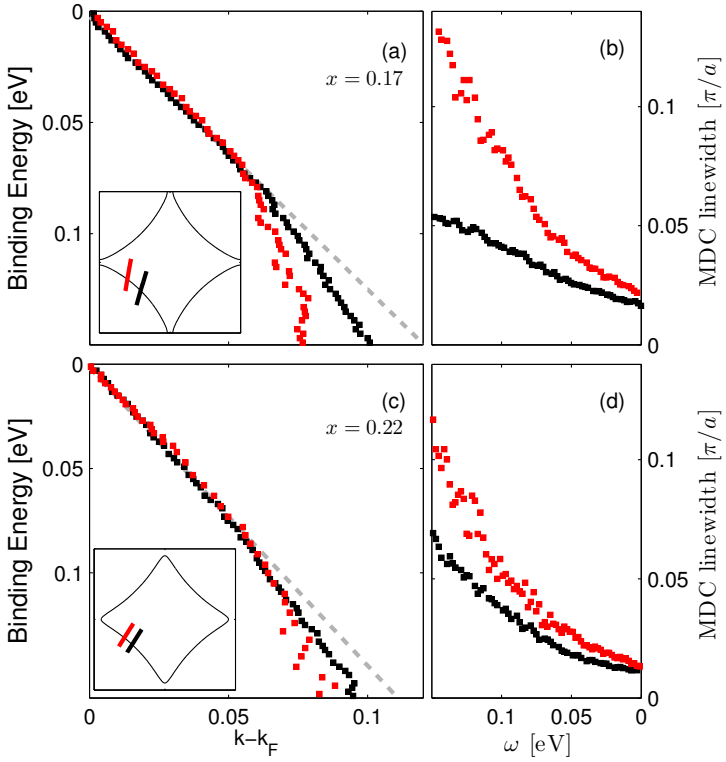

FIGURE 6.23: (a) and (c) Dispersion of the MDC peak for spectra with momenta as indicated in the respective bottom inset. The data are recorded on $x = 0.17$ and $x = 0.22$, respectively. (b) and (d) The MDC linewidth as a function of binding energy for the same spectra shown in (a) and (c).

For a more overdoped sample $x = 0.22$, the kink is less pronounced, see figure 6.23(c), consistently with existing literature [273]. Although less visible, the effect of the kink is again stronger for off-nodal spectrum. The MDC linewidth for the two spectra is shown in figure 6.23(d). Remark that the ω-dependence of the linewidth is no longer linear as for $x = 0.17$. Instead a ω^n-dependence with $n > 1$ was found (the exact ω-dependence will be discussed in a later section). From the linewidth as presented in figure 6.23(d), it is difficult to extract any kink feature for the cut close to the nodal point. For the off-nodal cut a change in the ω-dependence is seen around $E_0 \approx 70$ meV.

Let us now turn to the momentum dependence of the kink. In figure 6.24 the ϕ-dependence of $\mathcal{Z}_k$ is shown for $x = 0.17$ and $x = 0.22$. As expected the factor $\mathcal{Z}_k$ is larger for $x = 0.22$ than for $x = 0.17$. For both doping compositions a clear momentum dependence is observed. Moving away from the nodal point the effect of the kink becomes stronger, resulting in a reduced value of $\mathcal{Z}_k$.

While there is a degree of concensus on the experimental observations of the nodal kink E_0, the mechanism behind the kink is still strongly debated. So far it has been difficult to distinguish

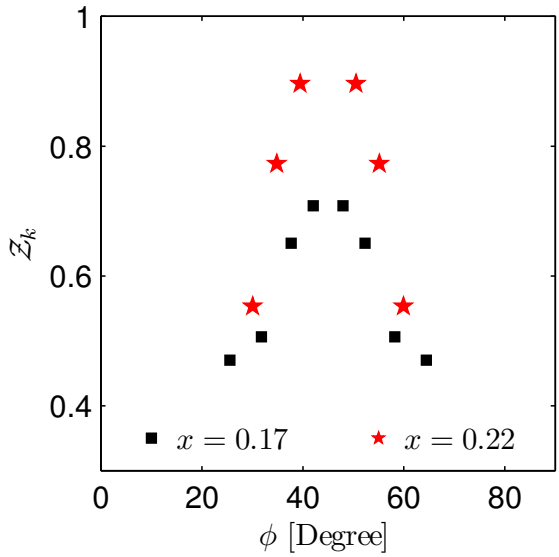

FIGURE 6.24: Z_k as a function of ϕ for $x = 0.17$ and $x = 0.22$. For both compositions a symmetrization around $\phi = \pi/4$ was done. In case of $x = 0.17$, ten spectra were analyzed and after symmetrization the data were binned with a step of two degrees.

whether the kink originates from a coupling to a magnetic mode [314] or a phonon mode [315]. The momentum dependence of the kink reported here puts stronger constrains to both scenarios. However, this observation does not exclude neither of the two scenarios.

6.6.2 Novel kink in overdoped LSCO $x = 0.22$. I am now going to present evidence of a novel kink E_n in the nodal spectra of overdoped LSCO $x = 0.22$. Figure 6.25(a) and (b) present the MDC dispersion and linewidth of the same nodal spectrum as shown in figure 6.23(c) and (d). The difference is that the energy scale is extended to 0.4 eV in figure 6.25 compared to 0.15 eV in figure 6.23(c) and (d). An abrupt change is observed both in the dispersion and the linewidth as a function of ω at $E_n \approx 200$ meV, see the arrow in figure 6.25(a) and (b). This provides therefore strong evidence for a new characteristic energy scale in the overdoped part of the phase diagram. It should be emphasized that this kink was also observed for cuts taken in between the nodal antinodal point.

As for the low-energy kink E_0, it is not easy to understand the underlying nature of the novel kink E_n just from the observation. However, the high-energy scale ($E_n \approx 200$ meV) excludes that phonons are responsible for this kink. Possible candidates may be spin fluctuations or simple electronic electron-electron interactions.

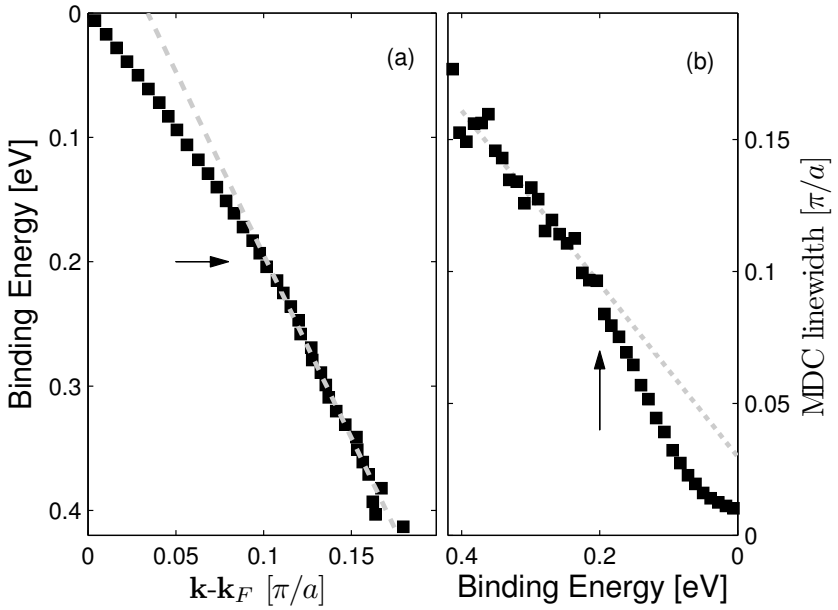

FIGURE 6.25: (a) MDC dispersion of a spectrum recorded close to the nodal point. (b) The MDC linewidth as a function of binding energy. Note that this is same spectrum shown in figure 6.23(c) and (d) but here the energy scale is 0-0.4 eV instead of 0-0.15 eV.

6.6.3 Conclusions. In summary this section described kinks observed in the overdoped region part of the phase diagram. Two new results were obtained.

First it was found that the nodal low-energy kink at $E_0 \approx 70$ meV is momentum dependent. The kink becomes more pronounced for cuts away from the zone diagonal. The quantity $Z_k = \frac{v_L}{v_H}$ which is some models are the quasiparticle spectral weight was measured in a systematic fashion as a function of momentum. It was found that the quasiparticle spectral weight is maximum along the zone diagonal and that it decreases for momenta away from the nodal direction.

A second result was the discovery of a novel kink in $x = 0.22$ at rather high-energy $E_n \approx 200$ meV. However the mechanism underlying this novel kink remains incompletely understood. Studies at higher doping levels and of other compounds with a similar doping are required to clarify this issue. For completeness it should be mentioned that novel kinks were recently observed at $\omega = 115$ meV and $\omega = 150$ meV in optimally doped Bi2212 [316]. Whether these energy scales are related to E_n is still an open question.

6.7 HIGH-ENERGY EXCITATIONS

This section is devoted to the high-energy part ($0.1 - 1$ eV) of the ARPES spectra. For many years ARPES studies focused almost entirely on the low-energy electronic properties. However, recently the high-energy part of the spectrum has received considerable attention. Enormous anomalies in the nodal dispersion were reported at energies as high as 0.4 eV. These high-energy scales are the subject of this section.

6.7.1 Waterfall in the ARPES spectra. The high-energy part ($\omega < 0.6$ eV) of the ARPES spectrum of LSCO with $x = 0.17$ is the subject of this section. I am going to present evidences for the existence of a characteristic energy scale E_1, measured relative to E_F, at which the QP dispersion becomes infinite. To this end, I plot in figures 6.26(a)-(c) the normalized ARPES intensity as a function of binding energy and momentum along three cuts in the BZ see inset in figure 6.26(c). All three cuts show a high-intensity feature close to E_F. This feature has been extensively studied and interpreted as evidence for the existence of QPs [250, 251]. As mentioned before, a discontinuity in the slope of the QP dispersion [green arrow in the inset of figures 6.26(a) and 6.26(b)] is observed at the binding energy $E_0 \approx 0.07$ eV. At the binding energy E_1, white arrow in figures 6.26(a)-(c), a less intense vertical feature emerges.

Such a high-energy threshold E_1 was recently observed in the Bi2212-based and La-based family of cuprates [317–322] and in the Mott insulator $Ca_2CuO_2Cl_2$ [323]. The excitation spectra can be analyzed via either momentum distribution curves (MDCs) or energy distribution curves (EDCs) [250, 251]. EDCs and MDCs for the spectra in figure 6.26(a) are presented in figures 6.26(d) and (e), respectively. While peaks appear in the MDCs for all binding energies, the EDC peaks exist only between E_F and E_1. Thus, fits to the Lorentzian line shapes of the MDCs provide the only way to extract the maximum intensities of the spectral function within the 0.6 eV large energy window.

The position of the MDC peaks are depicted by a thin black line in figures 6.26(a) and (b). Remarkably, in two cuts, figures 6.26(a) and (b), it is possible to identify *different* values for E_1 depicted by the white arrow, below which the thin black line becomes vertical. As mentioned in section 6.4.3 it is possible to fit the measured QP dispersion of the high-intensity feature using a tight-binding (TB) non-interacting model as explained in the caption of figure 6.26. However, since a QP is defined by a sharp peak in both EDCs and MDCs, it makes no sense to fit the thin black line for binding energies higher than E_1 on the basis of a single-particle picture. Inspection of figure 6.26(d) implies the existence of QPs with energies between E_F and E_1 whereas the QP picture breaks down for binding energies higher than E_1. Although the main purpose of this paper is to study the momentum dependence of E_1, we need to start with the Fermi surface as it is the reference for the low-energy physics. The inset of figure 6.27(a) shows the Fermi surface (FS), as determined by using MDC cuts at the fixed energy E_F, and eight selected momentum cuts for which we will gradually increase the binding energy from E_F all the way to 0.6 eV. The cuts are numbered in ascending order as their intersections with the Fermi surface move from the nodal region to the antinodal region. In figure 6.27(a) the relative MDC peak positions are shown as a function of binding energy [the color code is consistent with the inset]. With increasing binding energy, the MDC peaks disperse until they reach E_1 denoted by black arrows.

For binding energies higher than E_1 the MDC peaks are pinned in momentum. In some in-

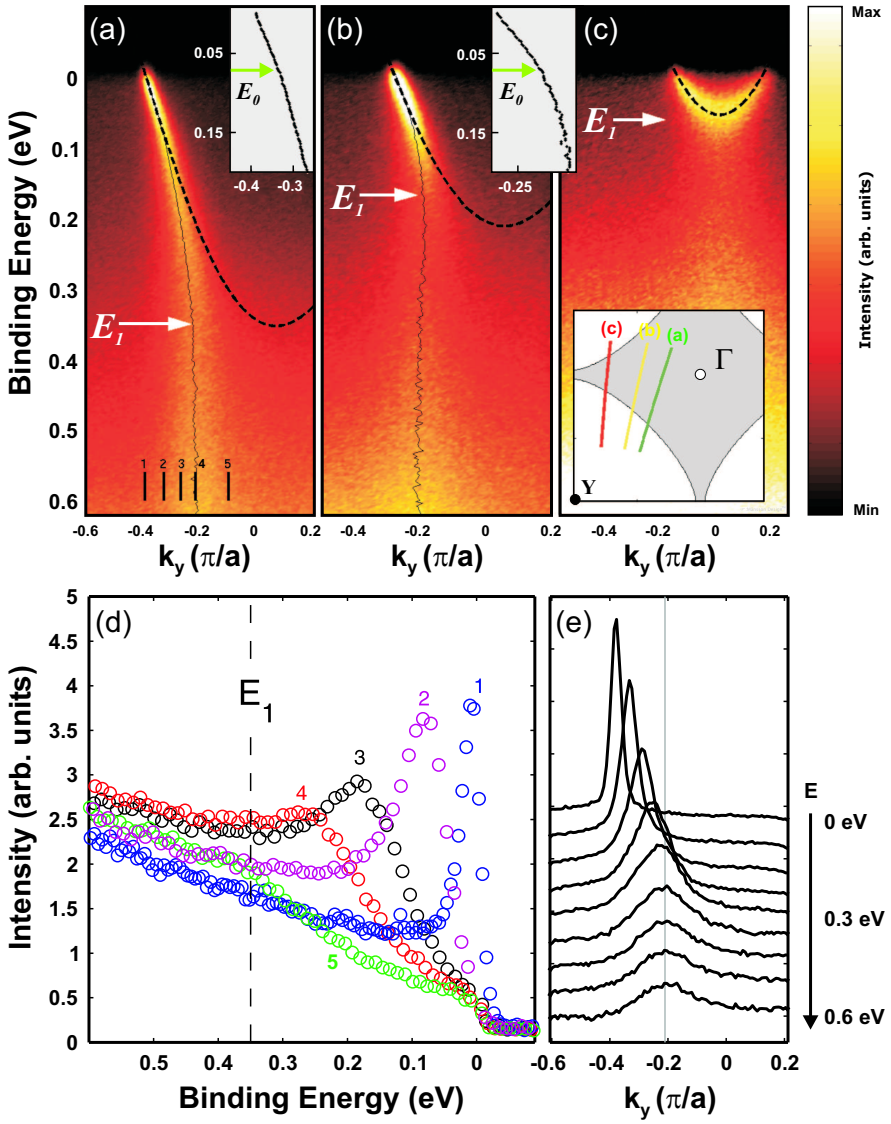

FIGURE 6.26: (a)-(c) Plots of normalized ARPES intensity as a function of binding energy and momentum taken along the three cuts a, b, and c shown in the bottom right inset. The intensity is given by a false color scale where white is the most intense. The maximum intensity indicated by the colorbar is the same for (a) and (b) while for (c) it is 2/3 times smaller. The thin black line represents the MDC peak positions. Zooms of the brightest part of the dispersion are shown in the top insets. The kink E_0 and the high-energy threshold E_1 are defined in the text. The dashed black line represents the tight-binding model dispersion (see Eq. 6.24) along each of the cuts in the Brillouin zone. The ratios $\mu/t = 0.84$, $t'/t = -0.144$, and $t''/t = 0.072$ are chosen so as to fit the measured FS (see also table 6.2). The band width, set by $t = 162.5$ meV, is determined by the measured Fermi velocity at the nodal point. (d) Five EDCs of the spectra in (a) denoted by vertical lines in (a). (e) MDCs with binding energies between E_F and 0.6 eV for the spectra shown in (a).

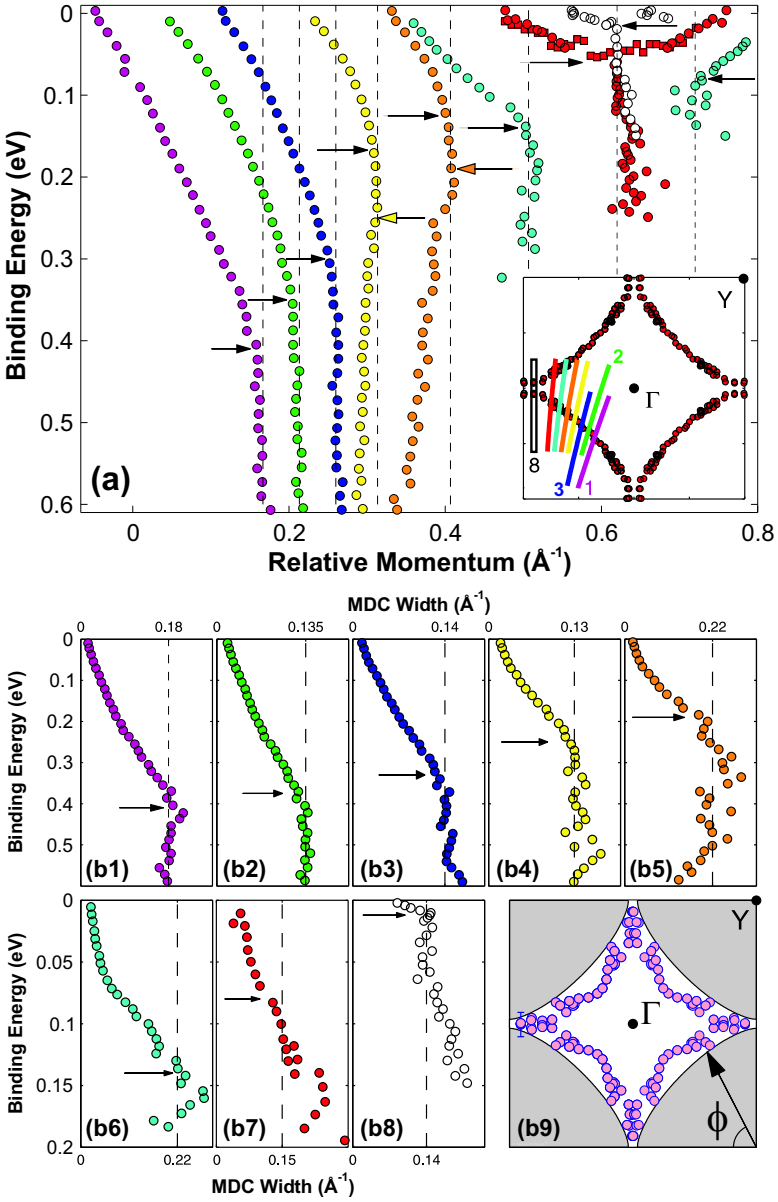

FIGURE 6.27: (a) MDC peak positions as a function of binding energy are shown for the eight different cuts from the inset. (The inset also shows the peak positions of MDCs at E_F, thereby mapping out the Fermi surface.) For cut seven, red squares correspond to the EDC peak positions. The horizontal scale indicates relative momentum position. (b1)-(b8) The binding energy dependence of $\Gamma_{\mathrm{MDC}}(E)$ for each of the eight cuts from the inset in (a). In figures (a) and (b), black arrows indicate the high-energy threshold. Colored arrows in (a) indicate reentrance of dispersion (see the text). The color code and the numbering are consistent with the inset in (a). (b9) Position of E_1 (circles) in the first Brillouin zone. Definition of angle ϕ along the Fermi surface is shown in lower right corner.

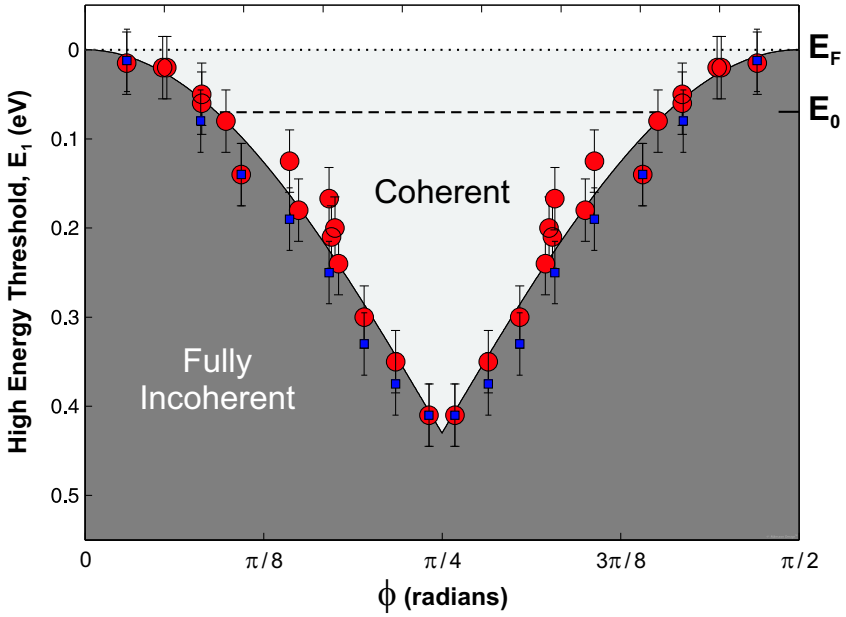

FIGURE 6.28: Dispersion of E_1 as a function of the angle ϕ defined in figure 6.27(b9). Red circles represent $E_1(\phi)$ as extracted from the onset of a vertical feature of the MDC peak positions (see the black arrows in figure 6.27(a)). Blue squares denote $E_1(\phi)$ as extracted from the onset of the saturation of the MDC HWHM (see the black arrows in figure 6.27(b1)-(b8)).

stances a colored arrow indicates a reentrance of dispersion. As the cuts approach the antinodal region the threshold value E_1 approaches E_F. For symmetry reasons two QP branches are observed in cuts six, seven, and eight. For cuts seven and eight these two branches merge at higher binding energy hereby defining E_1. An alternative characterization of the high-energy threshold E_1 can be done by analyzing the half width at half maximum (HWHM) of the MDCs that we denote by $\Gamma_{\mathrm{MDC}}(E) = \Delta k/2$ as a function of binding energy. figures 6.27(b1)-(b8) show the energy dependence of $\Gamma_{\mathrm{MDC}}(E)$ for the eight cuts. The black arrows denote the threshold binding energy at which $\Gamma_{\mathrm{MDC}}(E)$ becomes approximately constant at around 0.2 $\mathrm{\AA}^{-1}$, corresponding to a coherence length of a few lattice spacings. The arrows in figures 6.27(b1)-(b8) correspond well to the black arrows in figure 6.27(a) for all cuts, except for cuts four and five for which they match the colored arrows in figure 6.27(a). Notice that in the regime between E_0 and E_1 the line width scales approximately with the binding energy as expected, for example, from marginal Fermi liquid theory [324]. A detailed analysis will be given later.

The white arrows in figures 6.26(a)-(c) and the black arrows in figures 6.27(a) and (b1)-(b8) demonstrate that the high-energy threshold approaches the Fermi level when moving from the nodal to the antinodal region. Moreover, the locus of E_1 in reciprocal space traces a border between coherent and fully incoherent excitations that resembles the FS, see figure 6.27(b9). We plot in figure 6.28 $E_1(\phi_{WF})$ as a function of the azimuthal FS angle ϕ_{WF}, defined in figure 6.27(b9).

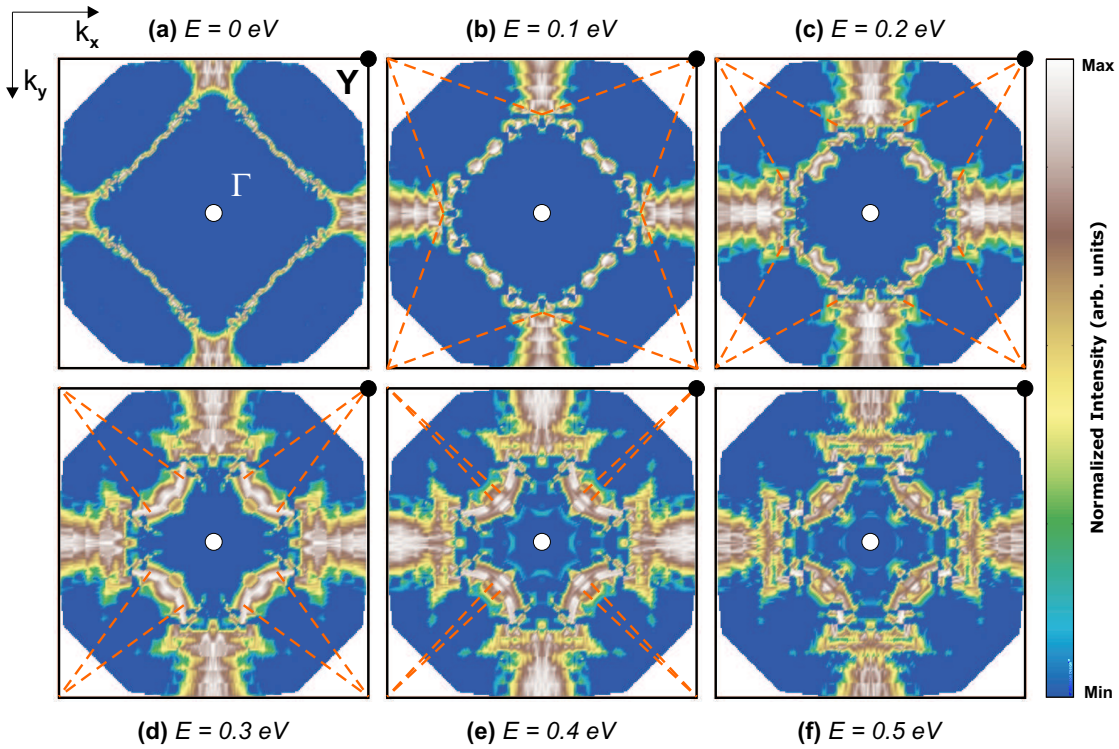

FIGURE 6.29: (a)-(f) Constant energy maps at binding energies $E = 0, 0.1, 0.2, 0.3, 0.4$, and 0.5 eV. All maps are composed of background subtracted MDCs and the intensities have been normalized such that $I_{max} = 1$ for each MDC cut. Dashed lines represent the crossover between coherent (QP) and fully incoherent regimes as defined in figure 6.28. (b)-(f) is integrated over ± 0.15 eV.

Notice that ϕ_{WF} is calculated from the locus of E_1. The red circles represent $E_1(\phi_{WF})$ as extracted from the onset of a vertical feature of the MDC peak positions [see the black arrows in figure 6.27(a)]. The blue squares denote $E_1(\phi_{WF})$ as extracted from the onset of the saturation of the MDC HWHM [see the black arrows in figure 6.27(b1)-(b8)]. The dispersion $E_1(\phi_{WF})$ is well described by

$$E_1(\phi_{WF}) = E_1(\pi/4) \times (1 - |\cos 2\phi_{WF}|). \tag{6.29}$$

For the doping level studied here, we found $E_1(\pi/4) = 0.43$ eV. It is remarkable that the angular dependence of the d-wave gap, $\cos 2\phi_{WF}$, a low-energy property of quasiparticles, enters in the dependence $E_1(\phi)$. Note that the decrease in energy of $E_1(\phi_{WF})$ between $\phi_{WF} = \pi/4$ (nodal region) and $\phi_{WF} = \pi/2$ (antinodal region) is considerable (0.4 eV). The boundary given by the data points in figure 6.28 delimits a coherent regime in which the excitations probed by ARPES are characterized by peaks in both EDC and MDC cuts from a fully incoherent regime in which excitations probed by ARPES are only characterized by broad MDC peaks. A consequence of the dispersion of E_1 is that, near the antinodal region, its energy becomes comparable to the energy of the kink, E_0. Where measurable, E_0 remains roughly constant along the FS as illustrated by the horizontal dashed line in figure 6.28.

The momentum dependence of the ARPES spectral weight at the fixed energies $E = 0$, 0.1, 0.2, 0.3, 0.4, and 0.5 eV is shown in figures 6.29(a)-(f), respectively. As expected, at the lowest binding energy, figure 6.29(a), the spectral weight is concentrated along the FS determined from the MDC peak positions, see the inset of figure 6.27(a). At this low-energy, sharp coherent QPs are observed at each FS point. The MDC widths are anisotropic and sharpest close to $0.4(\pi,\pi)$. Moving toward higher binding energy, two changes can be noticed: first the locus of intensity along the (π,π) directions moves toward $(\pi/4,\pi/4)$ and, second, the regions where QPs exist continuously shrink to single points along the diagonals [at $E_1(\pi/4)$], see figure 6.29(e), to eventually disappear completely for energies larger than $E_1(\pi/4)$ [figure 6.29(f)]. Remarkably, at these high-energies, the spectral function, although fully incoherent, remains strongly anisotropic. In figure 6.29 the dashed lines represent the crossover between coherent and fully incoherent regimes as defined in figure 6.28.

6.7.2 Interpretations of the waterfall. Due to the shape of the high-energy dispersion the anomaly E_1 has also become known as the waterfall feature. The waterfall structure has been observed in a series of compounds such as Bi2212 [317, 318], $Bi_2Sr_2Cu_{6+\delta}$, LSCO [320, 322], LBCO [319], $Pr_{1-x}LaCe_xCu0_4$, $Ca_2CuO_2Cl_2$ [323, 325], and $Ba_2Ca_3Cu_40_8$ at binding energies $\sim 0.3-0.5$ eV. Although there is a high degree of consistency between the measurements, a diverse number of interpretations have been suggested. Above the waterfall structure was discussed in terms of a coherent-incoherent crossover which is an interpretation shared with Pan *et al.* [326]. The waterfall has generally been interpreted in terms of many-body interactions [302, 327–333]. For example it has been proposed (i) that the waterfall marks a bifurcation of the quasiparticle band into a spinon and a holon branch [317, 334, 335], (ii) different variations of the $t-J$ model [336–340], (iii) a phenomenon which is not inherent to the single-particle spectral function [341], and (iv) renormalization effect of the self-energy related to spin fluctuation [319] or quantum criticality [327].

Although some of these interpretations stand orthogonal to each other, each of them has their relevance at the moment of writing. Probably a second generation of refined experiment is required in order to reduce the number of possible explanations.

A natural step is to study the self-energy and the renormalization effects at high binding energy. So far little is known experimentally about the self-energy in the cuprates in the high-energy limit. Therefore we decide to study the high-energy scattering rate which is directly related to the self-energy function.

6.8 ANISOTROPIC QUASIPARTICLE SCATTERING

The quasiparticles in a conventional Fermi liquid scatter in an isotropic fashion. This is, however not necessarily true for strongly correlated electrons. For example, in the heavy Fermion system $CeCoIn_5$ an anisotropic break down of the Wiedermann-Franz law was observed by A. Tanatar *et al.* [342]. Even more recently anisotropic QP renormalization was reported in $Na_{0.73}CoO_2$ [343]. Evidence for an angle dependent quasiparticle weights was already infered from the study of the low-energy kink E_0, see section 6.6. A theoretical framework to describe the variation of the QP weight on moving around the Fermi surface in a correlated metal was recently given by Pouyan Ghaemi *et al.* [344]. In this section the momentum dependence of the scattering rate in LSCO will be discussed.

6.8.1 Anisotropic scattering. In figure 6.30(a) I show the ARPES intensity, recorded on $x = 0.145$, up to very high binding energy for the nodal cut shown in the inset. The background was subtracted and the intensity was normalized to the maximum intensity of the momentum distribution curves (MDC) for each energy step, as discussed in section 6.3. The open black points indicate the dispersion extracted from MDC analysis according to figure 6.30(b) and the blue lines will be explained below. As previously reported [317], the nodal spectra exhibit two high-energy anomalies, E_1 and E_2, as indicated by black arrows in figure 6.30(a). For $E_1 < \omega < E_2$ the MDC peaks are pinned at $\mathbf{k}_{WF} \approx (\pi/4, \pi/4)$, while for $\omega > E_2$ the MDC peaks disperse again. These anomalies have become known as the waterfall (WF) feature. Herein, the waterfall refers to the anomaly $E_1(\mathbf{k})$ and $\mathbf{k}_{WF}$ is the momentum associated with $E_1(\mathbf{k})$. We use the notation $\mathbf{k} = (|\mathbf{k}|, \phi)$, where the angle ϕ is defined as shown in figure 6.31(c). This section is dedicated to the study of $\Gamma(\mathbf{k}, \omega) = \Delta k/2$ in the regime $\omega < E_1$, i.e., we limit our analysis to $\omega < 0.6$ eV. In this ω-range, well-defined Lorentzian-shaped peaks, on nearly flat background, are observed in the MDC, shown in figure 6.30(b).

We examine the low- and high-energy dependence of the half-width half-maximum (HWHM) $\Gamma(\mathbf{k}, \omega)$ extracted from Lorentzian fits to the MDC from figures 6.31(a) to (d). The Fermi surfaces of LSCO with $x = 0.145$ and $x = 0.17$, shown in figures 6.31(b) and (c) respectively, are consistent with previous reports [149] as discussed in section 6.4. The color code of the cuts in figures 6.31(b) and (c) is the same as that in figures 6.31(a) and (d).

Before studying $\Gamma(\mathbf{k}, \omega)$, we first discuss the $\mathbf{k}$-dependence of the high-energy anomaly E_1. Figure 6.32(a) shows E_1 extracted from the anomaly in the scattering rate shown in figure 6.31(d). $E_1(\phi_{WF})$ disperses strongly and it can be described by phenomenological form given in Eq. 6.29. Within the experimental uncertainty, there is no significant difference between $E_1(\phi_{WF})$ for LSCO with $x = 0.145$ and $x = 0.17$.

The energy scales E_0 and E_1 define three distinct characteristic regimes shown in figure 6.32(a). Regime I is the low-energy regime $E_F < \omega < \min(E_0, E_1(\mathbf{k}))$, followed by an intermediate regime II defined by $E_0 < \omega < E_1(\mathbf{k})$. Finally, we define the high-energy regime III by $E_1(\mathbf{k}) < \omega$.

I now turn to the momentum- and ω-dependence of $\Gamma(\mathbf{k}, \omega)$. Although it is difficult to model $\Gamma(\mathbf{k}, \omega)$ for $\omega < 2\Delta < E_0$ (regime I), we assumed here a linear ω-dependence for $\omega \to 0$ as suggested by Kaminski *et al.* [345]

$$\Gamma_I(\mathbf{k}, \omega) = \Gamma_0(\mathbf{k}) + \alpha_I(\mathbf{k})\omega. \tag{6.30}$$

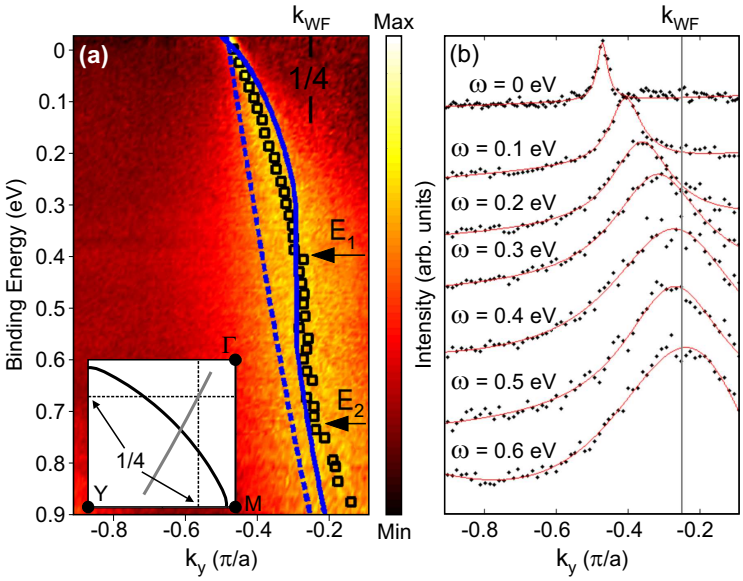

FIGURE 6.30: (a) MDC-normalized ARPES spectra, recorded on $x = 0.145$, for the nodal cut shown in the inset. Square points represent MDC peak positions extracted from a Lorentzian function fit. Dashed blue line represents the bare band dispersion $\varepsilon_{\mathbf{k}}$. Solid blue line represents the renormalized dispersion obtained from discussions below. (b) MDCs for ω up to 0.6 eV. The red lines are Lorentzian fits to the data.

We see from figures 6.20(a) and (b) that the elastic term $\Gamma_0(\mathbf{k})$ is highly anisotropic. In figure 6.32(b), we show the complete ϕ_{FS}-dependence of the elastic MDC linewidth $\Gamma_0(\phi_{FS})$. Note that the uncertainty, related to the fact that the cuts are not exactly perpendicular to the FS, can not account for the anisotropic dependence. An anisotropic MDC linewidth was also reported by Yoshida *et al.* [150]. Notice that the work of Yoshida *et al.* [150] finds a nodal MDC linewidth of ~ 50 Å^{-1} while this work finds $\Gamma_0(\pi/4) \approx 27$ Å^{-1}.

Next, I am going to discuss the inelastic scattering. The parameter $\alpha_I(\mathbf{k})$, related to the inelastic scattering, is analyzed by linear fits to the scattering rate $\Gamma_I(\omega)$, see dashed lines in figure 6.31(a). We show in figure 6.32(c) the angular dependence of $\alpha_I(\phi_{FS})$ in the vicinity of the nodal point. In contrast to previous reports on optimally doped Bi2212 [345] we find that $\alpha_I(\mathbf{k})$ is strongly anisotropic for $La_{2-x}Sr_xCuO_4$ with $x = 0.145$.

Next, we examine regime II where $\Gamma_{II}(\mathbf{k},\omega)$ can be described by:

$$\Gamma_{II}(\mathbf{k},\omega) = \beta(\mathbf{k}) + \alpha_{II}(\mathbf{k})\omega. \tag{6.31}$$

As for $\alpha_I(\mathbf{k})$, we analyze $\alpha_{II}(\mathbf{k})$ by linear fits to the scattering rate $\Gamma_{II}(\mathbf{k},\omega)$. For $x = 0.145$, $\beta(\mathbf{k})$ is neglectable and the angular dependence of $\alpha_{II}(\phi_{WF})$ is shown in figure 6.32(c). Observe that the coefficient α_{II} is the same for both $T_c > T = 15$ K and $T_c < T = 40$ K, see figure 6.31. This expected since the relevant energy scale in Regime II is an order of magnitude larger than the maximum of the superconducting gap. Hence the linear dependence on ω cannot be attributed

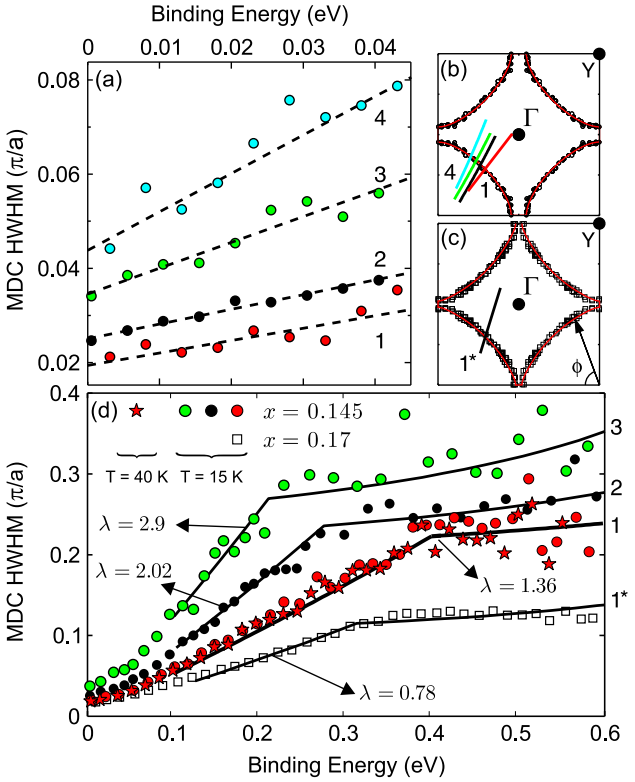

FIGURE 6.31: (a) Low-energy dependence of the MDC linewidths for the cuts shown in (b). Dashed lines represent linear fits of the measured scattering rate. (b-c) Fermi Surface of x =0.145 and x =0.17, respectively. (d) ω-dependence of MDC linewidth for cuts 1-3 in (b) and the cut in (c). Cut 1 in (b) was measured both in the superconducting state (circular points) and in the normal state (star points) at $T = 40$ K. The solid lines are $\mathrm{Im}\Sigma(\omega)/v_{\mathbf{k}}$ where $\mathrm{Im}\Sigma(\omega)$ and $v_{\mathbf{k}}$ are given in the text.

to d-wave nodes. Nevertheless and remarkably $\alpha_{II}(\phi_{WF})$ exhibits the same anisotropic dependence as $\alpha_I(\phi_{FS})$ and $\Gamma_0(\phi_{FS})$. To show this, we plot $\Gamma_0(\phi_{FS})/\Gamma_0(\pi/4)$, $\alpha_I(\phi_{FS})/\alpha_I(\pi/4)$ and $\alpha_{II}(\phi_{WF})/\alpha_{II}(\pi/4)$ in figure 6.32(d). For $x = 0.17$ we find the same anisotropic dependence although with a slightly weaker and flatter dependence around the nodal direction, see figure 6.32(e).

6.8.2 Marginal Fermi liquid phenomenology. The approximate Lorentzian shape of the MDCs suggests that one can neglect the **k**- and ω-dependence of the photoelectron matrix elements. If so, we can approximate the ARPES intensity by the single-particle spectral function

$$A(\mathbf{k},\omega) = \frac{1}{\pi}\frac{-\mathrm{Im}\Sigma(\mathbf{k},\omega)}{[\omega - \mathrm{Re}\Sigma(\mathbf{k},\omega) - \varepsilon_{\mathbf{k}}]^2 + [\mathrm{Im}\Sigma(\mathbf{k},\omega)]^2}. \tag{6.32}$$

Here $\Sigma(\mathbf{k},\omega)$ is the self-energy and $\varepsilon_{\mathbf{k}}$ is the bare band dispersion. We model $\varepsilon_{\mathbf{k}}$ with the tight-binding dispersion given in Eq. 6.24. The ratios μ/t, t'/t, and t''/t, given in table 6.2, are chosen such that $\varepsilon_{\mathbf{k}} = 0$ fits the experimentally determined Fermi surfaces, see figures 6.31(b) and (c). Assuming that the bandwidth t varies slowly within the doping range of interest, we use for the bare band dispersion $\varepsilon_{\mathbf{k}}$ (see dashed blue line in figure 6.30) $t = 0.48$ eV for both $x = 0.145$ and $x = 0.17$ [346].

In the following I analyze the cuts shown in figures 6.31(b) and (c) with a generalized MFL self-energy

$$\mathrm{Im}\Sigma(\mathbf{k},\omega) = \frac{-\lambda(\phi_{WF})\pi}{2}\begin{cases}|\omega|, & |\omega| < \omega_c(\phi_{WF}),\\ \omega_c(\phi_{WF}), & |\omega| > \omega_c(\phi_{WF}),\end{cases} \tag{6.33}$$

and

$$\mathrm{Re}\Sigma(\mathbf{k},\omega) = -\lambda(\phi_{WF})\left[\omega\ln\left(\frac{\omega_c(\phi_{WF})}{\omega}\right)+...\right]. \tag{6.34}$$

The conventional MFL ansatz [324, 327, 347] for the self-energy assumes that the dimensionless coupling λ and the characteristic energy cutoff ω_c are $\mathbf{k}$-independent. Motivated by Eqs. 6.30 and 6.31, we are going to relax this assumption in order to describe the MDC linewidth of figure 6.31 from Eqs. 6.32, 6.24, 6.33, and 6.34. Along the cuts shown in figures 6.31(b) and (c), the MDCs have a Lorentzian shape with HWHM $\Gamma(\mathbf{k},\omega) = \mathrm{Im}\Sigma(\mathbf{k},\omega)/v_{\mathbf{k}}$ where $v_{\mathbf{k}}$ is the bare band velocity [265]. Combining Eqs. 6.31 and 6.33, it then follows that

$$\pi\lambda(\phi_{WF}) = \alpha_{II}(\phi_{WF})v_{\mathbf{k}} \approx \alpha_{II}(\phi_{WF})v_{\mathbf{k}_{WF}}. \tag{6.35}$$

This approximation is valid in the vicinity of the nodal point where the bare-band velocity $v_{\mathbf{k}}$ is weakly dependent on $\mathbf{k}$ for $\omega < 0.6$ eV but breaks down upon approaching the van Hove singularity of $\varepsilon_{\mathbf{k}}$ in the antinodal region. Second, we approximate the cutoff energy by

$$\omega_c(\phi_{WF}) \approx E_1(\phi_{WF}). \tag{6.36}$$

Now, the renormalized dispersion is the solution of $\omega_p(\mathbf{k}) = \mathrm{Re}\Sigma(\omega_p(\mathbf{k})) + \varepsilon_{\mathbf{k}}$. In this fashion we obtain a consistent agreement for both the renormalized dispersion (solid blue line in figure 6.30(a)) and the MDC linewidth (solid lines in figure 6.31(d)). Thus, in contrast to earlier claims [348], we have shown that the WF features can be described by a Kramers-Kronig consistent self-energy function $\Sigma(\mathbf{k},\omega)$. We would like to stress that the $\alpha_{II}(\phi_{WF})$ and $v_{\mathbf{k}_{WF}}$ dependencies on ϕ_{WF} do not cancel out, leaving a net anisotropic coupling parameter $\lambda(\phi_{WF})$. Furthermore, the observation that $\alpha_{II}(\mathbf{k})$ has a stronger dependence on doping than $\varepsilon_{\mathbf{k}}$ implies that the coupling constant $\lambda(\phi_{WF})$ decreases with overdoping.

6.8.3 Discussion. We have shown that both the elastic and inelastic scattering rates are highly anisotropic. However, an isotropic channel may be hidden by the dominant anisotropic scattering channel. Recently, two scattering channels have been identified, in the overdoped regime of Tl2201, by an angular magnetoresistance oscillation (AMRO) study [349]. One channel, related to electron-electron scattering, is isotropic and exhibits T^2-dependence. A second channel, of unknown origin, is anisotropic and depends linearly on T. For even more overdoped samples, resistivity measurements on $La_{2-x}Sr_xCuO_4$ have demonstrated that the electron-electron scattering channel is completely dominant [37, 349]. More recently, it has been shown that there is a correlation between the anisotropic scattering and T_c [350].

The picture that emerges from this work and previous transport measurements [37, 349] is the following. In the optimally doped regime the dominant scattering channel is highly anisotropic and exhibits MFL behavior. Upon further hole doping this channel gradually decreases and conventional electron-electron interactions become increasingly important. Eventually in the extremely overdoped regime, $x > 0.3$, electron-electron interactions are the dominant scattering mechanism.

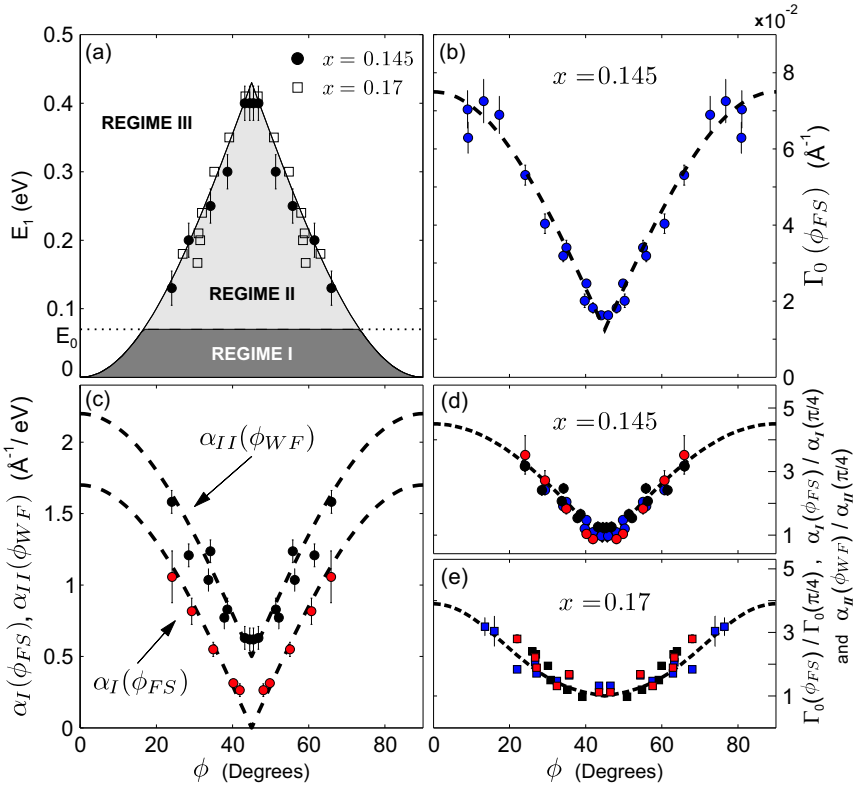

FIGURE 6.32: (a) Momentum dependence of E_1. Solid line is obtained from Eq. 6.29. (b) MDC linewidth Γ_0 as a function of the FS angle ϕ_{FS}. (c) Angular dependence of $\alpha_I(\phi)$ and $\alpha_{II}(\phi)$. (d-e) $\Gamma_0(\phi_{FS})/\Gamma_0(\pi/4)$, $\alpha_I(\phi_{FS})/\alpha_I(\pi/4)$ and $\alpha_{II}(\phi_{WF})/\alpha_{II}(\pi/4)$ for $x = 0.145$ and $x = 0.17$, respectively. Circular points are $x = 0.145$ and square points are $x = 0.17$. Data have been symmetrized with respect to the nodal direction. Dashed lines are guides to the eye.

The main question to be answered is related to the mechanism producing the anisotropic inelastic scattering in LSCO. The fact that MFL phenomenology can quantitatively account for the ω-dependence of $\Gamma(\mathbf{k}, \omega)$ may be an important hint. A MFL response is a typical signature of a quantum critical point (QCP). Distinct proposals for a QCP hidden under the SC dome have been made [74, 351, 352]. Recently a QCP, separating an antiferromagnetic (AF) ordered phase and a magnetically disordered phase, has been identified in LSCO near $x \approx 0.13$ [189] (a confirmation of this was discussed in a previous chapter). As a consequence strong AF spin fluctuations are expected in the vicinity of this QCP, and it has been shown that the spin fluctuations couple anisotropically to the quasiparticles [70]. More recently a theoretical study has suggested that the high-energy anomaly E_1 is a result of a coupling to high-energy spin fluctuations [331]. However, to the best of our knowledge, the exact MFL spectrum has not yet been derived from models based on spin fluctuations.

6.8.4 Overdoped region. Let us now discuss the scattering rate in the overdoped region of LSCO. It has previously been shown in section 6.6 that in $x = 0.22$, there exists a low-energy kink $E_0 \approx 0.07$ eV and a high-energy kink $E_n \approx 0.2$ eV. Here I am going to discuss the **k**- and ω-dependence of MDC linewidth in the range $E_0 < \omega < E_n$. In figure 6.33 the ω-dependence of the MDC linewidth is shown for three different spectra with momenta as indicated in the inset. Notice that both axes are logarithmic. Remember from figure 6.23(d) that a non-linear ω-dependence of the MDC linewidth was observed for $\omega > E_0$. Figure 6.33 demonstrates that the ω-dependence of the MDC linewidth follows a power law dependence for $E_0 < \omega < E_n$. A fit to ω^n in the range $E_0 < \omega < E_n$ gives $n = 1.4 \pm 0.1$ independently of momentum as shown in figure 6.35(a). To make this non-linear dependence even more evident a comparison with MDC linewidth observed on $x = 0.145$ is shown in figure 6.34.

There is an other interesting point to notice from figure 6.33. Remember that the low-energy kink E_0 was very difficult to identify, by the naked eye, from the MDC linewidth, see figure 6.23. However, on the logarithmic plot, the kink E_0 appears more visible. The ω-dependence of the linewidth is rather flat for $\omega < E_0$ and is markedly distinguishable from the $\omega^{1.4}$-dependence for $\omega > E_0$. The low-energy kink E_0 observed in $x = 0.22$ therefore manifests a marked change in the scattering rate. This observation is different from $x = 0.145$ and $x = 0.17$ where a linear ω-dependence was observed both below and above E_0.

Now let us turn back to the $\omega^{1.4}$-dependence of the MDC linewidth. Since the MDC linewidth is related to the quasiparticle lifetime (see Eq. 6.19), a comparison to transport measurements is relevant. In the normal state of overdoped cuprates, a T^n-dependence of the in-plane resistivity ρ_{ab} has been observed [353]. In LSCO with $x = 0.25$ a $T^{1.4}$-dependence was reported [354], see also the work of B. Battlog [41]. A general trend is that the power n increases gradually from one around optimally doping to two in the strongly overdoped region, see figure 6.35(b). Recently, this T^n-dependence has been interpreted in terms of two scattering channels [350]. One channel has a linear T-dependence as observed in optimally doped cuprates. The other channel has a T^2-dependence as expected in a Fermi liquid and as observed in the non-superconducting compound $x = 0.3$.

To test this idea, the MDC linewidth $\Gamma(\omega)$ was fitted to functional dependence which is composed of a linear and quadratic ω-dependence

$$\Gamma(\omega) \sim \alpha_{II}(k)\omega + \beta_{II}(k)\omega^2. \tag{6.37}$$

In figure 6.34 the dashed lines indicate power law with different exponents as indicated. The fit to the composed ω-dependence is shown by the solid line in figure 6.34. In the range $E_0 < \omega < E_n$ where the fit is performed, it is very hard to distinguish it from the $\omega^{1.4}$-dependence. The data can therefore be described equally well by a power law dependence and a linear plus a quadratic ω-dependence.

In figure 6.35(c) the slope of the linear component α_{II} is compared with the slope obtained on $x = 0.145$ and $x = 0.17$. The doping dependence of the nodal values of α_{II} is presented in figure 6.35(d). Consistently with AMRO measurements on Tl2202, a decreasing value of the linear component is found with overdoping [350]. From the amount of ARPES data it is however not possible to establish a direct relation to T_c as was suggested by AMRO experiments [350].

The exact **k**-dependence of the linear component is more complicated when two scattering mechanisms are present. To model the data one needs insight into the bare band dispersion. In-

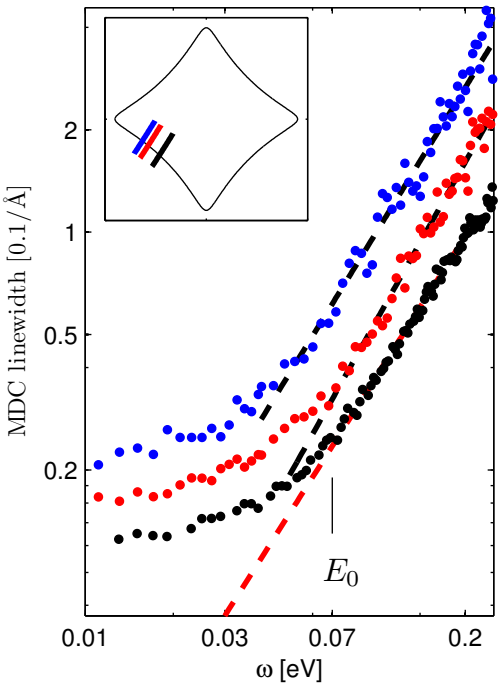

FIGURE 6.33: Energy dependence of the MDC linewidth recorded on $x = 0.22$ for the three cuts shown in the top inset. Both axes are in logarithmic scale. Dashed lines are power law fits to the data.

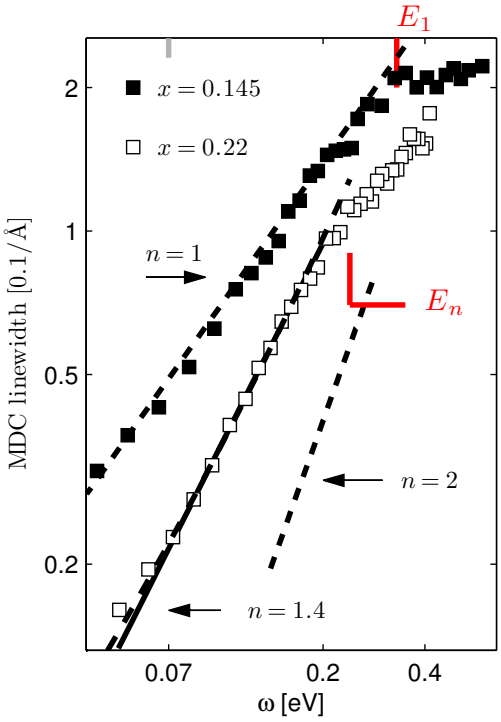

FIGURE 6.34: MDC linewidth as a function of binding energy close to the nodal point for $x = 0.145$ and $x = 0.22$. Both axes are plotted with a logarithmic scale. The dashed lines are $\Gamma \sim \omega^n$ with $n = 1$, $n = 1.4$, and $n = 2$. The solid line is a fit to $\Gamma = \alpha_{II}\omega + \beta_{II}\omega^2$, with constant α_{II} and β_{II}.

stead of doing this, the qualitative **k**-dependence can be examined by hand waving arguments. Figure 6.33 demonstrates that the MDC linewidth increases systematically as one moves away from the nodal point. Now if we assume that the quadratic component is **k**-independent, then the increasing linewidth must be related to the linear component and/or bare band velocity effects. Most likely the velocity effect alone can not explain the increased linewidth, therefore the linear component must increase as one moves away from the zone diagonal. Hence it can be concluded that the **k**-dependence of α_{II} in $x = 0.22$ is similar to that observed in $x = 0.145$ and $x = 0.17$.

It was previously suggested that the linear component could originate from a coupling to spin fluctuations. With overdoping the spin fluctuations spectrum in LSCO changes significantly in particular the spectral distribution of spectral weigth [162]. Generally the spectral weight decreases with overdoping. consistenly with the observation that α_{II} decreases with overdoping.

The main question that arise from the here presented ARPES measurements and the mentioned bulk measurements is how the normal state of HTSC evolves from a Fermi liquid like state in the strongly overdoped region to a marginal Fermi liquid around optimally doping. From the

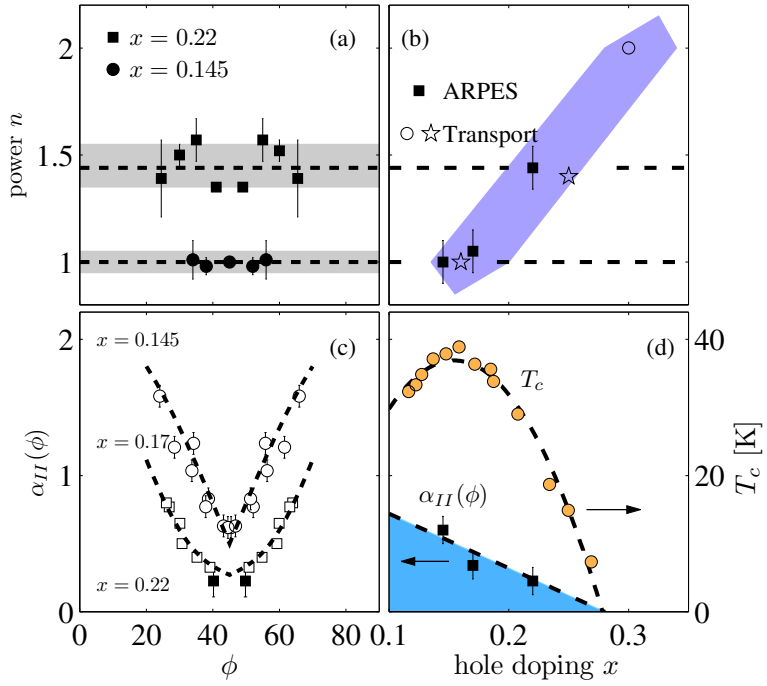

FIGURE 6.35: (a) Momentum dependence of the power n for $x = 0.145$ and $x = 0.22$. (b) Doping dependence of n. Solid squares are ARPES data and open symbols are extracted from transport measurements (circle from [37] and star from [354]). (c) Angular dependence of α_{II} for $x = 0.145$ and $x = 0.17$ compared with the nodal value of α_{II} for $x = 0.22$. (d) The value of α_{II} as a function of doping. For comparison the doping evolution of the superconducting transition T_c is shown. All the dashed lines are guides to the eye.

experimental results two indistingushable senarios are possible: (i) the self-energy is described by a power law $\mathrm{Im}\Sigma \sim \omega^n$ where n change gradually from $n = 2$ in the overdoped regime to $n = 1$ near optimally doping (see figure 6.35(b)) or (ii) the scattering mechanism responsible for the linear ω-dependence near optimally doping gradually vanish with overdoping (see figure 6.35(d)). From our high-energy ARPES data it is difficult to distinguish conclusively between the two scenarios. The best way to solve this issue would probably be to measure the scattering rate near the Fermi surface at very low temperature in the normal state. This can be realized by resistivity measurements in high magnetic field that suppresses superconductivity.

6.9 SUMMARY

In this chapter we have studied the single-particle spectra of LSCO from the underdoped to overdoped region. Below a summary of the most important results is given.

1. The low-energy electronic structure was found to be in perfect agreement with existing literature. It was found that the mean free path and the lifetime of the nodal quasiparticles are longer in the overdoped region compared to the slightly underdoped part of the phase diagram.

2. The superconducting gap and pseudo gap were investigated in NDLSCO, and LSCO with $x = 0.105$ and $x = 0.145$. The superconducting gap exhibits a predominant d-wave shape and the amplitude $\Delta_{sc}(\pi, 0)$ is found to increase with underdoping. In the normal state of underdoped LSCO a pseudo gap is observed but only in vicinity the (π,0) point. Upon moving towards the nodal point the pseudo gap vanish and an arc of gapless excitations appear. These results are fully consistent with the gap as observed by ARPES in Bi2212.

3. The so-called low-energy kink at $E_0 \approx 70$ meV was studied in the overdoped region of the phase diagram. Although the kink energy scale was found to be independent of momentum and doping, the strength of the kink was found to be strongly dependent of both momentum and doping. The kink appears weakest in the nodal direction and is more evident away from the nodal direction.

4. The high-energy part was investigated in LSCO with $x = 0.145$ and $x = 0.17$. A strong anomaly was discovered in the nodal spectrum at $E_1 \sim 0.4$ eV. At this energy, the dispersion is approximately pinned in momentum until a reentrance of the dispersion appears at $E_2 \sim 0.8$ eV. Due to this structure of the dispersion this feature has become known as the waterfall. A main result presented in this thesis is that the high-energy scale E_1 disperses systematically as one moves from the nodal to the antinodal direction.

5. The MDC linewidth was investigated in a systematic fashion as a function of momentum and binding energy for $x = 0.145$ and $x = 0.17$. It was found that the MDC linewidth scales linearly with binding energy ω up to $E_1 \sim 0.4$ eV. Notice that this energy scale corresponds to several thousands of degrees Kelvin. The linearity is therefore analogue to the linear scaling of the in-plane resistivity as a function of temperature. The momentum dependence of the MDC linewidth was found to be strongly anisotropic. The data were successfully modeled with the marginal Fermi liquid self-energy function. Due to the anisotropies of E_1 and the MDC linewidth an anisotropic coupling constant and cutoff energy were introduced. In other words the anisotropic MDC linewidth could not be explained from a bare band velocity effect alone. Although the MFL self-energy is purely phenomenological function, the high-energy scattering was discussed in terms of spin fluctuations.

6. The MDC linewidth was also investigated in the overdoped region of the phase diagram. Here the situation is very different from the optimally doped regime. A novel kink structure was observed both in the nodal dispersion and in the MDC linewidth at $E_n \sim 0.2$ eV. The MDC linewidth was analyzed systematically in the energy range between the low-energy

kink E_0 and E_n. A power law dependence ω^n with $n = 1.45 \pm 0.1$ was found independent of momentum. This observation is incompatible with MFL phenomenology, however the data could be modeled by a self-energy composed of a MFL plus a Fermi liquid term.

6.9.1 Perspectives. Due to the above discussed results several new questions arise naturally. As mentioned before, the nature of the pseudo gap is still strongly debated. A systematic study of the superconducting gap and the pseudo gap as a function of underdoping in LSCO would therefore be of great interest.

Another issue discussed in this chapter was the high-energy part of the ARPES spectrum. Herein the optimally doped region and the overdoped part of the phase diagram were discussed, however no data in the strongly underdoped part of the phase diagram was presented. The evolution of the high-energy part of the spectrum from the Mott insulator to the optimally doped ground state would definitively help to understand the nature of the high-energy excitations.

Chapter 7

Conclusions and outlook

Superconductivity in the cuprate materials is a problem that defies a solution for more than two decades. The phase diagram of high-T_c materials is extremely rich and complex. A precise characterization of these materials may therefore be the only way to obtain a better understanding of the interactions responsible for superconductivity. In this thesis a series of very high quality single crystals with compositions in the range $x = 0.10 - 0.22$ were studied experimentally. Both neutron scattering and angle resolved photoemission spectroscopy were applied to the very same crystals. A number of new results were inferred from these experiments.

The vortex lattice in LSCO at $T \ll T_c$ was studied in a systematic fashion as a function of doping and applied magnetic field by small angle neutron scattering. A large part of the doping-field phase diagram is dominated by a square lattice structure oriented along the Cu-O-Cu (antinodal) directions. It was previously suggested theoretically that the square vortex lattice is stabilized by the proximity of the van Hove singularity to the Fermi level. The systematic experimental study presented here provides empirical evidence that supports this scenario. This strongly suggests that the phase diagram of the vortex lattice should be understood from the electronic structure and possibly also from the quasiparticle spectral weight.

Many physical properties are governed by the quasiparticle spectral weight near the Fermi level. The electronic structure and the quasiparticle scattering rate were studied as a function of momentum and doping by ARPES. In optimally doped LSCO our ARPES measurements reveal a large Fermi surface with spectral peaks throughout the whole Brillouin zone. An important result obtained here is that the quasiparticle spectral weight is strongly anisotropic with maximum along the zone diagonal and minimum near the zone boundary.

As a function of underdoping the fight between magnetic and electronic orders becomes ever more intense. This competition was studied carefully in particular around the so-called 1/8-anomaly. It has been shown by neutron scattering that it is possible to induce a spin-density-wave order in LSCO $x = 0.145$ by application of a magnetic field larger than 7 tesla. Such a spin-density-wave instability of the Fermi surface implies a smooth recnstruction of the Fermi surface starting by a suppression of the quasiparticle spectral weight around the hot spots which in LSCO are situated close to the zone boundaries. Unfortunately it is impossible to demonstrate this suppression directly by an ARPES experiment since this technique is only applicable in zero field. Instead, an indirect experiment was performed through the vortex lattice, which was shown to be

very sensitive to the electronic structure near the zone boundary. As the spin-density-wave instability is approached the diffracted intensity from the vortex lattice vanishes, consistently with a Fermi surface reconstruction.

Next the spin-density-wave order was studied in a systematic fashion as a function of doping and applied magnetic field. In the so-called 1/8-compound, NDLSCO, the spin-density-wave order was found to be fully developed even in zero magnetic field. By ARPES we could therefore study how nature choose to solve the competition between magnetic and electronic orders. In the normal state the quasiparticle spectral weight was completely suppressed around the zone boundary and quasiparticles exist only on an arc around the zone diagonal. This observation is also consistent with a Fermi surface reconstruction.

Now let us turn back to the field-induced spin-density-wave instability. Through inelastic neutron scattering it was shown that the spin gap extrapolates to zero at the critical field for the spin-density-wave order. The critical field was therefore interpreted in terms of a quantum critical point, separating two distinct ground states. A quantum phase transition is realized, strictly speaking, only at zero temperature. However, the effects of the critical spin fluctuations may be observed long before the critical point is reached. Evidence for critical AF spin fluctuations was observed for $H = 0$ T and $T > T_c$ in LSCO with $x = 0.14$ by G. Aepplie *et al.* [232]. Linear resistivity is thought to be another signature of quantum criticality. It is therefore possible that one can study how the quasiparticles are scattered by the critical AF spin fluctuations even in zero field.

In this thesis a systematic study of the quasiparticle scattering rate in zero field as a function of doping x, momentum $\mathbf{k}$, and binding energy ω was given. As the AF spin fluctuations extend up $2J \sim 300$ meV the high-energy part of the electronic spectrum is of particular interest in this context. Although most of the measurements were done in the superconducting state the high-energy part of the spectrum ($\omega \gg \Delta_{sc}$) is unaffected by superconductivity. Electron-phonon scattering is also negligile in this regime. For $x = 0.145$ it was found that the quasiparticle scattering rate scales linearly with the binding energy for $\omega \gg \Delta_{sc}$, i.e.

$$\mathrm{Im}\Sigma(\mathbf{k},\omega,x) \sim \lambda(\mathbf{k},x)\sqrt{\omega^2 + (k_B T)^2} \approx \lambda(\mathbf{k},x)\omega. \tag{7.1}$$

The coupling constant λ was found to be strongly momentum dependent with a minimum along the zone diagonal. As the distance to the quantum critical point is increased by increasing the doping content the coupling constant decreases in a systematic fashion.

The above given self-energy is nothing else than the marginal Fermi liquid self-energy introduced by Ch. Varma *et al.* to explain the ω/T scaling observed by many experimental probes. In several strongly correlated electron systems there is a direct linkage between non Fermi liquid phenomenology and quantum criticality. From the experimental evidence presented here I therefore interpret the quasiparticle scattering rate in LSCO $x = 0.145$ in terms of critical antiferromagnetical spin fluctuations.

The spin-density-wave type of quantum criticality discussed here is shared with many heavy fermion materials. There exists strong empirical evidence that anisotropic superconductivity in heavy fermion compounds exists only near such spin-density-wave instabilities [210]. This might suggest that there is a correlation between this type of quantum criticality and anisotropic superconductivity. At least both the cuprates and some heavy fermion materials share the same type of quantum criticality, the non Fermi liquid behavior, and unconventional superconductivity.

Antiferromagnetic quantum criticality in three and two dimensions and with or without superconductivity is still a subject of intense research and many questions remain open [355]. The possible link between this type of criticality and anisotropic superconductivity would be an interesting subject for further research. One would then need to establish such a spin-density-wave instability in other cuprate compounds such as YBCO. The observation of electron and hole pockets in underdoped YBCO under application of $H \sim 50$ T [211] may be an indication of a competing order parameters [215]. However such an order parameter remains to be identified by for example neutron scattering. An interesting next step, in the context of this work, would therefore be to investigate underdoped YBCO with respect to a spin-density-wave order. It would also be exciting to access the quantum criticality, in for example LSCO, by pressure tuning. Due to the richness of the phase diagram I could continue to suggest experiments for a long time and it is my hope that this work will stimulate further research and new exciting experiments.

Appendix A

The Laue back-scattering technique

Laue back-scattering has been used frequently during this thesis work to align and co-align samples for both neutron and ARPES experiments. Usually a 40 mA X-ray source with a voltage of 40 keV was used. Typical distance between sample and camera [camera distance] was $5-10$ cm. For LSCO, 2 min. of exposure time is enough to get a high quality picture with the recently installed digital camera. Figure A.1 shows a typical example of a diffraction pattern obtained with this camera. With this Laue technique it is possible to co-align two or more single crystals with a mosaicity of less than one degree as shown in figure A.2.

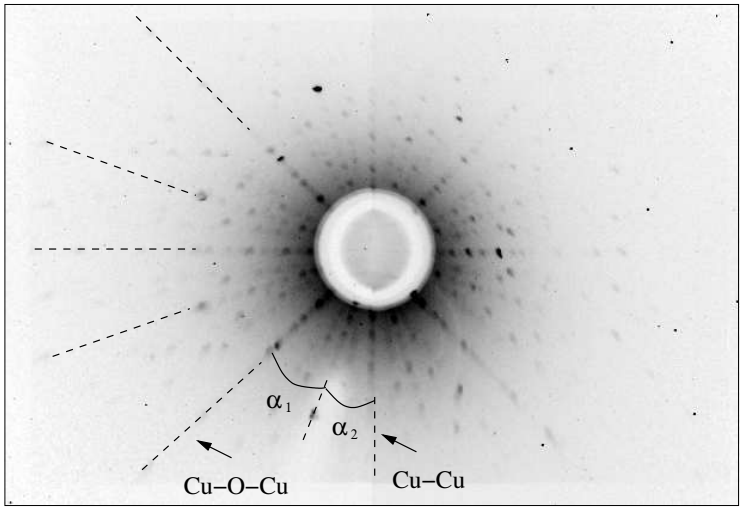

FIGURE A.1: Diffraction spots from LSCO observed with back-scattered X-rays. Here the crystal was oriented such that the *c*-axis was parallel with the X-ray beam. The symmetry of the main crystallographic axis allows you to distinguish the Cu-O-Cu axis from the Cu-Cu axis.

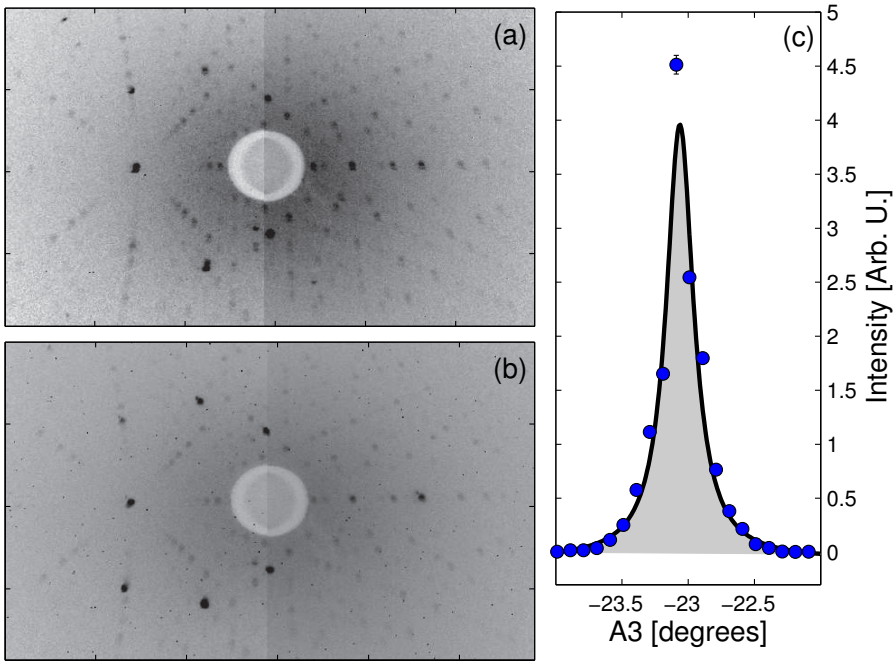

FIGURE A.2: (a) and (b) Laue back-scattering diffraction spots from two co-aligned LSCO crystals. Here the *c*-axes are aligned vertically (perpendicular to the X-ray beam). (c) The (200) reflex [orthorhombic notation] measured by neutron scattering for the two crystals. A3 is the sample rotation angle. The overall mosaicity of the sample alignment is ~ 0.25 degrees.

Appendix B

The μSR technique

The zero field muon spin rotation experiments were performed at the πM3 beamline of the Paul Scherrer Institute, which provides 100 % spin-polarized positive muons. They are incorporated in the host lattice of the sample to be studied. The muons thermalize without loss of initial polarization and come to rest at interstitial lattice sites. The spin of the muon acts as a very sensitive local magnetic probe through its precession in the internal field with a frequency $\nu = \gamma B_{loc}$ where $\gamma = 2\pi \cdot 135.5$ MHz T^{-1} is the gyromagnetic ratio of the muon and B_{loc} is the local internal field at the muon site. In high-T_c oxides the muon stopping site is close to an apical oxygen and the local internal field arises from dipolar fields created by the surrounding Cu^{2+} moments [356]. The time evolution of the muon spin polarization is conveniently determined by the fact that when a muon decays (half-life 2.2 μs) the resulting positron is emitted preferentially in the direction of the instantaneous polarization.

The number of detected positrons as a function of time t in the forward and the backward detector is denoted $N_F(t)$ and $N_B(t)$, respectively. Asymmetry function $A(t)$ is defined by [357]

$$A(t) = \frac{N_B(t) - N_F(t)}{N_B(t) + N_F(t)}. \tag{B.1}$$

The Fourier transform of the asymmetry function yields the field distribution $P(\nu)$ experienced by the muons. In chapter 5 the experimental data were presented in terms of the asymmetry function $A(t)$ (figure 5.7). The same data is here presented in terms of field distribution $P(\nu)$, see figure B.1. To get out a weighted local field one can calculate the second moment M

$$M = \frac{\int P(\nu)\nu^2 d\nu}{\int P(\nu)}. \tag{B.2}$$

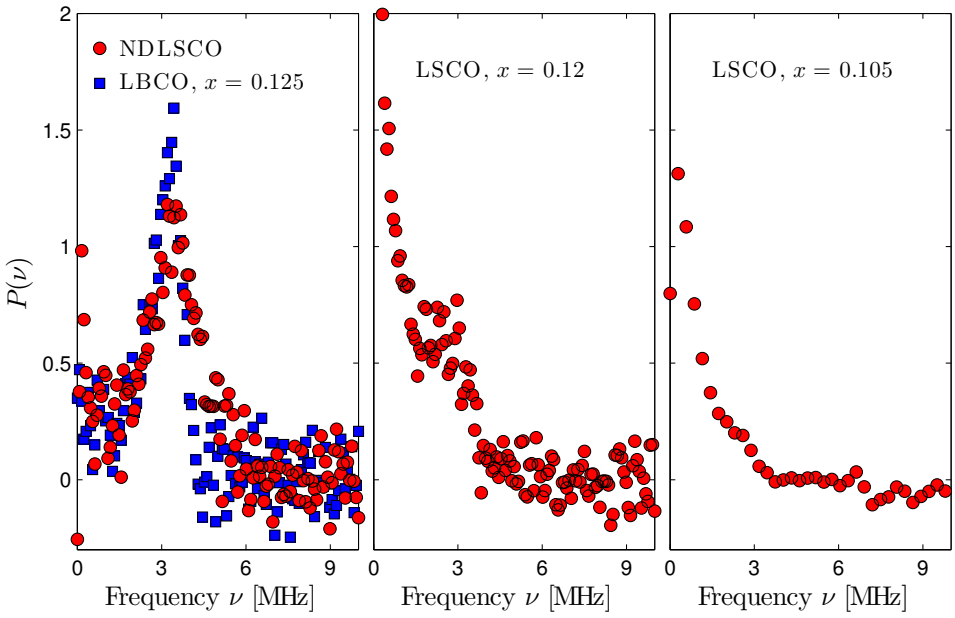

FIGURE B.1: Frequency distribution $P(\nu)$ for NDLSCO and LBCO with $x = 0.125$, LSCO with $x = 0.12$ and $x = 0.105$.

Bibliography

[1] Alexis P. Malozemoff, Jochen Mannhart, and Douglas Scalapino. High-temperature cuprates superconductors get to work. *Physics Today*, 58:41, 2005.

[2] J. Clarke and DC. Larbalestier. Wired for the future. *Nature Physics*, 2:794–796, 2006.

[3] Elbio Dagotto. Complexity in strongly correlated electronic systems. *Science*, 309:257, 2005.

[4] Elbio Dagotto. *New Journal of Physics*, 7:67, 2005.

[5] Myron B. Salamon and Marcelo Jaime. The physics of manganites: Structure and transport. *Rev. Mod. Phys.*, 73(3):583–628, Aug 2001.

[6] Y. Tokura and N. Nagaosa. Orbital physics in transition-metal oxides. *Science*, 288:462, 2000.

[7] Charles Day et al. *Physics Today*, 60:12, 2007.

[8] Yayu Wang, N.S. Rogado, R.J. Cava, and N.P. Ong. Spin entropy as the likely source of enhanced thermopower in $Na_xCo_2O_4$. *Nature*, 423:425, 2003.

[9] Kazunori Takada, Hiroya Sakurai, Eiji Takayama-Muromachi, Fujio Izumi, Ruben A. Dilanian, and Takayoshi Sasaki. Superconductivity in two-dimensional coo_2 layers. *Nature*, 422:53, 2003.

[10] S.-H. Lee and S-W. Cheong. Melting of Quasi-Two-Dimensional Charge Stripes in $La_{5/3}Sr_{1/3}NiO_4$. *Phys. Rev. Lett.*, 79(13):2514–2517, Sep 1997.

[11] A. T. Boothroyd, P. G. Freeman, D. Prabhakaran, A. Hiess, M. Enderle, J. Kulda, and F. Altorfer. Spin correlations among the charge carriers in an ordered stripe phase. *Phys. Rev. Lett.*, 91(25):257201, Dec 2003.

[12] J.G. Bednorz and K.A. Mueller. *Z. Phys. B*, 64:189, 1986.

[13] M. K. Wu, J. R. Ashburn, C. J. Torng, P. H. Hor, R. L. Meng, L. Gao, Z. J. Huang, Y. Q. Wang, and C. W. Chu. Superconductivity at 93 k in a new mixed-phase yb-ba-cu-o compound system at ambient pressure. *Phys. Rev. Lett.*, 58(9):908–910, Mar 1987.

[14] R. J. Cava, B. Batlogg, R. B. van Dover, D. W. Murphy, S. Sunshine, T. Siegrist, J. P. Remeika, E. A. Rietman, S. Zahurak, and G. P. Espinosa. Bulk superconductivity at 91 K in single-phase oxygen-deficient perovskite $Ba_2YCu_3O_{9-\delta}$. *Phys. Rev. Lett.*, 58(16):1676–1679, Apr 1987.

[15] Maeda et al. *J. Appl. Phys. Lett.*, 4:L209, 1988.

[16] C. W. Chu, J. Bechtold, L. Gao, P. H. Hor, Z. J. Huang, R. L. Meng, Y. Y. Sun, Y. Q. Wang, and Y. Y. Xue. Superconductivity up to 114 K in the Bi-Al-Ca-Sr-Cu-O compound system without rare-earth elements. *Phys. Rev. Lett.*, 60(10):941–943, Mar 1988.

[17] H. Eisaki, N. Kaneko, D. L. Feng, A. Damascelli, P. K. Mang, K. M. Shen, Z.-X. Shen, and M. Greven. Effect of chemical inhomogeneity in bismuth-based copper oxide superconductors. *Physical Review B (Condensed Matter and Materials Physics)*, 69(6):064512, 2004.

[18] A. Schilling, M. Cantoni, J.D. Guo, and H.R. Ott. *Nature*, 363:56, 1993.

[19] C.W. Chu, L. GAO, F. CHEN, Z.J. HUANG, R.L. MENG, and Y.Y. XUE. Superconductvity above 150-K in $HgBa_2Ca_2Cu_3O_{8+\delta}$ at high-pressures. *Nature*, 365:323, 1993.

[20] H. Kamerlingh Onnes. *Phys. Lab. Univ. Leiden*, 120b,122b,124c, 1911.

[21] W. Meissner and R. Ochsenfeld. *Naturwissenschaften*, 21:787, 1933.

[22] J. Bardeen, L. N. Cooper, and J. R. Schrieffer. Theory of superconductivity. *Phys. Rev.*, 108(5):1175–1204, Dec 1957.

[23] Leon N. Cooper. Bound electron pairs in a degenerate fermi gas. *Phys. Rev.*, 104(4):1189–1190, Nov 1956.

[24] C.E. Gough, M.S. Colclough, E.M. Forgan, R.G. Jordan, M. Keene, C.M. Muirhead, A.I.M. Rae, N. Thomas, J.S. Abell, and S. Sutton. Flux-quantization in a high-t_c superconductor. *Nature*, 326:855, 1987.

[25] B. D. JOSEPHSON. Coupled superconductors. *Rev. Mod. Phys.*, 36(1):216–220, Jan 1964.

[26] L. P. Gorkov. *Sov. Phys.-JETP*, 9:1364, 1959.

[27] C. C. Tsuei and J. R. Kirtley. Pairing symmetry in cuprate superconductors. *Rev. Mod. Phys.*, 72(4):969, Oct 2000.

[28] H. Ding, M. R. Norman, J. C. Campuzano, M. Randeria, A. F. Bellman, T. Yokoya, T. Takahashi, T. Mochiku, and K. Kadowaki. Angle-resolved photoemission spectroscopy study of the superconducting gap anisotropy in $Bi_2Sr_2CaCu_2O_{8+x}$. *Phys. Rev. B*, 54(14):R9678–R9681, Oct 1996.

[29] V.J. Emery and S.A. Kivelson. *Nature*, 374:434, 1995.

[30] P.W. Anderson. *Science*, 316:1705, 2007.

[31] Patrick A. Lee, Naoto Nagaosa, and Xiao-Gang Wen. Doping a mott insulator: Physics of high-temperature superconductivity. *Reviews of Modern Physics*, 78(1):17, 2006.

[32] J. Orenstein and A.T. Millis. Advances in the physics of high-temperature superconductivity. *Science*, 288:468, 2000.

[33] M R Norman. The electronic nature of high temperature cuprate superconductors. *Rep. Prog. Phys.*, 66:1547–1610, 2003.

[34] Masatoshi Imada, Atsushi Fujimori, and Yoshinori Tokura. Metal-insulator transitions. *Rev. Mod. Phys.*, 70(4):1039–1263, Oct 1998.

[35] R. Coldea, S. M. Hayden, G. Aeppli, T. G. Perring, C. D. Frost, T. E. Mason, S.-W. Cheong, and Z. Fisk. Spin Waves and Electronic Interactions in La_2CuO_4. *Phys. Rev. Lett.*, 86(23):5377–5380, Jun 2001.

[36] G. Wiedemann and R. Franz. *Ann. Phys.*, 89:497, 1853.

[37] S. Nakamae, K. Behnia, N. Mangkorntong, M. Nohara, H. Takagi, S. J. C. Yates, and N. E. Hussey. Electronic ground state of heavily overdoped nonsuperconducting $La_{2-x}Sr_xCuO_4$. *Phys. Rev. B*, 68(10):100502, Sep 2003.

[38] Cyril Proust, Etienne Boaknin, R. W. Hill, Louis Taillefer, and A. P. Mackenzie. Heat Transport in a Strongly Overdoped Cuprate: Fermi Liquid and a Pure *d*-Wave BCS Superconductor. *Phys. Rev. Lett.*, 89(14):147003, Sep 2002.

[39] M. Gurvitch and A. T. Fiory. Resistivity of $La_{1.825}Sr_{0.175}CuO_4$ and $YBa_2Cu_3O_7$ to 1100 K: Absence of saturation and its implications. *Phys. Rev. Lett.*, 59(12):1337–1340, Sep 1987.

[40] H. Takagi, B. Batlogg, H. L. Kao, J. Kwo, R. J. Cava, J. J. Krajewski, and W. F. Peck. Systematic evolution of temperature-dependent resistivity in $La_{2-x}Sr_xCuO_4$. *Phys. Rev. Lett.*, 69(20):2975–2978, Nov 1992.

[41] B. Batlogg, H.Y. Hwang, H. Takagi, H.L. Kao, J. Kwo, and R.J. CAVA. Charge dynamics in $(La,Sr)_2CuO_4$ - from underdoping to overdoping . *Journal of Low Temperature Physics*, 95:23, 1994.

[42] Cyril Proust, Kamran Behnia, Romain Bel, Duncan Maude, and S. I. Vedeneev. Heat transport in $Bi_{2+x}Sr_{2-x}CuO_{6+\delta}$: Departure from the Wiedemann-Franz law in the vicinity of the metal-insulator transition. *Physical Review B (Condensed Matter and Materials Physics)*, 72(21):214511, 2005.

[43] B. Batlogg, H.Y. Hwang, H. Takagi, R.J. Cava, H.L. Kao, and J. Kwo. Normal-state phase-diagram of $(La,Sr)_2CuO_4$ from charge and spin dynamics. *Physica C*, 235-240:130, 1994.

[44] H. Ding, T. Yokoya, J.C. Campuzano, T.Takahashi, M. Randeria, M.R. Norman, T. Mochiku, K. Kadowaki, and J. Giapintzakis. *Nature*, 382:51, 1996.

[45] Tom Timusk and Bryan Statt. *Rep. Prog. Phys.*, 62:61–122, 1999.

[46] J. C. Campuzano, H. Ding, M. R. Norman, H. M. Fretwell, M. Randeria, A. Kaminski, J. Mesot, T. Takeuchi, T. Sato, T. Yokoya, T. Takahashi, T. Mochiku, K. Kadowaki, P. Guptasarma, D. G. Hinks, Z. Konstantinovic, Z. Z. Li, and H. Raffy. Electronic Spectra and Their Relation to the (π,π) Collective Mode in High- T_c Superconductors. *Phys. Rev. Lett.*, 83(18):3709–3712, Nov 1999.

[47] T. Valla, A.V. Fedorov snd J. Lee, J.C. Davis, and G.D. Gu. The ground state of the pseudogap in cuprate superconductors. *Science*, 314, 2006.

[48] Z.A. Xu, N.P. Ong, Y. Wang, T. Kakeshita, and S. Uchida. Vortex-like excitations and the onset of superconducting phase fluctuation in underdoped $La_{2-x}Sr_xCuO_4$. *Nature*, 406:486, 2000.

[49] Yayu Wang, Z. A. Xu, T. Kakeshita, S. Uchida, S. Ono, Yoichi Ando, and N. P. Ong. Onset of the vortexlike Nernst signal above T_c in $La_{2-x}Sr_xCuO_4$ and $Bi_2Sr_{2-y}La_yCuO_6$. *Phys. Rev. B*, 64(22):224519, Nov 2001.

[50] Yayu Wang, N. P. Ong, Z. A. Xu, T. Kakeshita, S. Uchida, D. A. Bonn, R. Liang, and W. N. Hardy. High field phase diagram of cuprates derived from the nernst effect. *Phys. Rev. Lett.*, 88(25):257003, Jun 2002.

[51] N.P. Ong and Yayu Wang. *Physica C*, 408-410:11–15, 2003.

[52] Y.Y. Wang, S. Ono, Y. Onose, G. Gu, Y. Ando, Y. Tokura, S. Uchida, and N.P. Ong. Dependence of upper critical field and pairing strength on doping in cuprates. *Science*, 299:86, 2003.

[53] N.D. Marthur et al. Magnetically mediated superconductivity in heavy fermion compounds. *Nature*, 394:39, 1998.

[54] Hilbert v. Löhneysen, Achim Rosch, Matthias Vojta, and Peter Wölfle. Fermi-liquid instabilities at magnetic quantum phase transitions. *Reviews of Modern Physics*, 79(3):1015, 2007.

[55] P. Coleman et al. How do fermi liquids get heavi and die? *J. Phys.: Condens. Matter*, 13:R723, 2001.

[56] Yoichi Ando, G. S. Boebinger, A. Passner, Tsuyoshi Kimura, and Kohji Kishio. Logarithmic Divergence of both In-Plane and Out-of-Plane Normal-State Resistivities of Superconducting $La_{2-x}Sr_xCuO_4$ in the Zero-Temperature Limit. *Phys. Rev. Lett.*, 75(25):4662–4665, Dec 1995.

[57] G. S. Boebinger, Yoichi Ando, A. Passner, T. Kimura, M. Okuya, J. Shimoyama, K. Kishio, K. Tamasaku, N. Ichikawa, and S. Uchida. Insulator-to-Metal Crossover in the Normal State of $La_{2-x}Sr_xCuO_4$ Near Optimum Doping. *Phys. Rev. Lett.*, 77(27):5417–5420, Dec 1996.

[58] E. Miranda and V. Dobrosavijevic. *Rep. Prog. Phys*, 68:2337, 2005.

[59] N. J. Curro, T. Imai, C. P. Slichter, and B. Dabrowski. High-temperature $^{63}Cu(2)$ nuclear quadrupole and magnetic resonance measurements of $YBa_2Cu_4O_8$. *Phys. Rev. B*, 56(2):877–885, Jul 1997.

[60] David C. Johnston. Magnetic Susceptibility Scaling in $La_{2-x}Sr_xCuO_{4-y}$. *Phys. Rev. Lett.*, 62(8):957–960, Feb 1989.

[61] T. Nakano, M. Oda, C. Manabe, N. Momono, Y. Miura, and M. Ido. Magnetic properties and electronic conduction of superconducting $La_{2-x}Sr_xCuO_4$. *Phys. Rev. B*, 49(22):16000–16008, Jun 1994.

[62] M. R. Norman, D. Pines, and C. Kallin. *Adv. Phys.*, 54:715, 2005.

[63] Towards a complete theory of high T_c. *Nature Physics*, 2:138, 2006.

[64] Jinho Lee, K. Fujita, K. McElroy, J. A. Slezak, M. Wang, Y. Aiura, H. Bando, M. Ishikado, T. Masui, J.-X. Zhu, A. V. Balatsky, H. Eisaki, S. Uchida, and J. C. Davis. Interplay of electron-lattice interactions and superconductivity in $Bi_2Sr_2CaCu_2O_{8+\delta}$. *Nature*, 442:546, 2006.

[65] Nuh Gedik, Ding-Shyue Yang, Gennady Logvenov, Ivan Bozovic, and Ahmed H. Zewail. *Science*, 316:425, 2007.

[66] P.W. Anderson. *Science*, 235:1196, 1987.

[67] P.W. Anderson. The 'strange metal' is a projected Fermi liquid with edge singularities. *Nature Physics*, 2:626, 2006.

[68] P.W. Anderson et al. The physics behind high-temperature superconducting cuprates: the 'plain vanilla' version of RVB. *J. Phys.: Condens. Matter*, 16:R755, 2004.

[69] A. V. Chubukov and D.K. Morr. *Phys. Rep.*, 288:355–387, 1997.

[70] A. Abanov and A.V. Chubukov and J. Schmalian. Quantum-critical theory of the spin fermion model and its application to cuprates: normal state analysis. *Advances in Physics*, 52:119, 2003.

[71] S. A. Kivelson, I. P. Bindloss, E. Fradkin, V. Oganesyan, J. M. Tranquada, A. Kapitulnik, and C. Howald. How to detect fluctuating stripes in the high-temperature superconductors. *Reviews of Modern Physics*, 75(4):1201, 2003.

[72] A. Kaminski and S. Rosenkranz and H.M. Fretwell and J.C. Campuzano and Z. Li and H. Raffy and W.G. Cullen and H. You and C.G. Olson and C.M. Varma and H. Hochst. Spontaneous breaking of time-reversal symmetry in the pseudogap state of a high-T_c superconductor. *Nature*, 416:610, 2002.

[73] B. Fauqué and Y. Sidis and V. Hinkov and S. Pailhès and C. T. Lin and X. Chaud and P. Bourges. Magnetic Order in the Pseudogap Phase of High-T_c Superconductors. *Physical Review Letters*, 96(19):197001, 2006.

[74] Sudip Chakravarty et al. Hidden order in the cuprates. *Phys. Rev. B*, 63(9):094503, Jan 2001.

[75] S.A. Kivelson, E. Fradkin, and V.J. Emery. Electronic liquid-crystal phases of a doped mott insulator. *Nature*, 393:550, 1998.

[76] Matthias Vojta, Ying Zhang, and Subir Sachdev. Quantum Phase Transitions in d-Wave Superconductors. *Phys. Rev. Lett.*, 85(23):4940–4943, Dec 2000.

[77] Eugene Demler, Werner Hanke, and Shou-Cheng Zhang. So(5) theory of antiferromagnetism and superconductivity. *Reviews of Modern Physics*, 76(3):909, 2004.

[78] Bogdan Povh and Mitja Rosina. *Scattering and Structures*. Springer, 2002.

[79] Henrik Bruus and Karsten Flensberg. *Many-Body Quantum Theory in Condensed Matter Physics*. Oxford University Press, 2004.

[80] Gerald D. Mahan. *Many-Particle Physics*. Plenum Press, 1993.

[81] G.L. Squires. *Introduction to the Theory of Thermal Neutron Scattering*. Cambridge University Press, 1978.

[82] P.M. Chaikin and T.C. Lubensky. *Principles of condensed matter physics*. Cambridge University Press, 1995.

[83] Michael Plischke and Birger Bergersen. *EQUILIBRIUM STATISTICAL PHYSICS*. World Scientific, 1994.

[84] T. Nakano, N. Momono, M. Oda, and M. Ido. Correlation between the doping dependences of superconducting gap magnitude 2Δ and pseudogap temperature T^* in high-T_c cuprates. *J. Phys. Soc. Jpn.*, 67:2622, 1998.

[85] http://hoffman.physics.harvard.edu/research/SCmaterials.php.

[86] S Wakimoto, H Kimura, M Fujita, K Yamada, Y Nodai, G Shirane, G Gu, H Kim, and RJ Birgeneau. Incommensurate lattice distortion in the high temperature tetragonal phase of $La_{2-x}(Sr,Ba)_xCuO_4$. *JOURNAL OF THE PHYSICAL SOCIETY OF JAPAN*, 75:074714, Jul 2006.

[87] Raffaele Gilardi. PhD thesis, ETH Zurich, 2004.

[88] http://www.qdusa.com/products/ppms.html.

[89] M. Oda, T. Ohguro, N. Yamada, and M. Ido. Magnetic-susceptibility and superconductivity in $(La_{1-x}Sr_x)_2CuO_4$. *J. Phys. Soc. Japan*, 58:1137, 1989.

[90] N. Yamada and M. Ido. *Physica C*, 203:240–246, 1992.

[91] S. Arumugam et al. *International Journal of Modern Physics B*, 14:3328–3333, 2000.

[92] J.P. Locquet, J. Perret, J. Fompeyrine, E. Machler, J.W. Seo, and G. Van Tendeloo. Doubling the critical temperature of $La_{1.9}Sr_{0.1}CuO_4$ using epitaxial strain. *Nature*, 394:453, 1998.

[93] J. S. Schilling, see Handbook of High Temperature Superconductivity, Springer 2007.

[94] K. Binder and A. P. Young. Spin glasses: Experimental facts, theoretical concepts, and open questions. *Rev. Mod. Phys.*, 58(4):801–976, Oct 1986.

[95] F. C. Chou, N. R. Belk, M. A. Kastner, R. J. Birgeneau, and Amnon Aharony. Spin-Glass Behavior in $La_{1.96}Sr_{0.04}CuO_4$. *Phys. Rev. Lett.*, 75(11):2204–2207, Sep 1995.

[96] S. Wakimoto, S. Ueki, Y. Endoh, and K. Yamada. Systematic study of short-range antiferromagnetic order and the spin-glass state in lightly doped $La_{2-x}Sr_xCuO_4$. *Phys. Rev. B*, 62(5):3547–3553, Aug 2000.

[97] A. N. Lavrov, Yoichi Ando, Seiki Komiya, and I. Tsukada. Unusual Magnetic Susceptibility Anisotropy in Untwinned $La_{2-x}Sr_xCuO_4$ Single Crystals in the Lightly Doped Region. *Phys. Rev. Lett.*, 87(1):017007, Jun 2001.

[98] T. Sasagawa, P. K. Mang, O. P. Vajk, A. Kapitulnik, and M. Greven. Bulk magnetic properties and phase diagram of Li-doped La_2CuO_4 : Common magnetic response of hole-doped CuO_2 planes. *Phys. Rev. B*, 66(18):184512, Nov 2002.

[99] Tuson Park, Z. Nussinov, K. R. A. Hazzard, V. A. Sidorov, A. V. Balatsky, J. L. Sarrao, S.-W. Cheong, M. F. Hundley, Jang-Sik Lee, Q. X. Jia, and J. D. Thompson. Novel Dielectric Anomaly in the Hole-Doped $La_2Cu_{1-x}Li_xO_4$ and $La_{2-x}Sr_xNiO_4$ Insulators: Signature of an Electronic Glassy State. *Physical Review Letters*, 94(1):017002, 2005.

[100] D. Vaknin, S. K. Sinha, D. E. Moncton, D. C. Johnston, J. M. Newsam, C. R. Safinya, and H. E. King. Antiferromagnetism in La_2CuO_{4-y}. *Phys. Rev. Lett.*, 58(26):2802–2805, Jun 1987.

[101] S. Wakimoto, R. J. Birgeneau, Y. S. Lee, and G. Shirane. Hole concentration dependence of the magnetic moment in superconducting and insulating $La_{2-x}Sr_xCuO_4$. *Phys. Rev. B*, 63(17):172501, Mar 2001.

[102] M. Matsuda, M. Fujita, K. Yamada, R. J. Birgeneau, Y. Endoh, and G. Shirane. Electronic phase separation in lightly doped $La_{2-x}Sr_xCuO_4$. *Phys. Rev. B*, 65(13):134515, Mar 2002.

[103] J.M. Tranquada, B.J. Sternlieb, J.D. Axe, Y. Nakamura, and S. Uchida. Evidence for stripe correlations of spins and holes in copper oxide superconductors. *Nature*, 375:561, 1995.

[104] Elbio Dagotto and T. M. Rice. Surprises on the way from one- to two- dimensional quantum magnets: The ladder materials. *Science*, 271:618, 1996.

[105] Troyer, Matthias and Tsunetsugu, Hirokazu and Würtz, Diethelm . Thermodynamics and spin gap of the heisenberg ladder calculated by the look-ahead lanczos algorithm. *Phys. Rev. B*, 50(18):13515–13527, Nov 1994.

[106] D. C. Johnston. Antiferromagnetic exchange in two-leg spin-1/2 ladders. *Phys. Rev. B*, 54(18):13009–13016, Nov 1996.

[107] J. M. Tranquada, J. D. Axe, N. Ichikawa, Y. Nakamura, S. Uchida, and B. Nachumi. Neutron-scattering study of stripe-phase order of holes and spins in $La_{1.48}Nd_{0.4}Sr_{0.12}CuO_4$. *Phys. Rev. B*, 54(10):7489–7499, Sep 1996.

[108] R. Gilardi, S. Streule, N. Momono, M. Oda, and J. Mesot. Doping dependence of the vortex glass and sublimation transitions in the high-T-c superconductor $La_{2-x}Sr_xCuO_4$ as determined from macroscopic measurements. *EUROPEAN PHYSICAL JOURNAL B*, 47:231–237, 2005.

[109] T. Sasagawa, K. Kishio, Y. Togawa, J. Shimoyama, and K. Kitazawa. First-Order Vortex-Lattice Phase Transition in $(La_{1-x}Sr_x)_2CuO_4$ Single Crystals: Universal Scaling of the Transition Lines in High-Temperature Superconductors. *Phys. Rev. Lett.*, 80(19):4297–4300, May 1998.

[110] Jönsson, B. J. and Rao, K. V. and Yun, S. H. and Karlsson, U. O. Method to extract the critical current density and the flux-creep exponent in high-T_c thin films using ac susceptibility measurements. *Phys. Rev. B*, 58(9):5862–5867, Sep 1998.

[111] J. Gutierrez. *Nature Physics*, 6:367, 2007.

[112] Nakai, N. and Miranović, P. and Ichioka, M. and Machida, K. Reentrant vortex lattice transformation in fourfold symmetric superconductors. *Phys. Rev. Lett.*, 89(23):237004, Nov 2002.

[113] R. Gilardi, J. Mesot, A. Drew, U. Divakar, S. L. Lee, E. M. Forgan, O. Zaharko, K. Conder, V. K. Aswal, C. D. Dewhurst, R. Cubitt, N. Momono, and M. Oda. Direct Evidence for an Intrinsic Square Vortex Lattice in the Overdoped High- T_c Superconductor $La_{1.83}Sr_{0.17}CuO_{4+\delta}$. *Phys. Rev. Lett.*, 88(21):217003, May 2002.

[114] B. Keimer, W. Y. Shih, R. W. Erwin, J. W. Lynn, F. Dogan, and I. A. Aksay. Vortex Lattice Symmetry and Electronic Structure in $YBa_2Cu_3O_7$. *Phys. Rev. Lett.*, 73(25):3459–3462, Dec 1994.

[115] S. P. Brown, D. Charalambous, E. C. Jones, E. M. Forgan, P. G. Kealey, A. Erb, and J. Kohlbrecher. Triangular to Square Flux Lattice Phase Transition in $YBa_2Cu_3O_7$. *Physical Review Letters*, 92(6):067004, 2004.

[116] Oystein Fischer, Martin Kugler, Ivan Maggio-Aprile, Christophe Berthod, and Christoph Renner. Scanning tunneling spectroscopy of high-temperature superconductors. *Reviews of Modern Physics*, 79(1):353, 2007.

[117] G. Blatter, M. V. Feigel'man, V. B. Geshkenbein, A. I. Larkin, and V. M. Vinokur. Vortices in high-temperature superconductors. *Rev. Mod. Phys.*, 66(4):1125–1388, Oct 1994.

[118] Laurent-Patrick Levy. *Magnetisme et Superconductivite*. CNRS, 1997.

[119] G. Blatter and V. Geshkenbein. *Vortex matter inThe physics of Superconductors* , volume 1. Springer, 2003.

[120] Jeff E. Sonier, Jess H. Brewer, and Robert F. Kiefl. μSR studies of the vortex state in type-II superconductors. *Rev. Mod. Phys.*, 72(3):769–811, Jul 2000.

[121] T. Sasagawa, Y. Togawa, J. Shimoyama, A. Kapitulnik, K. Kitazawa, and K. Kishio. Magnetization and resistivity measurements of the first-order vortex phase transition in $(La_{1-x}Sr_x)_2CuO_4$. *Phys. Rev. B*, 61(2):1610–1617, Jan 2000.

[122] A. De Col, G. I. Menon, V. B. Geshkenbein, and G. Blatter. Surface melting of the vortex lattice. *Physical Review Letters*, 96(17):177001, 2006.

[123] Q.S. Mei and K. Lu. *Progress in Materials Science*, 52:1175, 2007.

[124] R. Cubitt, E.M. Forgan, G. Yang, S.L. Lee, D.M. Paul, H.A. Mook, M. Yethiraj, P.H. Kes, T.W. Li, A.A. Menovsky, Z. Tarnawski, and K. Mortensen. Direct observation of magnetic-flux lattice melting and decomposition in the high-t_c superconductor $bi_{2.15}sr_{1.95}cacu_2o_{8+x}$. *Nature*, 365:407, 1993.

[125] Lee, S. L. and Zimmermann, P. and Keller, H. and Warden, M. and Savić, I. M. and Schauwecker, R. and Zech, D. and Cubitt, R. and Forgan, E. M. and Kes, P. H. and Li, T. W. and Menovsky, A. A. and Tarnawski, Z. . Evidence for flux-lattice melting and a dimensional crossover in single-crystal $Bi_{2.15}Sr_{1.85}CaCu_2O_{8+\delta}$ from muon spin rotation studies. *Phys. Rev. Lett.*, 71(23):3862–3865, Dec 1993.

[126] L. I. Glazman and A. E. Koshelev. Thermal fluctuations and phase transitions in the vortex state of a layered superconductor. *Phys. Rev. B*, 43(4):2835–2843, Feb 1991.

[127] John R. Clem. Two-dimensional vortices in a stack of thin superconducting films: A model for high-temperature superconducting multilayers. *Phys. Rev. B*, 43(10):7837–7846, Apr 1991.

[128] J.E. Sonier. *Rep. Prog. Phys.*, 70:1717, 2007.

[129] A. N. Grigorenko, S. J. Bending, I. V. Grigorieva, A. E. Koshelev, T. Tamegai, and S. Ooi. Tilt of pancake vortex stacks in layered superconductors in the crossing lattice regime. *Physical Review Letters*, 94(6):067001, 2005.

[130] G. J. Dolan, F. Holtzberg, C. Feild, and T. R. Dinger. Anisotropic vortex structure in $Y_1Ba_2Cu_3O_7$. *Phys. Rev. Lett.*, 62(18):2184–2187, May 1989.

[131] Joachim Kohlbrecher and Werner Wagner. *J. Appl. Cryst*, 33:804–806, 2000.

[132] http://sans2.web.psi.ch/.

[133] Stephen Phillip Brown. PhD thesis, University of Birmingham, 2005.

[134] James F. Annett. *Superconductivity, Superfluids and Condensates*. Oxford University Press, 2004.

[135] C. Panagopoulos, T. Xiang, W. Anukool, J. R. Cooper, Y. S. Wang, and C. W. Chu. Superfluid response in monolayer high-T_c cuprates. *Phys. Rev. B*, 67(22):220502, Jun 2003.

[136] Qiang Li, M. Suenaga, T. Kimura, and K. Kishio. Magnetic penetration depth of $(La_{1-x}Sr_x)_2CuO_4$ single crystals. *Phys. Rev. B*, 47(5):2854–2860, Feb 1993.

[137] T. Kimura et al. *Physica C*, 192:247, 1992.

[138] W. H. Kleiner, L. M. Roth, and S. H. Autler. Bulk solution of ginzburg-landau equations for type ii superconductors: Upper critical field region. *Phys. Rev.*, 133(5A):A1226–A1227, Mar 1964.

[139] M. Ichioka, N. Hayashi, N. Enomoto, and K. Machida. Vortex structure in d-wave superconductors. *Phys. Rev. B*, 53(22):15316–15326, Jun 1996.

[140] A. J. Berlinsky, A. L. Fetter, M. Franz, C. Kallin, and P. I. Soininen. Ginzburg-Landau Theory of Vortices in *d*-Wave Superconductors. *Phys. Rev. Lett.*, 75(11):2200–2203, Sep 1995.

[141] B. Khaykovich, S. Wakimoto, R. J. Birgeneau, M. A. Kastner, Y. S. Lee, P. Smeibidl, P. Vorderwisch, and K. Yamada. Field-induced transition between magnetically disordered and ordered phases in underdoped $La_{2-x}Sr_xCuO_4$. *Phys. Rev. B*, 71(22):220508, Jun 2005.

[142] S. T. Johnson, E. M. Forgan, S. H. Lloyd, C. M. Aegerter, S. L. Lee, R. Cubitt, P. G. Kealey, C. Ager, S. Tajima, A. Rykov, and D. McK. Paul. Flux-Line Lattice Structures in Untwinned $YBa_2Cu_3O_{7-\delta}$. *Phys. Rev. Lett.*, 82(13):2792–2795, Mar 1999.

[143] Lars Maechler. PhD thesis, ETH Zurich, 2007.

[144] J. Chang, J. Mesot, R. Gilardi, J. Kohlbrecher, A.J. Drew, U. Divakar, S.J. Lister, S.L. Lee, S.P. Brown, D. Charalambous, E.M. Forgan, C.D. Dewhurst, R. Cubitt, N. Momono, and M. Oda. Neutron scattering investigations of the abrikosov state of high-temperature superconductors. *Physica B-Condensed matter*, 385-386:35–37, 2006.

[145] H. Iwasaki, T. Chigira, T. Naito, S. Moriyama, Y. Iwasa, T. Nishizaki, and N. Kobayashi. Observation of the vortex lattice phase transition in the specific heat in $La_{1.86}Sr_{0.14}CuO_4$ single crystal. *Physica C*, 366:129, 2002.

[146] M.-H. Julien. Magnetic order and superconductivity in $La_{2-x}Sr_xCuO_4$: a review. *Physica B*, 329-333:693–693, 2003.

[147] U. Divakar, A. J. Drew, S. L. Lee, R. Gilardi, J. Mesot, F. Y. Ogrin, D. Charalambous, E. M. Forgan, G. I. Menon, N. Momono, M. Oda, C. D. Dewhurst, and C. Baines. Direct observation of the flux-line vortex glass phase in a type ii superconductor. *Physical Review Letters*, 92(23):237004, 2004.

[148] R. Gilardi, J. Mesot, A.J. Drew, U. Divakar, S.L. Lee, N.H. Andersen, J. Kohlbrecher, N. Momono, and M. Oda. Field-induced hexagonal to square transition of the vortex lattice in overdoped $La_{1.8}Sr_{0.2}CuO_4$. *Physica C*, 408-410:491, 2004.

[149] T. Yoshida, X. J. Zhou, K. Tanaka, W. L. Yang, Z. Hussain, Z.-X. Shen, A. Fujimori, S. Sahrakorpi, M. Lindroos, R. S. Markiewicz, A. Bansil, Seiki Komiya, Yoichi Ando, H. Eisaki, T. Kakeshita, and S. Uchida. Systematic doping evolution of the underlying Fermi surface of $La_{2-x}Sr_xCuO_4$. *Phys. Rev. B*, 74(22):224510, Dec 2006.

[150] T. Yoshida, X. J. Zhou, D. H. Lu, Seiki Komiya, Yoichi Ando, H. Eisaki, T. Kakeshita, S. Uchida, Z. Hussain, Z.-X. Shen, and A. Fujimori. Low-Energy Electronic Structure of the High-Tc Cuprates $La_{2-x}Sr_xCuO_4$ Studied by Angle-resolved Photoemission Spectroscopy. *J. Phys.: Condens. Matter*, 19:125209, 2007.

[151] K. Lefmann, B. Lake, G. Aeppli, S.W. Cheong, N.B. Christensen, K.N. Clausen, S. Hayden, T.E. Mason, D.F. McMorrow, H.A. Mook, H.M. Rønnow, and H. Takagi. Static and Dynamics Spins in Superconducting $La_{2-x}Sr_xCuO_4$: The Risoe Years. *Journal of Low Temperature Physics*, 135:621, 2004.

[152] John M. Tranquada. *cond-mat/0512115*.

[153] R.J. Birgeneau, C. Stock, J.M. Tranquada, and K. Yamada. Magnetic neutron scattering in hole-doped cuprate superconductors. *JOURNAL OF THE PHYSICAL SOCIETY OF JAPAN*, 75:11.

[154] G. Shirane and S.M. Shapiro and J.M. Tranquada. *Neutron Scattering with a Triple Axis Spectrometer: Basic Techniques*. Cambridge University Press, 2002.

[155] O. Halpern and M. H. Johnson. On the magnetic scattering of neutrons. *Phys. Rev.*, 55(10):898–923, May 1939.

[156] C.R.H. Bahl et al. *NUCLEAR INSTRUMENTS & METHODS IN PHYSICS RESEARCH SECTION B-BEAM INTERACTIONS WITH MATERIALS AND ATOMS*, 226:667–681, 2004.

[157] C.R.H. Bahl et al. *NUCLEAR INSTRUMENTS & METHODS IN PHYSICS RESEARCH SECTION B-BEAM INTERACTIONS WITH MATERIALS AND ATOMS*, 246:452–462, 2006.

[158] S. M. Hayden, G. Aeppli, R. Osborn, A. D. Taylor, T. G. Perring, S-W. Cheong, and Z. Fisk. High-energy spin waves in La_2CuO_4. *Phys. Rev. Lett.*, 67(25):3622–3625, Dec 1991.

[159] M. Fujita, K. Yamada, H. Hiraka, P. M. Gehring, S. H. Lee, S. Wakimoto, and G. Shirane. Static magnetic correlations near the insulating-superconducting phase boundary in $La_{2-x}Sr_xCuO_4$. *Phys. Rev. B*, 65(6):064505, Jan 2002.

[160] S. Wakimoto, H. Zhang, K. Yamada, I. Swainson, Hyunkyung Kim, and R. J. Birgeneau. Direct Relation between the Low-Energy Spin Excitations and Superconductivity of Overdoped High-T_c Superconductors. *Physical Review Letters*, 92(21):217004, 2004.

[161] S. Wakimoto, K. Yamada, J. M. Tranquada, C. D. Frost, R. J. Birgeneau, and H. Zhang. Disappearance of Antiferromagnetic Spin Excitations in Overdoped $La_{2-x}Sr_xCuO_4$. *Physical Review Letters*, 98(24):247003, 2007.

[162] O. J. Lipscombe, S. M. Hayden, B. Vignolle, D. F. McMorrow, and T. G. Perring. Persistence of High-Frequency Spin Fluctuations in Overdoped Superconducting $La_{2-x}Sr_xCuO_4$ ($x = 0.22$). *Physical Review Letters*, 99(6):067002, 2007.

[163] B. Vignolle and S. M. Hayden and D. F. McMorrow and H. M. Rønnow and B. Lake and C. D. Frost and T. G. Perrring. Two energy scales in the spin excitations of the high-temperature superconductor $La_{2x}Sr_xCuO_4$. *Nat. Phys.*, 3:163, 2007.

[164] N. B. Christensen and D. F. McMorrow and H. M. Rønnow and B. Lake and S. M. Hayden and G. Aeppli and T. G. Perring and M. Mangkorntong and M. Nohara and H. Takagi. Dispersive Excitations in the High-Temperature Superconductor $La_{2-x}Sr_xCuO_4$. *Physical Review Letters*, 93(14):147002, 2004.

[165] Hayden SM, Mook HA, Dai PC, Perring TG, and Dogan F. The structure of the high-energy spin excitations in a high-transition-temperature superconductor. *Nature*, 429:531, 2004.

[166] Tranquada JM, Woo H, Perring TG, Goka H, Gu GD, Xu G, Fujita M, and Yamada K. Quantum magnetic excitations from stripes in copper oxide superconductors. *Nature*, 429:534, 2004.

[167] Ph. Bourges, B. Keimer, S. Pailhes, L.P. Regnault, Y. Sidis, and C. Ulrich. The resonant magnetic mode: A common feature of high-T_c superconductors. *Physica C*, 424:45–49, 2005.

[168] H. He, Y. Sidis, P. Bourges, G. D. Gu, A. Ivanov, N. Koshizuka, B. Liang, C. T. Lin, L. P. Regnault, E. Schoenherr, and B. Keimer. Resonant spin excitation in an overdoped high temperature superconductor. *Phys. Rev. Lett.*, 86(8):1610–1613, Feb 2001.

[169] Ch. Niedermayer, C. Bernhard, T. Blasius, A. Golnik, A. Moodenbaugh, and J. I. Budnick. Common Phase Diagram for Antiferromagnetism in $La_{2-x}Sr_xCuO_4$ and $Y_{1-x}Ca_xBa_2Cu_3O_6$ as Seen by Muon Spin Rotation. *Phys. Rev. Lett.*, 80(17):3843–3846, Apr 1998.

[170] A. R. Moodenbaugh, Youwen Xu, M. Suenaga, T. J. Folkerts, and R. N. Shelton. Superconducting properties of $La_{2-x}Ba_xCuO_4$. *Phys. Rev. B*, 38(7):4596–4600, Sep 1988.

[171] J. D. Axe, A. H. Moudden, D. Hohlwein, D. E. Cox, K. M. Mohanty, A. R. Moodenbaugh, and Youwen Xu. Structural phase transformations and superconductivity in $La_{2-x}Ba_xCuO_4$. *Phys. Rev. Lett.*, 62(23):2751–2754, Jun 1989.

[172] K. Kumagai, K. Kawano, H. Kagami, G. Suzuki, Y. Matsuda, I. Watanabe, K. Nishiyama, and K. Nagamine. Magnetic order and suppression of superconductivity around $x = 0.12$ in $La_{2-x}Sr_xCuO_4$ and $La_{2-x}Ba_xCuO_4$. *Physica C*, 235-240:1715, 1994.

[173] K. Kumagai, K. Kawano, I. Watanabe, K. Nishiyama, and K. Nagamine. Magnetic order and evolution of the electronic-state around $x = 0.12$ IN $La_{2-x}Ba_xCuO_4$ AND $La_{2-x}Sr_xCuO_4$. *J. Supercond.*, 7:63, 1994.

[174] J. M. Tranquada, J. D. Axe, N. Ichikawa, A. R. Moodenbaugh, Y. Nakamura, and S. Uchida. Coexistence of, and Competition between, Superconductivity and Charge-Stripe Order in $La_{1.6-x}Nd_{0.4}Sr_xCuO_4$. *Phys. Rev. Lett.*, 78(2):338–341, Jan 1997.

[175] N. B. Christensen, H. M. Rønnow, J. Mesot, R. A. Ewings, N. Momono, M. Oda, M. Ido, M. Enderle, D. F. McMorrow, and A. T. Boothroyd. Nature of the Magnetic Order in the Charge-Ordered Cuprate $La_{1.48}Nd_{0.4}Sr_{0.12}CuO_4$. *Physical Review Letters*, 98(19):197003, 2007.

[176] M. Fujita, H. Goka, K. Yamada, and M. Matsuda. Competition between Charge- and Spin-Density-Wave Order and Superconductivity in $La_{1.875}Ba_{0.125-x}Sr_xCuO_4$. *Phys. Rev. Lett.*, 88(16):167008, Apr 2002.

[177] M. Fujita, H. Goka, K. Yamada, and M. Matsuda. Structural effect on the static spin and charge correlations in $La_{1.875}Ba_{0.125-x}Sr_xCuO_4$. *Phys. Rev. B*, 66(18):184503, Nov 2002.

[178] H. Kimura, Y. Noda, H. Goka, M. Fujita, K. Yamada, M. Mizumaki, N. Ikeda, and H. Ohsumi. Relationship between charge stripe order and structural phase transitions in $La_{1.875}Ba_{0.125-x}Sr_xCuO_4$. *Physical Review B (Condensed Matter and Materials Physics)*, 70(13):134512, 2004.

[179] I. Watanabe, T. Adachi, K. Takahashi, S. Yairi, Y. Koike, and K. Nagamine. Muon-spin-relaxation study of the effect of nonmagnetic impurities on the Cu-spin fluctuations in $La_{2-x}Sr_xCu_{1-y}Zn_yO_4$ around $x = 0.115$. *Phys. Rev. B*, 65(18):180516, May 2002.

[180] Megumi Akoshima, Takashi Noji, Yasuhiro Ono, and Yoji Koike. Anomalous suppression of superconductivity in Zn-substituted $Bi_2Sr_2Ca_{1-x}Y_x(Cu_{1-y}Zn_y)_2O_{8+\delta}$. *Phys. Rev. B*, 57(13):7491–7494, Apr 1998.

[181] Y. Koike, M. Akoshima, M. Aoyama, K. Nishimaki, T. Kawamata, T. Adachi, T. Noji, I. Watanabe, S. Ohira, W. Higemoto, and K. Nagamine. Possible charge and/or spin ordering in the bi-2212, y-123 and la-214 phases. *Int. J. of Mod. Phys. B*, 14:3520, 2000.

[182] Susumu Katano, Masugu Sato, Kazuyoshi Yamada, Takao Suzuki, and Tetsuo Fukase. Enhancement of static antiferromagnetic correlations by magnetic field in a superconductor $La_{2-x}Sr_xCuO_4$ with $x = 0.12$. *Phys. Rev. B*, 62(22):R14677–R14680, Dec 2000.

[183] B. Lake, H. M. Rønnow, N. B. Christensen, G. Aeppli, K. Lefmann, D.F.McMorrow, P.Vorderwisch, P. Smeibidl, N.Mangkorntong, T. Sasagawa, M. Noharaand H. Takagi, and T. E. Mason. *Nature*, 415:299, 2002.

[184] Arumugam, S. and Môri, N. and Takeshita, N. and Takashima, H. and Noda, T. and Eisaki, H. and Uchida, S. . Competition of Static Stripe and Superconducting Phases in $La_{1.48}Nd_{0.4}Sr_{0.12}CuO_4$ Controlled by Pressure. *Phys. Rev. Lett.*, 88(24):247001, May 2002.

[185] B. Khaykovich, Y. S. Lee, R. W. Erwin, S.-H. Lee, S. Wakimoto, K. J. Thomas, M. A. Kastner, and R. J. Birgeneau. Enhancement of long-range magnetic order by magnetic field in superconducting La_2CuO_{4+y}. *Phys. Rev. B*, 66(1):014528, Jul 2002.

[186] B. Khaykovich, R. J. Birgeneau, F. C. Chou, R. W. Erwin, M. A. Kastner, S.-H. Lee, Y. S. Lee, P. Smeibidl, P. Vorderwisch, and S. Wakimoto. Effect of a magnetic field on long-range magnetic order in stage-4 and stage-6 superconducting La_2CuO_{4+y} . *Phys. Rev. B*, 67(5):054501, Feb 2003.

[187] M. Matsuda, M. Fujita, K. Yamada, R. J. Birgeneau, Y. Endoh, and G. Shirane. Magnetic field effects and magnetic anisotropy in lightly doped $La_{2-x}Sr_xCuO_4$. *Phys. Rev. B*, 66(17):174508, Nov 2002.

[188] S. Wakimoto, R. J. Birgeneau, Y. Fujimaki, N. Ichikawa, T. Kasuga, Y. J. Kim, K. M. Kojima, S.-H. Lee, H. Niko, J. M. Tranquada, S. Uchida, and M. v. Zimmermann. Effect of a magnetic field on the spin- and charge-density-wave order in $La_{1.45}Nd_{0.4}Sr_{0.15}CuO_4$. *Physical Review B (Condensed Matter and Materials Physics)*, 67(18):184419, 2003.

[189] B. Khaykovich, S. Wakimoto, R. J. Birgeneau, M. A. Kastner, Y. S. Lee, P. Smeibidl, P. Vorderwisch, and K. Yamada. Field-induced transition between magnetically disordered and ordered phases in underdoped $La_{2-x}Sr_xCuO_4$. *Physical Review B (Condensed Matter and Materials Physics)*, 71(22):220508, 2005.

[190] Le, L. P. and Keren, A. and Luke, G. M. and Sternlieb, B. J. and Wu, W. D. and Uemura, Y. J. and Brewer, J. H. and Riseman, T. M. and Upasani, R. V. and Chiang, L. Y. and Kang, W. and Chaikin, P. M. and Csiba, T. and Grüner, G. . Muon-spin-rotation and relaxation studies in $(TMTSF)_2$-X compounds. *Phys. Rev. B*, 48(10):7284–7296, Sep 1993.

[191] A. T. Savici, Y. Fudamoto, I. M. Gat, T. Ito, M. I. Larkin, Y. J. Uemura, G. M. Luke, K. M. Kojima, Y. S. Lee, M. A. Kastner, R. J. Birgeneau, and K. Yamada. Muon spin relaxation studies of incommensurate magnetism and superconductivity in stage-4 $La_2CuO_{4.11}$ and $La_{1.88}Sr_{0.12}CuO_4$. *Phys. Rev. B*, 66(1):014524, Jul 2002.

[192] B. Nachumi, Y. Fudamoto, A. Keren, K. M. Kojima, M. Larkin, G. M. Luke, J. Merrin, O. Tchernyshyov, Y. J. Uemura, N. Ichikawa, M. Goto, H. Takagi, S. Uchida, M. K. Crawford, E. M. McCarron, D. E. MacLaughlin, and R. H. Heffner. Muon spin relaxation study of the stripe phase order in $La_{1.6-x}Nd_{0.4}Sr_xCuO_4$ and related 214 cuprates. *Phys. Rev. B*, 58(13):8760–8772, Oct 1998.

[193] M. Fujita, H. Goka, K. Yamada, J. M. Tranquada, and L. P. Regnault. Stripe order, depinning, and fluctuations in La[sub 1.875]Ba[sub 0.125]CuO[sub 4] and $La_{1.875}Ba_{0.075}Sr_{0.050}CuO_4$. *Physical Review B (Condensed Matter and Materials Physics)*, 70(10):104517, 2004.

[194] M. Fujita, M. Matsuda, H. Gokaa, T. Adachi, Y. Koike, and K. Yamada. Magnetic field-effect on static spin correlation in static stripe ordered phase of $La_{2-x}Ba_xCuO_4$. *J. Phys. Conf. Ser.*, 51:510, 2006.

[195] H. E. Mohotalla, B.O. Wells, J.I. Budnick, W.A. Hines, C. Niedermayer, L. Udby, C. Bernhard, A.R. Moodenbaugh, and F.C. Chou. Phase separation in superoxygenated $La_{2-x}Sr_xCuO_{4+y}$. *Nat. Mat.*, 5:377, 2006.

[196] Y. J. Uemura, W. J. Kossler, X. H. Yu, J. R. Kempton, H. E. Schone, D. Opie, C. E. Stronach, D. C. Johnston, M. S. Alvarez, and D. P. Goshorn. Antiferromagnetism of La_2CuO_{4-y} studied by muon-spin rotation. *Phys. Rev. Lett.*, 59(9):1045–1048, Aug 1987.

[197] J.I. Budnick, A. Golnik, C. Niedermayer, E. Recknagel, M. Rossmanith, A. Weidinger, B. Chamberland, M. Filipkowski, and D.P. Yang. Observation of magnetic-ordering in La_2CuO_4 by muon spin rotation spectroscopy. *Phys. Lett. A*, 124:103, 1987.

[198] J.I. Budnick, B. Chamberland, D.P. Yang, C. Niedermayer, A. Golnik, E. Recknagel, M. Rossmanith, and A. Weidinger. Dependence of the neel-temperatures of La_2CuO_4 on sr-doping studied by muon spin rotation. *Europhysics letters*, 5:651, 1988.

[199] Y.J. Uemura. Combination of muon spin relaxation and neutron-scattering studies on magnetism. *Hyperfine Interact.*, 49:205, 1989.

[200] A. T. Savici, A. Fukaya, I. M. Gat-Malureanu, T. Ito, P. L. Russo, Y. J. Uemura, C. R. Wiebe, P. P. Kyriakou, G. J. MacDougall, M. T. Rovers, G. M. Luke, K. M. Kojima, M. Goto, S. Uchida, R. Kadono, K. Yamada, S. Tajima, T. Masui, H. Eisaki, N. Kaneko, M. Greven, and G. D. Gu. Muon Spin Relaxation Studies of Magnetic-Field-Induced Effects in High-T_c Superconductors. *Physical Review Letters*, 95(15):157001, 2005.

[201] Matthias Mayr et al. One-particle spectral function and local density of states in a phenomenological mixed-phase model for high-temperature superconductors. *Phys. Rev. B*, 73(1):014509, 2006.

[202] Gonzalo Alvarez et al. Areas of superconductivity and giant proximity effects in underdoped cuprates. *Phys. Rev. B*, 71(1):014514, Jan 2005.

[203] R. S. Hayano et al. Zero-and low-field spin relaxation studied by positive muons. *Phys. Rev. B*, 20(3):850–859, Aug 1979.

[204] Eugene Demler, Subir Sachdev, and Ying Zhang. Spin-ordering quantum transitions of superconductors in a magnetic field. *Phys. Rev. Lett.*, 87(6):067202, Jul 2001.

[205] Ying Zhang, Eugene Demler, and Subir Sachdev. Competing orders in a magnetic field: Spin and charge order in the cuprate superconductors. *Phys. Rev. B*, 66(9):094501, Sep 2002.

[206] Subir Sachdev. Colloquium: Order and quantum phase transitions in the cuprate superconductors. *Rev. Mod. Phys.*, 75(3):913–932, Jul 2003.

[207] a similar phase diagram was reported by J. M. Tranquada, see Handbook of High Temperature Superconductivity, Springer 2007.

[208] M. Lee, A. Husmann, T. F. Rosenbaum, and G. Aeppli. High resolution study of magnetic ordering at absolute zero. *Physical Review Letters*, 92(18):187201, 2004.

[209] M. R. Norman, Qimiao Si, Ya. B. Bazaliy, and R. Ramazashvili. Hall effect in nested antiferromagnets near the quantum critical point. *Phys. Rev. Lett.*, 90(11):116601, Mar 2003.

[210] Philipp Gegenwart et al. *arXiv:0712.2045*.

[211] Nicolas Doiron-Leyraud, C. Proust, D. LeBoeuf, J. Levallois, J.B. Bonnemaison, R.X. Liang, D.A. Bonn, W.N. Hardy, and L. Taillefer. Quantum oscillations and the Fermi surface in an underdoped high-T_c superconductor . *Nature*, 447:565, 2007.

[212] E. A. Yelland, J. Singleton, C. H. Mielke, N. Harrison, F. F. Balakirev, B. Dabrowski, and J. R. Cooper. Quantum Oscillations in the Underdoped Cuprate $YBa_2Cu_4O_8$. *Physical Review Letters*, 100(4):047003, 2008.

[213] A. F. Bangura, J. D. Fletcher, A. Carrington, J. Levallois, M. Nardone, B. Vignolle, P. J. Heard, N. Doiron-Leyraud, D. LeBoeuf, L. Taillefer, S. Adachi, C. Proust, and N. E. Hussey. Small Fermi Surface Pockets in Underdoped High Temperature Superconductors: Observation of Shubnikov–de Haas Oscillations in $YBa_2Cu_4O_8$. *Physical Review Letters*, 100(4):047004, 2008.

[214] C. Jaudet et al. *arXiv:0711.3559*.

[215] Sudip Chakravarty and Hae-Young Lee Kee. *arXiv:0707.0608*.

[216] H. Kimura, M. Kofu, Y. Matsumoto, and K. Hirota. Novel In-Gap Spin State in Zn-Doped $La_{1.85}Sr_{0.15}CuO_4$. *Phys. Rev. Lett.*, 91(6):067002, Aug 2003.

[217] Brian M. Andersen, P. J. Hirschfeld, Arno P. Kampf, and Markus Schmid. Disorder-induced static antiferromagnetism in cuprate superconductors. *Physical Review Letters*, 99(14):147002, 2007.

[218] K. Fujita, T. Noda, K. M. Kojima, H. Eisaki, and S. Uchida. Effect of Disorder Outside the CuO_2 Planes on T_c of Copper Oxide Superconductors. *Physical Review Letters*, 95(9):097006, 2005.

[219] F. Rullier-Albenque et al. *arXiv:0710.3737*.

[220] S. Sanna, G. Allodi, G. Concas, A. D. Hillier, and R. De Renzi. Nanoscopic Coexistence of Magnetism and Superconductivity in $YBa_2Cu_3O_{6+x}$ Detected by Muon Spin Rotation. *Physical Review Letters*, 93(20):207001, 2004.

[221] J. Bardeen, L. N. Cooper, and J. R. Schrieffer. Theory of superconductivity. *Phys. Rev.*, 108(5):1175–1204, Dec 1957.

[222] T. E. Mason, G. Aeppli, and H. A. Mook. Magnetic dynamics of superconducting $La_{1.86}Sr_{0.14}CuO_4$. *Phys. Rev. Lett.*, 68(9):1414–1417, Mar 1992.

[223] K. Yamada, S. Wakimoto, G. Shirane, C. H. Lee, M. A. Kastner, S. Hosoya, M. Greven, Y. Endoh, and R. J. Birgeneau. Direct Observation of a Magnetic Gap in Superconducting $La_{1.85}Sr_{0.15}CuO_4$ ($T_c = 37.3K$). *Phys. Rev. Lett.*, 75(8):1626–1629, Aug 1995.

[224] T. E. Mason, G. Aeppli, S. M. Hayden, A. P. Ramirez, and H. A. Mook. Low energy excitations in superconducting $La_{1.86}Sr_{0.14}CuO_4$. *Phys. Rev. Lett.*, 71(6):919–922, Aug 1993.

[225] Mason, T. E. and Schröder, A. and Aeppli, G. and Mook, H. A. and Hayden, S. M. New Magnetic Coherence Effect in Superconducting $La_{2-x}Sr_xCuO_4$. *Phys. Rev. Lett.*, 77(8):1604–1607, Aug 1996.

[226] J. Chang and A. P. Schnyder and R. Gilardi and H. M. Rønnow and S. Pailhes and N. B. Christensen and Ch. Niedermayer and D. F. McMorrow and A. Hiess and A. Stunault and M. Enderle and B. Lake and O. Sobolev and N. Momono and M. Oda and M. Ido and C. Mudry and J. Mesot. Magnetic-Field-Induced Spin Excitations and Renormalized Spin Gap of the Underdoped $La_{1.895}Sr_{0.105}CuO_4$ Superconductor. *Physical Review Letters*, 98(7):077004, 2007.

[227] B Lake. Spin gap and magnetic coherence in a clean high-temperature superconductor. *NATURE*, 400:43–46, 1999.

[228] E. M. Motoyama, P. K. Mang, D. Petitgrand, G. Yu, O. P. Vajk, I. M. Vishik, and M. Greven. Magnetic Field Effect on the Superconducting Magnetic Gap of $Nd_{1.85}Ce_{0.15}CuO_4$. *Physical Review Letters*, 96(13):137002, 2006.

[229] D. J. Scalapino, E. Loh, and J. E. Hirsch. *d*-wave pairing near a spin-density-wave instability. *Phys. Rev. B*, 34(11):8190–8192, Dec 1986.

[230] Toru Moriya and Kazuo Ueda. *Rep. Prog. Phys.*, 66:1299–1341, 2003.

[231] Migaku Oda, Naoki Momono, and Masayuki Ido. What is the energy scale in determining the T_c of cuprate superconductivity? *Supercond. Sci. Technol.*, 13:R139, 2000.

[232] G. Aeppli, T.E. Mason, S.M. Hayden, H.A. Mook, and J. Kulda. Nearly singular magnetic fluctuations in the normal state of a high-tc cuprate superconductor. *Science*, 278:1432, 1997.

[233] J. M. Tranquada and C. H. Lee and K. Yamada and Y. S. Lee and L. P. Regnault and H. M. Rønnow. Evidence for an incommensurate magnetic resonance in $La_{2-x}Sr_xCuO_4$. *Physical Review B (Condensed Matter and Materials Physics)*, 69(17):174507, 2004.

[234] B. Lake, G. Aeppli, K.N. Clausen, D.F. McMorrow, K. Lefmann, N.E. Hussey, N. Mangkorntong, M. Nohara, H. Takagi, T.E. Mason, and A. Schroder. Spins in the vortices of a high-temperature superconductor. *Science*, 291:1759, 2001.

[235] R. Gilardi, A. Hiess, N. Momono, M. Oda, M. Ido, and Mesot J. Unusual interplay between copper-spin and vortex dynamics in slightly overdoped $La_{1.83}Sr_{0.17}CuO_4$. *Europhysics Letters*, 66:840, 2004.

[236] Subir Sachdev. *Quantum Phase Transitions*. Cambridge University Press, 1999.

[237] C.-H. Lee et al. *J. Phys. Soc. Jpn.*, 69:1170, 2000.

[238] S. Pailhès and Y. Sidis and P. Bourges and V. Hinkov and A. Ivanov and C. Ulrich and L. P. Regnault and B. Keimer. Resonant Magnetic Excitations at High Energy in Superconducting $YBa_2Cu_3O_{6.85}$. *Physical Review Letters*, 93(16):167001, 2004.

[239] I. Eremin, D. K. Morr, A. V. Chubukov, K. H. Bennemann, and M. R. Norman. Novel neutron resonance mode in $d_{x_2-y_2}$-wave superconductors. *Physical Review Letters*, 94(14):147001, 2005.

[240] N. Bulut and D. J. Scalapino. Neutron scattering from a collective spin fluctuation mode in a CuO_2 bilayer. *Phys. Rev. B*, 53(9):5149–5152, Mar 1996.

[241] M. R. Norman. Linear response theory and the universal nature of the magnetic excitation spectrum of the cuprates. *Physical Review B (Condensed Matter and Materials Physics)*, 75(18):184514, 2007.

[242] J. Mesot, M. R. Norman, H. Ding, M. Randeria, J. C. Campuzano, A. Paramekanti, H. M. Fretwell, A. Kaminski, T. Takeuchi, T. Yokoya, T. Sato, T. Takahashi, T. Mochiku, and K. Kadowaki. Superconducting gap anisotropy and quasiparticle interactions: A doping dependent photoemission study. *Phys. Rev. Lett.*, 83(4):840–843, Jul 1999.

[243] S. V. Borisenko, A. A. Kordyuk, T. K. Kim, S. Legner, K. A. Nenkov, M. Knupfer, M. S. Golden, J. Fink, H. Berger, and R. Follath. Superconducting gap in the presence of bilayer splitting in underdoped $(Pb,Bi)_2Sr_2CaCu_2O_{8+\delta}$. *Phys. Rev. B*, 66(14):140509, Oct 2002.

[244] A. P. Schnyder, A. Bill, C. Mudry, R. Gilardi, H. M. Rønnow, and J. Mesot. Influence of higher d-wave gap harmonics on the dynamical magnetic susceptibility of high-temperature superconductors. *Physical Review B (Condensed Matter and Materials Physics)*, 70(21):214511, 2004.

[245] C. Stock, W. J. L. Buyers, Z. Yamani, C. L. Broholm, J.-H. Chung, Z. Tun, R. Liang, D. Bonn, W. N. Hardy, and R. J. Birgeneau. Central mode and spin confinement near the boundary of the superconducting phase in $YBa_2Cu_3O_6.353$ ($T_c = 18$ K). *Physical Review B (Condensed Matter and Materials Physics)*, 73(10):100504, 2006.

[246] A. Schneidewind et al. *Physica B*, 385:1089, 2006.

[247] P. Bourges, L.P. Regnault, J.Y. Henry, C. Vettier, Y. Sidis, and P. Burlet. Spin dynamics in the metallic state of the high-T_c superconducting system $YBa_2Cu_3O_{6+x}$. *Physica B*, 215:30–40, 1995.

[248] Dai, Pengcheng and Mook, H. A. and Hunt, R. D. and Doğan, F. Evolution of the resonance and incommensurate spin fluctuations in superconducting $YBa_2Cu_3O_{6+x}$. *Phys. Rev. B*, 63(5):054525, Jan 2001.

[249] Shiliang Li, Zahra Yamani, Hye Jung Kang, Kouji Segawa, Yoichi Ando, Xin Yao, H. A. Mook, and Pengcheng Dai. Quantum spin excitations through the metal-to-insulator crossover in $YBa_2Cu_3O_{6+y}$. *Physical Review B (Condensed Matter and Materials Physics)*, 77(1):014523, 2008.

[250] J. C. Campuzano *et al. Physics of Conventional Superconductors*. Spinger-Verlag, 2004.

[251] Andrea Damascelli, Zahid Hussain, and Zhi-Xun Shen. Angle-resolved photoemission studies of the cuprate superconductors. *Reviews of Modern Physics*, 75(2):473, 2003.

[252] Kiyohisa Tanaka, W.S. Lee, D.H. Lu, A. Fujimori, T. Fujii, Risdiana, I. Terasaki, D.J. Scalapino, T.P. Devereaux, Z. Hussain, and Z.-X. Shen. Distinct fermi-momentum-dependent energy gaps in deeply underdoped bi2212. *Science*, 314:1910, 2006.

[253] A. Kanigel et al. *arXiv:0708.4099*.

[254] Ofer Yuli, Itay Asulin, Oded Millo, and Gad Koren. Scanning tunneling spectroscopy characterization of the pseudogap and the $x = (1/8)$ anomaly in $La_{2-x}Sr_xCuO_4$ thin films. *Physical Review B (Condensed Matter and Materials Physics)*, 75(18):184521, 2007.

[255] M. Le Tacon, A. Sacuto, A. Georges, G. Kotliar, Y. Gallais, and D. Colson A. Forget. Two energy scales and two distinct quasiparticle dynamics in the superconducting state of underdoped cuprates. *Nature Physics*, 2:537, 2006.

[256] N.W. Ashcroft and N.D. Mermin. *Solid State Physics*.

[257] N. Hussey. *Handbook of High-Temperature Superconductivity*. springer, 2007.

[258] D. N. Basov and T. Timusk. Electrodynamics of high-T_c superconductors. *Reviews of Modern Physics*, 77(2):721, 2005.

[259] Heinrich Hertz. *Annalen der Physik*, 33:983, 1887.

[260] A. Kaminski, S. Rosenkranz, H. M. Fretwell, M. R. Norman, M. Randeria, J. C. Campuzano, J-M. Park, Z. Z. Li, and H. Raffy. Change of Fermi-surface topology in $Bi_2Sr_2CaCu_2O_{8+\delta}$ with doping. *Physical Review B (Condensed Matter and Materials Physics)*, 73(17):174511, 2006.

[261] H. Ding, A. F. Bellman, J. C. Campuzano, M. Randeria, M. R. Norman, T. Yokoya, T. Takahashi, H. Katayama-Yoshida, T. Mochiku, K. Kadowaki, G. Jennings, and G. P. Brivio. Electronic Excitations in $Bi_2Sr_2CaCu_2O_8$: Fermi Surface, Dispersion, and Absence of Bilayer Splitting. *Phys. Rev. Lett.*, 76(9):1533–1536, Feb 1996.

[262] D. S. Marshall, D. S. Dessau, A. G. Loeser, C-H. Park, A. Y. Matsuura, J. N. Eckstein, I. Bozovic, P. Fournier, A. Kapitulnik, W. E. Spicer, and Z.-X. Shen. Unconventional Electronic Structure Evolution with Hole Doping in $Bi_2Sr_2CaCu_2O_{8+\delta}$: Angle-Resolved Photoemission Results. *Phys. Rev. Lett.*, 76(25):4841–4844, Jun 1996.

[263] A.G. Loeser, Z.X. Shen, D.S. Dessau, D.S. Marshall, C.H. Park, P. Fournier, and A. Kapitulnik. Excitation gap in the normal state of underdoped $Bi_2Sr_2CaCu_2O_{8+\delta}$. *Science*, 273:325, 1996.

[264] A. Kaminski, M. Randeria, J. C. Campuzano, M. R. Norman, H. Fretwell, J. Mesot, T. Sato, T. Takahashi, and K. Kadowaki. Renormalization of Spectral Line Shape and Dispersion below T_c in $Bi_2Sr_2CaCu_2O_{8+\delta}$. *Phys. Rev. Lett.*, 86(6):1070–1073, Feb 2001.

[265] T. Valla, A.V. Fedorov, P.D. Johnson, B.O. Wells, S.L. Hulbert, Q. Li, G.D. Gu, and N. Koshizuka. Evidence for quantum critical behavior in the optimally doped cuprate $Bi_2Sr_2CaCu_2O_{8+\delta}$. *Science*, 285, 1999.

[266] Akihiro Ino, Changyoung Kim, Takashi Mizokawa, Zhi-Xun Shen, Atsushi Fujimori, Masamitsu Takaba, Kenji Tamasaku, Hiroshi Eisaki, and Shinichi Uchida. Fermi Surface and Band Dispersion in $La_{2-x}Sr_xCuO_4$. *J. Phys. Soc. Jpn.*, 68:1496, 1999.

[267] A. Ino, C. Kim, M. Nakamura, T. Yoshida, T. Mizokawa, Z.-X. Shen, A. Fujimori, T. Kakeshita, H. Eisaki, and S. Uchida. Electronic structure of $La_{2-x}Sr_xCuO_4$ in the vicinity of the superconductor-insulator transition. *Phys. Rev. B*, 62(6):4137–4141, Aug 2000.

[268] A. Ino, C. Kim, M. Nakamura, T. Yoshida, T. Mizokawa, A. Fujimori, Z.-X. Shen, T. Kakeshita, H. Eisaki, and S. Uchida. Doping-dependent evolution of the electronic structure of $La_{2-x}Sr_xCuO_4$ in the superconducting and metallic phases. *Phys. Rev. B*, 65(9):094504, Feb 2002.

[269] C. N. Berglund and W. E. Spicer. Photoemission studies of copper and silver: Theory. *Phys. Rev.*, 136(4A):A1030–A1044, Nov 1964.

[270] Wolfgang Schattke and Michel A. Van Hove, editors. *Solid-State Photoemmission and Related methods*. WILEY, 2003.

[271] J.J. Sakurai. *Modern Quantum Mechanics*. ADDISON WESLEY, 1994.

[272] Stefan Hufner. *Photoelectron Spectroscopy*. Springer, 2003.

[273] X. J. Zhou, T. Cuk, T. Devereaux, N. Nagaosa, and Z.-X. Shen. Angle-resolved photoemission spectroscopy on electronic structure and electron-phonon coupling in cuprate superconductors. *cond-mat/0604284*, 2006.

[274] M. P. Seah and W. A. Dench. *Surface and Interface Analysis*, 1:2, 1979.

[275] Martin Månsson and Thomas Claesson and Ulf O. Karlsson and Oscar Tjernberg and Stéphane Pailhés and Johan Chang and Joël Mesot and Ming Shi and Luc Patthey and Naoki Momono and Migaku Oda and Masayuki Ido. On-board sample cleaver. *Review of Scientific Instruments*, 78(7):076103, 2007.

[276] Kyle Michael Shen. PhD thesis, Stanford University, 2005.

[277] Reinert, F. and Nicolay, G. and Schmidt, S. and Ehm, D. and Hüfner, S. . Direct measurements of the l-gap surface states on the (111) face of noble metals by photoelectron spectroscopy. *Phys. Rev. B*, 63(11):115415, Mar 2001.

[278] Friedrich Reinert and Stefan Hüfner. Photoemission spectroscopy - from early days to recent applications. *New Journal of Physics*, 7:97, 2005.

[279] A. Kaminski, S. Rosenkranz, H. M. Fretwell, J. Mesot, M. Randeria, J. C. Campuzano, M. R. Norman, Z. Z. Li, H. Raffy, T. Sato, T. Takahashi, and K. Kadowaki. Identifying the background signal in angle-resolved photoemission spectra of high-temperature cuprate superconductors. *Physical Review B (Condensed Matter and Materials Physics)*, 69(21):212509, 2004.

[280] M.R. Norman, H. Ding, M. Randeria, J.C. Campuzano, T. Yokoya, T. Takeuchi, T. Takahashi, T. Mochiku, K. Kadowaki, P. Guptasarma, and D.G. Hinks. Destruction of the Fermi surface underdoped high-T_c superconductors. *Nature*, 392:157, 1998.

[281] D. V. Evtushinsky and A. A. Kordyuk and S. V. Borisenko and V. B. Zabolotnyy and M. Knupfer and J. Fink and B. Büchner and A. V. Pan and A. Erb and C. T. Lin and H. Berger. Unadulterated spectral function of low-energy quasiparticles in $Bi_2Sr_2CaCu_2O_{8+delta}$. *Physical Review B (Condensed Matter and Materials Physics)*, 74(17):172509, 2006.

[282] K. Ishizaka et al. *arXiv:0710.2962*, 2007.

[283] J. Mesot, M. Randeria, M. R. Norman, A. Kaminski, H. M. Fretwell, J. C. Campuzano, H. Ding, T. Takeuchi, T. Sato, T. Yokoya, T. Takahashi, I. Chong, T. Terashima, M. Takano, T. Mochiku, and K. Kadowaki. Determination of the Fermi surface in high-T_c superconductors by angle-resolved photoemission spectroscopy. *Phys. Rev. B*, 63(22):224516, May 2001.

[284] T. Yoshida, X. J. Zhou, M. Nakamura, S. A. Kellar, P. V. Bogdanov, E. D. Lu, A. Lanzara, Z. Hussain, A. Ino, T. Mizokawa, A. Fujimori, H. Eisaki, C. Kim, Z.-X. Shen, T. Kakeshita, and S. Uchida. Electronlike Fermi surface and remnant $(\pi, 0)$ feature in overdoped $La_{1.78}Sr_{0.22}CuO_4$. *Phys. Rev. B*, 63(22):220501, May 2001.

[285] A. Narduzzo et al. *arXiv:0707.4601*.

[286] T. Yoshida, X. J. Zhou, T. Sasagawa, W. L. Yang, P. V. Bogdanov, A. Lanzara, Z. Hussain, T. Mizokawa, A. Fujimori, H. Eisaki, Z.-X. Shen, T. Kakeshita, and S. Uchida. Metallic Behavior of Lightly Doped $La_{2-x}Sr_xCuO_4$ with a Fermi Surface Forming an Arc. *Physical Review Letters*, 91(2):027001, 2003.

[287] X.J. Zhou, T. Yoshida, A. Lanzara, P.V. Bogdanov, S.A. Kellar, K.M. Shen, W.L. Yang, F. Ronning, T. Sasagawa, T. Kakeshita, T. Noda, H. Eisaki, S. Uchida, C.T. Lin, F. Zhou, J.W. Xiong, W.X. Ti, Z.X. Zhao, A. Fujimori, Z. Hussain, and Z.X. Shen. Universal nodal fermi velocity. *Nature*, 423:398, 2003.

[288] J. M. Luttinger. Fermi surface and some simple equilibrium properties of a system of interacting fermions. *Phys. Rev.*, 119(4):1153–1163, Aug 1960.

[289] Masaki Oshikawa. Topological approach to luttinger's theorem and the fermi surface of a kondo lattice. *Phys. Rev. Lett.*, 84(15):3370–3373, Apr 2000.

[290] S. Sahrakorpi, M. Lindroos, R. S. Markiewicz, and A. Bansil. Evolution of Midgap States and Residual Three Dimensionality in $La_{2-x}Sr_xCuO_4$. *Physical Review Letters*, 95(15):157601, 2005.

[291] N. Hussey, M. Abdel-Jawad, A. Carrington, A.P. Mackenzie, and L. Balicas. A coherent three-dimensional fermi surface in a high-transition-temperature superconductor. *Nature*, 425:814, 2003.

[292] Lee et al. *cond-mat/0606347*, 2006. and references therein.

[293] M. Platé and J. D. F. Mottershead and I. S. Elfimov and D. C. Peets and Ruixing Liang and D. A. Bonn and W. N. Hardy and S. Chiuzbaian and M. Falub and M. Shi and L. Patthey and A. Damascelli. Fermi Surface and Quasiparticle Excitations of Overdoped $Tl_2Ba_2CuO_{6+delta}$. *Physical Review Letters*, 95(7):077001, 2005.

[294] M. Hashimoto, T. Yoshida, K. Tanaka, A. Fujimori, M. Okusawa, S. Wakimoto, K. Yamada, T. Kakeshita, H. Eisaki, and S. Uchida. Distinct doping dependences of the pseudogap and superconducting gap of $La_{2-x}Sr_xCuO_4$ cuprate superconductors. *Physical Review B (Condensed Matter and Materials Physics)*, 75(14):140503, 2007.

[295] W. S. Lee, I.M. Vishik, K. Tanaka, D.H. Lu, T. Sasagawa, N. Nagaosa, T.P. Devereaux, Z. Hussain, and Z.X. Shen. Abrupt onset of a second energy gap at the superconducting transition of underdoped bi2212. *Nature*, 450:81, 2007.

[296] K. Terashima, H. Matsui, T. Sato, T. Takahashi, M. Kofu, and K. Hirota. Anomalous Momentum Dependence of the Superconducting Coherence Peak and Its Relation to the Pseudogap of $La_1.85Sr_0.15CuO_4$. *Physical Review Letters*, 99(1):017003, 2007.

[297] Takeshi Kondo, Tsunehiro Takeuchi, Adam Kaminski, Syunsuke Tsuda, and Shik Shin. Evidence for Two Energy Scales in the Superconducting State of Optimally Doped $(Bi,Pb)_2(Sr,La)_2CuO_{6+\delta}$. *Physical Review Letters*, 98(26):267004, 2007.

[298] W. Guyard et al. *Condmat*, page 0708.3732, 2007.

[299] M. Aichhorn, E. Arrigoni, Z. B. Huang, and W. Hanke. Superconducting Gap in the Hubbard Model and the Two-Gap Energy Scales of High-T_c Cuprate Superconductors. *Physical Review Letters*, 99(25):257002, 2007.

[300] A. Kanigel, M.R. Norman, M. Randeria, U. Chatterjee, S. Souma, A. Kaminski H.M. Fretwell, S. Rosenkranz, M. Shi, T. Sato, T. Takahashi, Z.Z. Li, H. Raffy, K. Kadowaki, D. Hinks, L. Ozyuzer, and J.C. Campuzano. Evolution of the pseudogap from fermi arcs to the nodal liquid. *Nature Physics*, 2:447–451, 2006.

[301] M. R. Norman, M. Randeria, H. Ding, and J. C. Campuzano. Phenomenology of the low-energy spectral function in high-T_c superconductors. *Phys. Rev. B*, 57(18):R11093–R11096, May 1998.

[302] K. Buczuk et al. *Nat. Phys.*, 3:168, 2007.

[303] Z. Sun, Y.-D. Chuang, A. V. Fedorov, J. F. Douglas, D. Reznik, F. Weber, N. Aliouane, D. N. Argyriou, H. Zheng, J. F. Mitchell, T. Kimura, Y. Tokura, A. Revcolevschi, and D. S. Dessau. Quasiparticlelike Peaks, Kinks, and Electron-Phonon Coupling at the (pi,0)

Regions in the CMR Oxide $La_{2-2x}Sr_{1+2x}Mn_2O_7$. *Physical Review Letters*, 97(5):056401, 2006.

[304] K. Sugawara, T. Sato, S. Souma, T. Takahashi, and H. Suematsu. Anomalous quasiparticle lifetime and strong electron-phonon coupling in graphite. *Physical Review Letters*, 98(3):036801, 2007.

[305] T. Valla, A. V. Fedorov, P. D. Johnson, and S. L. Hulbert. Many-body effects in angle-resolved photoemission: Quasiparticle energy and lifetime of a mo(110) surface state. *Phys. Rev. Lett.*, 83(10):2085–2088, Sep 1999.

[306] A. Kaminski, J. Mesot, H. Fretwell, J. C. Campuzano, M. R. Norman, M. Randeria, H. Ding, T. Sato, T. Takahashi, T. Mochiku, K. Kadowaki, and H. Hoechst. Quasiparticles in the Superconducting State of $Bi_2Sr_2CaCu_2O_{8+\delta}$. *Phys. Rev. Lett.*, 84(8):1788–1791, Feb 2000.

[307] A. Lanzara, P.V. Bogdanov, X.J. Zhou, S.A. Kellar, D.L. Feng, E.D Lu, T. Yoshida, H. Eisaki, A. Fujimori, K. Kishio, J.I. Shimoyama, T. Noda, S. Uchida, Z. Hussain, and Z.X. Shen. Evidence for ubiquitous strong electron-phonon coupling in high-temperature superconductors. *Nature*, 412:510, 2001.

[308] P. D. Johnson, T. Valla, A. V. Fedorov, Z. Yusof, B. O. Wells, Q. Li, A. R. Moodenbaugh, G. D. Gu, N. Koshizuka, C. Kendziora, Sha Jian, and D. G. Hinks. Doping and Temperature Dependence of the Mass Enhancement Observed in the Cuprate $Bi_2Sr_2CaCu_2O_{8+\delta}$. *Phys. Rev. Lett.*, 87(17):177007, Oct 2001.

[309] P. V. Bogdanov, A. Lanzara, S. A. Kellar, X. J. Zhou, E. D. Lu, W. J. Zheng, G. Gu, J.-I. Shimoyama, K. Kishio, H. Ikeda, R. Yoshizaki, Z. Hussain, and Z. X. Shen. Evidence for an Energy Scale for Quasiparticle Dispersion in $Bi_2Sr_2CaCu_2O_8$. *Phys. Rev. Lett.*, 85(12):2581–2584, Sep 2000.

[310] S. V. Borisenko, A. A. Kordyuk, T. K. Kim, A. Koitzsch, M. Knupfer, J. Fink, M. S. Golden, M. Eschrig, H. Berger, and R. Follath. Anomalous enhancement of the coupling to the magnetic resonance mode in underdoped pb-bi2212. *Physical Review Letters*, 90(20):207001, 2003.

[311] X. J. Zhou, T. Yoshida, D.-H. Lee, W. L. Yang, V. Brouet, F. Zhou, W. X. Ti, J. W. Xiong, Z. X. Zhao, T. Sasagawa, T. Kakeshita, H. Eisaki, S. Uchida, A. Fujimori, Z. Hussain, and Z.-X. Shen. Dichotomy between Nodal and Antinodal Quasiparticles in Underdoped $La_{2-x}Sr_xCuO_4$ Superconductors. *Physical Review Letters*, 92(18):187001, 2004.

[312] X. J. Zhou, Junren Shi, T. Yoshida, T. Cuk, W. L. Yang, V. Brouet, J. Nakamura, N. Mannella, Seiki Komiya, Yoichi Ando, F. Zhou, W. X. Ti, J. W. Xiong, Z. X. Zhao, T. Sasagawa, T. Kakeshita, H. Eisaki, S. Uchida, A. Fujimori, Zhenyu Zhang, E. W. Plummer, R. B. Laughlin, Z. Hussain, and Z.-X. Shen. Multiple Bosonic Mode Coupling in the Electron Self-Energy of $La_{2-x}Sr_xCuO_4$. *Physical Review Letters*, 95(11):117001, 2005.

[313] Mohit Randeria, Arun Paramekanti, and Nandini Trivedi. Nodal quasiparticle dispersion in strongly correlated d-wave superconductors. *Physical Review B (Condensed Matter and Materials Physics)*, 69(14):144509, 2004.

[314] H. He, P. Bourges, Y. Sidis, C. Ulrich, L.P. Regnault, S. Pailhes, N.S. Berzigiarova, N.N. Kolesnikov, and B. Keimer. Magnetic resonant mode in the single-layer high-temperature superconductor $Tl_2Ba_2CuO_{6+\delta}$. *Science*, 295:1045, 2002.

[315] L. Pintschovius, W. Reichardt, M. Kläser, T. Wolf, and H. v. Löhneysen. Pronounced In-Plane Anisotropy of Phonon Anomalies in $YBa_2Cu_3O_{6.6}$. *Phys. Rev. Lett.*, 89(3):037001, Jun 2002.

[316] Wentao Zhang, Guodong Liu, Lin Zhao, Haiyun Liu, Jianqiao Meng, Xiaoli Dong, Wei Lu, J. S. Wen, Z. J. Xu, G. D. Gu, T. Sasagawa, Guiling Wang, Yong Zhu, Hongbo Zhang, Yong Zhou, Xiaoyang Wang, Zhongxian Zhao, Chuangtian Chen, Zuyan Xu, and X. J. Zhou. Identification of a new form of electron coupling in the bi[sub 2]sr[sub 2]cacu[sub 2]o[sub 8] superconductor by laser-based angle-resolved photoemission spectroscopy. *Physical Review Letters*, 100(10):107002, 2008.

[317] J. Graf, G.-H. Gweon, K. McElroy, S. Y. Zhou, C. Jozwiak, E. Rotenberg, A. Bill, T. Sasagawa, H. Eisaki, S. Uchida, H. Takagi, D.-H. Lee, and A. Lanzara. Universal high energy anomaly in the angle-resolved photoemission spectra of high temperature superconductors: Possible evidence of spinon and holon branches. *Physical Review Letters*, 98(6):067004, 2007.

[318] B. P. Xie, K. Yang, D. W. Shen, J. F. Zhao, H. W. Ou, J. Wei, S. Y. Gu, M. Arita, S. Qiao, H. Namatame, M. Taniguchi, N. Kaneko, H. Eisaki, K. D. Tsuei, C. M. Cheng, I. Vobornik, J. Fujii, G. Rossi, Z. Q. Yang, and D. L. Feng. High-energy scale revival and giant kink in the dispersion of a cuprate superconductor. *Physical Review Letters*, 98(14):147001, 2007.

[319] T. Valla, T. E. Kidd, W.-G. Yin, G. D. Gu, P. D. Johnson, Z.-H. Pan, and A. V. Fedorov. High-energy kink observed in the electron dispersion of high-temperature cuprate superconductors. *Physical Review Letters*, 98(16):167003, 2007.

[320] J. Chang, S. Pailhes, M. Shi, M. Mnsson, T. Claesson, O. Tjernberg, J. Voigt, V. Perez, L. Patthey, N. Momono, M. Oda, M. Ido, A. Schnyder, C. Mudry, and J. Mesot. When low- and high-energy electronic responses meet in cuprate superconductors. *Physical Review B (Condensed Matter and Materials Physics)*, 75(22):224508, 2007.

[321] J. Hwang, E. J. Nicol, T. Timusk, A. Knigavko, and J. P. Carbotte. High energy scales in the optical self-energy of the cuprate superconductors. *Physical Review Letters*, 98(20):207002, 2007.

[322] W. Meevasana, X. J. Zhou, S. Sahrakorpi, W. S. Lee, W. L. Yang, K. Tanaka, N. Mannella, T. Yoshida, D. H. Lu, Y. L. Chen, R. H. He, Hsin Lin, S. Komiya, Y. Ando, F. Zhou, W. X. Ti, J. W. Xiong, Z. X. Zhao, T. Sasagawa, T. Kakeshita, K. Fujita, S. Uchida, H. Eisaki, A. Fujimori, Z. Hussain, R. S. Markiewicz, A. Bansil, N. Nagaosa, J. Zaanen,

T. P. Devereaux, and Z.-X. Shen. Hierarchy of multiple many-body interaction scales in high-temperature superconductors. *Physical Review B (Condensed Matter and Materials Physics)*, 75(17):174506, 2007.

[323] F. Ronning, K. M. Shen, N. P. Armitage, A. Damascelli, D. H. Lu, Z.-X. Shen, L. L. Miller, and C. Kim. Anomalous high-energy dispersion in angle-resolved photoemission spectra from the insulating cuprate $Ca_2CuO_2Cl_2$. *Physical Review B (Condensed Matter and Materials Physics)*, 71(9):094518, 2005.

[324] C. M. Varma, P. B. Littlewood, S. Schmitt-Rink, E. Abrahams, and A. E. Ruckenstein. Phenomenology of the normal state of cu-o high-temperature superconductors. *Phys. Rev. Lett.*, 63(18):1996–1999, Oct 1989.

[325] Chul Kim, S. R. Park, C. S. Leem, D. J. Song, H. U. Jin, H.-D. Kim, F. Ronning, and C. Kim. Electron removal self-energy and its application to $Ca_2CuO_2Cl_2$. *Physical Review B (Condensed Matter and Materials Physics)*, 76(10):104505, 2007.

[326] X.-H. Pan *et al. cond-mat/0610442*, 2006.

[327] Lijun Zhu, Vivek Aji, Arkady Shekhter, and C. M. Varma. Universality of single-particle spectra of cuprate superconductors. *Physical Review Letters*, 100(5):057001, 2008.

[328] T. Zhou and Z. D. Wang. High-energy dispersion anomaly induced by the charge modulation in high-T_c superconductors. *Physical Review B (Condensed Matter and Materials Physics)*, 75(18):184506, 2007.

[329] Efstratios Manousakis. String excitations of a hole in a quantum antiferromagnet and photoelectron spectroscopy. *Physical Review B (Condensed Matter and Materials Physics)*, 75(3):035106, 2007.

[330] Qiang-Hua Wang *et al. cond-mat/0610491*, 2006.

[331] Alexandru Macridin, M. Jarrell, Thomas Maier, and D. J. Scalapino. High-energy kink in the single-particle spectra of the two-dimensional hubbard model. *Physical Review Letters*, 99(23):237001, 2007.

[332] R. S. Markiewicz, S. Sahrakorpi, and A. Bansil. Paramagnon-induced dispersion anomalies in the cuprates. *Physical Review B (Condensed Matter and Materials Physics)*, 76(17):174514, 2007.

[333] A. S. Alexandrov and K. Reynolds. Angle-resolved photoemission spectroscopy of band tails in lightly doped cuprates. *Physical Review B (Condensed Matter and Materials Physics)*, 76(13):132506, 2007.

[334] Robert G. Leigh, Philip Phillips, and Ting-Pong Choy. Hidden charge 2e boson in doped mott insulators. *Physical Review Letters*, 99(4):046404, 2007.

[335] J. Graf, GH. Gweon, and A. Lanzara. *Physica C*, 194-197:460, 2007.

[336] Efstratios Manousakis. String excitations of a hole in a quantum antiferromagnet and photoelectron spectroscopy. *Physical Review B (Condensed Matter and Materials Physics)*, 75(3):035106, 2007.

[337] E. Manousakis. Possible observation of string excitations of a hole in a quantum antiferromagnet. *Physics Letters A*, 362:86, 2007.

[338] Andres Greco. $t-J$ model one-electron renormalizations: High energy features in photoemission experiments on high-T_c cuprates. *Solid state communication*, 142:318, 2007.

[339] Fei Tan, Yuan Wan, and Qiang-Hua Wang. Theory of high-energy features in single-particle spectra of hole-doped cuprates. *Physical Review B (Condensed Matter and Materials Physics)*, 76(5):054505, 2007.

[340] Pooja Srivastava, Saptarshi Ghosh, and Avinash Singh. High-energy kink in the dispersion of a hole in an antiferromagnet: Double-occupancy effects on electronic excitations. *Physical Review B (Condensed Matter and Materials Physics)*, 76(18):184435, 2007.

[341] D. S. Inosov and J. Fink and A. A. Kordyuk and S. V. Borisenko and V. B. Zabolotnyy and R. Schuster and M. Knupfer and B. Büchner and R. Follath and H. A. Dürr and W. Eberhardt and V. Hinkov and B. Keimer and H. Berger. Momentum and energy dependence of the anomalous high-energy dispersion in the electronic structure of high temperature superconductors. *Physical Review Letters*, 99(23):237002, 2007.

[342] A. Tanatar, J. Paglione, and L. Taillefer C. Petrovic. Anisotropic violation of the wiedemann-franz law at a quantum critical point. *Science*, 316:1320, 2007.

[343] J. Geck and S. V. Borisenko and H. Berger and H. Eschrig and J. Fink and M. Knupfer and K. Koepernik and A. Koitzsch and A. A. Kordyuk and V. B. Zabolotnyy and B. Büchner. Anomalous Quasiparticle Renormalization in $Na_0.73CoO_2$: Role of Interorbital Interactions and Magnetic Correlations. *Physical Review Letters*, 99(4):046403, 2007.

[344] Pouyan Ghaemi et al. *arXiv:0710.2526*.

[345] A. Kaminski, H. M. Fretwell, M. R. Norman, M. Randeria, S. Rosenkranz, U. Chatterjee, J. C. Campuzano, J. Mesot, T. Sato, T. Takahashi, T. Terashima, M. Takano, K. Kadowaki, Z. Z. Li, and H. Raffy. Momentum anisotropy of the scattering rate in cuprate superconductors. *Physical Review B (Condensed Matter and Materials Physics)*, 71(1):014517, 2005.

[346] E. Pavarini, I. Dasgupta, T. Saha-Dasgupta, O. Jepsen, and O. K. Andersen. Band-Structure Trend in Hole-Doped Cuprates and Correlation with T_{cmax}. *Phys. Rev. Lett.*, 87(4):047003, Jul 2001.

[347] C.M. Varma, Z. Nussinov, and Wim van Saarloos. Singular or non-fermi liquids. *Physics Reports*, 361:267–417, 2002.

[348] D. S. Inosov *et al. cond-mat/0703223*, 2007.

[349] M. Abdel-Jawad, M. P. Kennett, L. Balicas, A. Carrington, A. P. Mackenzie, R. H. McKenzie, and N. E. Hussey. Anisotropic scattering and anomalous normal-state transport in a high-temperature superconductor. *Nat. Phys.*, 2:821, 2006.

[350] M. Abdel-Jawad and J. G. Analytis and L. Balicas and A. Carrington and J. P. H. Charmant and M. M. J. French and N. E. Hussey. Correlation between the Superconducting Transition Temperature and Anisotropic Quasiparticle Scattering in $Tl_2Ba_2CuO_{6+\delta}$. *Physical Review Letters*, 99(10):107002, 2007.

[351] C. M. Varma. Pseudogap phase and the quantum-critical point in copper-oxide metals. *Phys. Rev. Lett.*, 83(17):3538–3541, Oct 1999.

[352] Eun-Ah Kim *et al. cond-mat/0705.4099*, 2007.

[353] Y. Kubo, Y. Shimakawa, T. Manako, and H. Igarashi. Transport and magnetic properties of $Tl_2Ba_2CuO_{6+\delta}$ showing a δ-dependent gradual transition from an 85-K superconductor to a nonsuperconducting metal. *Phys. Rev. B*, 43(10):7875–7882, Apr 1991.

[354] Shunji Sugai, Y. Takayanagi, J. Nohara, R. Shiozaki, and K. Takenaka. Electric resistivity and phase diagram viewed from charges in $La_{2-x}Sr_xCuO_4$. *Journal of the Physical Society of Japan*, 76:043710, 2007.

[355] Piers Coleman and Andrew J. Schofield. Quantum criticality. *Nature*, 433:226, 2005.

[356] M. Weber, P. Birrer, F. N. Gygax, B. Hitti, E. Lippelt, H. Maletta, and A. Schenck. *Hyperfine Interact.*, 63:207, 1990.

[357] Stephen Blundell. *Magnetism in Condensed Matter*. Oxford University Press, 2001.

Acknowledgment

There is a long list of people to whom I am grateful for their help and advice during the past three years. First of all I would like to thank Joël Mesot for giving me the opportunity to work on this Ph.D. project. During the last three years Joël has continued to support, advice, and to give constructive criticism from which I have benefited tremendously. I would also like to direct a thanks to my second supervisor Bertram Batlogg with whom I had several enlightening discussions. I also had many and long conversations with Christof Niedermayer and I did benefit a lot from his enormous knowledge collected during his many years of research in the field of high-T_c.

I have also had a vast number of very useful discussions with Stephane Pailhés, Henrik Rønnow, Niels Bech Christensen, Christopher Mudry and Ming Shi. Henrik introduced me very efficiently to the triple axis neutron scattering technique and I appreciated the dynamic atmosphere during the experiments. On the ARPES technique, both Stephane and I have profited from many discussions with Ming. The energy and enthusiasm coming from Ming, even between four and five in the morning, was appreciated as well.

During the years, I have spent days and nights with many interesting people who have been a great source of inspiration to me. The SANS experiments were often done together with the group of Ted Forgan. It was a pleasure to do experiments with Ted, Charlotte Bowel, Mark Laver, Stephen Brown, and recently also Jonathan White. I would also like to thank all the SANS instrument responsibles, Thomas Geue, Ronny Vavrin, Joachim Kohlbrecher, Robert Cubitt, and Charles Dewhurst, who all have helped me during the last three years. The experiments with Lars Märchler and Simon Strässle were also very fruitful. Finally, I should not forget to thank Joël for introducing me to this technique and if not physically present then always available on the phone.

I was very efficiently introduced to the triple axis technique, by Henrik as I mentioned above. The experiments on RITA II were done together with Niels and Christof to whom I am grateful for their high involvement in the experiments. I would also like to thank the instrument responsibles of IN14 and PANDA, Arno Hiess, Martin Boehm, Astrid Schneidewind, and Peter Link. They were always very efficient and helpful during the experiments. A thanks goes also to Kim Lefmann who has given me instructive lessons in triple axis spectroscopy. I also enjoyed the experiments with Linda Udby, Thomas Jensen, Niels Hessel Andersen, Stephane, Des McMorrow, Andrew Boothroyd, Russell Ewings, Lars Mächler, and Jorge Gavilano.

This Ph.D. work overlapped shortly with the work of Raffaele Gilardi and Jörg Voigt who kindly introduced me to the sample preparation techniques for the ARPES experiments. The demanding ARPES experiments could not have been done without the fruitful collaboration with the KTH-group, alias Martin Månsson, Thomas Claesson, and Oscar Tjernberg. Their key contributions to this project can not be emphasized enough. Stephane and Ming were also a lifeline

for me during these experiments. I should also not forget to thank Virginia Peres, Azzedine Bendounan, and Yasmine Sassa. Last but not least, I would like to thank the instrument responsibles Luc Patthey and Ming once again.

None of these experiments could have been done without the high quality crystals from Naoki Momono, Migaku Oda, and M. Ido. Their contributions are highly appreciated and I enjoyed meeting Naoki and Migaku at various conferences. Samples from O. Lipscompe and S.M. Hayden was also highly appreciated. Sample holders were always constructed with high precision (in both spatial and temporal dimensions) by the Christian Kägi group. I would also like to mention that Heinz Heer and Uwe Filges kindly assisted me in any issue related to hard- or soft-ware problems.

Over the years I also had useful discussions and theoretical input from many people. I would like to thank Andreas Schnyder, Sebastion Guerrero, Christopher Mudry, Chandra Varma and Christophe Berthod.

A special thanks goes to Michael Schneider with whom I shared office and who never hesitated to give me a hand if necessary. Michael helped me with many things ranging from administration issues at ETH to technical problems with the PPMS or magnets in generally. I really appreciated his help. A special thanks goes also to Petra Häfliger, Krunoslav Prsa and Nikolai Tsyrulin for the good office atmosphere. Thanks also to all my Ph.D. colleagues at LNS; Beni Thielemann, Sabine Streule, Conradin Krämer, Gelu Rotaru, Mark Janoschek, Britt Hansen, Mohamed Zayed, Jari í Hjøllum *et al.*.

Finally I would like to thank all the LNS and SLS staff who have not been mentioned explicitly so far. A thanks goes also to the people at ETH with whom I have been involved.

My family Simon and Chieko have also been extremely important to me during the last three years. Unfortunately they often had to live with my mental or physical absence when thing went well and with my difficult mood in the less good periods. Without the support from Chieko, I would never have been able to finish this project. Chieko also took the pain to proofread this thesis.

Despite the fact that I received help and advice from so many people, there might still be many mistakes and misunderstandings included in this thesis, for which I am entirely responsible.

Curriculum Vitae

Johan Chang
Weiermattweg 7
5200 Brugg

johan.chang@psi.ch

Surname: Chang
First name: Johan
Nationality: Danish
Date of birth:3. of September 1978

Education

[2004-] Ph.D. student affiliated to Laboratory for Neutron Scattering, Paul Scherrer Institute and ETH Zurich, Switzerland.
[2002-2004] Master degree in physics, at the university of Copenhagen. Result: 10/13. (This work was done mainly at Nagoya University in Japan)
[2001-2002] French degree: Diplôme d'études approfondies (DEA) "Physique de la matière et du rayonnement", Doctoral School of Physics, Université Joseph Fourier, Grenoble. Result: 12/20
[1998-2001] Bachelor degree in physics, University of Copenhagen, Niels Bohr institute. Result: 9.1/13
[1998-2001] Bachelor degree in mathematics, University of Copenhagen, Institute of mathematics. Result: 9.1/13
[1995-1998] High school in Vordingborg, Denmark. Result: 10/13

Communication skills

Danish - Mother tongue
English - Excellent (TOEFL 253/300)
French - Intermediate level (TCF 338)
Japanese - Intermediate level
German - High school level

Publications related to this thesis

Tuning competing orders in $La_{2-x}Sr_xCuO_4$ cuprate superconductors by the application of an external magnetic field
J. Chang, Ch. Niedermayer, R. Gilardi, N.B. Christensen, H.M. Rønnow, D.F. McMorrow, M. Ay, J. Stahn, O. Sobolev, A. Hiess, S. Pailhes, C. Baines, N. Momono, M. Oda, M. Ido and J. Mesot
arXiv:0712.2181, Submitted to PRL

Anisotropic scattering in slightly underdoped to optimally doped $La_{2-x}Sr_xCuO_4$
J. Chang, M. Shi, S. Pailhes , M. Månsson, T. Claesson, O. Tjernberg, A. Bendounan, L. Patthey, N. Momono, M. Ido, M. Oda, C. Mudry and J. Mesot
arXiv:0708.2782, Submitted to PRL

The coherent d-wave gap in underdoped $La_{1.855}Sr_{0.145}CuO_4$ as studied by angle resolved photoemission.
M. Shi, J. Chang, S. Pailhes, M.R. Norman, J.C. Campuzano , M. Månsson, T. Claesson, O. Tjernberg, A. Bendounan, L. Patthey, N. Momono, M. Ido, M. Oda, C. Mudry and J. Mesot
arXiv:0708.2333, Submitted to PRL

When low- and high-energy electronic responses meet in cuprates superconductors
J. Chang, S. Pailhes, M. Shi, M. Månsson, T. Claesson, O. Tjernberg, J. Voigt, V. Perez, L. Patthey, N. Momono, M. Ido, M. Oda, A. Schnyder, C. Mudry and J. Mesot
Physical Review B,**75**,224508 (2007)

On-board sample cleaver
M. Månsson, T. Claesson, U.O. Karlsson, O. Tjernberg, S. Pailhes, J. Chang, J. Mesot, M. Shi, L. Patthey, N. Momono, M. Oda, M. Ido
Review of scientific instuments,**78**, 076103 (2007)

Magnetic-field-induced spin excitations and renormalized spin gap of the underdoped superconductor $La_{1.895}Sr_{0.105}CuO_4$
J. Chang, A. Schnyder, R. Gilardi, H.M. Rønnow, S. Pailhes, N.B. Christensen, Ch. Niedermayer, D.F. McMorrow, A. Hiess, A. Stunault, M. Enderle, B. Lake, O. Sobolev N. Momono, M. Ido, M. Oda, C. Mudry and J. Mesot
Physical Review Letters,**98**,77004 (2007)

Neutron scattering investigations of the Abrikosov state of high-temperature superconductors
J. Chang, J. Mesot, R. Gilardi, J. Kohlbrecher, A.J. Drew , U. Divakar, S.J. Lister, S.L. Lee, S.P. Brown, D. Charalambous, E.M. Forgan, C.D. Dewhurst, R. Cubitt, N. Momono, and M. Oda
Physica B, **385**, 35 (2006)

Publications related to the master thesis

Birth and Morphological Evolution of Step Bunches under Electromigration
J. Chang, O. Pierre-louis and C. Misbah
Physical Review Letters, **96**, 195901 (2006)

Surface and bulk melting of small metal clusters
J. Chang and Erik Johnson
Philosophical Magazine, **85**, 3617-3627 (2005)

Melting temperature of a conical-needle shaped Sn
J. Chang, T. Sakai and H. Saka
Philosophical Magazine Letters, **85**, 247-257 (2005)

Nonlinear dynamics of vicinal surfaces
O. Pierre-Louis, G. Danker, J. Chang, K. Kassner and C. Misbah
Journal of Crystal Growth, **275**, 56-64 (2005)